

**PREDICTIVE MODEL ON WIND-DRIVEN RAINWATER
COLLECTIONS AT CURTAIN WALL FAÇADES OF TALL
BUILDINGS TOWARDS NEW VERTICAL RAINWATER
HARVESTING SYSTEMS IN TROPICAL URBAN SETTING**

MOZHGAN SAMZADEH

**FACULTY OF BUILT ENVIRONMENT
UNIVERSITI MALAYA
KUALA LUMPUR**

2024

**PREDICTIVE MODEL ON WIND-DRIVEN RAINWATER
COLLECTIONS AT CURTAIN WALL FAÇADES OF TALL
BUILDINGS TOWARDS NEW VERTICAL RAINWATER
HARVESTING SYSTEMS IN TROPICAL URBAN SETTING**

MOZHGAN SAMZADEH

**THESIS SUBMITTED IN FULFILMENT OF THE
REQUIREMENTS FOR THE DEGREE OF DOCTOR OF
PHILOSOPHY**

**FACULTY OF BUILT ENVIRONMENT
UNIVERSITI MALAYA
KUALA LUMPUR**

2024

ABSTRACT

Recent extreme precipitation events in frequency and intensity and increasing impervious surfaces – horizontally and vertically – in urban areas due to rapid horizontal and vertical expansion of built-up areas have resulted in increasing rainfall-runoff volume, amplifying urban flooding, as well as freshwater scarcity. Buildings can become more water-sustainable by adopting rainwater harvesting (RWH), which is a readily available alternative freshwater supply. However, the impact of vertical developments (a) on city level has resulted in distortion of the runoff process, 3D flow pattern, and sub-basin division, and (b) on building level has diminished the applicability of horizontal rooftop RWH because the ratio of roof surface area to vertical façade surface area has reduced significantly in tall buildings and roof RWH has been mainly replaced with roof garden concept.

In light of these challenges, this research aims to evaluate the possibility of incorporating curtainwall building façades into an existing catchment area for Wind-Driven Rain (WDR) harvesting. This would divert WDR loads from the avenue runoff. This study employed (1) one-year in-situ measurement to quantify WDR amounts on building façades (rainfall-runoff) in urban areas and (2) semi-empirical models to predict the spatial distribution of WDR loads. In-situ measurements of WDR amount (S_{wdr}) and meteorological parameters, i.e., wind direction (D), wind speed (U), and horizontal rainfall (S_h), were performed on a pilot building at the campus of Universiti Malaya in Kuala Lumpur, Malaysia. The influence of local wind speed (U) and horizontal rainfall intensity (R_h) on WDR intensity (R_{wdr}) was analysed. After the data cleaning process, only 65 out of 93 rain events were confirmed to be valid in-situ datasets for model validation. The R_{wdr} was subsequently calculated by the WDR equations of the semi-empirical models, i.e., ISO standard 15927-3 and ASHRAE standard 160P. The accuracy performance of both models to predict R_{wdr} were analysed mainly through analytical

comparative assessments, i.e., coefficient of determinations (R^2) and normalised root mean square deviation (NRMSD) between the in-situ dataset and the calculated dataset of R_{wdr} (mm/h). Through the cross-multiplication method using in-situ datasets and semi-empirical models' datasets, the proposed WDR coefficients were determined for ISO (α) and ASHRAE (F_L) models to predict the spatial distribution of WDR on tall building façades (up to > 50 m) in Kuala Lumpur. The results declared that the higher the building façade height, the greater the harvested R_{wdr} would be. The ISO model predicted 56% to 70% for non-potable usage reduction per square metre (lcd) at heights less than 10 metres to greater than 10 metres, respectively. The ASHRAE model predicted 57% to 109% for non-potable usage reduction per square metre (lcd) at heights less than 10 metres to greater than 50 metres, respectively. This research output, combined with further experimental investigations on actual tall building curtain walls, may lead to the adoption of vertical rainwater harvesting as a feasible method for water sustainability in tall buildings. The generated in-situ dataset can also be subjected to computational fluid dynamic analysis and model validation for WDR research in building science.

Keywords: Vertical rainwater harvesting (VRWH), 3D rainwater harvesting, Wind-driven rain (WDR), Experimental measurement, Semi-empirical models

ABSTRAK

Kejadian hujan yang melampau baru-baru ini dalam kekerapan dan keamatan dan peningkatan permukaan kalis air - secara mendatar dan menegak - di kawasan bandar akibat pengembangan kawasan binaan mendatar dan menegak yang pesat telah mengakibatkan peningkatan jumlah air larian hujan, menguatkan banjir bandar dan juga kekurangan air tawar. Bangunan boleh menjadi lebih lestari air dengan mengguna pakai penuaian air hujan (RWH), yang merupakan bekalan air tawar alternatif yang sedia ada. Walau bagaimanapun, kesan pembangunan menegak (a) pada aras bandar telah mengakibatkan herotan proses larian, corak aliran 3D, dan pembahagian sub-lembangan, dan (b) pada aras bangunan telah mengurangkan kebolehgunaan RWH atas bumbung mendatar kerana nisbah luas permukaan bumbung kepada luas permukaan fasad menegak telah berkurangan dengan ketara di bangunan tinggi dan bumbung RWH telah digantikan dengan konsep taman bumbung.

Memandangkan cabaran ini, penyelidikan ini bertujuan untuk menilai kebolehlaksanaan untuk menggabungkan Hujan dipacu angin (WDR) yang jatuh pada fasad bangunan yang tidak digunakan ke dalam kawasan tadahan sedia ada untuk kegunaan tidak boleh diminum, sekali gus mengalihkannya daripada air larian jalan. Kajian ini menggunakan (1) pengukuran in-situ satu tahun untuk mengukur jumlah WDR pada fasad bangunan (curahan air larian) di kawasan bandar dan (2) model separa empirikal untuk meramalkan taburan ruang bagi beban WDR. Pengukuran in-situ bagi jumlah WDR (S_{wdr}) dan parameter meteorologi iaitu, arah angin (D), kelajuan angin (U), dan hujan mendatar (S_h) telah dilakukan ke atas bangunan perintis di kampus Universiti Malaya di Kuala Lumpur, Malaysia. Pengaruh kelajuan angin tempatan (U) dan intensiti hujan mendatar (R_h) terhadap keamatan WDR (R_{wdr}) telah dianalisis. Selepas proses pembersihan data, hanya 65 daripada 93 kejadian hujan telah disahkan sebagai set data yang sah untuk pengesahan model. R_{wdr} kemudiannya dikira oleh persamaan WDR bagi model separa empirikal iaitu,

standard ISO 15927-3 dan standard ASHRAE 160P. Prestasi ketepatan kedua-dua model untuk meramalkan R_{wdr} dianalisis terutamanya melalui penilaian perbandingan analitikal iaitu, pekali penentuan (R^2) dan sisihan purata kuasa dua punca ternormal (NRMSD) antara set data in-situ dan set data terkira R_{wdr} (mm/h). Melalui kaedah pendaraban silang menggunakan set data in-situ dan set data model separa empirikal, pekali WDR yang dicadangkan telah ditentukan untuk model ISO (α) dan ASHRAE (F_L) untuk meramalkan taburan ruang WDR pada fasad bangunan tinggi (sehingga > 50 m) di Kuala Lumpur. Keputusan mengisytiharkan bahawa semakin tinggi ketinggian fasad bangunan, semakin besar R_{wdr} yang dituai. Model ISO meramalkan 56% hingga 70% untuk pengurangan penggunaan tidak boleh diminum pada ketinggian kurang daripada 10 meter hingga lebih daripada 10 metre masing-masing. Model ASHRAE meramalkan 57% hingga 109% untuk pengurangan penggunaan tidak boleh diminum bagi setiap meter persegi pada ketinggian kurang daripada 10 meter hingga lebih daripada 50 meter masing-masing. Dengan penyiasatan eksperimen lanjut ke atas dinding tirai bangunan tinggi sebenar, hasil penyelidikan ini mungkin membawa kepada penggunaan penuaian air hujan menegak sebagai kaedah yang boleh dilaksanakan untuk kelestarian air di bangunan tinggi. Dataset in-situ yang dijana juga boleh tertakluk kepada analisis dinamik bendalir pengiraan dan pengesahan model untuk kerja penyelidikan WDR dalam sains pembinaan.

Kata kunci: Penuaian air hujan menegak (VRWH), penuaian air hujan 3D, Hujan dipacu angin (WDR), Pengukuran eksperimen, Model separa empirikal

ACKNOWLEDGEMENTS

I would like to express my heartfelt gratitude and appreciation to my supervisors; Dr. Zunaibi Abdullah, who allowed me to contribute to this groundbreaking topic and be part of his research team prior to his retirement; Associate. Prof. Ts. Dr. Nazli Che Din for his never-ending support, guidance, and trust in me and his enthusiastic and optimistic attitude; and Associate. Prof. Sr. Dr. Norhayati Mahyuddin for her priceless wisdom, counsel, and standing by me through thick and thin during this long journey.

I would also like to thank Dr. Muhammad Azzam Ismail; Dr. Mastura Adam; and Sr. Dr. Raha Sulaiman for their constructive comments, which helped me to improve this manuscript. Many thanks to all the faculty of Built Environment staff (management, academic, and non-academic) for their incredible assistance whenever I needed sound advice or a helping hand.

I gratefully acknowledge the funding source that made the WDR gauges' manufacturing and one-year measurement's equipment and process possible; Institute of Research Management & Services (IPPP), Research Management & Innovation Complex, Universiti Malaya, Kuala Lumpur, Malaysia, Grant No.: RG317-14AFR. I would like to acknowledge METMalaysia-Utama (Malaysian Meteorological Department) for providing the daily horizontal rainfall data (S_h).

My eternal appreciation goes to my parents for their immense love, patience, and support to start this academic journey during their lives on Mother Earth, and for being my true guiding light since they transitioned. I am extremely grateful to my sister and life mentor, Dr. Zhaleh, for showing me how to stand up for what I believe in – in life, in love, and everything in between – which helped me to complete this challenging course in the school of Earth.

TABLE OF CONTENTS

Abstract.....	ii
<i>Abstrak.....</i>	iv
Acknowledgements.....	vi
Table of Contents	vii
List of Figures.....	xiv
List of Tables	xxii
List of Symbols and Abbreviations.....	xxviii
List of Appendices.....	xxx
CHAPTER 1: INTRODUCTION.....	1
1.1. Preface.....	1
1.2. Problem Statement	2
1.3. Research Gap	5
1.4. Research Questions	8
1.5. Research Aim and Objectives	9
1.6. Research Methodology.....	9
1.7. Significance of the Study	14
1.8. Research Scope and Limitations	16
1.9. Summary	16
CHAPTER 2: LITERATURE REVIEW.....	20
2.1. Climate Change and Freshwater Accessibility	20
2.1.1. Malaysia Water Status	23
2.1.2. Water Sustainability	25
2.1.3. Built Environment Developments Impacts on Natural Water Cycle	27
2.2. Rainwater Harvesting (RWH).....	28

2.2.1. Drivers for RWH	29
2.2.2. Benefits of RWH	30
2.2.3. Definitions of RWH.....	33
2.2.4. Components of RWH	34
2.2.4.1. Catchment Materials	35
2.2.4.2. Runoff Coefficient	37
2.2.4.3. Catchment Location	39
2.2.4.4. Catchment Size.....	39
2.2.4.5. Conveyance System	40
2.2.5. Implementation of RWH in Malaysia	43
2.3. Vertical Expansion – The Dominant Built-Up Pattern	46
2.3.1. Definition of Vertical Expansion – Vertical Urbanisation	47
2.3.2. Definition of Tall Building	48
2.3.3. Wind Flow Patterns around Tall Buildings	49
2.3.4. Distortion of the Runoff Process by Tall Buildings	51
2.3.5. Three-Dimensional Flow Path.....	52
2.3.6. Sub-Basin Division.....	54
2.3.7. Water Sustainability in Tall Buildings	55
2.3.8. Façade Rainwater Harvesting	56
2.4. Seasonal Classifications in Malaysia	57
2.4.1. Wind	58
2.4.2. Rainfall	58
2.4.3. An overview on the weather conditions in Malaysia from 2017 to 2021.....	59
2.4.3.1. Wind and Rainfall Patterns in 2017	60
2.4.3.2. Wind and Rainfall Patterns in 2018	61
2.4.3.3. Wind and Rainfall Patterns in 2019	62

2.4.3.4. Wind and Rainfall Patterns in 2020	63
2.4.3.5. Wind and Rainfall Patterns in 2021	64
2.5. Experimental Field Measurement – Meteorological Parameters	66
2.5.1. Wind Measurement – Wind Speed (U) and Wind Direction (D)	67
2.5.2. Horizontal Rainfall (S_h) Measurement	70
2.6. Experimental Field Measurement – WDR	72
2.6.1. WDR Definition	72
2.6.2. Wall-Mounted WDR Gauges	74
2.6.2.1. CTH Gauge	75
2.6.2.2. TUD Gauge	76
2.6.2.3. TUE-I Gauge	77
2.6.2.4. TUE-II Gauge	77
2.6.2.5. CTH-II Gauge	78
2.6.2.6. EMPA Gauge	79
2.6.2.7. KUT Gauge	79
2.6.3. WDR Gauge Design Guidelines	80
2.6.4. WDR Measurement (S_{wdr})	81
2.7. Spatial Distribution Pattern of WDR on Building Façades	83
2.7.1. WDR Catch Ratio (η)	83
2.7.2. WDR Intensity (R_{wdr})	87
2.8. Semi-Empirical Model – WDR Prediction	89
2.8.1. Overview of Semi-Empirical Models’ Development	91
2.8.2. ISO Standard 15927-3 Model	95
2.8.2.1. Terrain Roughness Coefficient (C_R)	97
2.8.2.2. Terrain Topography Coefficient (C_T)	98
2.8.2.3. Obstruction Factor (O)	98

2.8.2.4. Wall Factor (W)	99
2.8.2.5. The Hourly Reference Wind Speed (U_{10})	100
2.8.2.6. The Angle ($D - \theta$)°	101
2.8.2.7. Spell / Rain Event.....	101
2.8.3. ASHRAE Standard 160P Model	102
2.8.3.1. Exposure Factor (F_E).....	103
2.8.3.2. Rain Deposition Factor (F_D).....	103
2.9. Summary	104
CHAPTER 3: METHODOLOGY.....	107
3.1. UM WDR Gauge.....	108
3.1.1. UM WDR Wall-Mounted Gauge Design	108
3.2. Experimental Measurement (In-Situ).....	112
3.2.1. Building Site	112
3.2.2. Measurement Setup	113
3.2.2.1. Wind Speed (U) and Wind Direction (D)	114
3.2.2.2. Horizontal Rainfall (S_h).....	114
3.2.2.3. WDR (S_{wdr}) – Vertical WDR Harvesting.....	116
3.2.2.4. Time Accuracy of the Data Logger.....	118
3.3. Data Cleaning Process – Generating In-Situ Dataset.....	119
3.3.1. Preprocessing of In-Situ Measured Data	119
3.3.2. Data Units’ Conversions.....	120
3.3.3. Spatial Distribution of WDR – Catch Ratio (η) Calculation	122
3.3.4. Data Cleaning Process – Generating In-situ Dataset.....	122
3.4. Semi-Empirical Models	123
3.4.1. Application of the Models – Generating the Models’ Datasets.....	123
3.4.2. Validation of the Models – Accuracy Performance Assessments.....	124

3.4.3. Prediction of Mean R_{wdr} – Application of Proposed WDR Coefficients	124
3.5. Summary	126
CHAPTER 4: RESULTS AND ANALYSES	128
4.1. Preprocessing of In-Situ Measured Data.....	128
4.1.1. Meteorological Raw Data and Harvested WDR - Season 1	130
4.1.2. Meteorological Raw Data and Harvested WDR - Season 2	131
4.1.3. Meteorological Raw Data and Harvested WDR - Season 3	133
4.1.4. Meteorological Raw Data and Harvested WDR - Season 4	134
4.1.5. Summary of Findings – In-Situ Measured Data.....	136
4.1.6. WDR Intensity (R_{wdr}) (mm/h)	141
4.1.7. Impact of Horizontal Rainfall Intensity (R_h) and Wind Speed (U) on the WDR Intensity (R_{wdr})	142
4.2. Data Cleaning Process – Generating In-Situ Dataset.....	146
4.2.1. Data Cleaning Process – Season 1	147
4.2.2. Data Cleaning Process – Season 2	149
4.2.3. Data Cleaning Process – Season 3	151
4.2.4. Data Cleaning Process – Season 4	153
4.3. Spatial Distribution of Wind-Driven Rain – Catch Ratio (η) Calculation.....	155
4.3.1. WDR Catch Ratio (η) – Season 1	155
4.3.2. WDR Catch Ratio (η) – Season 2	159
4.3.3. WDR Catch Ratio (η) – Season 3	163
4.3.4. WDR Catch Ratio (η) – Season 4	166
4.3.5. WDR Catch Ratio (η) As a Function of Wind Speed (U) and Height (H)..	169
4.3.6. WDR Catch Ratio (η) As a Function of Horizontal Rainfall Intensity (R_h) and Height (H)	173
4.3.7. Summary of Findings – WDR Catch Ratio (η)	177

4.4. Semi-Empirical Models	178
4.4.1. Application of the Models	178
4.4.1.1. Step One: Determining Validated In-Situ R_{wdr} Dataset	179
4.4.1.2. Step Two: Determining Correction Factors and Parameters for ISO Standard 15927-3 and ASHRAE Standard 160P Models	180
4.5. R_{wdr} Datasets of In-Situ and Predicted ISO Standard 15927-3 and ASHRAE STANDARD 160P Models.....	186
4.5.1. In-situ and Predicted R_{wdr} Datasets – Season 1	187
4.5.2. In-situ and Predicted R_{wdr} Datasets – Season 2	189
4.5.3. In-situ and Predicted R_{wdr} Datasets – Season 3	191
4.5.4. In-situ and Predicted R_{wdr} Datasets – Season 4	193
4.5.5. Summary of Findings – Comparative Analyses of In-Situ and Predicted R_{wdr} Datasets.....	195
4.6. Validating the Semi-Empirical Models.....	196
4.6.1. Accuracy of the Predicted R_{wdr} Dataset – Season 1	199
4.6.2. Accuracy of the Predicted R_{wdr} Dataset – Season 2.....	202
4.6.3. Accuracy of the Predicted R_{wdr} Dataset – Season 3.....	205
4.6.4. Accuracy of the Predicted R_{wdr} Dataset – Season 4.....	208
4.6.5. Summary of Findings – Accuracy of the Predictive Performance of the Models	216
4.7. Determining WDR Coefficients for the Semi-Empirical Models.....	220
4.7.1. Application of the Proposed WDR Coefficients (α) and (F_L)	220
4.7.2. Comparison between R_{wdr} In-situ, Predicted ISO Standard 15927-3 and ASHRAE Standard 160P Models Using Proposed WDR Coefficients	223
4.7.2.1. Proposed R_{wdr} Dataset – Season 1	223
4.7.2.2. Proposed R_{wdr} Dataset – Season 2	226

4.7.2.3. Proposed R_{wdr} Dataset – Season 3	228
4.7.2.4. Proposed R_{wdr} Dataset – Season 4	231
4.7.2.5. Summary of Findings – Accuracy of the Predictive Performance of the Semi-empirical Models Using Proposed WDR Coefficients	238
4.8. Feasibility Analysis of Possible Vertical Harvestable WDR on Building Façade	239
4.9. Summary	246
CHAPTER 5: CONCLUSION	248
5.1. Summary of Findings	248
5.1.1. Research Objective 1	248
5.1.2. Research Objective 2	249
5.1.3. Research Objective 3	252
5.1.4. Research Objective 4	254
5.2. Research Contributions	257
5.3. Research Implications	259
5.4. Recommendations and Future Works	260
References	262
Appendices	284

List of Figures

Figure 1.1. Tall building surface areas; Roof area (a) and Façade areas (b).....	4
Figure 1.2. Classification of RWH based on the catchment surface area (Che-Ani et al., 2009; Iman, 2012; Jamaluddin & Huang, 2007; Sonbol, 2006; Zhong et al., 2022).....	6
Figure 1.3. Overview of the research flow diagram.....	10
Figure 1.4. Schematic representation of the two parts in WDR research: (a) assessment of the impinging WDR intensity (R_{wdr}) and (b) assessment of the response of the building wall (Blocken & Carmeliet, 2012; Blocken et al., 2013; Deb Nath, 2015; Van Goethem, 2014).	11
Figure 1.5. Research design diagram: research questions, research objectives, research methods, and expected outcomes	13
Figure 1.6. Research significance diagram	15
Figure 1.7. Research flow diagram	19
Figure 2.1. The hydrological cycle or water cycle (Skinn, 2020).....	22
Figure 2.2. Distribution of water resources on Earth (WASH, 2018)	23
Figure 2.3. Water as a connector among the global commitments adopted in 2015 (Uhlenbrook & Connor, 2019).....	26
Figure 2.4. Main RWH drivers and their reasons/causes (Mbua, 2013).....	30
Figure 2.5. Environmental and economic benefits of RWH.....	32
Figure 2.6. Simplified diagram illustrating absorption over time for several materials assuming a constant rainfall (Dorsey et al., 1996).....	36
Figure 2.7. Rainwater harvesting classification based on the size of catchment area (Jamaluddin & Huang, 2007; Shaari et al., 2009).....	40
Figure 2.8. RWH conveyance systems used in different building types, reproduced from (Adnan et al., 2020).....	41

Figure 2.9. Indirectly (a) and Directly (b) pumped RWH systems schematic diagrams (Istchuk & Ghisi, 2023)	43
Figure 2.10. Schematic depiction of the wind loading chain on tall building façades (Abu-Zidan, 2019; Abu-Zidan et al., 2022; Yuvaraj et al., 2022).....	50
Figure 2.11. Comparison of conventional flow path and changed flow path by a building (Yoo et al., 2021)	53
Figure 2.12. Comparison of sub-basin division and flow path in urban basin with and without the tall building (Yoo et al., 2021).....	55
Figure 2.13. Annual rainfall trends for Peninsular Malaysia (MESTECC, 2018).....	59
Figure 2.14. Total annual rainfall 2017 (METMalaysia, 2017).....	60
Figure 2.15. Total annual rainfall 2018 (METMalaysia, 2018).....	62
Figure 2.16. Total annual rainfall 2019 (METMalaysia, 2019).....	63
Figure 2.17. Total annual rainfall 2020 (METMalaysia, 2020).....	64
Figure 2.18. Total annual rainfall 2021 (METMalaysia, 2021).....	65
Figure 2.19. Van der Hoven horizontal wind-speed spectrum. The energy of the wind is mainly situated in the peaks that are situated at a period of 1 year, 4 days, 1 day and 1 minute. In the “spectral gap” between 10 minutes and about 1 hour, little energy is situated and the mean wind speed shows stationarity for these time periods (Amoloye, 2012; Blocken & Carmeliet, 2004; Patnaik & Samantaray, 2010).	70
Figure 2.20. Wind-driven rain vector.....	72
Figure 2.21. Wall-mounted plate-type Wind-driven rain gauge where the collection area fits flush into the vertical façade surface (Blocken and Carmeliet (2004))	75
Figure 2.22. Wind-driven rain gauge CTH (Hogberg et al., 1999).....	76
Figure 2.23. Wind-driven rain gauge TUD (Blocken & Carmeliet, 2006b; FJR van Mook, 2002)	76
Figure 2.24. Wind-driven rain gauge TUE-I (Van Mook (1998)	77

Figure 2.25. Wind-driven rain gauge TUE-II (Blocken & Carmeliet, 2006b)	78
Figure 2.26. Wind-driven rain gauge Tilted; CTH-II (Blocken & Carmeliet, 2006b; Hogberg, 2002)	78
Figure 2.27. Wind-driven rain gauge EMPA (Kubilay et al., 2014a).....	79
Figure 2.28. Wind-driven rain gauge KUT (Dobravalskis et al., 2018)	80
Figure 2.29. WDR catch ratio (η) distribution on the windward façade of the isolated high-rise building (a), with low-rise building present (b), for $U_{10} = 10$ m/s and $R_h = 5$ mm/h, (Blocken et al., 2009b).....	84
Figure 2.30. WDR catch ratio distribution on the windward façade of the isolated high-rise building (a), with low-rise building present (b), for $U_{10} = 10$ m/s and $R_h = 30$ mm/h, (Blocken et al., 2009b).....	85
Figure 2.31. Typical shape of vertical profile and spatial distribution of wind-driven rain (WDR) on building walls (Cho et al., 2020; Yoo et al., 2022)	87
Figure 2.32. Simplified spatial distribution of wind-driven rain (WDR) on building walls, adopted from (Cho et al., 2020)	89
Figure 2.33. Wall factor values (Coutu et al., 2013; Deb Nath, 2015; ISO 15927-3, 2009)	100
Figure 2.34. Conceptual research framework – Measurements and Modelling	106
Figure 3.1. Feasibility framework of vertical WDR harvesting from building façade (modified from Chacha (2015) and Li et al. (2010))	107
Figure 3.2. Elevation and section of the WDR gauge collector; dimensions in mm.	111
Figure 3.3. Aerial view of the building site	113
Figure 3.4. Meteorological instruments using by Malaysian Meteorological Department for horizontal rainfall (S_h) measurements, (a) tipping bucket, (b) automatic horizontal rain gauges, (c) conventional horizontal rain gauges (MMD, 2024)	115

Figure 3.5. The orientation of the pilot building and locations of the WDR gauges on the building: (a) Floor plan, (b) the façade (not to scale), (c) location of gauge T02 (at 2.75 m height), (d) location of gauge B02 (at 1 m height).....	117
Figure 3.6. The pilot building and position of the WDR gauges on the façades (a) South view (b) Meteorological mast on the rooftop of the building at the parking area.	117
Figure 3.7. Unit conversion steps to calculate WDR intensity value (mm/h)	121
Figure 3.8. Research methodology diagram	127
Figure 4.1. The daily harvested WDR amounts (S_{wdr}) measured by 8 WDR gauges during the Monsoon Transitional Period (Season 1)	131
Figure 4.2. The daily harvested WDR amounts (S_{wdr}) measured by 8 WDR gauges during the Southwest Monsoon (Season 2)	132
Figure 4.3. The daily harvested WDR amounts (S_{wdr}) measured by 8 WDR gauges during the Monsoon Transitional Period (Season 3)	134
Figure 4.4. The daily harvested WDR amounts (S_{wdr}) measured by 8 WDR gauges during the Northeast Monsoon (Season 4)	136
Figure 4.5. Measurements of WDR (ml) by 8 wall-mounted gauges installed on the Top Corner (T01-T04) and Bottom Middle (B01-B04) of the façades over each tropical season (April 2017 – March 2018)	139
Figure 4.6. Harvested WDR (ml) by 8 wall-mounted gauges (collector area of each gauge is $20 \times 20 \text{ cm}^2$) installed two (Top and Bottom) on each façade (NE, NW, SW, SE) during each tropical season (April 2017 – March 2018)	140
Figure 4.7. Seasonal calculated WDR intensity (R_{wdr}) for each façade (two WDR gauges on each façade) during 4 tropical seasons. (Rainfall intensity is determined as the average rainfall rate in mm/h for specific rainfall duration and a selected frequency. One millimetre (mm) of rainfall is the equivalent of one litre of water per square metre). .	142

Figure 4.8. Impact of seasonal meteorological data on WDR intensity (R_{wdr}) parameter during 4 tropical seasons (April 2017 – March 2018).	143
Figure 4.9. Daily meteorological data; wind speed (U) (km/h), horizontal rainfall intensity (R_h) (mm/h), and WDR intensity (R_{wdr}) (mm/h) for each season	145
Figure 4.10. Q-Q plot and box plot graphs of wind (U), horizontal rainfall intensity (R_h), and WDR intensity (R_{wdr}) in season one.....	148
Figure 4.11. Q-Q plot and box plot graphs of wind (U), horizontal rainfall intensity (R_h), and WDR intensity (R_{wdr}) in season two.....	150
Figure 4.12. Q-Q plot and box plot graphs of wind (U), horizontal rainfall intensity (R_h), and WDR intensity (R_{wdr}) in season three.....	152
Figure 4.13. Q-Q plot and box plot graphs of wind (U), horizontal rainfall intensity (R_h), and WDR intensity (R_{wdr}) in season four	154
Figure 4.14. Catch ratio values (η) at WDR gauge locations for the entire monitoring period of season 1.....	157
Figure 4.15. Average daily WDR catch ratio (η) and horizontal rainfall intensity (R_h) values at driving rain gauge locations based on the entire monitoring period of season 1	158
Figure 4.16. Catch ratio values (η) at WDR gauge locations for the entire monitoring period of season 2.....	161
Figure 4.17. Average daily WDR catch ratio (η) and horizontal rainfall intensity (R_h) values at driving rain gauge locations based on the entire monitoring period of season 2	162
Figure 4.18. Catch ratio values (η) at WDR gauge locations for the entire monitoring period of season 3.....	164

Figure 4.19. Average daily WDR catch ratio (η) and horizontal rainfall intensity (R_h) values at driving rain gauge locations based on the entire monitoring period of season 3	165
Figure 4.20. Catch ratio values (η) at WDR gauge locations for the entire monitoring period of season 4.....	167
Figure 4.21. Average daily WDR catch ratio (η) and horizontal rainfall intensity (R_h) values at driving rain gauge locations based on the entire monitoring period of season 4	168
Figure 4.22. Coefficient of determination (R^2) analysis results between WDR catch ratio (η) on windward façades and wind speed (m/s) during season 1 to season 4 (The R^2 shown is based on cubic polynomial regression; $0.2 < \text{Value} < 0.4$ is weak, $0.4 < \text{Value} < 0.6$ is moderate, and $0.6 < \text{Value} < 0.8$ means strong effect on the catch ratio variable).	173
Figure 4.23. Coefficient of determination (R^2) analysis results between WDR catch ratio (η) on windward façades and horizontal rainfall intensity (mm/h) during season 1 to season 4 (The R^2 shown is based on cubic polynomial regression; $0.2 < \text{Value} < 0.4$ is weak, $0.4 < \text{Value} < 0.6$ is moderate, and $0.6 < \text{Value} < 0.8$ means strong effect on the catch ratio variable).	176
Figure 4.24. Comparison of the Mean R_{wdr} (mm/h) between Experimental measurement, predicted ISO and ASHRAE models for two positions (Top and Bottom) on the windward façade (NW-SW) – Season One.....	188
Figure 4.25. Comparison of the Mean R_{wdr} (mm/h) between Experimental measurement, predicted ISO and ASHRAE models for two positions (Top and Bottom) on the windward façade (NW-SW) – Season Two	190
Figure 4.26. Comparison of the Mean R_{wdr} (mm/h) between Experimental measurement, predicted ISO and ASHRAE models for two positions (Top and Bottom) on the windward façade (NW-SW) – Season Three	192

Figure 4.27. Comparison of the Mean R_{wdr} (mm/h) between Experimental measurement, predicted ISO and ASHRAE models for two positions (Top and Bottom) on the windward façade (NE-NW) – Season Four	194
Figure 4.28. Experimental measurement vs. Predicted ISO and ASHRAE models' regression scatter plots of datasets Mean R_{wdr} (mm/h) for two positions (Top and Bottom) at the windward façade (NW-SW) during season One (The R^2 shown is based on order 4 (quadratic) polynomial regression; $0.2 < \text{Value} < 0.4$ is weak, $0.4 < \text{Value} < 0.6$ is moderate, and $0.6 < \text{Value} < 0.8$ means strong effect on the catch ratio variable).	202
Figure 4.29. Experimental measurement vs. Predicted ISO and ASHRAE models' regression scatter plots of datasets Mean R_{wdr} (mm/h) for two positions (Top and Bottom) at the windward façade (NW-SW) during season Two (The R^2 shown is based on order 4 (quadratic) polynomial regression; $0.2 < \text{Value} < 0.4$ is weak, $0.4 < \text{Value} < 0.6$ is moderate, and $0.6 < \text{Value} < 0.8$ means strong effect on the catch ratio variable).	205
Figure 4.30. Experimental measurement vs. Predicted ISO and ASHRAE models' regression scatter plots of datasets Mean R_{wdr} (mm/h) for two positions (Top and Bottom) at the windward façade (NW-SW) during season Three (The R^2 shown is based on order 4 (quadratic) polynomial regression; $0.2 < \text{Value} < 0.4$ is weak, $0.4 < \text{Value} < 0.6$ is moderate, and $0.6 < \text{Value} < 0.8$ means strong effect on the catch ratio variable).	208
Figure 4.31. Experimental measurement vs. Predicted ISO and ASHRAE Models' regression scatter plots of datasets Mean R_{wdr} (mm/h) for two positions (Top and Bottom) at the windward façade (NE-NW) during season Four (The R^2 shown is based on order 4 (quadratic) polynomial regression; $0.2 < \text{Value} < 0.4$ is weak, $0.4 < \text{Value} < 0.6$ is moderate, and $0.6 < \text{Value} < 0.8$ means strong effect on the catch ratio variable).	211
Figure 4.32. Comparison of the Mean R_{wdr} (mm/h) between Experimental measurement and Predicted values using the Proposed WDR coefficients for two positions (Top (a) and Bottom (b)) on the windward façade (NW-SW) – Season One.....	225

Figure 4.33. Comparison of the Mean R_{wdr} (mm/h) between Experimental measurement and Predicted values using the Proposed WDR coefficients for two positions (Top (a) and Bottom (b)) on the windward façade (NW-SW) – Season Two	227
Figure 4.34. Comparison of the Mean R_{wdr} (mm/h) between Experimental measurement and Predicted values using the Proposed WDR coefficients for two positions (Top (a) and Bottom (b)) on the windward façade (NW-SW) – Season Three	230
Figure 4.35. Comparison of the Mean R_{wdr} (mm/h) between Experimental measurement and Predicted values using the Proposed WDR coefficients for two positions (Top (a) and Bottom (b)) on the windward façade (NE-NW) – Season Four.....	232
Figure 4.36. Illustration of spatial distribution of Mean (daily average) R_{wdr} (WDR intensity) (mm/h) (annual (65 Rain events) and seasonal (S01, S02, S03, S04)) at different heights (m) on building windward façade (per square metre) based on the Proposed ISO 15927-3 and ASHRAE 160P models' WDR coefficients.....	243
Figure 4.37. Illustration of potential reduction non-potable (%) and potable (%) water usages based on Proposed model prediction of harvestable R_{wdr} (per square metre) at different heights (m) on building windward façade.....	245

List of Tables

Table 2.1. Rainwater demand for domestic application (MSMA, 2012).....	25
Table 2.2. Run-off coefficients for the traditional roofing materials (Biswas & Mandal, 2014; Eslamian & Eslamian, 2021; Sendanayake et al., 2014; Worm & Hattum, 2006)	38
Table 2.3. Policies and guidelines related to RWHS under Malaysian government (Fakhira & Nazri, 2022; Lee et al., 2016; Shaari, 2020).....	45
Table 2.4. Government act and strategic plan related to sustainable water management (12MP, 2021; Shaari, 2020).....	46
Table 2.5. Duration of seasons in Malaysia in 2017. Data derived from (Bahari et al., 2017)	58
Table 2.6. Summary of the WDR gauges characteristics.....	80
Table 2.7. Parameters in the ISO Standard roughness coefficient (C_R) (ASHRAE Standard 160P, 2016).....	98
Table 2.8. Obstruction factor (O) values (Coutu et al., 2013)	99
Table 2.9. Exponent for different upwind exposure (ASHRAE Standard 160P, 2016).....	101
Table 2.10. ASHRAE exposure factor (F_E) (ASHRAE Standard 160P, 2016)	103
Table 2.11. Rain deposition factor (F_D) (ASHRAE Standard 160P, 2016)	104
Table 3.1. Absolute adhesion water on five vertically placed plates made of different materials	108
Table 3.2. Possible error sources and modifications to minimize in the gauge design stage	110
Table 3.3. The WDR gauge components list	112
Table 3.4. Time reporting possible errors of the data logger and the implementation considerations.....	118

Table 4.1. Periods of seasons in Malaysia in 2017, data derived from Bahari et al. (2017)	129
Table 4.2. Maximum and minimum WDR receiver event (in total) in each season and the maximum and minimum WDR receiver gauge in each respective event (*Trace ≤ 1 ml WDR amounts (S_{wdr}))	141
Table 4.3. Normality tests processing and standard error summary of validated cases in season one (10 out of 14 cases (71%) were accepted)	147
Table 4.4. Normality tests processing and standard error summary of validated cases in season two (20 out of 22 cases (90%) were accepted)	149
Table 4.5. Normality tests processing and standard error summary of validated cases in season three (8 out of 13 cases (61%) were accepted)	151
Table 4.6. Normality tests processing and standard error summary of validated cases in season four (28 out of 44 cases (63%) were accepted)	153
Table 4.7. Average daily WDR catch ratio values (η) at driving rain gauge locations based on the entire monitoring period of season 1	159
Table 4.8. Average daily WDR catch ratio (η) values at driving rain gauge locations based on the entire monitoring period of season 2	160
Table 4.9. Average daily WDR catch ratio values (η) at driving rain gauge locations based on the entire monitoring period of season 3	166
Table 4.10. Average daily WDR catch ratio values (η) at driving rain gauge locations based on the entire monitoring period of season 4	166
Table 4.11. Parameters used for calculation of R_{wdr} by semi-empirical models ISO 15927-3 (2009) and ASHRAE Standard 160P (2016) in this study	180
Table 4.12. Determined parameters for ISO standard 15927-3 and ASHRAE standard 160P models - Season One	182

Table 4.13. Determined parameters for ISO standard 15927-3 and ASHRAE standard 160P models – Season Two	183
Table 4.14. Determined parameters for ISO standard 15927-3 and ASHRAE standard 160P models – Season Three	184
Table 4.15. Determined parameters for ISO standard 15927-3 and ASHRAE standard 160P models – Season Four	185
Table 4.16. R_{wdr} (WDR intensity) (mm/h) on windward façades - Experimental measurement / ISO model / ASHRAE model – Season One.....	188
Table 4.17. R_{wdr} (WDR intensity) (mm/h) on windward façades - Experimental measurement / ISO model / ASHRAE model – Season Two	191
Table 4.18. R_{wdr} (WDR intensity) (mm/h) on windward façades - Experimental measurement / ISO model / ASHRAE model – Season Three	193
Table 4.19. R_{wdr} (WDR intensity) (mm/h) on windward façades - Experimental measurement / ISO model / ASHRAE model – Season Four.....	195
Table 4.20. Performance of different coefficient of determinations (R^2) values by the polynomial regression analyses.....	198
Table 4.21. Difference (D) (Negative D value shows underestimation, Positive D value shows overestimation), coefficient of determination (R^2), root mean square deviation (RMSD), and normalised root mean square deviation (NRMSD) for predicted R_{wdr} (WDR intensity) (mm/h) by ISO model and ASHRAE model – Season One	212
Table 4.22. Difference (D) (Negative D value shows underestimation, Positive D value shows overestimation), coefficient of determination (R^2), root mean square deviation (RMSD), and normalised root mean square deviation (NRMSD) for predicted R_{wdr} (WDR intensity) (mm/h) by ISO model and ASHRAE model – Season Two.....	213
Table 4.23. Difference (D) (Negative D value shows underestimation, Positive D value shows overestimation), coefficient of determination (R^2), root mean square deviation	

(RMSD), and normalised root mean square deviation (NRMSD) for predicted R_{wdr} (WDR intensity) (mm/h) by ISO model and ASHRAE model – Season Three.....	214
Table 4.24. Difference (D) (Negative D value shows underestimation, Positive D value shows overestimation), coefficient of determination (R^2), root mean square deviation (RMSD), and normalised root mean square deviation (NRMSD) for predicted R_{wdr} (WDR intensity) (mm/h) by ISO model and ASHRAE model – Season Four.....	215
Table 4.25. Predictive performance of the ISO and ASHRAE models for the top and bottom locations on the building façade for each season ($0.20 < \text{NRMSD} < 0.50$ is relatively accurate).....	220
Table 4.26. Determined WDR Coefficient - Season One	221
Table 4.27. Determined WDR Coefficient – Season Two.....	221
Table 4.28. Determined WDR Coefficient – Season Three.....	221
Table 4.29. Determined WDR Coefficient – Season Four.....	222
Table 4.30. Proposed WDR coefficients for ISO Standard 15927-3 model (α) and ASHRAE STANDARD 160P model (F_L) to predict R_{wdr} for each tropical season in Kuala Lumpur, Malaysia	223
Table 4.31. R_{wdr} (WDR intensity) (mm/h) discrepancies (D) using the WDR coefficients of the Standard Models (ISO Standard 15927-3 and ASHRAE 160P) and the Proposed WDR Coefficients on windward façades (NW-SW) – Season One	225
Table 4.32. R_{wdr} (WDR intensity) (mm/h) discrepancies (D) using the WDR coefficients of the Standard Models (ISO Standard 15927-3 and ASHRAE 160P) and the Proposed WDR Coefficients on windward façades (NW-SW) – Season Two.....	228
Table 4.33. R_{wdr} (WDR intensity) (mm/h) discrepancies (D) using the WDR coefficients of the Standard Models (ISO Standard 15927-3 and ASHRAE 160P) and the Proposed WDR Coefficients on windward façades (NW-SW) – Season Three.....	230

Table 4.34. R_{wdr} (WDR intensity) (mm/h) discrepancies (D) using the WDR coefficients of the Standard Models (ISO Standard 15927-3 and ASHRAE 160P) and the Proposed WDR Coefficients on windward façades (NE-NW) – Season Four	233
Table 4.35. Proposed difference (D), coefficient of determination (R^2), root mean square deviation (RMSD), and normalised root mean square deviation (NRMSD) for predicted R_{wdr} (WDR intensity) (mm/h) by Proposed WDR coefficients for ISO Standard 15927-3 model (α) and ASHRAE standard 160P model (F_L) – Season One	234
Table 4.36. Proposed difference (D), coefficient of determination (R^2), root mean square deviation (RMSD), and normalised root mean square deviation (NRMSD) for predicted R_{wdr} (WDR intensity) (mm/h) by Proposed WDR coefficients for ISO Standard 15927-3 model (α) and ASHRAE standard 160P model (F_L) – Season Two	235
Table 4.37. Proposed difference (D), coefficient of determination (R^2), root mean square deviation (RMSD), and normalised root mean square deviation (NRMSD) for predicted R_{wdr} (WDR intensity) (mm/h) by Proposed WDR coefficients for ISO 15927-3 model (α) and ASHRAE 160p model (F_L) – Season Three	236
Table 4.38. Proposed difference (D), coefficient of determination (R^2), root mean square deviation (RMSD), and normalised root mean square deviation (NRMSD) for predicted R_{wdr} (WDR intensity) (mm/h) by Proposed WDR coefficients for ISO Standard 15927-3 model (α) and ASHRAE STANDARD 160P model (F_L) – Season Four	237
Table 4.39. Predictive performance of the ISO and ASHRAE models using Proposed WDR coefficients for the top and bottom locations on the building façade for each season ($0.20 < NRMSD < 0.50$ is relatively accurate)	238
Table 4.40. Determined parameters for Proposed ISO 15927-3 and ASHRAE standard 160P models at different heights (m) on building windward façade	240
Table 4.41. Spatial distribution of Mean (daily average) R_{wdr} (WDR intensity) (mm/h) (annual and seasonal (S01, S02, S03, S04)) at different heights (m) on building windward	

façade (per square metre) based on Proposed ISO 15927-3 and ASHRAE standard 160P models' WDR coefficients.....	241
Table 4.42. Potential reduction non-potable (%) and potable (%) water usages based on Proposed model prediction of harvestable R_{wdr} (per square metre) at different heights (m) on building windward façade derived from Table 4.42	244

Universiti Malaysia

List of Symbols and Abbreviations

Acronyms

<i>ASHRAE</i>	american society of heating, refrigerating and air conditioning engineers
<i>CFD</i>	computational fluid dynamics
<i>Exp.</i>	experimental (in-situ)
<i>HAM</i>	heat-air moisture
<i>ISO</i>	international organisation for standardisation
<i>NE</i>	north-east
<i>NRMSD</i>	normalised root mean square deviation
<i>NW</i>	north-west
<i>RMSD</i>	root mean square deviation
<i>RWH</i>	rainwater harvesting
<i>RWHS</i>	rainwater harvesting system
<i>SE</i>	south-east
<i>SW</i>	south-west
<i>VRWH</i>	vertical rainwater harvesting
<i>WDR</i>	wind-driven rain

Roman symbols

C_R	terrain roughness coefficient	-
C_T	topography coefficient	-
D	wind direction	°
F_D	rain deposition factor	-
F_E	rain exposure factor	-
F_L	empirical constant	kg·s/(m ³ .mm)
H	height	m
K_R	terrain factor	-
L	length	m
O	obstruction factor	-
R_h	horizontal rainfall intensity	mm/h
R_{wdr}	wind-driven rain intensity	mm/h
S_h	horizontal rainfall amount	mm
S_{wdr}	wind-driven rain amount	ml - mm
t	time	s
U	wind speed	m/s
U_{10}	reference wind speed at 10 m height	m/s
W	wall factor	-
W	width	m

x, y	cartesian coordinates	-
y	height above the ground	m
y_0	aerodynamic roughness length	m
y_{min}	minimum height	m
V_t	raindrop's terminal velocity	m/s

Greek symbols

α	WDR coefficient	s/m
η	catch ratio	-
θ	(D - θ) is the angle in the horizontal plane between the wind direction (D) and the normal to the façade (θ)	°

Universiti Malaysia

List of Appendices

APPENDIX A. Meteorological Raw Data and Harvested WDR	284
APPENDIX A 1. The meteorological data record of Monsoon Transitional Period (Season 1).....	284
APPENDIX A 2. The daily harvested WDR amounts (S_{wdr}) measured by 8 WDR gauges during the Monsoon Transitional Period (Season 1) (*WDR amounts of 1 ml or less from the tipping-bucket are considered as a “Trace” amount and is not recorded).....	285
APPENDIX A 3. The meteorological data record of Southwest Monsoon (Season 2)	286
APPENDIX A 4. The daily harvested WDR amounts (S_{wdr}) measured by 8 WDR gauges during the Southwest Monsoon (Season 2) (*WDR amounts of 1 ml or less from the tipping-bucket are considered as a “Trace” amount and is not recorded).....	287
APPENDIX A 5. The meteorological data record of Monsoon Transitional Period (Season 3).....	288
APPENDIX A 6. The daily harvested WDR amounts (S_{wdr}) measured by 8 WDR gauges during the Monsoon Transitional Period (Season 3) (*WDR amounts of 1 ml or less from the tipping-bucket are considered as a “Trace” amount and is not recorded).....	289
APPENDIX A 7. The meteorological data record of Northeast Monsoon (Season 4)	290
APPENDIX A 8. The daily harvested WDR amounts (S_{wdr}) measured by 8 WDR gauges during the Northeast Monsoon (Season 4) (*WDR amounts of 1 ml or less from the tipping-bucket are considered as a “Trace” amount and is not recorded).....	292
APPENDIX B. Determining Validated In-Situ Rwdr Dataset.....	294
APPENDIX B 1. Validated experimental (in-situ) measurement data (meteorological parameters and wind-driven rain intensity (R_{wdr}) values) for model validation – Season 1	294

APPENDIX B 2. Validated experimental (in-situ) measurement data (meteorological parameters and wind-driven rain intensity (R_{wdr}) values) for model validation – Season 2	295
APPENDIX B 3. Validated experimental (in-situ) measurement data (meteorological parameters and wind-driven rain intensity (R_{wdr}) values) for model validation – Season 3	296
APPENDIX B 4. Validated experimental (in-situ) measurement data (meteorological parameters and wind-driven rain intensity (R_{wdr}) values) for model validation – Season 4	297

CHAPTER 1: INTRODUCTION

1.1. Preface

Recently, Malaysia's water situation has shifted from one of relative abundance to one of scarcity; water management is becoming increasingly complicated due to large concentrations of population and commercial activities in the urban areas, particularly in the capital city, Vertical Kuala Lumpur (FAO, 2020).

Cities and local governments have started to realise that buildings are one of the main consumers of freshwater and have begun to take action. Endogenous development, as the core concept in the planning profession, strives to obtain self-sustained development in urban areas (Vázquez-Barquero & Rodríguez-Cohard, 2016), using local endogenous resources within the urban boundary to the maximum extent possible to supply the demand. Therefore, rainwater harvesting (RWH) has become more prominent in every development as part of its contribution to preserving freshwater resources and restoring Mother Earth.

However, traditional horizontal RWH approaches from rooftops and grounds are not responsive, practical, or economically viable in today's modern metropolitan environments due to the dominating built-up pattern of continual vertical expansion. In order to fully utilise this natural resource and enable the creation of sustainable buildings, we must devise a new method for harvesting rainwater for tall buildings.

As Dobravalskis et al. (2018) declared, all rain has a horizontal velocity due to wind acting upon rain droplets, which is called wind-driven rain (WDR). Due to this natural interaction, WDR hits all buildings' façades and it makes buildings' façades the available potential catchment areas for vertical RWH.

This new approach to water resource management brings along more benefits in comparison with the horizontal RWH, such as harvesting potentially cleaner water because it can collect rainwater before ground/roof contamination occurs and utilise it without significant treatment for non-potable purposes. Moreover, façade areas have not only larger surfaces but also more unused spaces compared to rooftops in modern urban areas.

Accordingly, tall buildings can benefit from integrated vertical RWH from façade areas in order to optimise their water consumption and minimise their impact on the potable water network supply and environment (Beorkrem & Damiano, 2018).

This study explores the feasibility of harvesting WDR from tall building's curtain walls as an alternative available water resource for non-potable usage in Kuala Lumpur city.

1.2. Problem Statement

Extreme precipitation events have increased in frequency and intensity (IPCC, 2018) and amplified the risk of flooding and landslide activity at regional scale (Blöschl et al., 2017; Gariano & Guzzetti, 2016) as a result of increasing global temperature (WMO, 2022).

Considering that the amount of freshwater on earth is ecologically intact and the population is growing rapidly, the world's water resources are in crisis, and freshwater scarcity is inevitable (National Geographic, 2023). A new report by the Global Commission on the Economics of Water has found that the supply of freshwater on Earth will fall short of the demand by 40% before 2030 (Mazzucato et al., 2023), mainly due to rising demand in the industrial and domestic sectors (WWAP, 2019). Water has become a major challenge in today's societies, particularly in the context of the transition to sustainability.

Malaysia is relatively rich in water resources, with an average annual rainfall of 2562.35 mm (Tan, 2018). But because of the uneven distribution of rainfall over space and time,

some areas have been suffering from dry spells, while others have been affected by major flooding over the last decades (Lani et al., 2018b).

Following the water crisis in 1998 (Lani et al., 2018b), the Malaysian government pays attention to the RWH system (RWHS) as an alternative resource to reduce overdependence on rivers and other surface water. The Ministry of Housing and Local Government has encouraged citizens to install RWHS in their existing dwellings. Now, RWHS is compulsory for new developments in Kuala Lumpur and encouraged in Selangor and Melaka (San, 2023).

Acknowledging that in rapid growing cities, horizontal expansion has become constrained and cities are growing vertically (Van Gerrewey et al., 2022). These tall buildings place additional load on the existing power grid, water supply, and sewer systems. Tall buildings require an abundance of energy for operations and utilities, including water. They also change and complicate the route of rainfall-runoff in urban areas.

On the other hand, over the past decade, the roof garden concept as a green infrastructure has become more popular; quite effective for alleviating the urban heat island effect in a city (Heidarinejad & Esmaili, 2015; Lehmann, 2014; Qin et al., 2013; Shafique et al., 2018). Residents prefer to use the building roof as a garden, since this has recreational benefits (Kim et al., 2018; Taib et al., 2019; Zhang et al., 2020), particularly in tall buildings. In addition, in these buildings, retention of rainwater operated by the vegetation (integration of green roof and roof RWH) may reduce the overall volume of collected water that may be used for exploitation (Cauteruccio & Lanza, 2023). Plus, the IGCC code (International Green Construction Code) does not allow for water to be collected by green roofs for potable water use; if used for irrigation, it would be fine, but it should be kept separate from other uses (ICC, 2021).

Under these circumstances, rooftop rainwater harvesting (two-dimensional / 2D RWHS) can be considered inadequate or impossible for not only potable water but also indoor non-potable water consumption in tall buildings. Furthermore, in tall buildings, the ratio of vertical façade surface areas is much higher than the ratio of roof surface areas (Figure 1.1). Considering the fact that all rain has a horizontal velocity due to wind interaction (wind-driven rain), therefore falls more and mainly onto the buildings' façades (Dobravalskis et al., 2018). Thus, building façades as available catchment areas in tall buildings can provide cleaner surfaces compared with rooftop areas for harvesting rainwater (three-dimensional / 3D RWHS).

These challenges and prospects highlight the potential to collect WDR from building façades as a new catchment area for rainwater harvesting. However, to the knowledge of the author and as Dobravalskis et al. (2018) have mentioned in their research (laboratory observation), there has not been any research on real-time and long-term WDR measurement to evaluate this possibility; it needs an in-situ dataset measured in real-time based on the guidelines and standards for generalisation through predictive model validation.

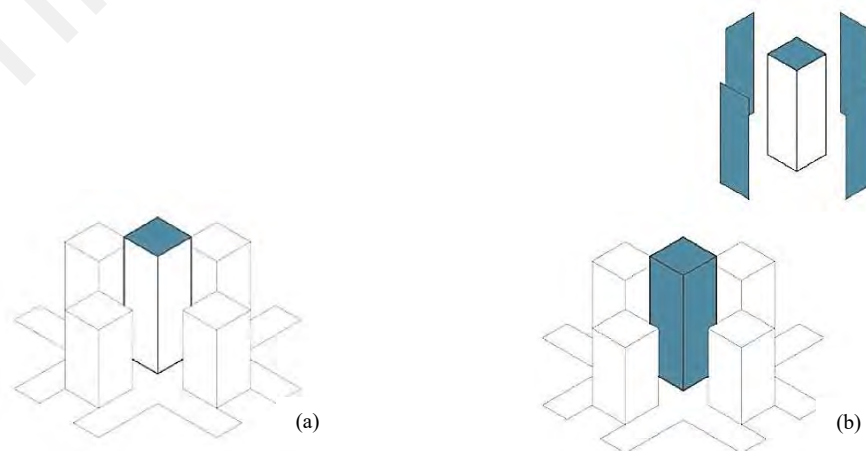


Figure 1.1. Tall building surface areas; Roof area (a) and Façade areas (b)

Besides, the impact of tall buildings on rainfall-runoff volume and flow path at the city level requires to be addressed too. In conventional two-dimensional cities, buildings were regarded as a factor that slows down the runoff, and their impact on changes in infiltration was important (Cea et al., 2010; Chan, 2012; Dottori & Todini, 2013; Schubert et al., 2008). While, as Yoo et al. (2021) discussed in the three-dimensional megacities, tall buildings play as an additional source of runoff through the intercepted rainfall by the façade surface areas. They contribute to distortion of the runoff process (Blocken et al., 2013; Gao et al., 2021; Zhou et al., 2018; Zhou et al., 2019), creating three-dimensional flow path, and sub-basin divisions that will be explained in more detail in Chapter 2.

In view of the water consumption pattern, Malaysia is categorised as one of the countries with high domestic water consumption, above the recommended target by the World Health Organisation (WHO) (Lani et al., 2018b). In some highly developed and populated areas, such as Selangor, Putrajaya, and the Federal Territory of Kuala Lumpur, the river resources have been fully exploited (Lani et al., 2018b), and 25 rivers have been declared dead due to high levels of pollution (Rahman, 2021). Hence, to alleviate strain on the water network, especially the potable supply, it is essential to make optimal use of the available rainfall for non-potable usage to mitigate pressure on the potable supply.

1.3. Research Gap

Considering all the aforementioned circumstances, challenges and prospects, in a tropical and vertically developing city like Kuala Lumpur, building walls can be a new available alternative catchment area to be explored for RWH (Figure 1.1), particularly for tall buildings. Note that wind causes a large portion of rain, which called wind-driven rain (WDR), to collide with the building wall surfaces, and making these surfaces even more suitable catchment areas for harvesting rainwater.

However, both the vertical surface areas and the presence of such natural phenomenon (WDR loads) have been completely disregarded (Dobravalskis et al., 2018), and resulting in increased rainfall-runoff volume on the avenue.

Figure 1.2 illustrates one of the most frequently used classification chart of existing in-used RWH systems at small– medium and large –scales based on the catchment area.

As indicated in the figure, one aspect of RWH that has not yet been practiced is façade surface areas at building scale (Che-Ani et al., 2009; Iman, 2012; Jamaluddin & Huang, 2007; Sonbol, 2006; Zhong et al., 2022).

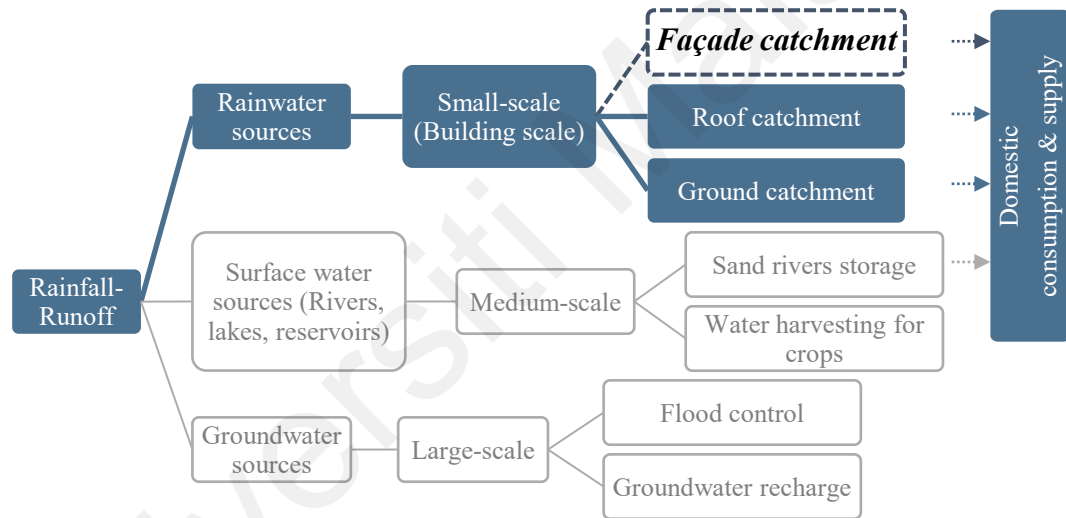


Figure 1.2. Classification of RWH based on the catchment surface area (Che-Ani et al., 2009; Iman, 2012; Jamaluddin & Huang, 2007; Sonbol, 2006; Zhong et al., 2022)

WDR has been studied and referred to as a damaging factor to the durability of building envelopes in scientific research publications since years ago. Only a few research papers recently in the field of WDR in scientific journals (Cho et al., 2020; Dobravalskis et al., 2018; Yoo et al., 2022), conference (Fernando R et al., 2014) and a project report (Pinto et al., 2020) have shown the growing interest in the new perspective towards the WDR phenomenon as a water resource for vertical RWH.

In these studies, WDR has been explored and collected in lab conditions (observation) or from a few rain events (in-situ measurement) and yet no research under real-time and in-situ conditions for a long-term have been carried out to generate a dataset for model validation to estimate the possible harvestable amount of WDR loads on building walls.

To determine the amount of WDR load on building façades, there are three scientific approaches, i.e., (1) measurements, (2) semi-empirical methods, and (3) numerical simulations (Blocken & Carmeliet, 2004). The measurement of WDR is time- and labor-intensive, expensive, and location-specific (Chen et al., 2022; Zhou et al., 2023); the semi-empirical methods are based on correlations between meteorological data, building geometry, topography and measured WDR load, noting that there is a dearth of such datasets globally (Zhou et al., 2023); and the numerical simulation methods are mainly used to evaluate the reaction of the building to WDR. As a result, the first two approaches have been primarily employed and cited in WDR studies when the aim of research is collecting, calculating, and estimating the quantification of WDR loads on building walls.

However, as Pérez-Bella et al. (2018) declared, access to hourly meteorological data as the fundamental prerequisite for the semi-empirical models is not possible in many places, which, together with the high calculation effort required, limits its use and the generalisation of reliable standards such as ISO standard 15927-3 and ASHRAE standard 160P. Thus, attempts to establish more valid datasets for this purpose are required. Deb Nath (2015) has also highlighted the essential need for WDR datasets derived from experimental measurements under different climatic conditions to develop and/or validate semi-empirical models, as well as numerical simulation models in the field of WDR research on building façades.

They also declared that the WDR estimated by semi-empirical models may show large deviations from the field measurements, and therefore, to improve the predictive performance of the models, the WDR coefficients need to be refined. To achieve the

suitable constant values conducting statistical equations and cross-comparison analyses are required. For instance, the ISO 15927-3 standard model does not consider façade orientation and offers the same values for all four façades. Thus, experimental measurements (in-situ) on more façade orientations are required to refine coefficient values.

Moreover, because of the limitations of the direct measurements of WDR there is a lack of study to investigate the influence of wind speed (U), wind direction (D) and horizontal rainfall intensity (R_h) on the spatial distribution of WDR (η) on building façades in a long-term measurement campaign (Deb Nath, 2015; Gao et al., 2021).

This thesis has provided the following research questions to address all the research gaps stated above.

1.4. Research Questions

The following research questions have been provided to address the aforementioned research gap:

1. What are the requirements to investigate the feasibility of vertical rainwater harvesting from tall building facades as a new catchment area in the tropical climate of Kuala Lumpur?
2. What is a scientific approach to quantify real-time WDR load on building façades and its meteorological dominant factors during the complete tropical monsoon seasons?
3. How should data transformation (extract/transform/load (ETL)) be processed to generate a valid WDR dataset for model validation?
4. How to predict the spatial distribution of harvestable amounts of WDR loads impinging on tall building façades in Kuala Lumpur?

1.5. Research Aim and Objectives

The aim of this study is to evaluate the feasibility of vertical RWH through in-situ measurement and predictive modelling of the WDR amount impinging on the curtain wall façades of the tall buildings, as a new catchment area. Research objectives to facilitate answering the research questions, and in line with the aim of this study, are articulated as follows:

1. To explore the feasibility of vertical rainwater harvesting system from wind-driven rain based on Kuala Lumpur's weather and vertical expansion pattern,
2. To investigate a complete tropical monsoon season under meteorological condition with in-situ experiment in Kuala Lumpur for real-time WDR load measurement on facades of tall buildings,
3. To generate a valid in-situ WDR dataset for the validation of semi-empirical models,
4. To determine WDR coefficient constants of the semi-empirical models to refine their predictive performance accuracy for estimation of harvestable amounts of WDR loads on building façades in Kuala Lumpur.

1.6. Research Methodology

To explore the possibility of vertical rainwater harvesting from building façades, existing literature regarding the current weather condition, freshwater status, tall building impacts, and vertical WDR harvesting is studied in chapter 2, literature review, as the first step of this research.

A quantitative approach is conducted to measure and predict WDR loads on building walls in the tropical city of Kuala Lumpur, Malaysia. Malaysia has a tropical climate. Each year has four tropical seasons. To understand climate patterns and changes, a one-

year measurement campaign is essential. For this reason, this study performs in-situ measurement over the course of one-year to collect and record WDR and local weather data patterns thoroughly.

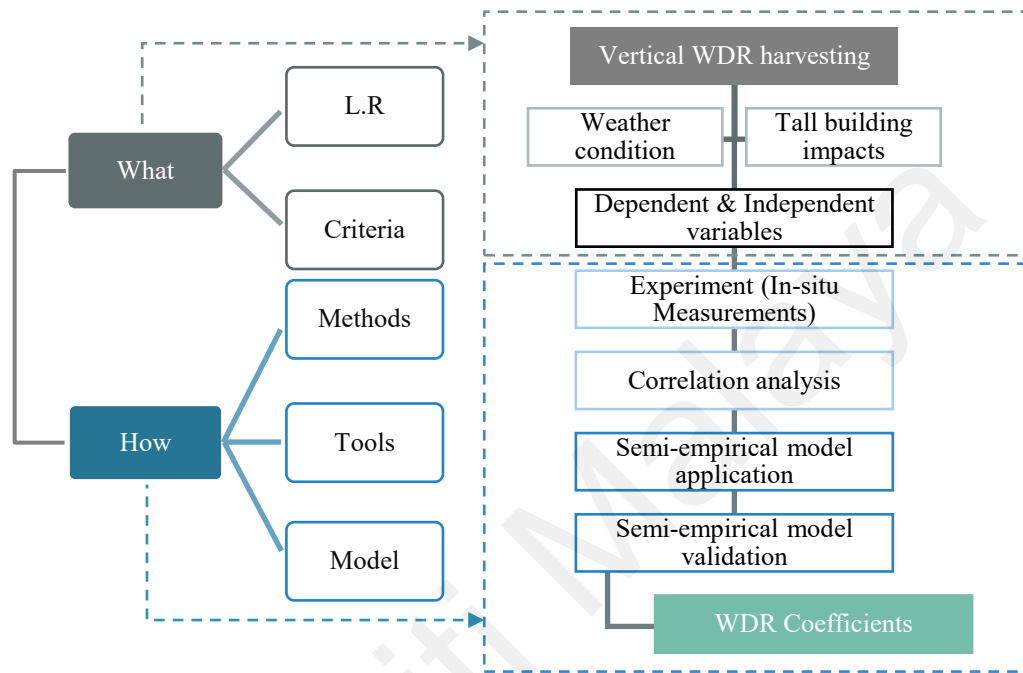


Figure 1.3. Overview of the research flow diagram

In the field of building science, research on WDR, concerning the interaction between WDR and building façades, two different aspects are discerned (Blocken & Carmeliet, 2004; Blocken et al., 2013) (Figure 1.4):

- a) the determination of impinging WDR, before impact, and
- b) the assessment of the reaction of the building to WDR

The scope of this research is related to the first part of WDR research; a) the determination of impinging WDR intensity (R_{wdr}) to investigate the amount of raindrops on the building wall. There are several factors influencing the WDR intensity (R_{wdr}) such as building geometry, wind speed (U), wind direction (D), and horizontal rainfall intensity (R_h).

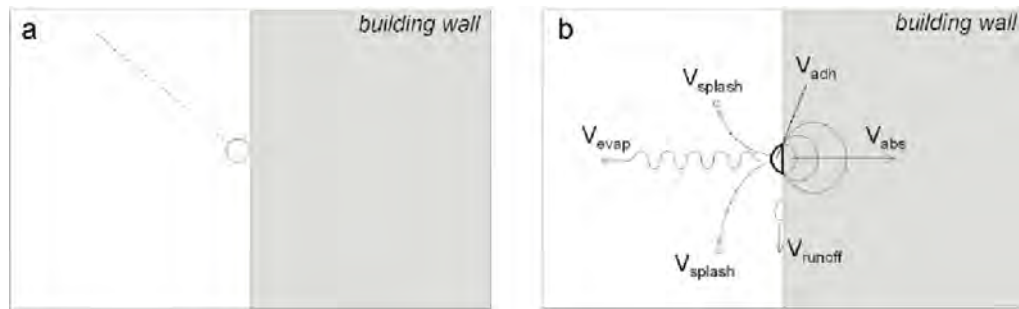


Figure 1.4. Schematic representation of the two parts in WDR research: (a) assessment of the impinging WDR intensity (R_{wdr}) and (b) assessment of the response of the building wall (Blocken & Carmeliet, 2012; Blocken et al., 2013; Deb Nath, 2015; Van Goethem, 2014).

According to the scientific reviews conducted by Blocken and Carmeliet (2004); Blocken et al. (2013), the assessment methods to quantify WDR loads on building façades can be categorised as:

- i. Experimental methods [In-situ methods]
- ii. Semi-empirical methods
- iii. Numerical methods [Simulation methods]

Numerical methods are mainly used for the second aspect of WDR research: assessment of the reaction of the building to WDR (Figure 1.4 – (b)). Only the semi-empirical methods allow characterising the exposure of a large number of sites with a reasonable use of time, resources and calculation effort (Pérez-Bella et al., 2018). ISO standard 15927-3 and ASHRAE standard 160P Models describe semi-empirical methods that establish the use of hourly climate data as a starting point for calculating directional WDR exposure (ASHRAE Standard 160P, 2016; ISO 15927-3, 2009). As stated by (Pérez-Bella et al., 2018) this directional calculation is based on the same WDR relationship used for the scalar calculation, also incorporating a cosine projection factor $\cos(D - \theta)$, which relates the wind direction and the orientation of the façade analysed. Furthermore, Blocken and Carmeliet (2004) emphasized that one should use these equations specifically for WDR on buildings, not for free-field WDR measurements. Because of

surrounding terrain and architectural factors, local phenomena affect the wind flow pattern and, in turn, the building's WDR loads, which might vary substantially from free-field WDR.

Thus, based on the scope of this study, the first two methods; Experimental and Semi-empirical methods, are employed for in-situ dataset generation and model validation to determine the WDR coefficient and predict the WDR intensity on the building wall for VRWH purposes.

Experimental method – Experimental measurements are a critical component of model validation and development, as they are needed to validate the accuracy of the model predictions (Dunbar, 2018). Although the experimental methods have provided extensive knowledge on the impingement of WDR on building façades, they are both labour-intensive and restricted in their use (Blocken & Carmeliet, 2004).

In this study, to generate a valid set of harvested WDR loads data on the façades of a building plus its relevant meteorological parameters' data, one-year in-situ WDR measurements are carried out at the campus of Universiti Malaya in Kuala Lumpur.

Semi-empirical method – Semi-empirical methods were initially established to investigate the relationships between the quantity of WDR intensity (R_{wdr}) and measured meteorological data such as wind speed (U), wind direction (D), and horizontal rainfall intensity (R_h). By comparing the in-situ measured dataset and the calculated results from the semi-empirical model equations (ISO standard 15927-3 Model and ASHRAE standard 160P Model), the WDR coefficient is determined, verified, and the model is validated to predict the WDR intensity on building façades based on the local climate in the future (see Figure 1.5).

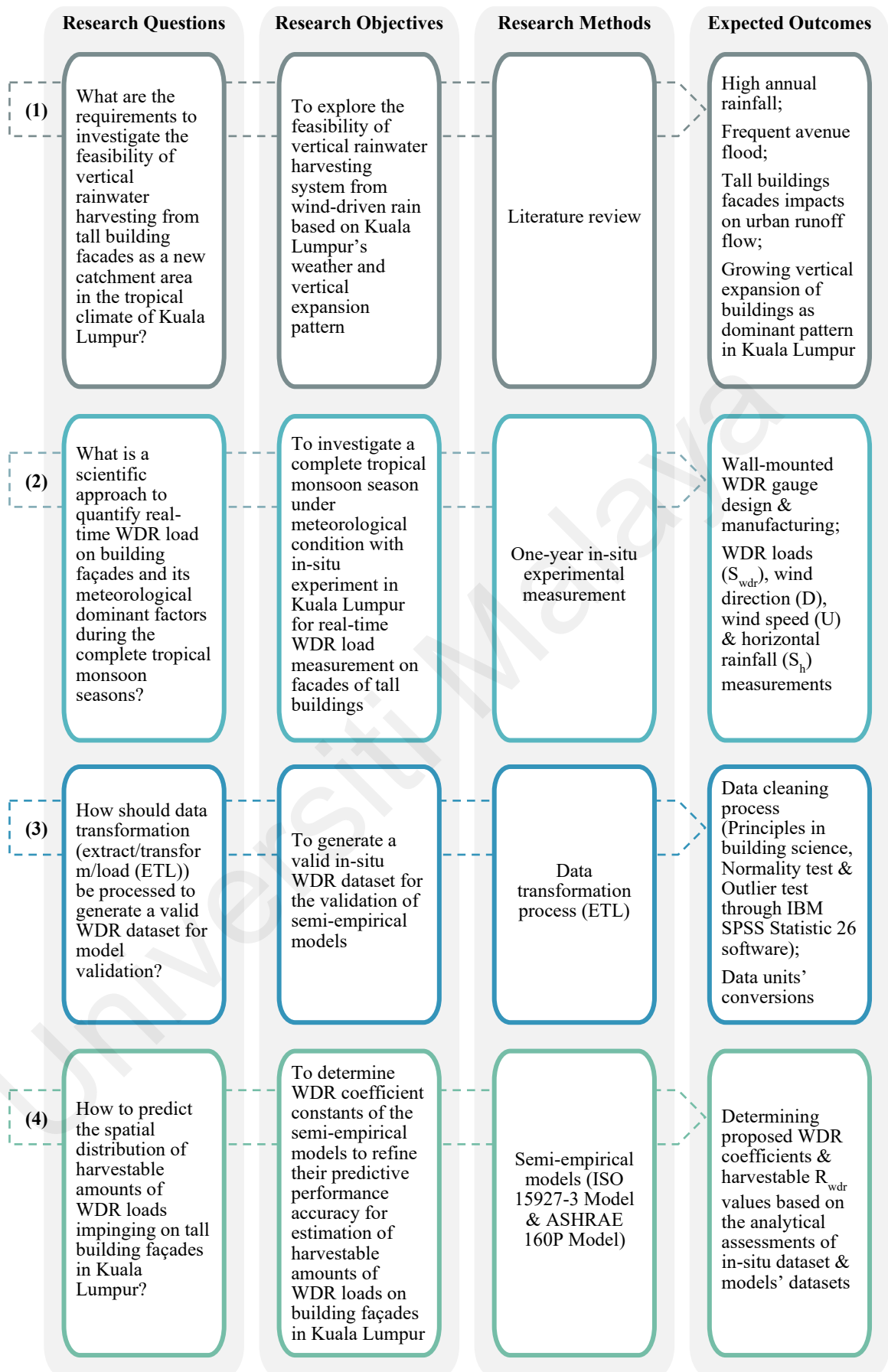


Figure 1.5. Research design diagram: research questions, research objectives, research methods, and expected outcomes

1.7. Significance of the Study

Freshwater is a significant challenge in today's built environment due to the growing emphasis on sustainability and the rising trend of vertical development. Such advancements in the built environment have already altered the natural water cycle. By comprehending and implementing water sustainability measures at the building level, we may start to address the difficulties posed by the decreasing availability of freshwater resources and the increasing levels of human water consumption at the urban level.

The Malaysian government has prioritised Rainwater Harvesting Systems (RWHS) as a viable and sustainable alternative to minimise reliance on rivers and other surface waters. However, in a vertical urban environment, the conventional horizontal 2D RWHS from rooftops of tall buildings is impractical.

This thesis claims that the façades of tall buildings can serve as available catchment surfaces to harvest rainwater, as a new and sustainable 3D RWHS. The rainfall is stored and utilised in the same location where it is captured. Furthermore, it decreases the volume, peak flow, and distortion process of rainfall-runoff due to the adverse effects of tall building developments on urban areas. These effects are caused by the increase in impervious areas and vertical sub-basin surfaces, which leads to avenue flooding.

The adoption of a sustainable and innovative 3D RWH, as opposed to the traditional 2D system, is the optimal approach in line with the national and global initiatives on water sustainability in tall buildings.

This study provides insights into the accessibility of a novel environmentally friendly vertical rainwater harvesting (VRWH) in tall buildings. It assists both building occupants and authorities in effectively managing household water supply and freshwater resources, respectively. A summary of this research significances are illustrated in Figure 1.6.

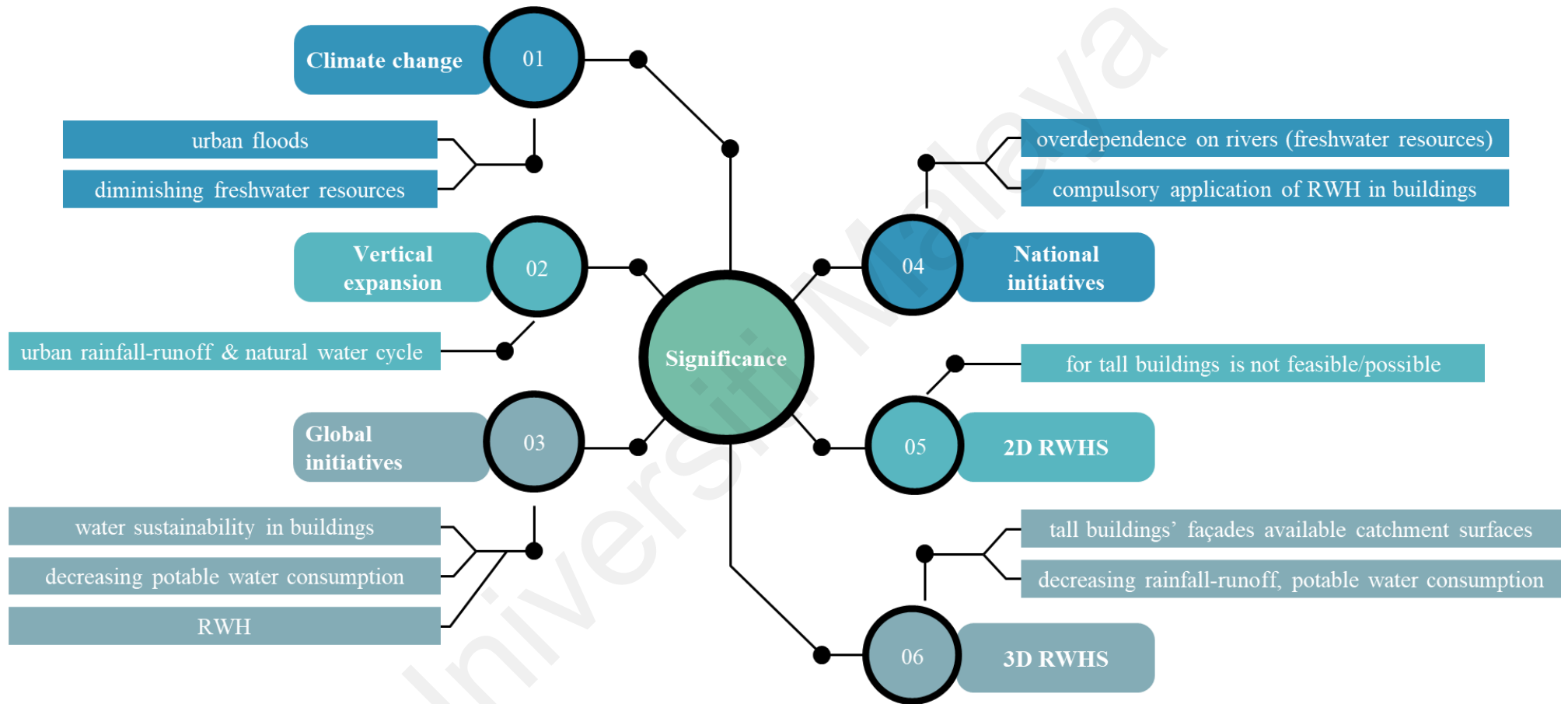


Figure 1.6. Research significance diagram

1.8. Research Scope and Limitations

This thesis explores the possibility of wind-driven rain (WDR) harvesting from building façade as a new catchment area in the context of sustainable architecture in the field of building science. It focuses on the characterization of in-situ measurements (experimental method) and predictive model validation (semi-empirical method) to determine the WDR coefficient to predict the value of WDR intensity (R_{wdr}) on the building façade (curtain wall) in the tropical climate of Kuala Lumpur.

The in-situ measurements are conducted for a period of one-year at the campus of Universiti Malaya (UM), Kuala Lumpur, Malaysia, where the pilot building is equipped with wall-mounted WDR gauges on all four façades and meets the research criteria (layout and orientation, safety and accessibility, size and scale, and surrounding area). The logging data excludes nocturnal precipitations (12 a.m. to 6 a.m.). Because it was impractical to manually record rainfall time (start and end of the rain event) and measure accumulated WDR during the entire day in a long-term (a complete tropical monsoon season) data collection campaign. However, according to the precipitation pattern record of Kuala Lumpur, the rainfall happens mostly in the afternoon time. Thus, it is hypothesised that this omission does not affect the primary goal of this research. Therefore, we anticipate that this research method and findings will be of interest to a broad range of scientists and researchers engaged in the field of water sustainability in tall buildings.

1.9. Summary

The four-stage research work of this thesis is structured into five chapters (Figure 1.7). The first two chapters, Introduction and Literature Review, include the output of the first stage (Theoretical and Review). Research Methodology, Chapter 3, provides a comprehensive discussion on the second stage, or methodology. Chapters four and five

comprise findings and analyses, discuss the respective outputs of the research methods and conclusion. The following overview provides a concise synopsis of each chapter:

Chapter 1 – The preface, problem statement, research gap, research questions, research aim and objectives, overview of research methodology, significance of the study, and research scope and limitations for this research have been stated in Chapter 1.

Chapter 2 – This chapter presents the scientific basis of the research, along with an exploration of the various meanings and implications of the key terminologies used in this thesis. This chapter first reviews briefly the current climate condition and freshwater accessibility status in Malaysia, city of Kuala Lumpur in particular. It is followed by the RWH drivers, benefits, definitions, components, and implementation in Malaysia. Then the impacts of tall buildings on rainfall-runoff distortion and the possibilities of collecting rainwater from the vertical façades are discussed. Tropical seasons' classification in Malaysia is explained as the primary division factor in dataset classifications in this thesis. In the experimental field measurement section, all the parameters, i.e., meteorological data and wall-mounted WDR gauge design and collection procedures are covered thoroughly. This chapter concludes by providing evaluation of the precise semi-empirical models that are currently applied in the field of building science for estimating WDR loads on building walls.

Chapter 3 – In this chapter, the adopted methodology based on the scope of this research is elaborated in detail. The adopted quantitative approach comprises experimental measurement (in-situ) and semi-empirical (ISO 15927-3 Model and ASHRAE 160P Model) methods. This chapter describes the pilot building, measurement sensors and gauges setup, data cleaning process, generating in-situ dataset, semi-empirical models' application and validation, WDR coefficients determination, and predicting harvestable WDR from building façade.

Chapter 4 – It provides results and analyses starting with preprocessing of in-situ data, data cleaning process of the in-situ dataset (R_{wdr}), calculation of spatial distribution of WDR (η) and its correlation analysis with meteorological parameters and building height. This is followed by fitting the semi-empirical models and the validation analyses through cross comparison charts of the Mean R_{wdr} (mm/h), statistical analyses assessment based on R^2 value, and NRMSD. In the final analysis section, the proposed WDR coefficients (α) for ISO standard 15927-3 and (F_L) for ASHRAE standard 160P) are applied to the WDR equations (the models) to predict the possible harvestable amount of Mean R_{wdr} (mm/h) on building façade at different height locations and in different tropical seasons.

Chapter 5 – Chapter 5 provides summary of findings in response to the research questions. It highlights the research contributions and recommendations for further works.

Lastly, the references section lists the references cited in this thesis.

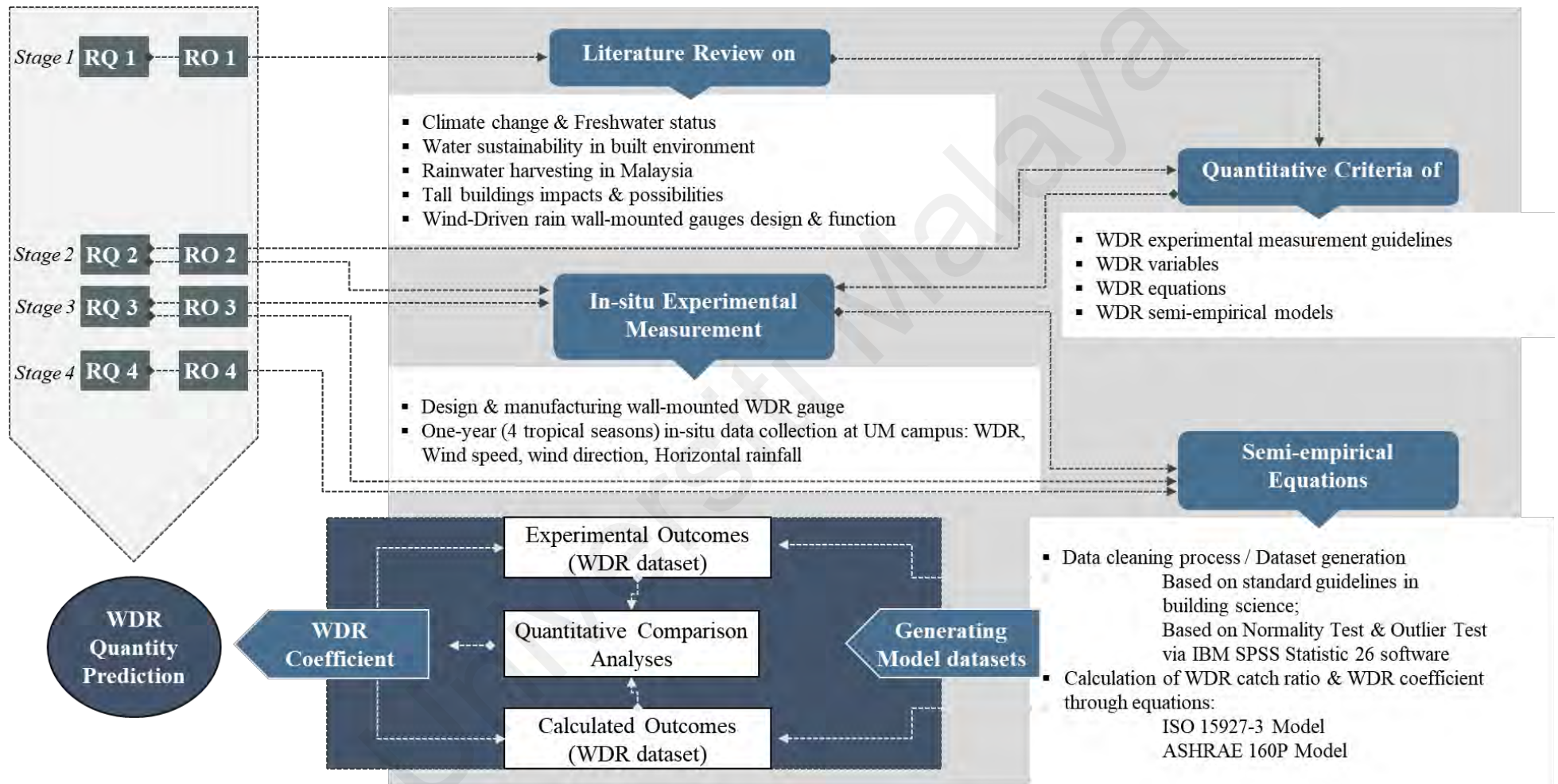


Figure 1.7. Research flow diagram

CHAPTER 2: LITERATURE REVIEW

This chapter outlines a review of the key terminologies and scientific basis of the research conducted related to the possibility of rainwater harvesting from the vertical surfaces of tall buildings through wind-driven rain collection. It begins with a brief overview of the climate condition and freshwater status in Kuala Lumpur, Malaysia. The role of built environment, in particular tall building façades as the scope of this study, in rainfall-runoff flow in urban areas and the drivers for harvesting rainwater from their façades as a new catchment area will be explored. This chapter recognises wind-driven rain as a potential freshwater resource and examines this phenomenon in the field of building science. Therefore, design principles and measurement guidelines related to wall-mounted WDR gauges will be presented in detail later. To predict the harvestable amount of WDR from building facades, this chapter delves into the two most frequently used methods as the approach of this work, i.e., experimental field measurement (in-situ) and semi-empirical model validation. Finally, this chapter presents its conceptual framework, which serves as the primary roadmap for the research process. This chapter is structured in eight sections, i.e., 2.1 Climate change and freshwater accessibility, 2.2 Rainwater harvesting, 2.3 Vertical expansion, 2.4 Seasonal classifications in Malaysia, 2.5 Experimental field measurement – meteorological parameters, 2.6 Experimental field measurement – WDR 2.7 Spatial distribution pattern of WDR on building façades, and 2.8 Semi-empirical model – WDR prediction.

2.1. Climate Change and Freshwater Accessibility

Climate change affects the hydrological cycle by affecting precipitation, evapotranspiration, and soil moisture (Abbas et al., 2022). A recent World Meteorological Organization report (WMO, 2022) indicated that the average global temperature has

increased by 0.8 °C since 1880, which in turn led to an increase in the intensity and frequency of extreme precipitation events on a global scale (IPCC, 2018). Regional scale flooding and landslide activity have increased due to intensified precipitation events (Blöschl et al., 2017; Gariano & Guzzetti, 2016; IPCC, 2014) and further intensification of extreme precipitation events is projected for the future (Ge et al., 2019; Prein et al., 2017; Ragno et al., 2018; Tabari et al., 2019). Due to different interacting drivers of extreme precipitation changes, the changes are not uniform in space and vary by region (Tabari, 2020).

However, recent studies have examined daily extreme precipitation changes in relation to water availability and found that 30-year averaged annual precipitation maxima aggregated over both dry and wet regions of the world are likely to increase (Donat et al., 2019; Donat et al., 2016).

Consequently, the stormwater infrastructure of urban areas will fail to control greater runoff volumes, and flooding will become more prevalent. In a recent report by the Malaysian Stormwater Organization (Shaari, 2019), it was stated that more upstream areas are developed without upgrading stormwater infrastructure downstream, which is why the number of downstream areas experiencing flooding has increased.

Excess runoff eventually travels to larger bodies of water like lakes, estuaries, and the ocean, polluting the water supply and limiting water access for humans and ecosystems (National Geographic, 2022).

The world is facing an unprecedented water crisis, with global freshwater demand predicted to exceed supply by 40% by 2030, reported by the UN (EcoWatch, 2023). The demand is expected to continue increasing at 1% per year until 2050, accounting for an increase of 20% to 30% above the current level of water use; mainly due to rising demand in the industrial and domestic sectors (WWAP, 2019).

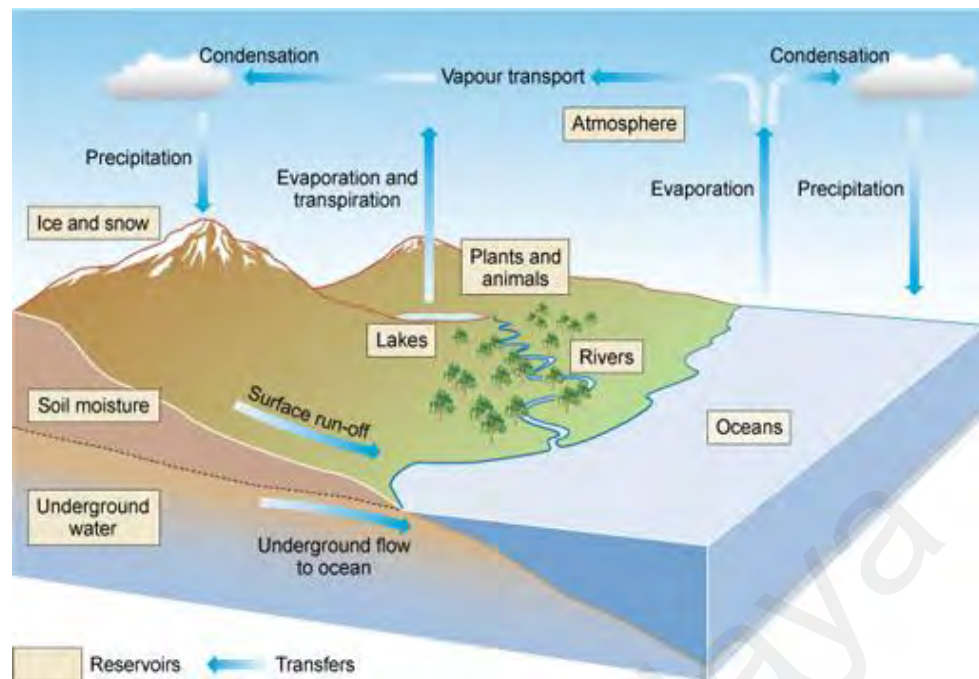


Figure 2.1. The hydrological cycle or water cycle (Skinn, 2020)

There is the same amount of freshwater on earth as there always has been, but the population has exploded, leaving the world's water resources in crisis; this means that every year competition for a clean, copious supply of water for drinking, cooking, bathing, and sustaining life intensifies (National Geographic, 2023).

Freshwater makes up a very small fraction of all water on the planet. While nearly two-third of the world is covered by water, around 97.5% by volume is saline and ocean-based, and only 2.5% of it is freshwater. Moreover, just 1% of the freshwater is accessible for agriculture and cities, with much of it trapped in glaciers and snowfields (Figure 2.2). In essence, only 0.007% of the planet's water is available to fuel and feed its 6.8 billion people. However it sounds inconceivable but according to UNDP (2006), this amount of available freshwater on the planet for seven billion people is enough but it is distributed unevenly (as natural phenomenon) and too much of it is wasted, polluted and unsustainably managed (as human-made phenomenon); and both phenomena resulted in water scarcity on the planet.

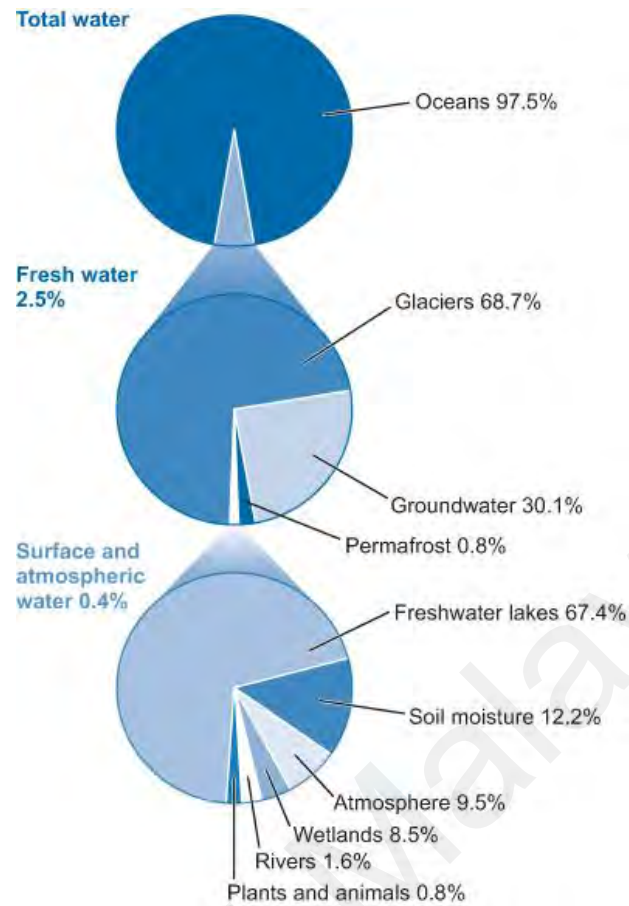


Figure 2.2. Distribution of water resources on Earth (WASH, 2018)

By 2025, an estimated 1.8 billion people will live in areas plagued by water scarcity, with two-third of the world's population living in water-stressed regions as a result of use, growth, and climate change (WHO, 2019). The challenge we now face as we head into the future is how to effectively conserve, manage, and distribute the freshwater we have.

2.1.1. Malaysia Water Status

Malaysia is a tropical country that is relatively rich in water resources, with an average annual rainfall of 2562.35 mm over the study area from 2007 to 2016 (Tan, 2018). Because of the uneven distribution of rainfall over space and time, some areas have been suffering from dry spells, while others have been affected by major flooding over the last decades (Lani et al., 2018b).

Malaysia falls into the category of countries with high domestic water consumption, ranging from 209 to 228 litres per capita per day (lcd), exceeding the World Health Organisation's (WHO) recommended target of 165 lcd (Lani et al., 2018b). According to the Malaysian Water Association (MWA, 2018), Malaysia needs to reduce its high water usage (201 litres/capita/day) by 18% to reach the recommended water-usage by the World Health Organization (WHO), i.e., 165 litres/capita/day. Therefore, if water consumption does not improve, Malaysia may face a water shortage crisis in the foreseeable future.

In Malaysia, about 97% of raw water supply for agricultural, domestic and industrial needs is derived from surface water sources, primarily rivers; there are 189 river basins: 89 in Peninsular Malaysia, 78 in Sabah, and 22 in Sarawak (WWF, 2014). However, in some highly developed and populated areas such as Selangor, Putrajaya, and the Federal Territory of Kuala Lumpur, the river resources have been fully exploited (Lani et al., 2018b), and 25 rivers are declared dead rivers in Malaysia, as highly polluted rivers; 16 rivers were found in Johor, 5 in Selangor, 3 in Penang, and 1 in Melaka (Rahman, 2021).

Urbanisation has caused significant environmental destruction and posed a serious threat to its survival. Sustainable development takes into account how we coexist with nature while preventing harm and devastation. The future of humanity is at the heart of this, since it lays forth the rules for the preservation and management of sustainability of resources, i.e., air quality, water quality, and ecosystems (Inyinbor Adejumo et al., 2018).

Table 2.1 shows the amount of average water consumption for different domestic appliances and the corresponding average rainwater demand. According to the environmental protection agency (EPA, 2023), toilets are by far the main source of non-potable water use in the home, accounting for nearly 30% of an average home's indoor water consumption.

Table 2.1. Rainwater demand for domestic application (MSMA, 2012)

Use (Appliances)	Type	Average consumption	Average Total rainwater demand
Indoor			
Toilet	Single flush Dual flush	9 L per flush 6 or 3 L per flush	120 L per day 40 L per day
Washing machine	Twin tube Front loading Top loading		40 L per wash 80 L per wash 170 L per wash
Dishwasher			20-50 L per load
General cleaning		10–20 L per minute	150 L per day
Outdoor			
Sprinkler or handheld hose		10–20 L per minute	1000 L per hour
Drip system			4 L per hour
Housing paths/Driveways Washing car with a running hose		20 L per minute 10–20 L per minute	200 L per wash 100-300 L per wash

2.1.2. Water Sustainability

When it comes to water and climate change within the 2030 Agenda, both Sustainable Development Goal (SDG) 6 and SDG 13 have a direct or indirect impact on all the other SDGs (WWDR, 2020). The challenges of development, poverty eradication, and sustainability are intricately interwoven with those of climate change mitigation and adaptation, especially through water. Water is not a sector, but a connector and the impacts induced by climate change touch all aspects of our society (economic, social and environmental) (White, 2018). Streamlining water into global climate, development, and DRR (disaster risk reduction) processes could be a means of connecting climate change issues with all the other SDGs (Figure 2.3). Water is the core of sustainable development, a finite and irreplaceable resource that is fundamental to human well-being and it is only renewable if well managed (UNDESA, 2023). It is an essential way forward to place water at the heart of these strategies. It helps the water community to deliver its message to the climate community and a broader audience.

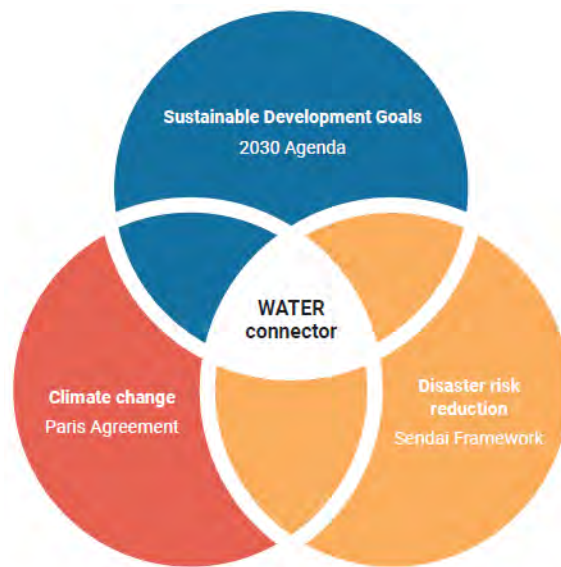


Figure 2.3. Water as a connector among the global commitments adopted in 2015 (Uhlenbrook & Connor, 2019)

The need to embrace sustainability has never been greater than it is now, given the 21st century's rapidly increasing economic and environmental pressures. By understanding and practicing sustainability at the building level, we may begin to overcome the challenges of the diminishing quantity of freshwater resources and the rising levels of human water consumption at city level.

In respect of the physical alternatives to fulfil sustainable management of freshwater, two main categories of solutions can be identified (Silva et al., 2015):

- i. Reduction of water consumption,
- ii. Identification of new water resources.

To date, much attention has been given to the former option and only limited attention has been given to the latter (Wu et al., 2017). This thesis is based on this premise and focuses on identification and exploration of new sustainable and available water resource at the building level.

As stated by Silva et al. (2015) even in countries with a favourable balance between water demand and water availability, there is interest in evaluating alternatives for improving

the efficient use of water. One way to achieve water sustainability is through rainwater harvesting, which is the most available alternative water resource. Rainwater harvesting gives city residents a clean, local, and renewable water source (UNFCCC, 2017), and as stated in the Urban Stormwater Management Manual for Malaysia (MSMA, 2012):

- i. It provides an alternative water supply to supplement piped water,
- ii. It is a green approach. It reduces the dependency of people on pipe water hence discourage dam construction and deforestation,
- iii. It reduces water bills for consumer. Occasionally, there are economic advantages such as rebates from municipalities for a reduction in use and dependency on municipal water,
- iv. On islands with limited freshwater, rainwater harvesting is the major source of water for domestic use,
- v. It reduces stormwater flooding and soil erosion.

Taking into account the aforementioned facts (potentials and challenges), it is crucial to contemplate RWH as an available alternative water resource to reduce overdependence on river basins for freshwater demand, as well as avenue flooding.

2.1.3. Built Environment Developments Impacts on Natural Water Cycle

As cities become more urbanised, the amount of areas where water cannot soak in (also known as impervious areas) increases; the hydrological processes of surface water runoff become more unnatural, causing damage to infrastructure and contamination of water by pollutants (Saraswat et al., 2016). In other words, buildings and impervious surfaces disrupt the natural water cycle. As a result, natural water flows are altered, and stormwater is created. Consequently, urban building development causes the following changes to the water cycle changes:

- i. Increasing surface imperviousness,
- ii. Decreasing infiltration,
- iii. Decreasing groundwater recharge,
- iv. Increasing runoff volumes and peak flows,
- v. Changes in runoff conveyance networks.

To reverse this situation, the built environment sector should strive to naturalise itself with the goal of reaching pre-development flow conditions.

Low-impact development (LID), a relatively recent approach to stormwater management, focuses on the minimization of runoff with the aim of reducing the impact of development on water resources. The LID practices include infiltrating (porous pavement), evaporating, and rainwater harvesting, which are retrofitting technologies that utilize rainfall on the site where it falls (Li et al., 2020).

2.2. Rainwater Harvesting (RWH)

As aforementioned, increasing population, higher levels of human activities, continuous depletion of fresh surface and groundwater, and climate change require that water resources be adequately managed to satisfy current demands and attain future sustainability. The use of rainwater has been widely accepted as a reliable alternative. RWH is broadly defined as the collection and concentration of runoff for domestic water supply, productive purposes, and livestock (Alamerew et al., 2002; Ali, 2017). Even in areas with abundant water resources, rainwater can offer benefits such as reducing water supply costs, reducing water extraction, and maintaining water security in emergencies.

Due to its ability to decrease reliance on the domestic water supply, RWHS has been implemented in various areas, such as agriculture, and commerce. The subsequent

sections provide an overview of the drivers, benefits, definitions, components and implementations of RWH in Malaysia.

2.2.1. Drivers for RWH

The aim of the ‘Malaysia Water Vision’ is to transition from the current state to a future state that can meet the future demand for water and ensure the sustainable utilisation of water resources. The main concern is water scarcity, which arises from unsustainable consumption and excessive extraction of surface and groundwater resources. These factors lead to water shortages and pose a threat to long-term sustainable development.

This drives the narrative for mainstreaming, efficiency measures such as rainwater harvesting (SQL Associates, 2018). The integration of rainwater harvesting (RWH) into water resource management has become even more of a priority towards water sustainability all over the world. Mbua (2013) identified four primary RWH drivers, as shown in Figure 2.4.

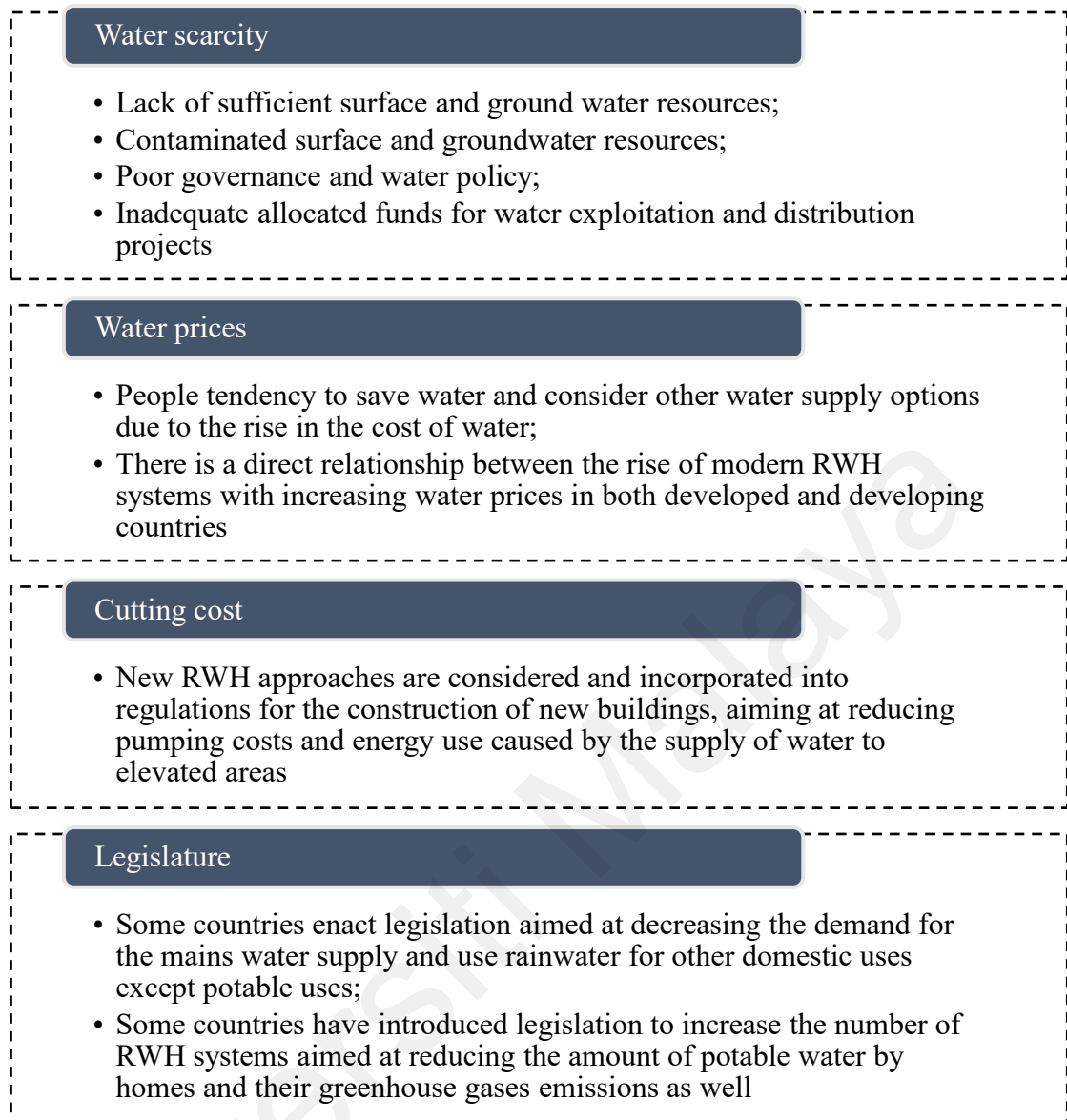


Figure 2.4. Main RWH drivers and their reasons/causes (Mbua, 2013)

2.2.2. Benefits of RWH

RWH has numerous benefits as well as some drawbacks, whether it is used for residential or other purposes. If the location is an industrial area prone to air pollution, the primary drawbacks pertain to construction costs and water quality. This could contaminate the rainwater prior to its collection. The RWH system's construction complexity essentially determines the cost issue. Furthermore, the quantity and frequency of rainfall cannot be predicted with 100% accuracy. Climate change impacts make weather much more

unpredictable, and this might be favourable for tropical areas (more intense rainfall), whereas arid regions will experience a decrease in the little rainfall they already have (Mbua, 2013).

In seasonal climates, rainwater collection is frequently used to supplement other water sources. Where climatic conditions are appropriate, it can be used as the primary source of drinking water, provided the rainwater collection and storage system has the capacity to supply sufficient quantities of safe drinking water to meet user needs (WHO, 2020).

The quality of the rainwater collected and stored in the storage tanks is theoretically less contaminated than water from other supply sources, such as underground or surface; therefore, this water is used for drinking in various sectors after a simple disinfection process (Hugues, 2019; Vilane & Mwendera, 2011). The quality of the water will vary depending on the environment in which the system is used; for instance, in the Netherlands, people utilise the collected water to irrigate gardens and crops, as well as to flush the toilet, because it lowers costs by not using potable water from the public system (García-Ávila et al., 2023).

The benefits of RWH can be classified into two categories, namely, environmental and economic (Jones & Hunt, 2010; Lani et al., 2018b). For environmental benefit, it can be used as an alternative water supply to supplement piped water. When used on a large scale, RWH can help reduce flash floods in urban areas and minimise soil erosion, as well as prevent pollutants from entering water bodies (Rahman et al., 2012).

The following (Figure 2.5) are the general benefits and advantages of RWH in transitioning in the built environment towards water sustainability for the development and management of rainwater (Barron & Salas, 2009; Mbua, 2013; San, 2023; Struk-Sokołowska et al., 2020; Toledo, 2015; Trenberth et al., 2007; Viljoen, 2014; Zhu et al., 2004):

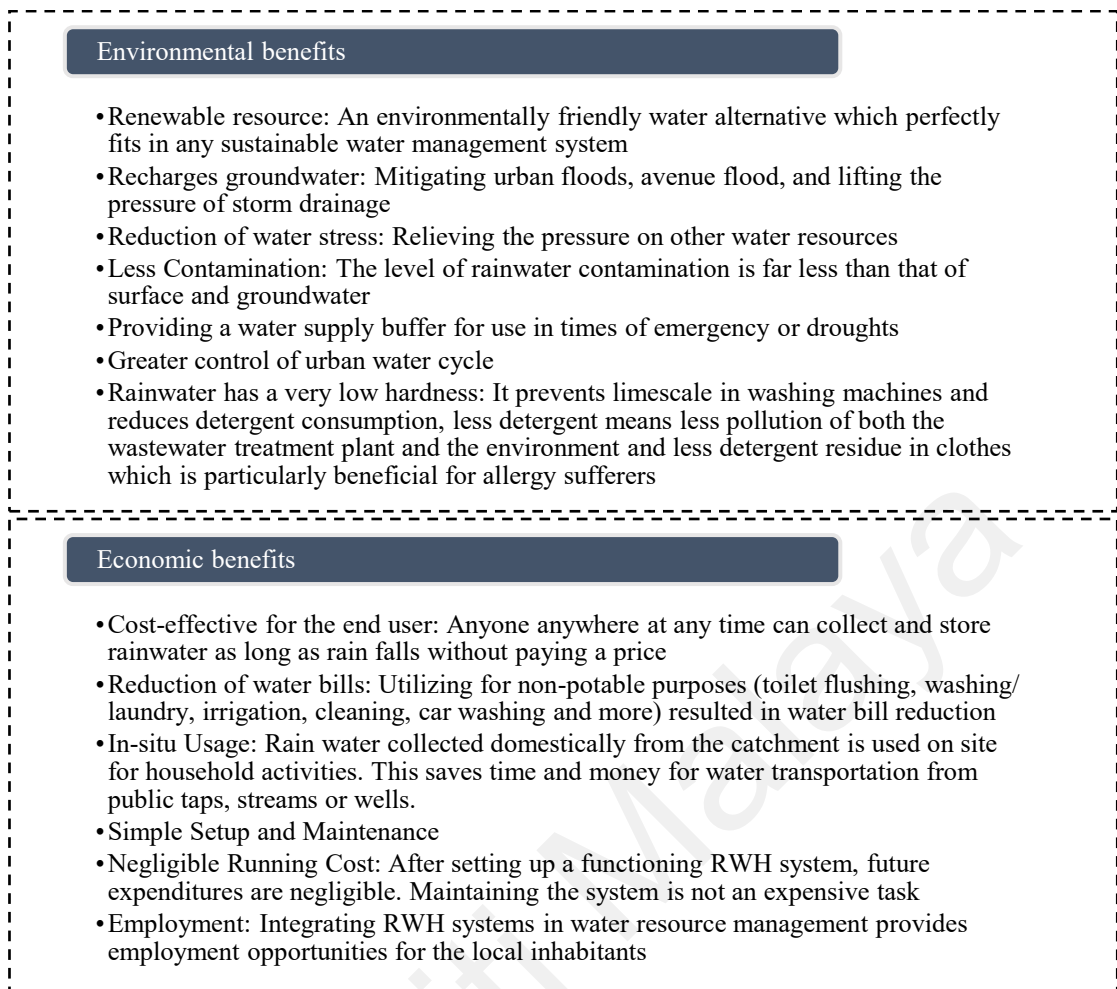


Figure 2.5. Environmental and economic benefits of RWH

Rainwater collection is a flexible approach that can be applied under a wide range of conditions. A RWH system's performance depends on a number of factors, including in-depth analysis of rainfall data, catchment characteristics, storage facilities, and maintenance, patterns of water usage, and population per capita income. Some drawbacks are mitigated by the use of locally produced materials and the community's participation in joint efforts with the local government and non-governmental organizations (who may provide financial support).

RWH has been practiced for centuries globally. However, centralization of water supply and technological development have gradually replaced the Taanka (underground tanks located in houses or within the courtyard) with the convenient piped water in the 20th

century. Taking the above-mentioned benefits of RWH into consideration, plus challenges such as population growth, surface and groundwater contamination issues, costs of water extraction and purification it is the necessity to revive and increase the effectiveness of RWH system for the new and rapid growing pattern in building development.

2.2.3. Definitions of RWH

Definitions and classifications of RWH techniques vary among regions. Geddes provided one of the earliest definitions of RWH, as quoted by Myers (1975): "The collection and storage of any farm waters, either runoff or creek flow, for irrigation use". Critchley et al. (1991) defined RWH as the collection of runoff for productive use. Oweis (2004) defined RWH as "The concentration of rainwater in runoff into smaller target areas for beneficial use." Kahinda et al. (2008) explained RWH as "The collection, storage, and use of rainwater for small-scale productive purposes." The World Overview of Conservation Approaches and Technologies (WOCAT) database (Mekdaschi & Liniger, 2013) recently described RWH as "The collection and management of floodwater or rainwater runoff to increase water availability for domestic and agricultural use as well as ecosystem sustenance."

According to the definitions, the common main purpose is to increase the amount of available freshwater by capturing rainwater for local use or for transfer to another area. The storage from the RWH system can be used for potable and non-potable uses. It is preferable to integrate the RWH systems with the existing conventional water supply systems (Chacha, 2015). The most widespread uses given to harvested rainwater are non-drinkable applications (i.e., toilet flushing, garden irrigation and domestic laundry use) (Roebuck et al., 2011). This will help to meet the increasing demand for water supply and contribute to the sustainability of the freshwater supply. In addition, several recent studies have quantified the average amount of water demand that RWH can meet, which is

strongly dependent on the local climate and consumption patterns. These studies conclude that those systems can supply 45% of domestic demand (Parés et al., 2004; Ratnayaka et al., 2009). RWHS can be applied to both small and large-scale premises, but certain criteria need to be satisfied before implementing the system.

2.2.4. Components of RWH

In the broadest sense, RWH in buildings is a technique that collects and stores runoff for use as non-potable sources instead of drinking water in domestic, commercial, institutional, and industrial sectors. All RWH systems consist of three main components, which are further subdivided into a number of smaller components. The following are the main components:

- i. A catchment surface: also known as a collection area, runoff area, or catchment surface, is typically a simple structure, such as a roof or gutters that directs rainwater to the storage facility,
- ii. A storage facility: the area that holds the harvested runoff water until it is used for people, crops, or animals. Water can be stored above ground (e.g., in reservoirs or ponds), in the soil profile, or in underground storage containers (e.g., cisterns),
- iii. A target: the endpoint of a rainwater harvesting system, the place where the harvested water is used for domestic use or crop production.

This research focuses on the first RWH component, the catchment surface. It is to be noted that in this study catchment surface is referred to:

- i. In in-situ measurement: the collection area of the WDR gauge that rain impinged on and runoff to the reservoir during the rain event,
- ii. In tall building façade area: the glass curtain wall façades of the tall buildings, as a prospect new catchment area.

In a horizontal or 2D RWH system, roofs are ideal catchment surfaces for harvesting rainwater, if they are clean. If a building or house with an impervious roof, which is resistant to rain, is already in place, the catchment area is available free of charge (Biswas & Mandal, 2014). The choice of roof material and the size of the effective area directly influence the efficiency, quantity, and quality of the collected rainwater. Catchment areas may also include driveways or swales in yards. However, rainwater harvested from catchment surfaces on the ground should only be used for irrigation because of the increased risk of contamination (Abdulla et al., 2021). The quantity and quality of the rainwater collected from the catchment area vary depending on the amount and intensity of rainfall, the surface area, the type of material, and the condition of the surrounding environment (Khoury-Nolde, 2010).

2.2.4.1. Catchment Materials

As Eslamian and Eslamian (2021) explained in their book, all catchment surfaces must be made of non-toxic material; painted surfaces should be avoided if possible, or, if the use of paint is unavoidable, only non-toxic paint should be used. Lead-, chromium-, or zinc-based paints are not suitable for catchment surfaces due to the presence of heavy metals, overhanging vegetation should also be avoided (Sendanayake & Eslamian, 2021) because birds and animals in the trees may defecate on the roofs (Fath & Jorgensen, 2020). Steep galvanised iron roofs have been found to be relatively efficient rainwater collectors, while flat concrete roofs are very inefficient (Eslamian & Eslamian, 2021).

In horizontal RWH (2D), catchment surfaces and collection devices should be cleaned regularly to remove dust, leaves, and bird droppings to minimise bacterial contamination and to maintain the quality of collected water (Fath & Jorgensen, 2020).

Runoff – The amount of catchment surface runoff is influenced by catchment material, as mentioned above, and rain properties such as rainfall duration, amount, and intensity

(Sitterson et al., 2018). Runoff occurs after rain impingement on the catchment surface. Runoff is generated by a combination of two mechanisms; saturation excess and infiltration excess over the catchment area (Yang et al., 2015). Saturation excess occurs when the catchment area becomes fully saturated with water, exceeding the water holding capacity of the material (Johnson et al., 2003); infiltration excess occurs when rainfall intensity exceeds the maximum rate that water can infiltrate into the material, and water must flow over the catchment surface (Yang et al., 2015). In other words, *runoff* occurs on non-absorbent materials (has a low absorptivity) or on fully saturated surfaces (has no more capacity to absorb water) (Dorsey et al., 1996), such as galvanised iron in horizontal and glass in vertical catchment surfaces. The absorption of water by the surface is controlled by the *absorptivity*, or rate of water uptake, and the *absorption*, or capacity to absorb water. Figure 2.6 illustrates the relationship between constant impinging rain, absorption, and runoff based on time and material characteristics.

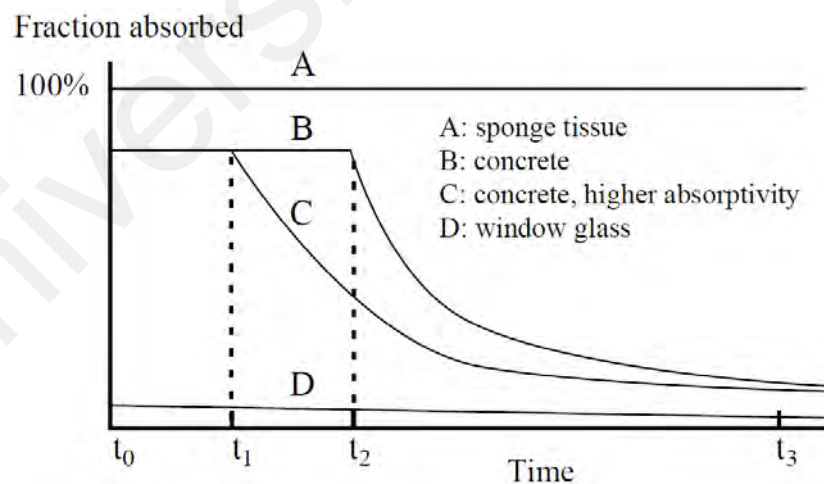


Figure 2.6. Simplified diagram illustrating absorption over time for several materials assuming a constant rainfall (Dorsey et al., 1996)

Line A represents a spongy material: high absorptivity and absorption, has the capacity to absorb all the incident water over time, thus having no runoff.

Curve B describes a moderately absorbent concrete: high absorptivity but a limited absorption capacity; from t_0 to t_2 , all incident water is absorbed and there is no runoff; from t_2 to t_3 , the absorbed amount is less than the incident amount because of saturation; hence, some rain is absorbed but an increasing quantity runs off.

Curve C shows the behaviour of a higher absorbent concrete: higher absorptivity, runoff starts sooner, from time t_1 , because the material becomes saturated more quickly.

Curve D illustrates a very non-absorbent material such as glass: the amount of water that is absorbed is very small and drops off slowly during the time span; thus, there is significant runoff from the beginning.

The diagram (Figure 2.6) illustrates that on a non-absorbent material such as glass (the most common material in tall buildings' curtain walls), runoff occurs after initial rainwater impingement with an insignificant absorption amount and significant runoff quantity in a uniform and steady trend on the vertical catchment surface.

2.2.4.2. Runoff Coefficient

The collection of rainwater is usually represented by a runoff coefficient. The runoff coefficient is a dimensionless coefficient defined as the ratio of the volume of water superficially drained during rainfall to the total volume of precipitation during a certain period (Machado et al., 2022; SWAMP, 2023).

Rooftop catchment efficiencies range from 70–90% (Eslamian & Eslamian, 2021); losses are due to roofing material, evaporation, losses occurring in gutters and storage tanks and inefficiencies in the collection process.

The rooftop catchment yield is typically estimated at 75% of the actual rainfall, although occasionally run-off coefficients for hard roofs in humid tropics are taken as 0.85

(Sendanayake, 2016a, 2016b, 2016c; Sendanayake, 2016d). Table 2.2 shows the run-off coefficients for the typical materials used for different types of catchments in 2D RWH. The glazed tiles as the closest material to the glass curtain walls shows high runoff coefficients (0.6-0.9).

Table 2.2. Run-off coefficients for the traditional roofing materials (Biswas & Mandal, 2014; Eslamian & Eslamian, 2021; Sendanayake et al., 2014; Worm & Hattum, 2006)

Material	Runoff coefficient
Galvanized iron sheets	> 0.9
Corrugated metal sheet	0.7–0.9
Glazed tiles	0.6–0.9
Tiles	0.8-0.9
Concrete	0.6-0.8
Flat cement roofs	0.6–0.7
Aluminium sheets	0.8–0.9
Asbestos-cement	0.8
Thatched/organic roofs	0.2
Brick pavement	0.5-0.6
Rocky natural catchment	0.2-0.5
Soil with slope	0.0-0.3
Green area	0.05-0.1

A runoff coefficient of 0.8 indicates that 80% of the rainfall will be captured. Therefore, as the runoff coefficient increases, the amount of rainwater collected also increases.

Precipitation is one of the most important factors in the evaluation and determination of the runoff coefficient, which may refer to isolated rainfall or to a time interval in which several rains occurred (de Campos & Machado, 2018; Júnior, 2022). When precipitation increases, the initial losses and the infiltration capacity are met (Machado et al., 2022).

Runoff coefficient is influenced not only by precipitation, but also characteristics such as intensity, duration and distribution of the rainfall play a significant role in runoff

occurrence and volume (Machado et al., 2022). Based on the catchment area characteristics, a runoff coefficient can be estimated by using referencing tables.

2.2.4.3. Catchment Location

RWH can be classified based on the catchment location; roof tops and other purpose-built catchments and also runoff from man-made or natural surface catchments for potable and non-potable uses (Lani et al., 2018b). This classification includes in-situ, micro-catchment system, and macro-catchment system (Mbilyi et al., 2005; Mishra, 2014; Oweis et al., 2012):

In-situ – The first category is in-situ RWH, where the rainfall is collected, stored, and used in the same area where it fell. Examples of this system are deep tillage, ridges, and borders, terraces, trash lines, rooftops, courtyards and similar compacted or treated surfaces that are used for domestic purpose or garden crops.

Micro-catchment – The second category is called a micro-catchment RWH that is a method of collecting surface runoff from a small catchment area and storing it in the root zone of an adjacent infiltration basin. The basin is planted with a tree, a bush or with annual crops. Some examples are contour bunds, semi-circular bunds and strip catchment tillage.

Macro-catchment – The third category is macro-catchment RWH, also called harvesting from external catchments, and is the case where the runoff area is large and located outside the cultivated area. Examples are dams.

The scope of this research is evaluation of RWH under the first classification, which is in-situ.

2.2.4.4. Catchment Size

The size of the catchment area can vary between a few square metres and several square kilometres. RWH systems have been variously classified, Ali (2017) stated that the most

commonly used RWH classification is based on the size of the catchment, namely, small, medium and large scales (Gould, 1999; Jamaluddin & Huang, 2007; Mohammed et al., 2007). This category of RWH systems is depicted in Figure 2.7.

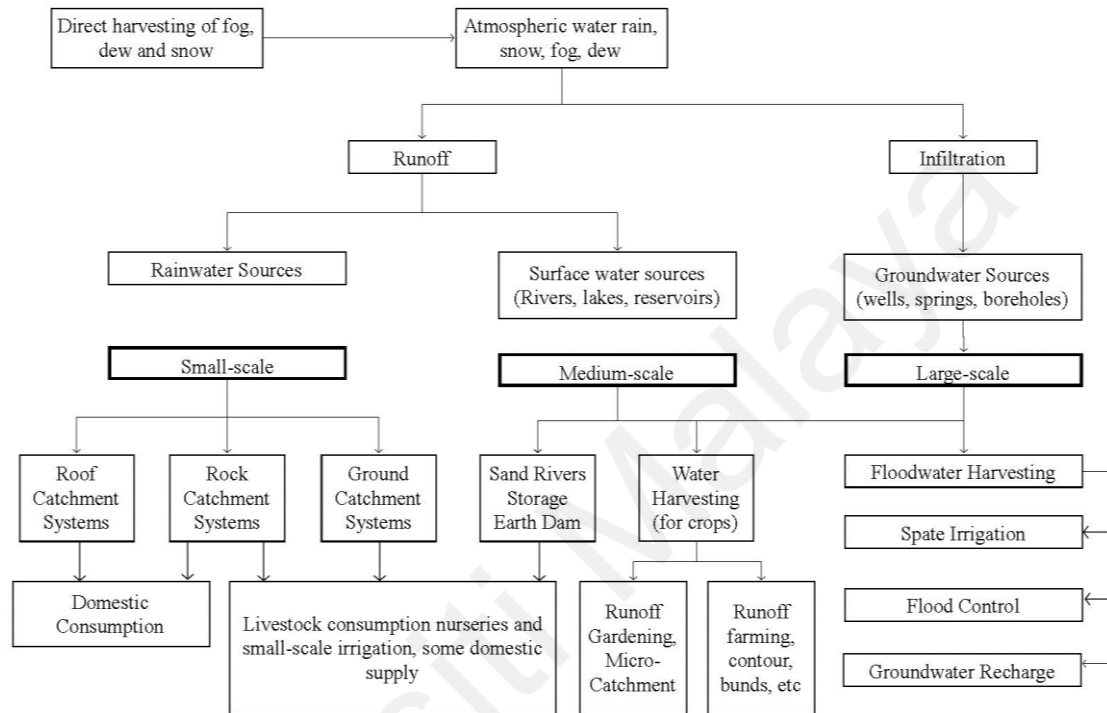


Figure 2.7. Rainwater harvesting classification based on the size of catchment area (Jamaluddin & Huang, 2007; Shaari et al., 2009)

2.2.4.5. Conveyance System

Conveyance systems are required to transfer the harvested rainwater from catchment surfaces to storage tanks. A downpipe connected to one or more collection devices is usually used for this purpose. The pipes used for conveying rainwater, wherever possible, should be made of plastic, polyvinyl chloride (PVC), or other inert substances because the pH of rainwater can be acidic and may cause corrosion and mobilisation of metals in metal pipes (Fath & Jorgensen, 2020).

Three types of RWH systems are able to convey rainwater to buildings for non-potable uses; gravity-fed, directly pumped, and indirectly pumped (Adnan et al., 2020; Leggett et al., 2001; Roebuck & Ashley, 2007):

Gravity-fed System (GFS) – This system requires cisterns to be located on top of the roof of a building in order to provide the amount of pressure head to be used for toilet flushing.

Indirectly Pumped System (IPS) – In this RWH system, rainwater or stormwater is pumped to a second holding tank, typically located on the roof, and then water is conveyed to toilets through the use of gravity.

Directly Pumped System (DPS) – This system skips the holding tank and pumps rainwater directly to the needed destination.

Results from the research analysis by Adnan et al. (2020) on utilization of these three RWH systems specified by NAHRIM (National Hydraulic Research Institute of Malaysia) and based on the building types are presented in Figure 2.8. It is worth mentioning that the catchment area in their research is the roof top of the buildings.

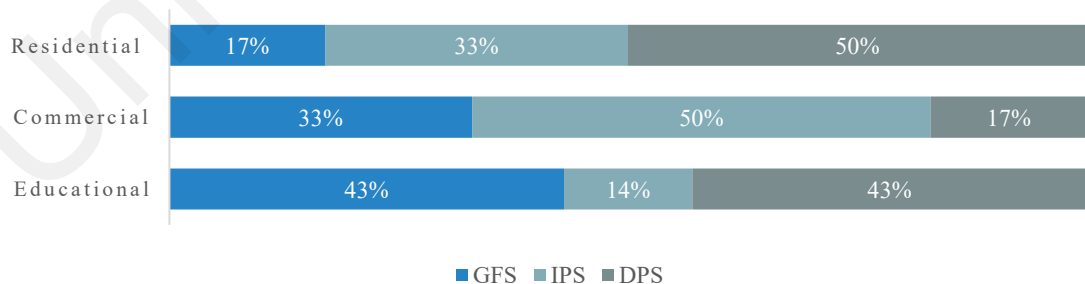


Figure 2.8. RWH conveyance systems used in different building types, reproduced from (Adnan et al., 2020)

The figure indicates that the most frequently used systems in different building types are varied; in residential buildings are directly pumped system (50%) and indirectly pumped

system (33%), in commercial buildings are indirectly pumped system (50%) and gravity-fed system (33%), and in educational buildings are gravity-fed (43%) and directly pumped systems (43%). Their analysis has also revealed that type of building does not affect the choice of system when the building is a multi-storey building (Adnan et al., 2020). Thus, tall buildings can benefit from each system according to the design and specifications.

Figure 2.9 illustrates details about the two configurations; Indirectly and Directly pumped RWH schemes, and as defined by Istchuk and Ghisi (2023):

- i. The indirect pumped RWH scheme comprises two rainwater tanks; collected rainwater flows by gravity to a lower tank, from which it is pumped to an upper tank, where again, by gravity, it is distributed to the water appliances,
- ii. In the direct scheme, collected rainwater is stored in the lower tank and distributed directly to the water appliances through a pressuriser.

The following are some advantages of indirectly pumped and/or gravity-fed RWH systems (Vargas, 2009):

- i. Provides water for non-potable uses in case of pump failure because it relies on gravity to distribute water to toilets,
- ii. More energy efficient because the water pump can run at full flow rather than only running at times when the supply is needed,
- iii. Can be connected to a backup water main pipe in case the water level at the header tank runs low and needs to be supplemented by potable water.

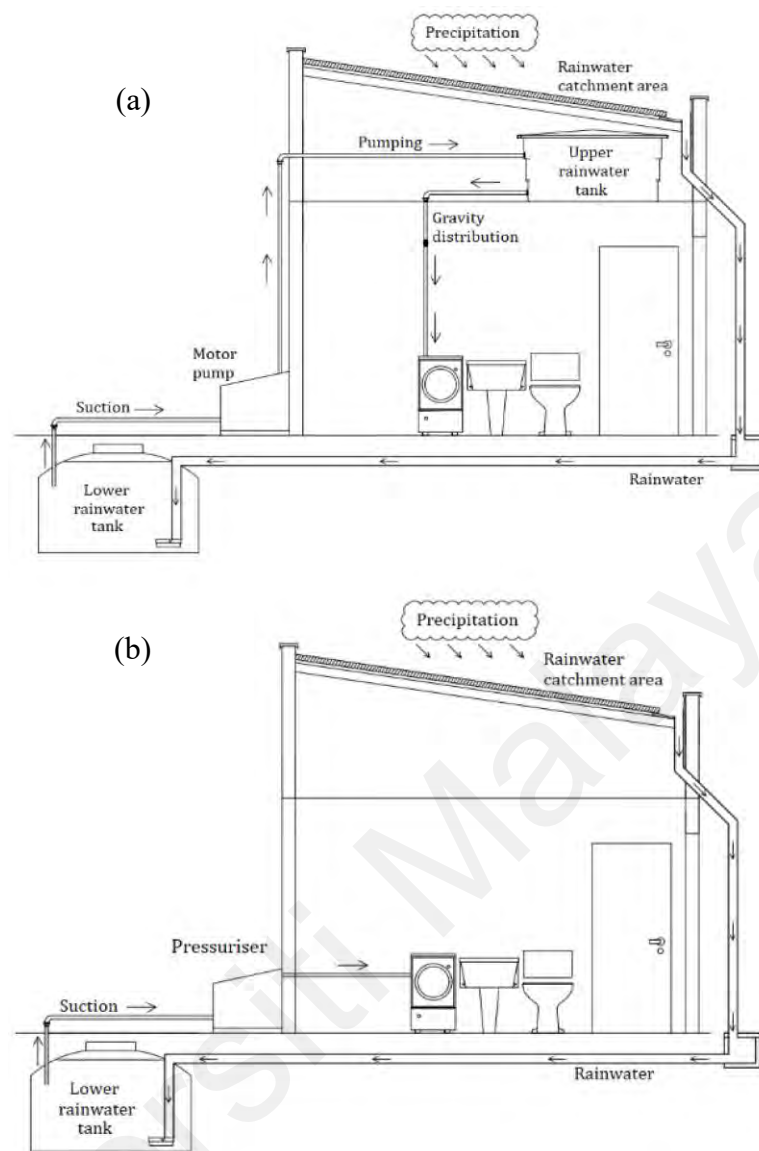


Figure 2.9. Indirectly (a) and Directly (b) pumped RWH systems schematic diagrams (Istchuk & Ghisi, 2023)

2.2.5. Implementation of RWH in Malaysia

Over the last decades, rainwater harvesting has been regarded as a sustainable system to cater for domestic and regional water deficiency issues all around the world, particularly in southeast Asia and Africa (Mbua, 2013). According to Jiménez et al. (2020), in the international arena, to achieve Sustainable Development Goals (SDG) 6, effective and sustainable water governance is crucial. Currently, Malaysia faces proactive and fast-developing political, legal, and economic environments; therefore, it is imperative to ensure the water resources are carefully managed and governed (Shaari, 2020). A good

governance approach towards water management in Malaysia will promote stakeholder participation, practitioners' involvement, and public awareness.

The severe drought in 1998, especially in Klang Valley, has triggered the Malaysian government to embark on RWHS (Lani et al., 2018b). Following this water crisis, the Ministry of Housing and Local Government introduced the guidelines for installing a Rainwater Collection and Utilisation System in 1999 and encouraged citizens to install RWHS in their existing dwellings (see Table 2.3), as the first step towards RWH implementation by the local authorities in Malaysia (Shaari et al., 2009). The goal was to reduce reliance on treated water and provide convenient water during water shortage emergencies (Fakhira & Nazri, 2022), to focus on “mini dams” construction or rainwater tanks in urban areas to reduce bigger dams construction on sections upstream (Mohd-Shawahid et al., 2007), as well as preventing flash floods (Fakhira & Nazri, 2022).

Fung et al. (2020) stated that the results of the spatial analysis indicated that most of the areas in the country are more prone to a short-term drought and higher severity, especially in the north part of the central region, the southern region, and the central part of the east coast. According to these microclimatic matters, there is an obvious need to adopt RWH as a promising water storage system for the citizens.

Since 2011, under the Local Government Department's Guidelines for Rainwater Harvesting and Utilisation System, local governments will not approve residential development plans that do not contain a rainwater harvesting system. RWHS is compulsory for new developments in Kuala Lumpur and encouraged in Selangor (San, 2023).

Table 2.3. Policies and guidelines related to RWHS under Malaysian government (Fakhira & Nazri, 2022; Lee et al., 2016; Shaari, 2020)

Guidelines	Department/Agency	Year
Guidelines for Installing a Rainwater Collection and Utilization System	Ministry of Housing and Local Government	1999
RWHS: Guidebook on Planning and Design	Department of Irrigation and Drainage Malaysia (DID Malaysia)	2009
Guideline on Eco-Efficiency in Water Infrastructure for public Buildings in Malaysia	National Hydraulic Research Institute of Malaysia	2011
Urban Stormwater Management Manual for Malaysia, MSMA 2nd Edition	DID Malaysia	2012
Panduan Pelaksanaan Inisiatif Pembangunan Kejiranan Hijau-Sistem Pengumpulan dan Penggunaan Semula Air Hujan	Federal Town and Country Planning Department	2012
Garis Panduan Perancangan Kejiranan Hijau	Federal Town and Country Planning Department	2012
Garis Panduan Sistem Pengumpulan dan Penggunaan Air Hujan	Federal Town and Country Planning Department, Ministry of Urban Wellbeing, Housing and Local Government	2013
Urban Stormwater Management - Part 6: RWHS, MS2526-6:2014	Department of Standards Malaysia	2014

Various initiatives in the form of policies and guidelines have been formulated by several agencies to facilitate and improve the implementation of RWHS for residential and government buildings in Malaysia (Table 2.3 and Table 2.4). The government gives full attention to RWHS as an alternative resource to reduce overdependence on rivers and other surface waters.

These findings highlight that rainwater harvesting (RWH) in Malaysia, especially in densely populated urban regions with high-rise buildings like Kuala Lumpur, is a promising and essential alternative water supply to be implemented. It also has significant potential for mitigating avenue floods.

Table 2.4. Government act and strategic plan related to sustainable water management (12MP, 2021; Shaari, 2020)

Act/ Strategic Plan	Statement
NAHRIM Strategic Plan (2016-2020)	Strategic Plan 1: Innovative research on water resource and water security for sustainable natural resources that aligned with National Water Policy 2012 and National Policy on Climate Change 2009.
National Policy on Climate Change 2009	Principles 2: Strengthen the implementation of climate change actions that contribute to environmental conservation and sustainable use of water resources. Key Action 1: Conduct systematic reviews and harmonized existing legislation, policies and plans on water resources.
National Policy on the Environment 2002	Principle 4: Manage natural resource utilization, sustain the resource base, and prevent degradation of the environment.
12th Malaysia Plan (2021-2025)	Chapter 9: Enhancing Energy Sustainability and Transforming the Water Sector
Integrated Water Resource Management of Malaysia (IWRM) 2016	10 Pillars for IWRM: Water for All 1- harmonizing water governance, 2-ensuring sustainable water resources, 3-mainstreaming water in national agendas, 4-innovative infrastructure design, 5-safe and affordable water services, 6-increase water ownership and participation, 7-transparent data-driven decision making, 8-creating business opportunities for water players, 9-strengthening disaster risk governance, 10-strengthening scientific community
National Landscape Policy 2011	Mission 2: To ensure a natural landscape resources are optimally utilized by considering protection, conservation, and preservation of sustainable management systems for the use of heritage and tourism.

2.3. Vertical Expansion – The Dominant Built-Up Pattern

As cities grow in density, they grow vertically, since their horizontal expansion becomes constrained by limitations imposed by the optimum horizontal scale for the functionality of cities. Even farming and other agricultural production activities are growing vertically through “vertical farms” (Van Gerrewey et al., 2022). Future cities will no longer be viewed as flat but as a three-dimensional (3D) manifestation of merged horizontal and vertical architecture (Ali & Al-Kodmany, 2012).

Tall buildings may have potential environmental advantages, such as ample access to sunlight and wind for the incorporation of solar panels and wind turbines, but they are environmentally damaging when they fail to incorporate energy-efficient design solutions in their heating, cooling, and ventilation systems. Furthermore, a new tall building will place additional load on transportation and infrastructure; existing power grid, water supply, and sewer systems.

Tall buildings require an abundance of energy for operation and utilities, including water. Many high-rises use more energy per resident than a well-built townhouse, and not much less than a small, well-built, single-family home (Fader, 2000). One of the principal problems with tall buildings of the past, even those offering great architecture, has been the failure to consider how the structure meets the ground and affects the surroundings environmentally (Ali & Al-Kodmany, 2012), as mentioned in Section 2.1.3 (and will be elaborated in detail in Sections 2.3.5 to 2.3.7) by changing the water cycle and runoff process.

2.3.1. Definition of Vertical Expansion – Vertical Urbanisation

Industrialization contributed to the growth of cities globally and resulted in the emergence of megalopolises (Saatcioglu, 2013); the spatial planning structure of cities developed horizontally, and the height of buildings and the number of floors increased (Jedwab et al., 2021).

Architects and researchers have always explored ideas for the development and reclamation of new lands in their projects; working with extreme climatic zones, with the elements of earth, water and air (Novikov & Gimazutdinova, 2021). In the age of rapid change, the 21st century, as Novikov and Gimazutdinova (2021) have discussed in their research, the vertical expansion of the cities has already started and is set to continue more vigorously in this century. Luca Curci Architects is actively developing projects for the

vertical arrangement in this paradigm of the cities; Vincent Callebaut puts forward many concepts for the future of these cities with an ecological aspect; John Wardle Architects and Stefano Boscuitti showcase the Multiplicity project, etc.

Among the indicators of urban growth, there is an index characterising intensity, type (horizontal vs. vertical), and spatial direction of growth over time, considering buildings with 4 (or more) floors as an expression of vertical urban expansion and buildings with 3 (or fewer) floors as reflecting horizontal growth (Zambon et al., 2019).

The concept of a vertical city was defined by Iusupova et al. (2019) and McManamay et al. (2019) as a set of vertical buildings with a developed infrastructure. According to Novikov and Gimazutdinova (2021), a vertical city is an entire ecosystem located in the air environment, significantly larger than a single building spot on Earth.

In this context, the development of architecture for the future vertical city and conceptual ideas for residential complexes should contribute to addressing environmental challenges and promoting de-urbanisation (Ahmadian et al., 2021; Bilorina, 2021; Mihaila, 2014). The development of innovative technologies in the field of building materials (Freitas & Brito, 2019; Gomez Jr, 2017), design features of high-rise buildings (Auerbach & Wan, 2020; He et al., 2021), and landscaping façades (Elsadek et al., 2019; Morakinyo et al., 2019) contributes to the expansion and systematisation of the future visions of vertical cities (Toivonen et al., 2021).

2.3.2. Definition of Tall Building

Governments around the world define tall buildings differently and there is no universal definition of the term (Al-Kodmany, 2012). The German regulations define tall buildings as buildings higher than 22 m (72 ft) with rooms for the permanent accommodations of people (Ross, 2004); the Leicester City Council in the U.K. defines a tall building as a building over 20 m (66 ft) in height, and/or a building of any height, which is substantially

higher than the predominant height of the buildings in the surrounding area (LCC, 2007); in Ireland, in the Cork City development plan (2022-2028), a tall building is defined as a building that is equal to or more than twice the height of the prevailing building height in a specific locality (CCC, 2021); the ASHRAE (American Society of Heating, Refrigerating and Air-conditioning Engineers), Technical Committee for Tall Buildings, defines tall buildings as buildings taller than 91 m (300 ft), they also addresses supertall buildings as taller than 300 m (984 ft) and megatall buildings as taller than 600 m (1968 ft) buildings (Simmonds, 2020) the Council for Tall Buildings and Urban Habitat (CTBUH, 2018) defines tall buildings as 50 m or more or 14 storeys or more, supertalls are 300 m and over, and megatalls are 600 m and over.

In Malaysia, high-rise buildings are defined as buildings that are seven storeys or more in height and are also referred to as tall buildings (Daud & Ishak, 2018) or a building taller than 23 m (75 ft) height (Yatim, 2009). Although the number of floors is not the best indicator of defining a tall building due to the changing floor-to-floor height between differing buildings and functions (e.g., office versus residential usage) (Nguyen, 2012), but for the scope of this research, it is a convenient way to distinguish them as buildings taller than 23 m height according to the definition of the term in the Malaysian context. The tall building term considered in this thesis is assumed to be office, commercial, residential, hotel, health-care, education, and mixed-use buildings, with a possibility of RWH from curtain wall façade areas.

2.3.3. Wind Flow Patterns around Tall Buildings

In nature, trees, hills, and mountains influence ground-level wind patterns. When these objects are in groups, such as forests and ridges, they have broader effects on the surrounding area.

In urban areas, tall buildings influence the wind pattern significantly, with the difference

that, unlike nature, buildings have sharp corners and rectangular shapes.

When wind hits a building wall, it is deflected in all directions. Some of the wind is deflected upwards and around the sides of the building, causing no effect at ground level; a significant portion of the air is deflected downward along the building wall, causing draughtiness and turbulence at ground level (Scarano, 2022) (Figure 2.10).

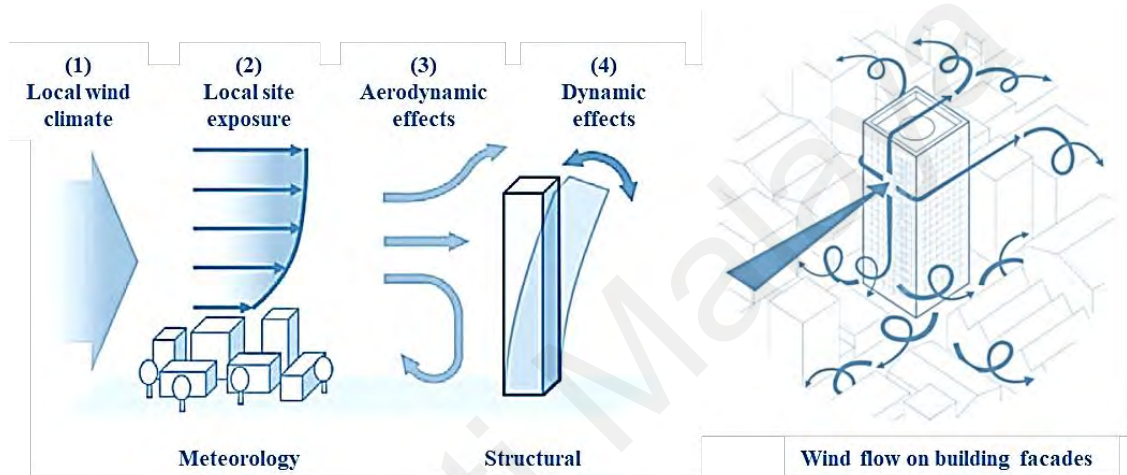


Figure 2.10. Schematic depiction of the wind loading chain on tall building façades (Abu-Zidan, 2019; Abu-Zidan et al., 2022; Yuvaraj et al., 2022)

At the windward façade, where the wind first strikes the building, the wind stream splits above and around the sides of the building; the airflow accelerates around the corners of the building (Scarano, 2022).

Figure 2.10 illustrates the systematic approach flow of the wind on a tall building façade; various contributing factors that include the local wind climate and site exposure, and the aerodynamic and structural properties of the building. Abu-Zidan (2019); Abu-Zidan et al. (2022) explained these factors as below:

- i. Local wind climate: this is where meteorological models are used to estimate design wind speeds for a given return period,

- ii. Local site exposure: when the approaching wind travels towards the building, it interacts with local site condition; including effects of typology, terrain roughness, and site exposure,
- iii. Aerodynamic effects: when the wind profile reaches the building, it generates aerodynamic loads that act on the structure,
- iv. Dynamic effects: they are influenced by structural properties, such as mass, stiffness, and damping.

Contributing factors related to local wind climate and local site exposure as the scope of this research are elaborating more in Section 2.5.

2.3.4. Distortion of the Runoff Process by Tall Buildings

The number of megacities with a population of 10 million or greater is also expected to rise from 33 to 43 in the period 2018-2030 (UNDESA, 2018). In those cities, the numbers of so-called high-rise buildings (e.g., 300-metre-or-higher tall buildings) are also increasing (Gabel & Shehadi, 2017; Safarik et al., 2015). Increased impervious areas in the city increases the runoff volume, as well as the runoff peak and consequently flood risk.

The effect of urbanisation on the rainfall-runoff analysis has been one of the most important issues in hydrology (Chen et al., 2015; Du et al., 2012; Hejazi & Markus, 2009; Jung & Kim, 2017; Li et al., 2013; Niemi et al., 2019; O'Driscoll et al., 2010; Prosdocimi et al., 2015; Roy et al., 2009; Yao et al., 2016). Most of these studies have focused on urban flooding, although some studies have also raised the problems of decreased infiltration and dry streams (Jung & Kim, 2017; O'Driscoll et al., 2010; Roy et al., 2009). In those analyses, urbanisation is considered simply by increasing the impervious areas. That is, the impervious area is the sole and key factor used to consider urbanisation (Yoo et al., 2021).

Megacities are three-dimensional. The conventional cities (two-dimensional) are characterised by impervious areas and megacities are characterised by additionally considering tall buildings. That is, in terms of rainfall-runoff, the two-dimensional cities consider the change in infiltration to be important, but the three-dimensional megacities should additionally consider the rainfall interception by the high-rise buildings. In previous studies, 2D cities, the interception of buildings was considered a loss (Grimmond & Oke, 1991; Hamdi et al., 2011; Lemonsu et al., 2007), or buildings were regarded as a factor that slows the runoff (Cea et al., 2010; Chan, 2012; Dottori & Todini, 2013; Schubert et al., 2008). However, Yoo et al. (2021) highlight that in 3D cities, the intercepted rainfall should be analysed as an additional source of runoff.

The role of interception by tall buildings in an urban basin is similar to the role of high mountains in a natural basin; both have a major effect on the interception of rainfall that falls obliquely due to the wind (Yoo et al., 2021). For example, Hughes et al. (2009) showed that the role of the mountain is to make different runoff patterns on its coastal side and its inland side. Simply, the mountain intercepts rainfall to make additional runoff on the coastal side. The role of the tall buildings in megacities can be assumed to be similar to that of the mountains. It is important to note that tall buildings alter and complicate the runoff pathway.

2.3.5. Three-Dimensional Flow Path

As it was stated in the previous section, high-rise buildings change the flow path of runoff in the basin. Generally, the flow path is considered over the two-dimensional plane. The flow length is estimated as the horizontal distance, and the flow velocity is determined by considering the slope of the land surface (Yoo et al., 2021). In urban basins, buildings are assumed to be simply a part of the impervious area. The building's shape, including its height and width, is not considered in the flow path. In some two-dimensional rainfall-runoff models, the flow path on the land surface is determined by considering the barrier

role of a building (Bisht et al., 2016; Huang & Jin, 2019; Leandro & Martins, 2016; Seyoum et al., 2012).

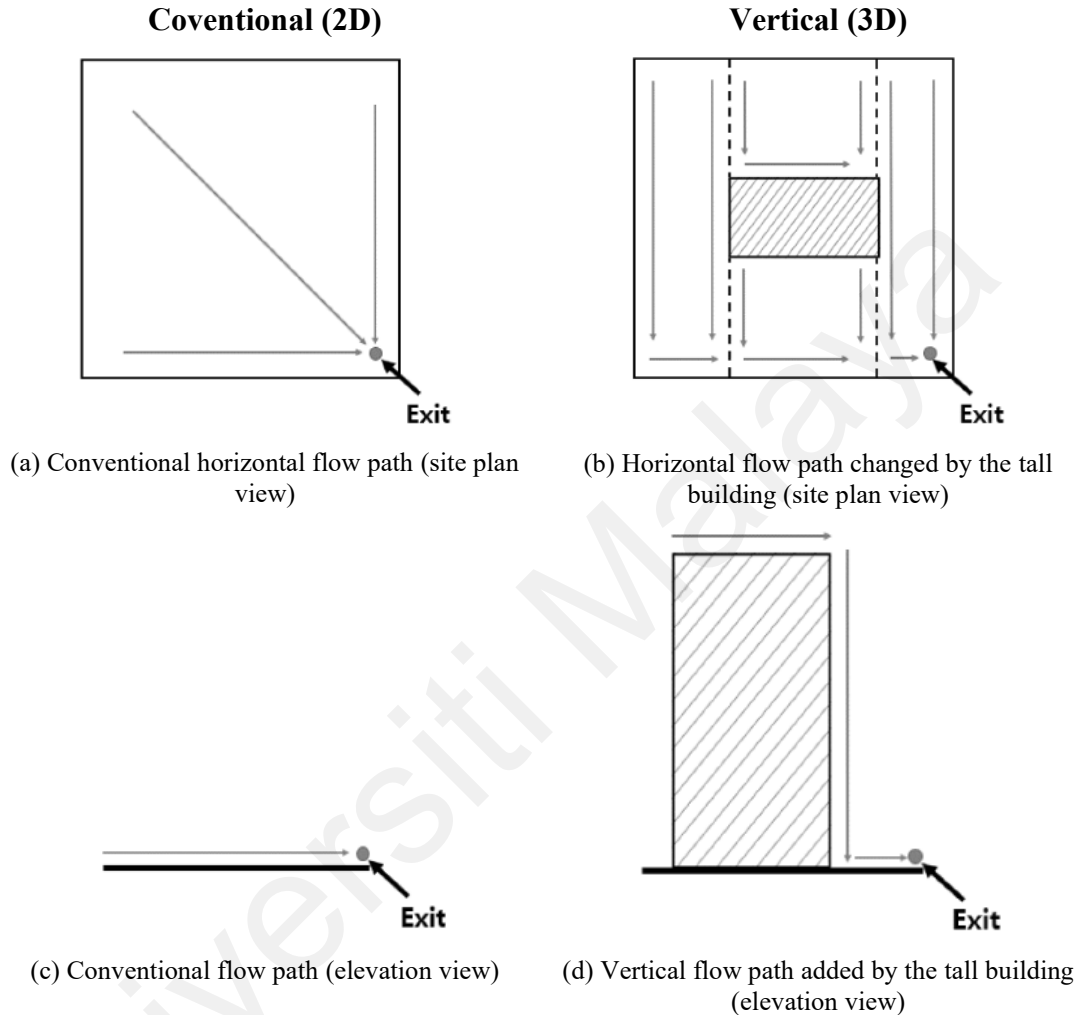


Figure 2.11. Comparison of conventional flow path and changed flow path by a building (Yoo et al., 2021)

Figure 2.11 illustrates the possible change of flow path due to a tall building; (b) shows the changed flow paths due to a tall building over the two-dimensional plane, which are very different from the conventional ones, as shown in (a). Additionally, the high-rise building makes the flow path three-dimensional (see (d)). The flow path cannot be two-dimensional, as is the case in the conventional model (see (c)). The vertical path is especially important in the case where the travel time from the rooftop of a building to

the ground is relatively long. In a small urban centre with many tall buildings, this change will undoubtedly be concentrated. In this case, the flow path from the building wall to the ground can also be considerable and important.

2.3.6. Sub-Basin Division

In the sub-basin division, it is important to consider various areas with different characteristics in the runoff estimation. In particular, the tall building itself can be divided into several sub-basins. Figure 2.12 (b) shows an example of the sub-basin division of a tall building. The conventional method of sub-basin division is as shown in Figure 2.12 (a), even in the case of considering a building as a barrier against surface runoff.

Figure 2.12 (b) illustrates the division of a tall building into one sub-basin of the rooftop and four building walls. The flow path from the rooftop of a building (sub-basin ① - 1) includes the rooftop itself and the flow through the vertical drainage pipe. The flow path from the building wall (sub-basins ① - 2 – ① - 5) is composed of the surface flow on the building wall, and the free fall again to the ground. In particular, when the wind is rather high, the sub-basins ① - 2 – ① - 5 (building walls) are important. If the wind speed exceeds 8.2 m/s, the intensity of wind-driven rain on building walls can be higher than that on a building's rooftop (Cho et al., 2020).

Yoo et al. (2021) confirmed the significant role of the building wall in increasing runoff volume and peak flow, particularly when the wind speed was high; if considering higher buildings, it becomes even higher. And based on Cho et al. (2020), if the ratio of the wall area to the rooftop area increases to 10, the amount of rainwater from the building wall can be larger than that from the rooftop, even in the case where the wind speed is only around 1 m/s.

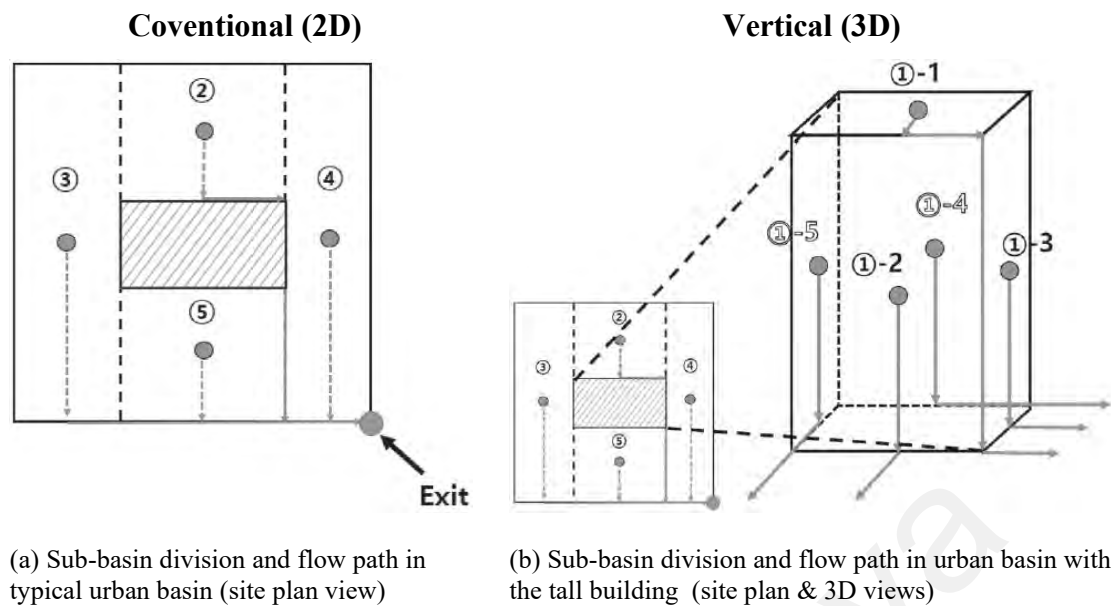


Figure 2.12. Comparison of sub-basin division and flow path in urban basin with and without the tall building (Yoo et al., 2021)

2.3.7. Water Sustainability in Tall Buildings

The RWH technologies decrease building energy usage by augmenting system efficiency (Liu et al., 2019). It is reported that the rainwater usage in residential areas of Brazil is able to promote drinking water savings of between 48% in the southeast area and 100% in the northern area (Ghisi et al., 2007; Ghisi & Ferreira, 2007). The objective of RWH is to conserve the quality and quantity of natural water sources with minimum degeneration, evacuation, and diversion by minimising freshwater usage. Ultimately, a water-sustainable building or water-independent building will balance the water consumption completely. The principal water resource consists of sources within the same position as the catchment area and aquifer of the building's water supply (Fowler et al., 2017).

The economic performance of RWHS was investigated by Lani et al. (2018a) in Malaysia, where the authors investigated rainwater harvesting for non-potable water consumption in small and large commercial buildings. They showed that RWHS is more efficient in large buildings compared to small buildings.

2.3.8. Façade Rainwater Harvesting

For most of history, buildings have been constructed using the exterior wall as the main structural system. Advancements in steel and reinforced concrete allowed the structural system to be independent of the façade and recede behind the envelope. The exterior walls were then allowed to be much lighter, and thus non-load-bearing. With this advancement, buildings used large glass façades in lieu of masonry walls. The Bauhaus movement started to incorporate the idea of a modern curtain wall, consisting of mullions and glass; the same idea predominates in much contemporary high-rise design.

Water and moisture have always been concerns in curtain wall construction. The materials used in the system are heavily dependent on how well they withstand corrosion and water accumulation. Modern curtain walls use an array of sealants, gaskets, and flashing to prevent such issues. Watertight construction is integral to the life of the façade system and the overall building. Hence, curtain walls have become vertical waterproof surfaces, non-absorbent (Section 2.2.4.1), and with high runoff coefficient (Section 2.2.4.2).

Large buildings have generally been required to introduce RWH facilities; globally, it has been a recommendation in some cities and an obligation in others. However, the roof garden as a green infrastructure has become more popular nowadays; (i) quite effective for alleviating the heat island effect in a city (Heidarinejad & Esmaili, 2015; Lehmann, 2014; Qin et al., 2013; Shafique et al., 2018), and (ii) residents prefer to use the building roof as a garden due to its recreational benefits (Kim et al., 2018; Taib et al., 2019; Zhang et al., 2020).

In recent studies, the method of rainwater harvesting with a green roof has been developed (Almeida et al., 2021; Monteiro et al., 2016; Pimentel-Rodrigues & Silva-Afonso, 2017), but its applicability is quite limited in most countries. In simple terms, the places for

rainwater harvesting decrease as the number of green infrastructures, such as roof gardens, increases.

Under these circumstances, a building wall can be a good alternative. On the other and, a large portion of wind-driven rain (WDR) collides with the building wall due to the wind. As stated earlier (Section 2.3.6), Cho et al. (2020) have also suggested the possibility of harvesting rainwater from the building wall. They showed that, in the case of a wind speed of 4 m/s or higher, the amount of harvested rainwater from the building wall could be higher than 50% of that from the building roof of the same area. Additionally, if the area of the building wall is 10 times larger than that of the building roof, the amount of harvested rainwater from the building wall could be more than that from the building roof, where the wind speed is only around 1 m/s. This estimation by Cho et al. (2020) is an analytical one, which should be proven by field measurements and evaluations.

2.4. Seasonal Classifications in Malaysia

In 2017, the tropical climate of Malaysia was greatly influenced by natural climate variability due to normal weather conditions and neutral ENSO (Bahari et al., 2017).

The ENSO index was neutral from January 2017 until the end of November 2017. A weak La Niña condition started in December 2017. Throughout 2017, Malaysia did not experience long-lasting hot and dry weather (Bahari et al., 2017). The haze phenomenon, drought, and heatwave also did not happen. Table 2.5 displays the classification of tropical seasons experienced in Malaysia in 2017.

In 2017, most of the stations recorded a consistent average wind speed compared to the long-term average. Generally, Malaysia has experienced normal tropical weather and climate conditions throughout 2017. Thus, in general, the climate condition during the measurement period of this research is considered reliable for further assessments and future potential research contributions.

Table 2.5. Duration of seasons in Malaysia in 2017. Data derived from (Bahari et al., 2017)

Seasons	Duration (month)
1. Monsoon Transitional Period	1.5
2. Southwest Monsoon	4.5
3. Monsoon Transitional Period	1.5
4. Northeast Monsoon	4.5

Malaysia's climate is characterised by three main components, namely temperature, wind pattern, and rainfall (Bahari et al., 2017). In this section, wind and rainfall patterns are briefly described as the main parameters affecting the WDR phenomenon.

2.4.1. Wind

The winds over the country are generally light and variable. There are, however, some uniform periodic changes in the wind flow patterns. North-easterly winds prevail during the boreal winter monsoon (locally known as the northeast monsoon) from November to March. South-westerly winds prevail during the boreal summer monsoon (locally known as the southwest monsoon) from May to September (MESTECC, 2018). These monsoons are separated by two shorter inter-monsoon periods.

2.4.2. Rainfall

Rainfall is characterised by two rainy seasons associated with the southwest monsoon (SWM) from May to September and the northeast monsoon (NEM) from November to March (Suhaila & Jemain, 2009; Tangang, 2001). The monsoon winds and topography are likely the main factors controlling the magnitude of the spatial rainfall variation in the country (Wong et al., 2016).

The Titiwangsa Range is a mountain range that forms the backbone of the peninsula. During the northeast monsoon (NEM), stronger winds blow to the exposed areas, e.g., the east coast of Peninsular Malaysia (Camerlengo & Demmler, 1997; Juneng et al., 2007;

Lim et al., 2013), thus these areas receive a substantial amount of rainfall. Higher wind speeds promote more evaporation, which destabilises the boundary layer, triggers deep convection, and hence increases rainfall (Back & Bretherton, 2005).

These features have blessed Malaysia with abundant annual rainfall, with an average ranging from about 2,000 mm to 4,000 mm (MESTECC, 2018). During the southwest monsoon and the inter-monsoon periods, heavy rain from convective showers and thunderstorms occurs in the late afternoons and evenings. Figure 2.13 shows the annual rainfall for Peninsular Malaysia from 1951 to 2015 (MESTECC, 2018). For this period, there is a very slight decreasing trend in the rainfall for Peninsular Malaysia. For a shorter time-frame from 1990 onwards, increasing trends in rainfall are observed for Peninsular Malaysia.

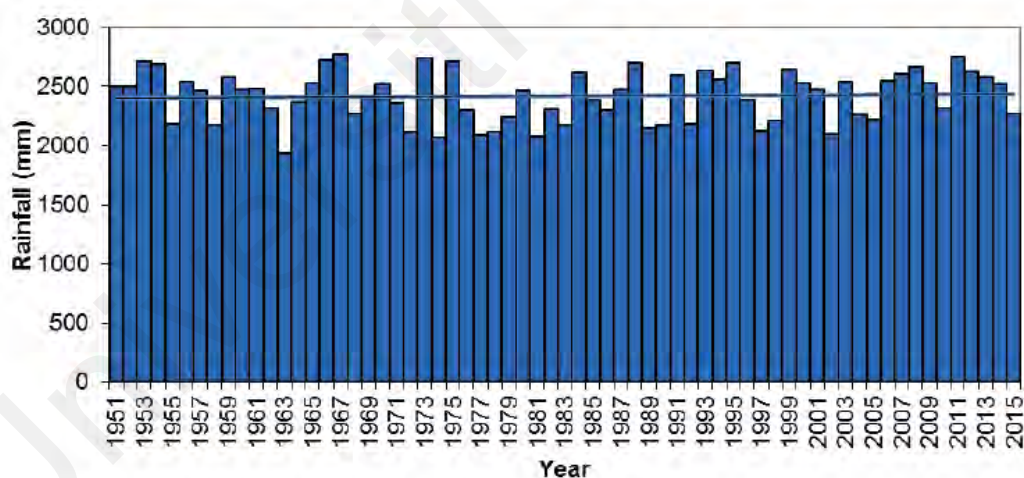


Figure 2.13. Annual rainfall trends for Peninsular Malaysia (MESTECC, 2018)

2.4.3. An overview on the weather conditions in Malaysia from 2017 to 2021

A summary of weather conditions (wind and rainfall), and seasonal classifications for each year between 2017 to 2021 that has been experienced in the region derived from the latest reports by the Malaysia Meteorological Department (METMalaysia, 2017, 2018, 2019, 2020, 2021) is presented below.

2.4.3.1. Wind and Rainfall Patterns in 2017

In 2017, the climate in Malaysia was greatly influenced by the natural climate variability due to the normal weather conditions and neutral ENSO. Most of the stations recorded a consistent average wind speed compared to the long-term average. In 2017, the rainfall recorded for the Peninsular Malaysia is between 1,311 mm and 6,078 mm (Figure 2.14). The highest daily average wind speed recorded all over Malaysia was 7.1 m/s in Kota Bharu on 31st December 2017. In general, throughout the year Malaysia has experienced normal weather and climate conditions. The neutral state of ENSO in 2017 was also a contributing factor to the lack of haze, drought, and heat waves phenomenon. Below are the periods of season experienced by Malaysia in 2017 (METMalaysia, 2017):

- i. Monsoon Transitional Period: April 2017 to 16th May 2017
- ii. Southeast Monsoon: 17th May 2017 to 5th October 2017
- iii. Monsoon Transitional Period: 6th October to 12th November 2017
- iv. Northeast Monsoon: 13th November to 27th March 2018

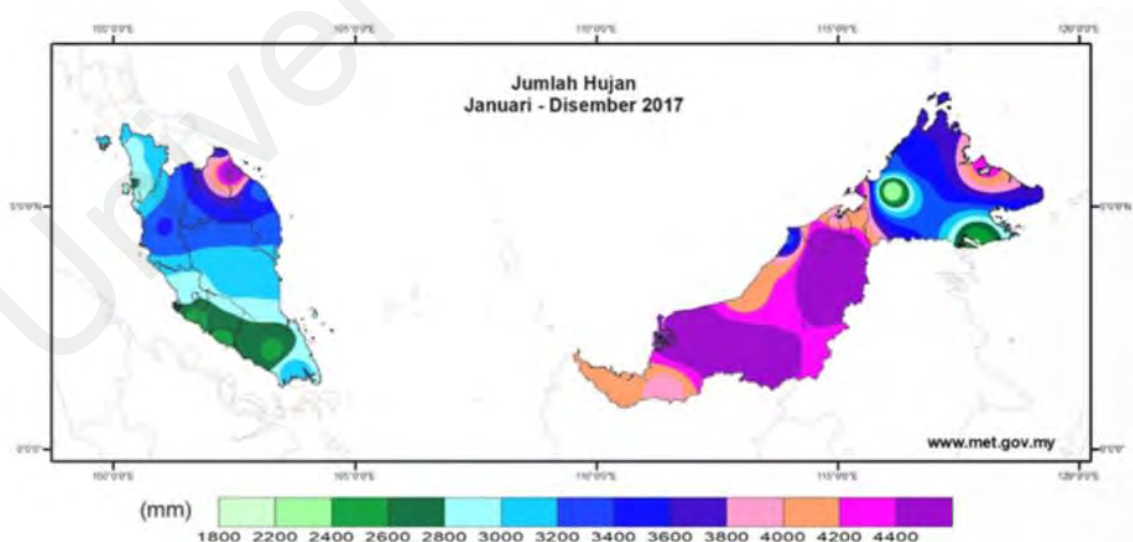


Figure 2.14. Total annual rainfall 2017 (METMalaysia, 2017)

2.4.3.2. Wind and Rainfall Patterns in 2018

In 2018, the climate in Malaysia was greatly influenced by the natural climate variability due to the normal weather conditions. The negative ENSO condition started since October 2017 until March 2018. This was a weak La Nina condition. The ENSO was neutral beginning April till September 2018 and became weak El Nino in October 2018. Throughout 2018, Malaysia did not experience long-lasting hot and dry weather. However, certain areas have experienced rainfall below normal and haze in August. The presence and formation of tropical storms or hurricanes in the South China Sea can affect rainfall and strong winds especially in the west coast of Sabah, northern Sarawak, north and northeast of the Peninsula. Although Malaysia is not directly affected from tropical storms, the impacts of a tropical storm can cause heavy rainfall, high winds and high tides around the trajectory area of the tropical storms. In 2018, the rainfall recorded for the Peninsular Malaysia is between 1,800 mm and 3,900 mm, mostly in Selangor (Figure 2.15). The highest daily average wind speed recorded all over Malaysia was 7.0 m/s in Kota Bharu, Kelantan pada on 1st January 2018. The following are the seasons and their duration encountered by Malaysia in 2018 (METMalaysia, 2018):

- i. Northeast Monsoon: 21st November 2017 to 2nd March 2018
- ii. Inter Monsoon: 3rd March to 8th May 2018
- iii. Southeast Monsoon: 9th May to 3rd October 2018
- iv. Inter Monsoon: 4th October to 26th 2018
- v. Northeast Monsoon: 26th October 2018 to 18th March 2019

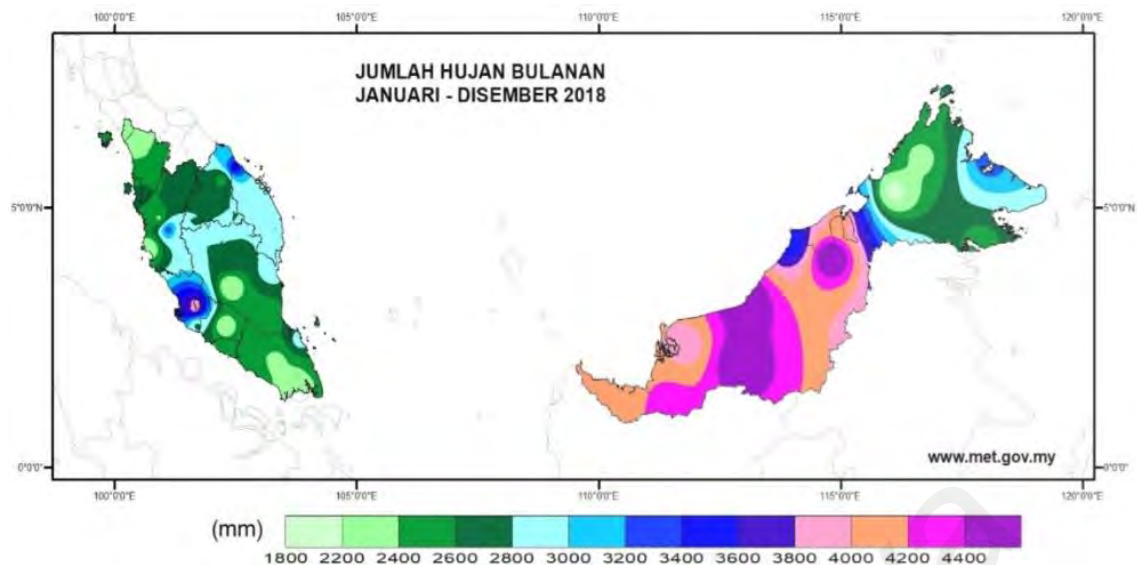


Figure 2.15. Total annual rainfall 2018 (METMalaysia, 2018)

2.4.3.3. Wind and Rainfall Patterns in 2019

In 2019, the climate in Malaysia was influenced by a weak phase of El-Nino which started in October 2018 and continued until June 2019, followed by a neutral ENSO that continued until December 2019. A weak El Nino phenomenon usually has a minimal impact on rainfall distribution in Malaysia. In 2019, the rainfall recorded for the Peninsular Malaysia is between 1,800 mm and 3,900 mm, mostly in Selangor (Figure 2.16). The highest daily average wind speed recorded all over Malaysia was 6.6 m/s in Mersing, Johor on 7th December 2019. The following are the seasons and their duration encountered by Malaysia in 2019 (METMalaysia, 2019):

- i. Northeat Monsoon: 26th October 2018 to 18th March 2019
- ii. Inter Monsoon: 19th March to 1st May 2019
- iii. Southesat Monsoon: 2nd May to 24th September 2019
- iv. Inter Monsoon: 25th September to 13th November 2019
- v. Northeast Monsoon: 14th November 2019 to 18th March 2020

During the northeast monsoon 2019/2020, seven episodes of heavy rainfall occurred in November and December 2019 which resulted in floods in Kelantan, Terengganu, Pahang, Johor, Negri Sembilan, and Sarawak. During the inter-monsoon period, several flash floods occurred in the west coast states of the Peninsula in October 2019. Two water spouts incidents were also reported in Penang on April 1st and Miri, Sarawak on April 15th, 2019. Although Malaysia is relatively safe from direct tropical cyclone hit, the presence of a tropical at a certain location may alter the wind pattern over the region, resulting in heavy rainfall, strong winds, and high waves. Typhoon Lekima which ravaged eastern China on August 9th, 2019, also adversely affected the weather condition over northern part of Peninsula.

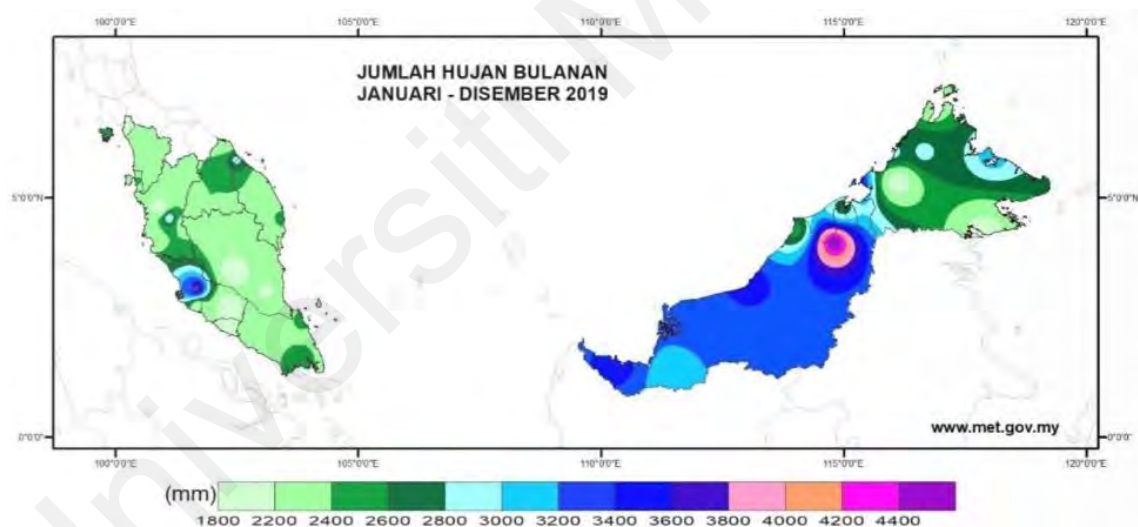


Figure 2.16. Total annual rainfall 2019 (METMalaysia, 2019)

2.4.3.4. Wind and Rainfall Patterns in 2020

In 2020, the climate in Malaysia was influenced by the natural climate variability due to the normal weather conditions and neutral ENSO until August and it was changed to a weak La Nino condition until the end of the year. This condition also affected the weather patterns which are usually dry and hazy during the southwest monsoon but have received

heavy rains especially in the west coastal states of Peninsular Malaysia. Almost all areas in Malaysia received an annual rainfall of an average of between 1,700 mm and 5800 mm (Figure 2.17). The west coast states of the Peninsula, especially Perak, Selangor, and the Federal Territory of Kuala Lumpur, are also among the areas that record high amounts of rainfall, usually due to thunderstorms during the monsoon transition (inter monsoon). The highest daily average wind speed recorded all over Malaysia was 7.6 m/s in Kota Bharu on 17th December 2020. The following are the seasons and their duration encountered by Malaysia in 2020 (METMalaysia, 2020):

- i. Inter Monsoon: 27th March to 17th May 2020
- ii. Southwest Monsoon: 18th May to 21st September 2020
- iii. Inter Monsoon: 23rd September to 10th November 2020
- iv. Northeast Monsoon: 11th November 2020 to 15th March 2021

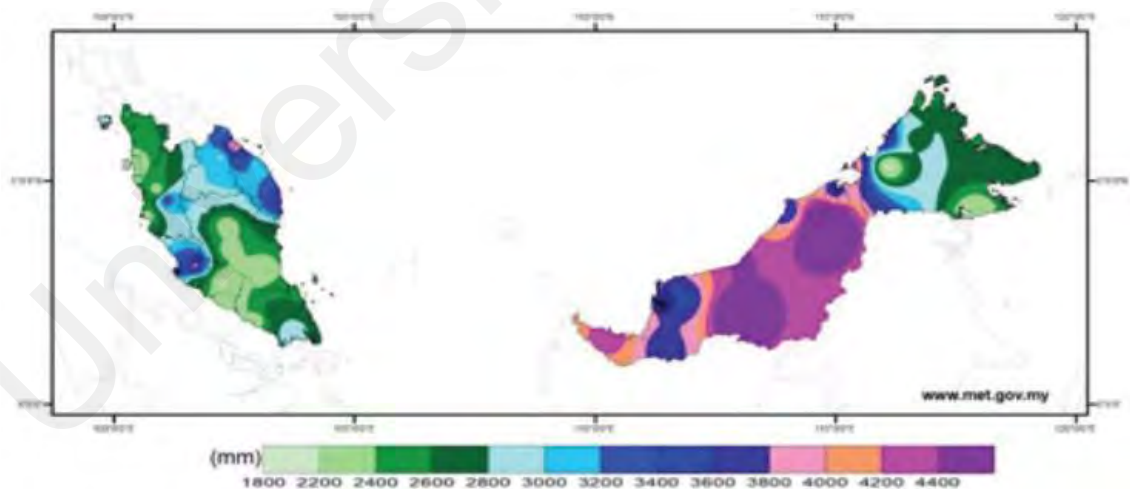


Figure 2.17. Total annual rainfall 2020 (METMalaysia, 2020)

2.4.3.5. Wind and Rainfall Patterns in 2021

A moderate La Niña phase began in August 2020, followed by a neutral ENSO in June to July and then a La Niña episode returned in August until the end of 2021.

The 2021/2022 northeast monsoon began on 3 November 2021 and ended on 15 March 2022. The widespread heavy rainfall episodes that occurred in November and December 2021 have resulted in several states, especially in the Peninsula, experiencing flooding.

The 2021 rainfall shows that almost all areas received annual rainfall at average levels except for a few areas in Pahang, Selangor, Perak, Melaka, Johor and Sabah which recorded slightly above average rainfall. The total rainfall recorded throughout 2021 was between 1500 mm to 5400 mm (Figure 2.18). The highest daily average wind speed recorded all over Malaysia was 7.9 m/s in Kota Bharu on 31st December 2021. The following are the seasons and their duration encountered by Malaysia in 2021 (METMalaysia, 2021):

- i. Inter Monsoon: 16th March to 18th May 2021
- ii. Southwest Monsoon: 19th May to 23rd September 2021
- iii. Inter Monsoon: 24th September to 2nd November 2021
- iv. Northeast Monsoon: 3rd November 2021 to 13th March 2022

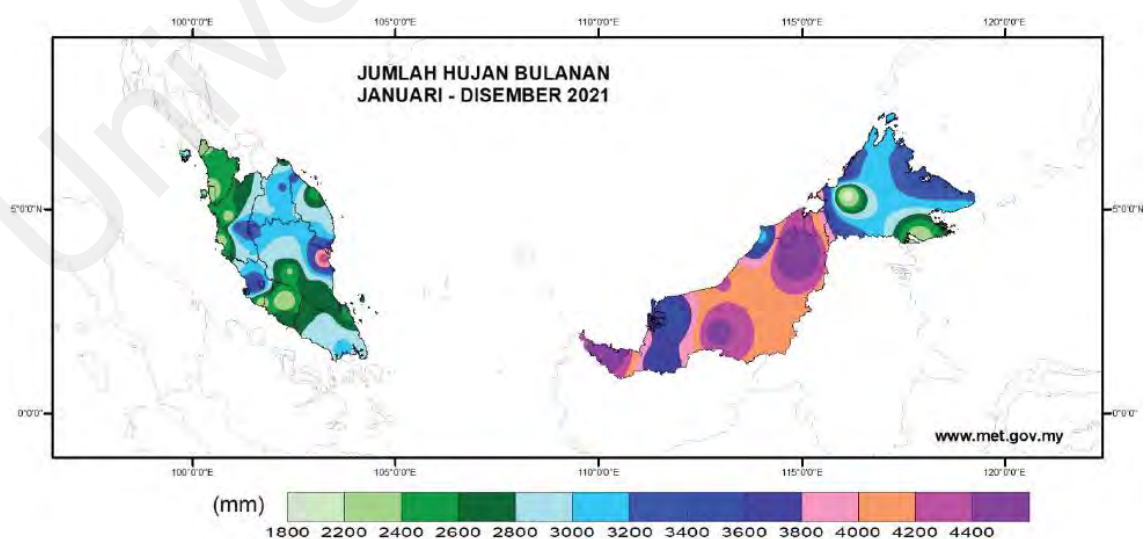


Figure 2.18. Total annual rainfall 2021 (METMalaysia, 2021)

2.5. Experimental Field Measurement – Meteorological Parameters

As mentioned earlier in Section 1.6, the first step to determine the amount of impinged WDR on the vertical surface in building science is conducting field measurement. This phase provides the amount of raindrops on the building wall as well as the meteorological factors influencing the WDR intensity (R_{wdr}) including wind speed (U), wind direction (D), and horizontal rainfall intensity (R_h) measurements.

The field measurement methods of WDR in building science have remained practically unchanged since the early driving rain research in the 1930s (Blocken & Carmeliet, 2004). WDR measurements on buildings have indicated that the ratio of WDR intensity is proportional to wind speed and horizontal rainfall intensity (Blocken & Carmeliet, 2007b). In a comprehensive review of WDR measurement methods by (Blocken & Carmeliet, 2004) it is mentioned that a systematic experimental approach to WDR assessment is not feasible, provides spatial and temporal information and measurements at a particular location, they are labour-intensive, expensive, difficult, and are not usually measured at meteorological stations. This explains why the datasets of WDR field measurements are not widely accessible.

They further discussed how, despite all its drawbacks, the experimental method remains important for scientific research in gaining knowledge on the interaction between WDR and buildings. Furthermore, the semi-empirical methods (WDR relationships) require the field measurements to be developed and validated as reliable models on a theoretical basis with coefficients that are determined from the measurements (Blocken & Carmeliet, 2004; Ge et al., 2017; Shi et al., 2016).

According to Blocken and Carmeliet (2005b), an adequate experimental WDR dataset should include the following information:

- i. Detailed descriptions of the building site,

- ii. Building geometry,
- iii. Measurement equipment and setup,
- iv. Measurements of the reference wind speed (U), reference wind direction (D) and horizontal rainfall (S_h) conducted near the building site and in free-field conditions, i.e., at a position that is not significantly influenced by the presence of the building,
- v. WDR (S_{wdr}) measurements at the façades with a sufficiently high resolution in space and time,
- vi. Error estimates for the WDR (S_{wdr}) measurements.

In this section, the basis on WDR measurement in building science and its dominant factors are reviewed. The next section (2.6) provides an overview of WDR gauge design and experimental measurement guidelines.

2.5.1. Wind Measurement – Wind Speed (U) and Wind Direction (D)

Field measurements of wind flow are used in WDR research to monitor local weather conditions during rain events. For this purpose, a meteorological mast is usually equipped with measurement devices to measure the wind direction and wind speed; and the position of the measurement devices is chosen close enough to the building but out of the region where the building causes upstream disturbances so that they will measure the incident wind profiles (Kubilay, 2014).

A standard wind measurement consists of measuring the mean horizontal wind speed (m/s) and wind direction (degrees clockwise from north: 0° - north wind (N)) (Blocken & Carmeliet, 2004). The instruments used to measure wind are known as anemometers and can record wind speed, direction and the strength of gusts. The most common combination unit is a cup anemometer to measure the horizontal component of the wind

speed vector, and a wind vane to measure the wind direction; they are described further as (WOW, 2018):

Cup anemometer – Wind speed is normally measured by a cup anemometer consisting of three or four cups, conical or hemispherical in shape, mounted symmetrically about a vertical spindle. When the wind blows into the cups, the spindle rotates. In standard instruments, the design of the cups is such that the rate of rotation is proportional to the speed of the wind to a sufficiently close approximation.

Wind vane – Wind direction is measured by a vane consisting of a thin horizontal arm carrying a vertical flat plate at one end with its edge to the wind, and at the other end a balance weight that also serves as a pointer. The arm is carried on a vertical spindle mounted on bearings, which allow it to turn freely in the wind. The anemometer and wind vane are each attached to a horizontal supporting arm at the top of a 10-metre mast.

The “cup overspeeding” problem is often quoted as one of the disadvantages of cup anemometers, since it leads to bias in the measured mean wind speed due to longitudinal wind speed fluctuating (turbulence). However, Kristensen (1992) has reported that overspeeding only exceeds about 2% in extreme cases. The most striking characteristic of the wind is its stochastic nature or randomness. There is a wide range of variability in the wind pattern; both geographically and temporally. Wind velocities are altered locally by obstacles in the surrounding area, such as trees or buildings. Patnaik and Samantaray (2010) explain that wind patterns vary from location to location, wind speed may change from year to year, and wind distribution will change from decade to decade. It is also clarified in their research that wind distribution is more predictable over a shorter time span, like a year, but on a shorter time-frame, like a few days, it is difficult to predict.

To obtain the mean wind speed over a certain time-frame, wind speed is usually sampled and averaged at short intervals; ranging from 1 minute to less than 1 second. In 1957, Van der Hoven generated a wind-speed spectrum from long- and short-term records at Brookhaven, New York (Van der Hoven, 1957). This spectrum is based on full-scale measurements and is illustrated in Figure 2.19. Their measurements revealed several distinctive characteristics and time scales of the wind speed spectrum (Amoloye, 2012), demonstrating clear peaks corresponding to the synoptic, diurnal, and turbulent effects:

- i. Wind speeds are driven by weather fluctuations, which vary on a macro-meteorological scale with periods in the order of hours and days (Isyumov, 2012),
- ii. Details of the wind structure in a strong wind are predominantly dependent on mechanically generated turbulence, which is generated at a micro-meteorological scale with periods of seconds and minutes (Amoloye, 2012),
- iii. The ‘spectral gap’ (the region with low energy in between the peaks) between the diurnal and turbulent peaks shows that these variations can be treated quite distinct from the higher-frequency fluctuations of turbulence (Patnaik & Samantaray, 2010),
- iv. The spectral gap stretches from periods of 10 minutes to periods of more than 1 hour, and the value of the mean wind speed is stationary in the gap. Hence, averaging wind-speed measurements over a period of 10 minutes to 1 hour yields relatively stable mean values; which is why these averaging intervals are practically always used (Blocken & Carmeliet, 2004).

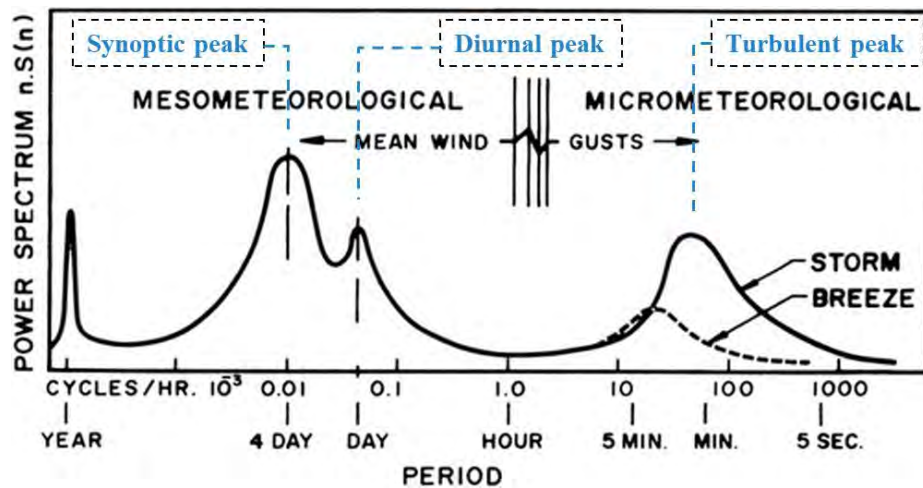


Figure 2.19. Van der Hoven horizontal wind-speed spectrum. The energy of the wind is mainly situated in the peaks that are situated at a period of 1 year, 4 days, 1 day and 1 minute. In the “spectral gap” between 10 minutes and about 1 hour, little energy is situated and the mean wind speed shows stationarity for these time periods (Amoloye, 2012; Blocken & Carmeliet, 2004; Patnaik & Samantaray, 2010).

According to the WMO (2018) standard, the height for wind measurements over land is 10 m. Blocken and Carmeliet (2004) highlighted that standard free-field wind speed and wind-direction measurements should be performed outside the wind-flow pattern that is disturbed by the building. In addition, given the fact that all wind directions are possible, they suggested keeping measurements sufficiently far away from the building so that they are out of the wake at all times.

2.5.2. Horizontal Rainfall (S_h) Measurement

To measure horizontal rainfall (S_h) and/or rainfall sum, many types of rain gauges have been developed; varying in shape, size and the measuring principle used (Blocken & Carmeliet, 2004). There are two types of recording gauges that are mostly used in building science; the tipping-bucket rain gauge, and the capacitance rain gauge. The tipping-bucket rain gauge is well-known, the capacitance gauge is less known and more expensive; consists of a cylindrical rainwater collector containing a probe made of a stainless steel rod covered by polytetrafluoroethylene.

Many researchers have studied errors in rainfall measurements in the past, with the wind error being considered the most important (Blocken & Carmeliet, 2004). There are a number of measures to minimise this error, all of which aim to achieve the same goal: to make the air flow horizontal above the gauge orifice (Blocken, 2010). To achieve this, three options are recommended:

- i. Ground-level gauges also known as rain gauges, are placed in pits with their orifices level with the ground surface,
- ii. To build a turf wall around the gauge,
- iii. To fix a shield around the rain gauge orifice.

Given the extreme variability of rain, it is important to carefully select the minimum sampling interval for rain measurements. Focusing on the use of meteorological data for Heat-Air-Moisture transfer analyses, in the guideline by Blocken and Carmeliet (2004), it is highlighted that Hens (1996) states that, given the fact that only hourly data are available for most weather stations and that the costs to obtain them are high, hourly data are often considered to be the best choice. But he also stresses that, as a general guideline, the time-averaging period should not induce loss of important information for the case analysed (Blocken & Carmeliet, 2004).

For this study, the daily-recorded horizontal rainfall amount (S_h) was provided by the nearest MMD to the campus of Universiti Malaya using the tipping-bucket method (is elaborated in detail in Section 3.2.2.2). The Malaysian Meteorological Department measures precipitation using conventional and automatic equipment. For automatic observation, several types of instruments have been developed, such as tipping buckets, weighing gauge and new technology devices that use laser technology. Tipping-buckets are the most widely used because their technology has been around for a long time and the mechanism is simple and mechanical (MMD, 2024).

2.6. Experimental Field Measurement – WDR

2.6.1. WDR Definition

According to Foroushani (2013), wind-driven rain (WDR) or driving rain is rain that is carried (driven) by wind and driven onto building envelopes with vector intensity, causing oblique rain with the influence of gravity (Figure 2.20).

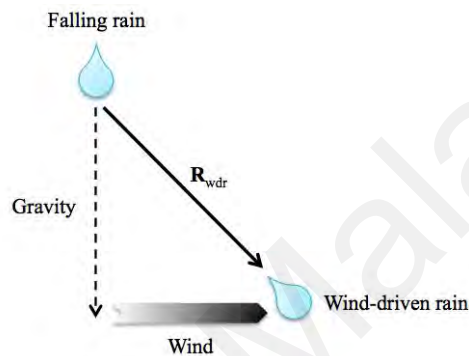


Figure 2.20. Wind-driven rain vector

Krpan (2013) reported that in meteorology, the catch is the quantity of rainwater received in the collector of a gauge and measured in the reservoir over a particular time period. When two gauges are used over the same period, the catch ratio is the quantity collected in one reservoir divided by the quantity collected in the other.

Frequently, the catch ratio is defined as the quantity collected in a gauge with a vertical aperture divided by the quantity collected in a gauge with a horizontal aperture (Blocken & Carmeliet, 2005a). Straube and Schumacher (2006) refer to the Rain Deposition Factor (RDF), which is similar to the catch ratio referred to by Blocken, but rather than being a ratio of rain deposited on a wall to horizontal rain, the RDF is a ratio of rain deposited on a wall to rain through a vertical plane measured under free-field conditions, which is not the case here.

Blocken and Carmeliet (2004); Deb Nath (2015) identify six main parameters that influence the catch ratio:

- i. building geometry and topography,
- ii. position on the building façade,
- iii. wind speed,
- iv. wind direction,
- v. horizontal rainfall intensity,
- vi. horizontal raindrop size distribution.

In theory, the catch ratio is the flux through a vertical aperture for a particular time period divided by the flux through a horizontal aperture over the same time period (Blocken & Carmeliet, 2004). Under steady conditions, the catch ratio is interpreted as the ratio of the wind-driven rain intensity to the horizontal rainfall intensity (Eq. (1)):

$$\eta = R_{\text{wdr}} / R_{\text{h}} \quad \text{Eq. (1)}$$

Where;

η = catch ratio,

R_{wdr} = wind-driven rain intensity,

R_{h} = horizontal rainfall intensity.

Wind-driven rain is measured in two locations:

- i. on buildings with gauges placed directly on wall surfaces to measure WDR loads,

- ii. under free-field conditions with gauges placed away from the influence of buildings and other obstructions to measure so-called free wind-driven rain (Krpan, 2013).

The former is generally of most interest for wind-driven rain research in building science (as well as the scope of this study); the latter is sometimes difficult to achieve in practice because of the nature of surrounding topography and other obstructions typical of urban environments.

2.6.2. Wall-Mounted WDR Gauges

Researchers use driving rain gauges that vary in size, shape, material, and recording mechanism, and the results can vary widely. The duration, intensity, type of rain event, and sampling frequency of measurement, all have an impact on the results.

WDR gauges are not manufactured industrially, and there is no standard for their design (Blocken & Carmeliet, 2004, 2005b, 2006b; Kubilay et al., 2014a). Holmgren (1972) stated that the first WDR gauge was designed as early as 1937, particularly for measurement on buildings in Trondheim, Norway. Nell designed and installed the next gauge at the façade surface of his house in Voorschoten, the Netherlands, in 1943 (Basart, 1946). According to Hogberg (1999b) and Masters et al. (2013), WDR gauges were initially made up of a plate comprising a collection area and a reservoir linked via a drainage channel (see Figure 2.21). The catchment area consists of a shallow tray mounted on the building façade. In order to prevent collecting water from outside the catchment area, a raised rim is designed around the catchment perimeter. Periodically, either manually or automatically, the accumulated runoff volume in the reservoir is recorded.

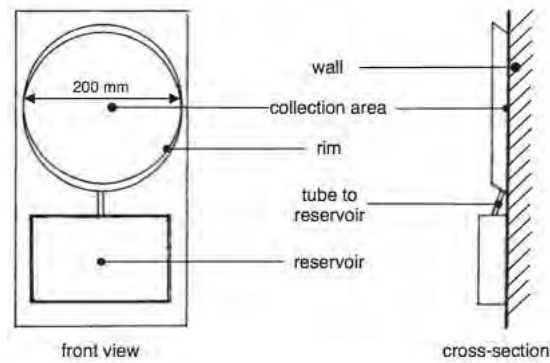


Figure 2.21. Wall-mounted plate-type Wind-driven rain gauge where the collection area fits flush into the vertical façade surface (Blocken and Carmeliet (2004))

As explained and experimented by Hogberg (1999b) and Masters et al. (2013), a basic wall mounted WDR gauge consists of:

- i. A catchment area (a shallow tray), which is mounted on the building façade; raindrops hit the tray, drip downwards and are collected via:
- ii. A drainage channel; which leads the collected rainwater to:
- iii. A reservoir or a water flux gauge; which enables the measurement of instantaneous driving rain intensities.

Table 2.6 demonstrates a summary of the characteristics of seven different types of wall-mounted WDR gauges, each of which is briefly described below:

2.6.2.1. CTH Gauge

The traditional WDR gauge (CTH) with a small catchment area was developed at Chalmers University of Technology, Sweden. Its material is Perspex, and the reservoir is measured by a tipping bucket with a tipping volume equal to 1 g of water (Figure 2.22). (Hogberg, 1998; Hogberg et al., 1999).

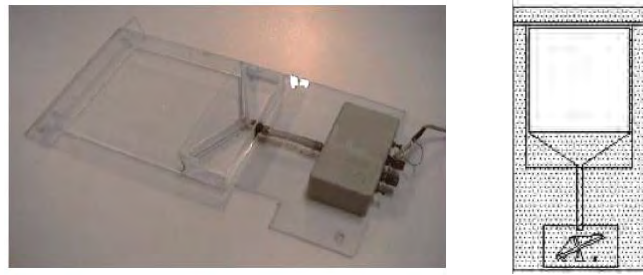


Figure 2.22. Wind-driven rain gauge CTH (Hogberg et al., 1999)

2.6.2.2. TUD Gauge

Kragh and Svendsen (1998) designed an improved WDR gauge at the Technical University of Denmark (TUD) to reduce the measurement errors of remaining droplets on the catchment area (Figure 2.23). This gauge came with a ‘load cell’ on top of the device to record rainwater both in the reservoir and on the catchment area (Blocken & Carmeliet, 2004). The collector is made out of a “stainless steel tray with a net mounted on the tray to reduce raindrop bouncing” (Hogberg et al., 1999). The readings were recorded every 10 minutes to reduce the measurement error due to the sensitivity of the gauge to wind fluctuations (FJR van Mook, 2002).

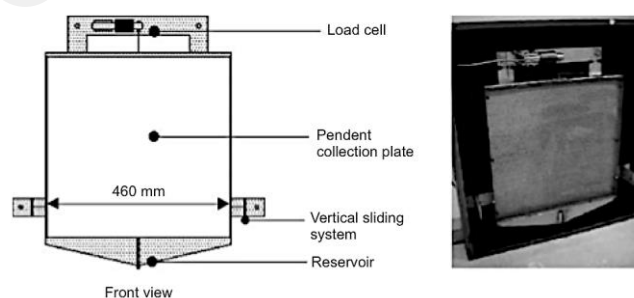


Figure 2.23. Wind-driven rain gauge TUD (Blocken & Carmeliet, 2006b; FJR van Mook, 2002)

2.6.2.3. TUE-I Gauge

The gauge TUE-I was manufactured at the Eindhoven University of Technology, Netherlands. This gauge (Figure 2.24) has a larger catchment area (0.527 m^2) compared to CTH (0.032 m^2). Teflon surface finish intends to enhance the process of dripping down the rainwater droplets to the reservoir (Hogberg et al., 1999). The drops are collected by a large funnel in the reservoir (Van Mook, 1998). A balance measures the reservoir with an accuracy of 0.1 g.

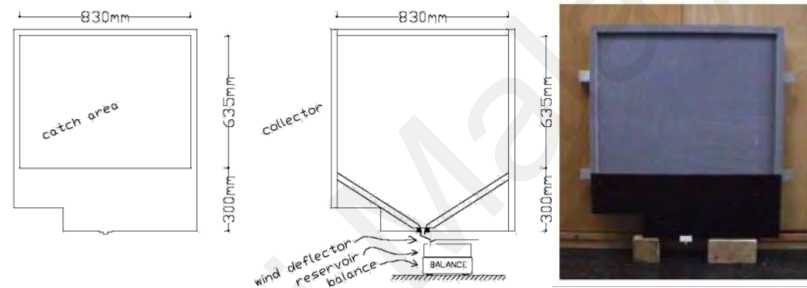


Figure 2.24. Wind-driven rain gauge TUE-I (Van Mook (1998))

2.6.2.4. TUE-II Gauge

Gauge TUE-II is similar to gauge TUE-I, it is an improved version of TUE-I. The coagulation and dripping-down of drops on the collector surface has been improved. The gauge TUE-II features a rotating wiper (Figure 2.25). The wiper collects all droplets on the catchment surface and does not allow any to remain on the surface. A rain indicator automatically switches on the wiper. “The speed is approx. 1 rotation per 3 seconds; after every 5 seconds, the wiper rests during 5 s to reduce wear and tear” (Van Mook, 1998).

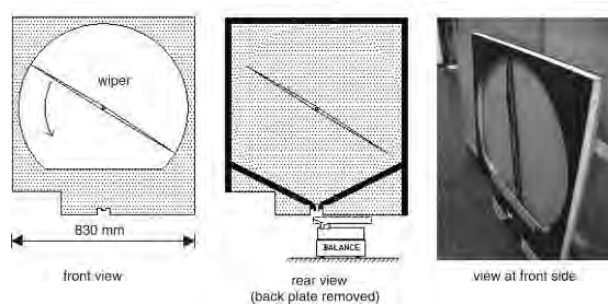


Figure 2.25. Wind-driven rain gauge TUE-II (Blocken & Carmeliet, 2006b)

2.6.2.5. CTH-II Gauge

Hogberg (2002) at the Chalmers University of Technology, Sweden, developed a WDR gauge with a deeply recessed catchment area composed of tilted surfaces to prevent raindrops from splashing (Figure 2.26). In Blocken and Carmeliet (2006b) study, it was stated that the performance of this gauge in terms of the amount of accumulated rainwater was better than that of non-recessed gauges for high wind speed and heavy rainfall intensities.

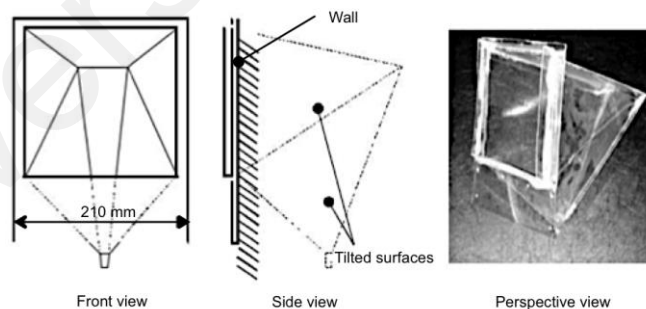


Figure 2.26. Wind-driven rain gauge Tilted; CTH-II (Blocken & Carmeliet, 2006b; Hogberg, 2002)

The recession, however, is responsible for some inconvenience, as it imposes restrictions on the locations where it can be installed, and it can be used when there are windows in suitable parts of the buildings or if holes can easily be cut. When this is not feasible, gauges must be mounted on the surface of the building. As a result, most researchers

abandoned the concept of recessed gauges and designed their own gauges, giving rise to a broad spectrum of existing gauges of different materials, shapes, and sizes.

2.6.2.6. EMPA Gauge

The EMPA WDR gauge was produced at the campus of the Swiss Federal Laboratories for Materials Science and Technology based on the guidelines of Blocken and Carmeliet (2006b) and Kubilay et al. (2014a). The gauge frame is made of aluminium, and the catch surface is ordinary glass sheets to promote runoff (Figure 2.27). A connecting pipe conveys rainwater from the catchment to the reservoir. The building houses the reservoir to avoid frost and evaporation problems (Kubilay et al., 2014a).

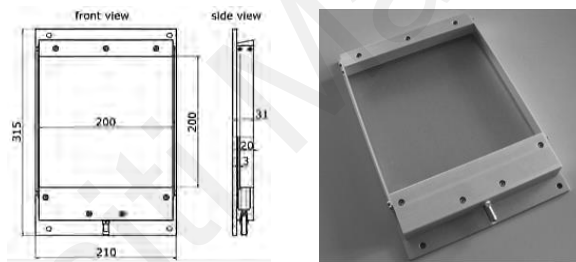


Figure 2.27. Wind-driven rain gauge EMPA (Kubilay et al., 2014a)

2.6.2.7. KUT Gauge

The KUT gauge (Figure 2.28) was constructed at the Kaunas University of Technology, Lithuania, to measure the rainwater collection rate (Dobravalskis et al., 2018). It is composed of two main parts; the RWH stand and the main control unit. The stand is a hermetic box with a depth of 58 mm: the front layer is an architectural façade panel of stainless steel expanded metal mesh. WDR permeates through the panel into the box and flows into scale 1 via an outlet hose, and the rainwater runoff that flows down on the outer surface of the mesh surface, leads into another gutter, and is measured by scale 2. The base consists of the main control unit; includes water-measuring scales, and a bulky

volume (1000 mm x 970 mm x 300 mm) made out of cement particleboard covered in aluminium sheeting to ensure the stability of the base in windy outdoor conditions.

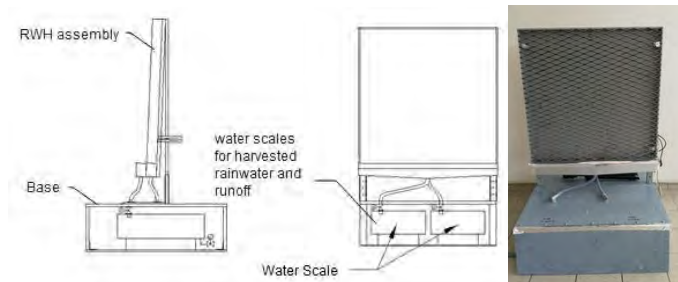


Figure 2.28. Wind-driven rain gauge KUT (Dobravalskis et al., 2018)

Table 2.6. Summary of the WDR gauges characteristics

Name	Principle	Material	Catchment area (m ²)
CTH	Traditional collector with tipping bucket ($V_{tip}=1\text{ g}$)	Perspex (solid transparent plastic made of polymethyl methacrylate)	$0.18 \times 0.18 = 0.032$
TUD	Collector weighted by a strain gauge ($\Delta m \sim 3\text{ g}$)	Stainless steel	$0.46 \times 0.46 = 0.21$
TUE-I	Rectangular catchment area with reservoir (2 liters) and balance ($\Delta m=1\text{ g}$)	Teflon coating (Polytetrafluoroethylene)	0.527
TUE-II	Round catchment area with a rotating wiper with reservoir (3 liters) and balance ($\Delta m=1\text{ g}$)	Teflon coating (Polytetrafluoroethylene)	0.492
EMPA	Rectangular catchment area with reservoir (1 ml)	Aluminium & Glass	$0.2 \times 0.2 = 0.04$
TILTED-CTH-II	Collection area is tilted surfaces and deeply recessed	-	-
KUT	Square catchment area with two water-measuring scales for WDR and Rainwater Runoff	Stainless steel expanded metal mesh façade panel	1

2.6.3. WDR Gauge Design Guidelines

The following guidelines for the design of WDR gauges were provided by (Blocken & Carmeliet, 2005a, 2006b) from (Adl-Zarrabi & Hogberg, 2001; FJR van Mook, 2002; Hogberg, 1999a; Hogberg et al., 1999):

- i. Limit the amount of adhesion water at the gauge collection area. For traditional plate-type gauges, plain sheet glass is preferred over PMMA and PVC. PTFE should not be used,
- ii. Limit the amount of adhesion water at the bottom part of the gauge and in the draining tube. The latter should be kept as short as possible, and the material type should be selected for minimal adhesion,
- iii. Minimise evaporative losses from the reservoir (e.g., by exposing only a small water surface to the ambient air, by minimising the ventilation rate in the reservoir, and by regularly adding a few drops of light oil),
- iv. If possible, direct the collected rainwater towards the inside of the building into reservoirs mounted at the inner wall surface to avoid frost damage to the reservoirs, to reduce the variability in the evaporative losses, and to avoid excessive evaporative losses due to heating by solar radiation.

The time resolution of WDR measurements depends on the purposes for which the data will be used. Heat- Air-Moisture transfer analyses are typically conducted with data on an hourly basis, so WDR measurements should at least be taken every hour. Note that it is not useful to conduct WDR measurements on a very short-term basis, as the time between the impact of raindrops on the collection area and the collection of this amount of water in the reservoir may be several seconds up to several minutes.

2.6.4. WDR Measurement (S_{wdr})

Evaporation - As claimed by Blocken and Carmeliet (2005b, 2006b), the most important cause of measurement errors is the evaporation of adhesion water on the gauge collection area, and this was confirmed in Nore et al. (2007), where the evaporation of adhesion water and the rest-water error in the tipping bucket were found to be the largest error sources.

During and after a rain event, there is always a certain amount of water adhered to the collection area, which is not measured by the gauge. A numerical study by Blocken and Carmeliet (2006b) showed that all the impinged droplets adhere to the surface until a certain threshold of impinged S_{wdr} is reached. After the threshold value, the total volume of adhered droplets remains constant, so the error is considered important, especially for light to moderate rainfall intensities. In order to keep the measurement errors due to the evaporation of adhered droplets as small as possible, rain events with large amounts of WDR must be selected. This ensures that the loss of water due to the evaporation of the adhered droplets is kept at a relatively limited amount (Kubilay et al., 2014a). Furthermore, rain events with less dry periods in between the rain showers are expected to limit the errors due to the evaporation of adhered droplets, as well as the rest-water error. Using a tipping bucket with a smaller bucket volume will also decrease the rest-water error by increasing the measurement resolution.

Splashing - The error due to splashing and the wind error are not as easy to estimate. It is argued that the selected rain events should have reference wind speed values (at $y = 10$ m) lower than 10 m/s and horizontal rainfall (R_h) intensities lower than 20 mm/h in order to keep splashing errors small (Blocken & Carmeliet, 2006b).

Condensation - Blocken and Carmeliet (2006b) and Nore et al. (2007) argue that the error associated with condensation on the collector surface is quite limited during rain events due to limited radiation losses to the sky. Finally, for a small wind error, the protrusion of the WDR gauge out of the plane of the façade should be small, the wind speed values should not be high, and the wind direction during the rain event must be approximately perpendicular to the building façade.

Other error sources that are considered of lesser importance include the following (Blocken & Carmeliet, 2004, 2006a, 2006b; Briggen et al., 2009; Deb Nath, 2015):

- i. Evaporative losses from reservoirs,
- ii. Splashing raindrops from the collection area,
- iii. Condensation on the collection area,
- iv. Wind errors, or smaller catches, that occur when the gauge body disturbs the wind flow,
- v. Deeply recessed collection areas composed of tilted surfaces to minimise splashing losses may show better performance for high wind speed and heavy rainfall intensities, but the large collection area is a compromise for evaporative losses important for light to moderate rainfall intensities.

2.7. Spatial Distribution Pattern of WDR on Building Façades

The spatial distribution pattern of WDR (η) on building façades in both real-life examples and computational simulations has shown similarities in the characteristics of WDR intensity (R_{wdr}) distribution, which will be explained in the following section, as declared in research results by Blocken and Carmeliet (2004, 2006a); Kubilay (2014).

2.7.1. WDR Catch Ratio (η)

Catch ratios (η) provide the basics for understanding the spatial distribution of WDR on building façades. The definition and significance of catch ratio (η) were defined in Section 2.6.1. The following are the characteristics of the catch ratio:

- i. Catch ratio values increase from bottom to top and from the middle to the sides of the façade,
- ii. The wetting gradient (highest values) is highest near the top edge (in the vertical direction) and near the top corners,
- iii. The middle-lower two-third of the façade have the lowest values.

Research findings indicate that the highest rainfall intensity values are at the top corners of the building façades; caused by the fact that at higher altitudes, wind speed values are higher and building edges are subjected to wind flow acceleration. Wetting gradients become smaller with increasing horizontal rainfall intensity (R_h), resulting in a decrease in maximum and an increase in minimum WDR catch ratios on the building façade. Kubilay et al. (2014a) particularly stated that the highest WDR catch ratio values belonged to the top corners and the least values to the middle-lower two-third of the façade.

Blocken et al. (2009b) conducted a numerical study to explore the influence of nearby buildings as another factor on the WDR intensity (R_{wdr}) distribution on the building façade. The configuration consists of a high-rise building ($L \times B \times H = 50 \times 12.5 \times 50 \text{ m}^3$) screened by a low-rise building ($L \times B \times H = 50 \times 12.5 \times 12.5 \text{ m}^3$), and the distance between both buildings is 25 m.

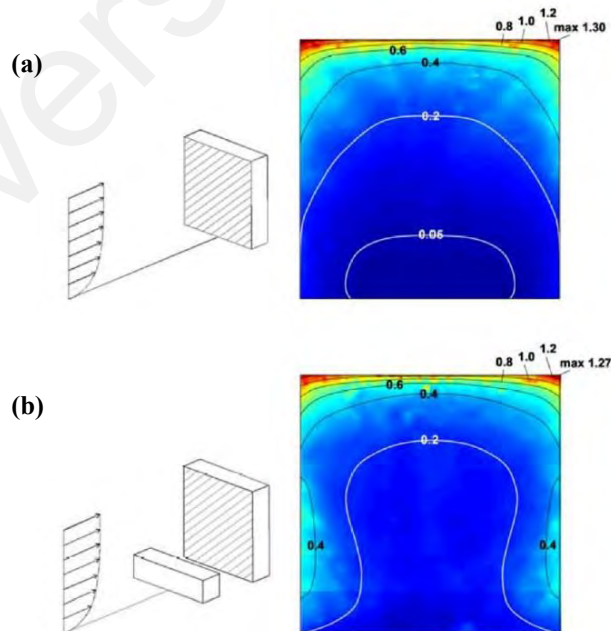


Figure 2.29. WDR catch ratio (η) distribution on the windward façade of the isolated high-rise building (a), with low-rise building present (b), for $U_{10} = 10 \text{ m/s}$ and $R_h = 5 \text{ mm/h}$, (Blocken et al., 2009b)

Figure 2.29 shows WDR catch ratio (η) contours on the windward façade of the high-rise building, without (a) and with (b) the presence of the low-rise building, for a wind speed (U) of 10 m/s and a rainfall intensity (R_h) of 5 mm/h. The low-rise building presence increases the WDR exposure of the lower part of the high-rise building façade, while the WDR of the upper part does not change significantly (Blocken et al., 2009b). Furthermore, the study revealed that the WDR catch ratio at the side edges increases by about a factor 2 in scenario (b) compared to scenario (a), and towards the middle of the lower part of the façade the WDR catch ratio increases by even more than factor 2. Figure 2.30 shows a similar effect for $R_h = 30$ mm/h. This means that, in essence, the low-rise building increases the force of the standing vortex; resulting in more WDR exposure for the high-rise.

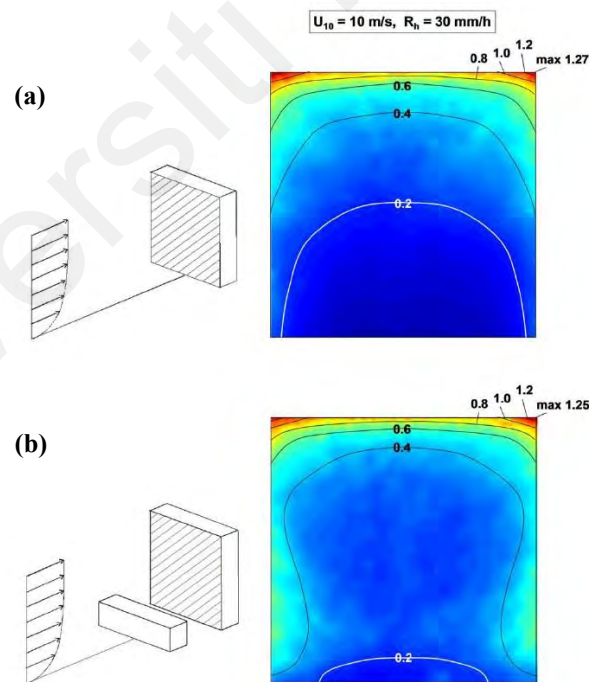


Figure 2.30. WDR catch ratio distribution on the windward façade of the isolated high-rise building (a), with low-rise building present (b), for $U_{10} = 10$ m/s and $R_h = 30$ mm/h, (Blocken et al., 2009b)

Details on the façade, e.g., roof overhang, are another parameter related to building geometry that affects the WDR intensity values. Three categories of WDR catch ratio charts (with and without roof overhang) were presented based on the experimental and numerical findings of research on the south-west façade of the VLIET test building of the Laboratory of Building Physics by Blocken and Carmeliet (2008). These charts provide comparisons between WDR catch ratio values at different reference wind speed and reference horizontal rainfall intensity values. The results indicated that the effect of the roof overhang causes large errors in WDR amount calculations. Thus, in the current study, to minimise the research errors, a pilot building with no roof overhang is selected.

The spatial distribution pattern of WDR over the building wall has been derived from the findings of several studies based on observation (Beijer, 1977; Blocken & Carmeliet, 2012; Briggen et al., 2009; El-Shimi et al., 1980; Fang et al., 2021; Hall & Kalimeris, 1982; Kubilay et al., 2014b; Van den Brande et al., 2014; Wang et al., 2020), and several simulation results by Choi (1991, 1994); Choi (1993). Figure 2.31 (b) sketches the spatial distribution of WDR. The vertical profile of the WDR can also be conjectured from this figure, which must be very similar to Figure 2.31 (a).

This vertical profile may be approximated by the first-order or second-order functions. Cho et al. (2020) reported that for the first-order function, the sum of rainfall over the building wall (per unit width) can be expressed as $q = 0.5 \times R_{\text{wdr}} \times H$, where H represents the height of a building wall; and under the assumption of the second-order function, it can be expressed as $q = 0.33 \times R_{\text{wdr}} \times H$.

The discussion in this section about spatial distribution of WDR on building façades or as described by Blocken and Carmeliet (2004), 'the classic wetting pattern of building façades', can be summarised in the following manner:

- i. The windward façade is wetted whereas the other façades remain relatively dry,

- ii. At the windward façade, the wetting increases from bottom to top and from the middle to the sides,
- iii. The WDR intensity at a given position increases approximately proportionally with wind speed and horizontal rainfall intensity,
- iv. Roof overhang, as the building geometry parameter, causes large errors in WDR amount calculations,
- v. R_{wdr} values on a tall building façade in the presence of a low-rise building do not change significantly on the upper part, and the lower part receives more WDR.

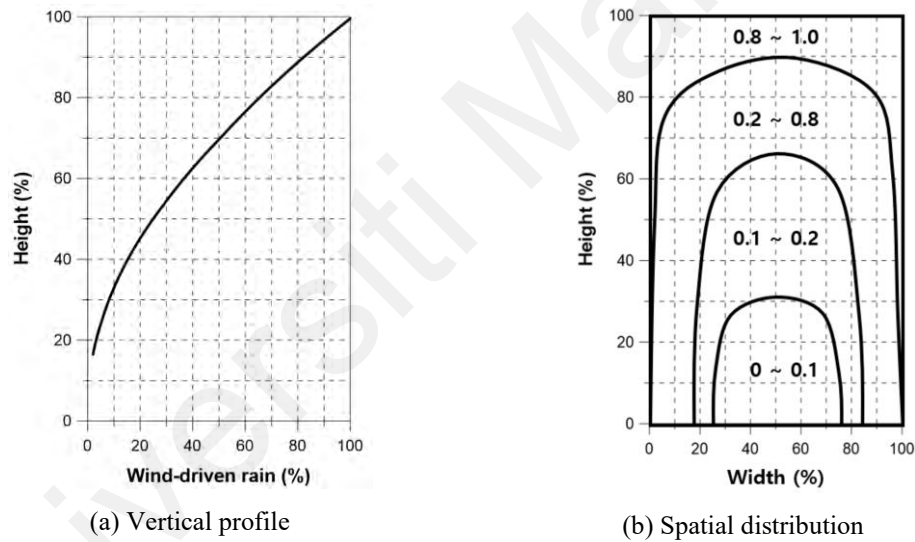


Figure 2.31. Typical shape of vertical profile and spatial distribution of wind-driven rain (WDR) on building walls (Cho et al., 2020; Yoo et al., 2022)

2.7.2. WDR Intensity (R_{wdr})

The basic equation of WDR intensity was defined by Hoppestad (1955) as follows:

$$R_{wdr} = R_h^{0.88} \times \frac{U}{V_t} \quad \text{Eq. (2)}$$

Where;

R_{wdr} is the intensity of the WDR (mm/h),

R_h is the rainfall intensity observed on the horizontal surface (mm/h),

U is the wind speed (m/s), and

V_t is the terminal velocity of rain drops (m/s).

Later, this equation was modified by Lacy (1965, 1977) by considering various results from observations as follows:

$$R_{\text{wdr}} = 0.222 \times U \times R_h^{0.88} \quad \text{Eq. (3)}$$

In this equation, the value of 0.222 is the WDR coefficient, which represents the inverse of the mean terminal velocity of various raindrops. The exponent 0.88 was modified from 1, by considering various observations. However, some cases still use the exponent 1 (Blocken & Carmeliet, 2005b; Hens, 2010; Straube, 2010). The above equations are for those cases where the wind direction is perpendicular to the building wall. If the building wall is not perpendicular to the wind direction, the intensity of the WDR should be corrected as follows:

$$R_{\text{wdr}} = 0.222 \times U \times R_h^{0.88} \times \cos \theta \quad \text{Eq. (4)}$$

Where;

θ is the angle between the wind direction and the building wall.

This equation is generalised by introducing the constant α , which is known to vary depending on the location of the building wall (Cho et al., 2020) as well as its shape (Yoo et al., 2022).

$$R_{\text{wdr}} = \alpha \times U \times R_h^{0.88} \times \cos \theta \quad \text{Eq. (5)}$$

The constant α has also been estimated by analysing the observed data; the smallest value of 0.02 was found in the study by Lacy (1965) and Hens and Ali Mohamed (1994), and the largest value of 0.26 was found by Flori (1992).

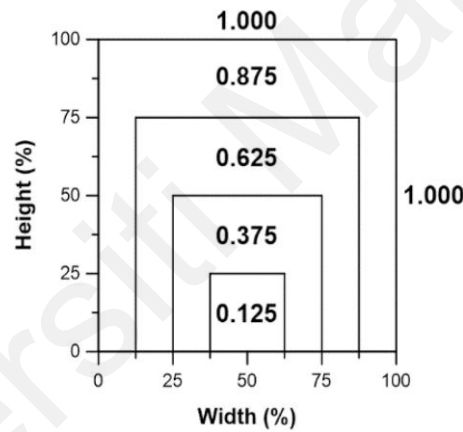


Figure 2.32. Simplified spatial distribution of wind-driven rain (WDR) on building walls, adopted from (Cho et al., 2020)

WDR quantity is estimated by semi-empirical models, such as the ASHRAE Standard 160P (2016), and the ISO 15927-3 (2009) standard models, which are discussed in the following section.

2.8. Semi-Empirical Model – WDR Prediction

Since at least 1937, researchers have measured and studied wind-driven rain on buildings, leading to the development of various approaches for predicting wind-driven rain loads

impinged on building walls. The semi-empirical WDR models are universally adopted and have been the most advanced and frequently used methodologies to predict the WDR quantity on building façades. The European Standard Draft PrEN13013-3 for WDR assessment is based on the WDR relationships; a large number of existing Heat-Air-Moisture (HAM) transfer simulation programmes employ these relationships to convert the standard meteorological data in the climate data files (wind speed (U), wind direction (D), and horizontal rainfall intensity (R_h)) to the corresponding WDR intensity (R_{wdr}) (Blocken & Carmeliet, 2004, 2005b; Blocken & Carmeliet, 2010; Blocken et al., 2009a; Blocken et al., 2010; CEN, 2009; Coutu et al., 2013; Gholamalipour et al., 2022; Zhou et al., 2023).

Predicted R_{wdr} using semi-empirical models may deviate significantly from actual observations (Blocken et al., 2010; Kubilay et al., 2014a) or by different semi-empirical models (Freitas et al., 2013). One possible explanation for these differences is the fact that semi-empirical approaches might only work in certain conditions because of the complicated interaction of buildings, wind, and rain in urban areas (Zhou et al., 2023). For instance, in reality, it is difficult to determine a unique wind direction (D) for WDR estimation, because of the ever-changing wind direction. Furthermore, it's not possible to estimate the amount of rainfall intercepted from wall to wall because WDR affects any one or two walls of a building during the rain event (Cho et al., 2020). The substantial uncertainty in the semi-empirical models is nevertheless ignored in a number of hygrothermal simulation studies.

However, in the recent studies of Pérez-Bella et al. (2020b); (Yoo et al., 2022) it was verified that the exposure of WDR on building façades can be adequately approximated through the semi-empirical models when considering all four building walls in the measurement stage. In addition, Ge et al. (2018) and Souri et al. (2021) declared that

shorter spell or rain event duration records and high-resolution on-site wind and rain observations can increase the accuracy performance of semi-empirical models.

2.8.1. Overview of Semi-Empirical Models' Development

The semi-empirical models were developed on the basis of Lacy's equation describing the intensity of the free WDR (Defo et al., 2019); under the assumptions that all raindrops are of the same size and that the wind flow is uniform, steady, horizontal and perpendicular at all times to the vertical surface. The intensity of WDR passing through a vertical plane can be expressed as stated in Hoppestad (1955); Korsgaard (1962); Lacy (1965) cited by Blocken and Carmeliet (2004):

$$R_{\text{wdr}} = R_h \cdot \frac{U}{V_t} \quad \text{Eq. (6)}$$

Where;

R_{wdr} is the rainfall intensity received on a vertical surface (mm/h),

R_h is the rainfall intensity received on a horizontal surface (mm/h),

U is the horizontal component of the wind speed (m/s),

V_t is the rain drop's terminal velocity (m/s).

The terminal velocity is a function of the raindrop size, which is a function of the horizontal rainfall intensity (Best, 1950). Lacy (1965) refined Eq. (6), which relates wind speed (U) and rainfall intensity (R_h) to free WDR intensity, by using the median rain drop size:

$$R_{\text{wdr}} = \alpha \cdot U \cdot R_h \quad \text{Eq. (7)}$$

Where;

α is the WDR coefficient (s/m), the inverse of the raindrop's terminal velocity.

However, it was explained in Section 1.6 that the amount of WDR on building façades (as the scope of this study) could widely differ from the 'free-field' WDR. According to Blocken et al. (2010) each WDR model expresses the deposition rate of WDR or WDR intensity, known as R_{wdr} , on 'building walls' as follows:

$$R_{wdr} = \alpha \cdot U_{10} \cdot R_h^{0.88} \cdot \cos \theta \quad \text{Eq. (8)}$$

Where;

α is the WDR coefficient,

θ is the angle – in a horizontal plane – between the wind direction and the normal to the building façade.

Depending on the model, different expressions for α have to be used (Blocken & Carmeliet, 2010), if the wind is perpendicular to the façade ($\theta = 0^\circ$, $\cos \theta = 1$), the α value is:

$$\alpha = \frac{\eta \cdot R_h^{0.12}}{U_{10}} \quad \text{Eq. (9)}$$

Where;

η is the WDR catch ratio (see Eq. (1)).

Previous studies have assessed that it is, in good approximation, a linear function of U_{10} , except at façade positions sheltered by horizontal projections, such as roof overhangs or balconies (Blocken & Carmeliet, 2002, 2006a, 2008; Blocken & Carmeliet, 2010), which is not the case in this study. Thus, α can be considered independent of U_{10} . Both η and α are functions of R_h .

Lacy (1965) reported a value of $\alpha = 0.222$ s/m, which corresponds to an average spell composed of a similar raindrop diameter of 1.2 mm with a terminal velocity of 4.5 m/s (Defo et al., 2019). Eq. (7) is a measure of the free WDR. However, to calculate the WDR quantity on an actual façade, both wind and building characteristics need to be considered; e.g., as Defo et al. (2019) precisely described, the wind speed at a specific location has to be adjusted by taking into account the effect of terrain, local topography, obstruction factors, as well as the height of the building.

Semi-empirical models use the cosine projection to look at how the direction of the wind affects the WDR load, taking into account factors that are specific to the area (Blocken & Carmeliet, 2006c). They are primarily based on the WDR relationships, which relate WDR intensity (R_{wdr}) to wind speed (U), wind direction (D) and horizontal rainfall intensity (R_h) (Blocken & Carmeliet, 2004).

Zhou et al. (2023) in their recent study have reaffirmed that the ISO Standard 15927-3 model is the most detailed among the different empirical models. The semi-empirical models ASHRAE standard 160P and ISO standard 15927-3 were derived from Eq. (7). They differ from each other in terms of the WDR coefficients and correction factors. The ISO model can consider the effect of surrounding buildings and terrain on WDR load with limitations in height locations on building wall. The ASHRAE model can consider the effect of surrounding buildings with several ranges of values for different height locations on building wall. By comparison, the other two models – the WUFI model and the Meteonorm model – do not have parameters to take into account the influence of

surrounding factors (Zhou et al., 2023). Thus, they are not aligned with the scope of the current study; tall building façades in the context of urban areas.

As mentioned in (Pérez-Bella et al., 2018), these semi-empirical WDR relationships, i.e., ISO and ASHRAE models, can also incorporate additional coefficients (wall indices) to reflect the influence of the topography, surroundings, obstructions and geometry of the building on the actual amount of WDR impinging on each façade.

These models are semi-empirical because they are based on theoretical deviations, while the WDR coefficient (α) is typically obtained based on experimental data (Blocken & Carmeliet, 2004). The WDR coefficient (α) is dependent upon the location of the building wall (Cho et al., 2020), a pronounced function of building geometry and position on the façade, and often assumed to be independent of wind speed (U), wind direction (D), and rainfall intensity (R_h), e.g., HAM software typically uses a constant WDR coefficient (Blocken & Carmeliet, 2005b). As Cho et al. (2020) have cited, the constant α can be estimated theoretically by multiplying the rain admittance factor and inverse terminal velocity of raindrops (Pérez-Bella et al., 2013a; Pérez-Bella et al., 2013b; Straube & Burnett, 2000) or by analysing the observed data. Lacy (1965) and Hens and Ali Mohamed (1994) reported the smallest value of α as 0.02, and the largest constant α as 0.26 by Flori (1992).

To validate these semi-empirical models, the gathered experimental data via observations or in-situ measurements are used (Blocken & Carmeliet, 2005b, 2006b). Deb Nath (2015); Kubilay et al. (2014a) stated that the two most commonly referenced models to estimate the quantity of WDR loads on the building façades are the semi-empirical models ISO 15927-3 (2009) and ASHRAE Standard 160P (2016). By comparing the calculated results of these models with the corresponding in-situ measurements dataset, the accuracy performance of these semi-empirical models is evaluated.

2.8.2. ISO Standard 15927-3 Model

The ISO Standard 15927-3 of 2009, entitled ‘Hygrothermal performance of buildings - calculation and presentation of climatic data - Part 3: Calculation of a driving rain index for vertical surfaces from hourly wind and rain data’ ISO 15927-3 (2009), is based on the British Standard BS8104 (BSI, 1992). The establishment of this semi-empirical model aims to define an international standard for estimating WDR (Tsoka & Thiis, 2018). This standard bases the estimation on local meteorological data, building characteristics, and parameters like terrain roughness, topography, nearby obstacles, and building geometry. Blocken and Carmeliet (2010) have provided a detailed description of the model for the calculation of WDR intensities on a building façade, while accounting for the surroundings and building geometry and considering hourly wind and rain data. It is one of the most advanced and most frequently used methodologies to estimate WDR volumes on façades (Blocken & Carmeliet, 2010; Blocken et al., 2010). The legitimacy and accuracy of this ISO have been investigated in a series of publications (Blocken et al., 2011; Blocken et al., 2009b; Ge et al., 2018; Juras & Jakubcik, 2017; Pérez-Bella et al., 2020a; Tsoka & Thiis, 2018; Zhou et al., 2023).

ISO 15927 lays out two approaches for analysing data from hourly observations of wind and rainfall to predict the amount of rainwater that will hit a wall of any given orientation, both on an annual average and during short-term periods. The first approach relies on hourly wind and rainfall observations and is heavily influenced by BS 8104 (1992) standard. A lengthy series of measurements of WDR on buildings in various parts of the United Kingdom led to the development of this standard. Therefore, the approach is valid for climates that are comparable to the UK's; for areas with very different climates, it is advised to measure WDR on sample buildings to ensure its validity (ISO 15927-3, 2009). If hourly rainfall and wind speed observations are unavailable, one can use the second approach, which utilizes the current weather code for precipitation and average wind

speeds (ISO 15927-3, 2009). These approaches from ISO 15927 are not applicable in the following situations:

- i. mountainous areas with sheer cliffs or deep gorges,
- ii. areas where severe convective storms account for more than 25% of the annual rainfall,
- iii. areas and periods when a significant proportion of precipitation is made up of snow or hail.

Hence, it is evident that in the case of the application of the ISO standard, model validation through experimental measurement of WDR in the specific research area is fundamentally necessary (Blocken & Carmeliet, 2004; Tsoka & Thiis, 2018). Pérez-Bella et al. (2018) also stated that ISO and ASHRAE standards necessitate hourly climate data, but many locations either do not have this data or the datasets are not representative enough to enable generalization of their use. Regardless of the significant impact of climatic conditions on the performance of these semi-empirical models, Straube and Burnett (2000) raised the importance of the WDR coefficient's role in the model's accuracy performance, bringing high uncertainty to the calculation: the constant value can vary between 0.1 and 0.5 s/m, depending on the conditions at each moment.

In the ISO model, the WDR intensity is defined as:

$$R_{\text{wdr}} = \frac{2}{9} C_R C_{\text{TOW}} U_{10} R_h^{0.88} \cos(D - \theta) \quad \text{Eq. (10)}$$

Where;

C_R is the terrain roughness coefficient, which considers terrain roughness in wind direction and the variability of wind velocity depending on the height of façades,

C_T is the terrain topography coefficient; it increases the airfield spell index if the area investigated is placed on a cliff or on the upper part of a hill,

O corresponds to the obstruction factor; the presence of obstacles surrounding the façade reduces the amount of rain getting to the building,

W stands for the wall factor; it aims to account for the variability of building geometry and its impact on rain reaching the façades, depending on the type of roof and height of the façade,

U_{10} is the hourly reference wind speed at 10 m height,

R_h is the rain intensity on the horizontal surface (mm/h),

$(D - \theta)$ is the angle in the horizontal plane between the wind direction (D) and the normal to the façade (θ).

2.8.2.1. Terrain Roughness Coefficient (C_R)

It takes into account the change in ‘mean wind speed’ at the site due to the height above the ground, and the roughness of the terrain in the direction from which, the wind is blowing. It is used to correct for the increasing wind velocity with the height in the ISO model and is given by:

$$C_R(y) = K_R \ln\left(\frac{y}{y_0}\right) \text{ for } y \geq y_{\min}$$

$$C_R(y) = C_R(y_{\min}) \text{ for } y < y_{\min}$$

Eq. (11)

Where;

y is the height above ground (m),

K_R is the terrain factor,

y_0 is the aerodynamic roughness length (m),

y_{\min} is the minimum height (m).

The values of K_R , y_0 , and y_{\min} as a function of the terrain category are given in Table 2.7.

Table 2.7. Parameters in the ISO Standard roughness coefficient (C_R) (ASHRAE Standard 160P, 2016)

Terrain category	Description	K_R	y_0	y_{min}
I	Rough open sea; lake shore with at least 5 km open water upwind and smooth flat country without obstacles	0.17	0.01	2
II	Farm land with boundary hedges, occasional small farm structures, houses or trees	0.19	0.05	4
III	Suburban or industrial areas and permanent forests	0.22	0.3	8
IV	Urban areas in which at least 15% of the surface is covered with buildings of average height exceeding 15 m	0.24	1	16

The ISO Standard Draft notes that if a change in upstream roughness occurs within 1 km, the smoothest upstream terrain category must be used; the smoothest terrain category provides the largest C_R value (Defo et al., 2019).

2.8.2.2. Terrain Topography Coefficient (C_T)

This parameter considers the increase in mean wind speed over isolated hills and escarpments. It is applied when the wind approaches the slope of the hill or the escarpment and when the building is located at “more than half way up the slope of a hill” or “within 1.5 times the height of the cliff from the base of a cliff.” It ranges from 1.0 for upstream slopes with less than 5% inclination to a peak value of 1.6 for buildings situated at the crest of steep cliffs or escarpments (Blocken & Carmeliet, 2010).

2.8.2.3. Obstruction Factor (O)

To evaluate the obstruction factor (O), as specified in the ISO standard (Table 2.8) one must determine the distance to the nearest obstacle that is at least as tall as the façade concerned.

Table 2.8. Obstruction factor (O) values (Coutu et al., 2013)

Distance to obstacle (m)	Obstruction factor (O)
From 0 to 1	0
From 1 to 4	0.1
From 4 to 8	0.2
From 8 to 15	0.3
From 15 to 25	0.4
From 25 to 40	0.5
From 40 to 60	0.6
From 60 to 80	0.7
From 80 to 100	0.8
From 100 to 120	0.9
Over 120	1

2.8.2.4. Wall Factor (W)

Building geometry partially determines the amount of rain that impinges on the façades. The ISO accounts for this with the wall factor (W) (Coutu et al., 2013). The wall factor is characteristic of a façade. Figure 2.33 shows the different wall factors depending on the roof angle, the overhangs of the roof, and the number of floors. It is worth mentioning that the ISO standard only provides wall factors for a limited range of building geometries, primarily low-rise buildings, restricting these factors to a few values for the entire façade without accounting for variations in the width and height of the façade (Defo et al., 2019).

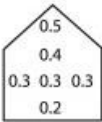
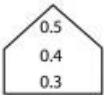
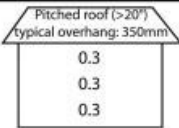
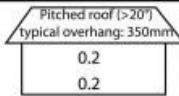
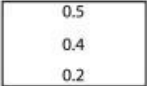
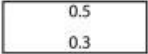
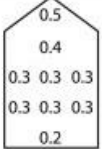
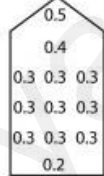
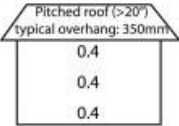
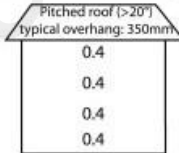
Two-storey gable		One-storey gable	
Average	0.4	Average	0.4
Two-storey wall with eaves		One-storey wall with eaves	
Average	0.4	Average	0.4
Two-storey building with flat roof (pitch <20°)		One-storey building with flat roof (pitch <20°)	
Average	0.4	Average	0.4
Three-storey gable		Multi-storey gables	
Average	0.4	Average	0.4
Three-storey wall with eaves		Multi-storey wall with eaves	
Average	0.4	Average	0.4
Multi-storey building with flat roof (pitch < 20°)		0.5 for top 2.5 m, 0.2 for remainder 0.2 for a ten-storey building, for example, but with a higher intensity at top	

Figure 2.33. Wall factor values (Coutu et al., 2013; Deb Nath, 2015; ISO 15927-3, 2009)

2.8.2.5. The Hourly Reference Wind Speed (U_{10})

The wind speed measured at any height (U_h), can be calculated using the following formula (ASHRAE Standard 160P, 2016; Defo et al., 2019; Ge, 2015):

$$U(h) = U_{10} \times (h/10)^\alpha \quad \text{Eq. (12)}$$

Where,

U_{10} is the standard wind speed (m/s) at 10 m above grade,

h is the height above grade (h),

α is the exposure exponent, shown in Table 2.9.

Table 2.9. Exponent for different upwind exposure (ASHRAE Standard 160P, 2016)

Exposure	Exponent α
Open country: level terrain or open water with few obstructions and only scattered buildings, trees or other obstruction	$1/7 = 0.14$
Suburban: urban areas, wooded terrain, or centres of small towns	$1/4 = 0.25$
City centre: large city centres, with heavy concentration of tall buildings, at least half over 4 stories	$3/8 = 0.36$

The fact that wind speed increases rather rapidly with height means that the driving rain exposure of tall buildings is much higher than for low-rise buildings (Plescia et al., 2008).

2.8.2.6. The Angle ($D - \theta$)°

It is the angle between the wind direction D (°) and the orientation of the façade θ (°) analysed. It requires a different calculation for each possible façade orientation θ , and only those results with a positive value are considered (WDR impinging on the specific façade orientation) (Pérez-Bella et al., 2020a).

In the absence of wind direction D (°) records, the study by Pérez-Bella et al. (2018) in two different locations, Chile and Spain, showed reasonable convergence of the correlations in these two distance zones between the ISO and ASHRAE models. It consolidates the possibility of assuming perpendicular direction to the corresponding façade orientation θ (°) for each rain event ($D = \theta$)° and $\cos 0^\circ = 1$.

2.8.2.7. Spell / Rain Event

Although the standard strictly guides the calculation of the average annual amount of WDR and the amount of WDR in the worst likely spell in a 3-year period, this method could theoretically be used to determine WDR intensities (R_{wdr}) or amounts (S_{wdr}) for any

spell within a year (Blocken & Carmeliet, 2010). Spells separated by 96 hours or more without WDR are considered, assuming that this interval is sufficient for evaporative losses to exceed prior rainwater gains (Pérez-Bella et al., 2024). The ISO Standard states that there can be periods of as long as 96 consecutive hours with no WDR within the spell before evaporative loss exceeds gain from the rain. Where D° is the hourly mean wind direction from north, θ° is the wall orientation relative to north. In this analysis, a rain event will be defined by a period of time when no horizontal amount is measured and the mean hourly wind direction is not directed at the considered wall. The definition of a rain event is not based on the hours when rain is present but rather on the length of the gaps in between two rain events when there is no WDR (Lobelle, 2012). When conducting WDR measurements, it should always be over a long period of time in order to generate reliable dataset (Lobelle, 2012).

Due to the ‘event-based averaged value’ approach of this study for all WDR measures, as will be elaborated in 3.2.2, and according to the research method development conducted by Narula and Sarkar (2019), in this study also a modified version of Eq. (10) will be used. The cosine of the directional component present in Eq. (10) is replaced with its maximum value, which is equal to one, as a moderation approach that is practiced in spell- or event-based methods (Narula & Sarkar, 2019).

2.8.3. ASHRAE Standard 160P Model

In the ASHRAE Standard 160P (2016) model - Criteria for Moisture Control Design Analysis in Buildings - the WDR intensity on building façades is defined as:

$$R_{wdr} = F_L F_E F_D U_{10} R_h \cos \theta \quad \text{Eq. (13)}$$

Where;

F_L is an empirical constant ($= 0.2 \text{ kg}\cdot\text{s}/(\text{m}^3\cdot\text{mm})$),

F_E is the rain exposure factor, depending on the building height, the terrain topography and the surroundings,

F_D the rain deposition factor accounting for the spatial distribution of the WDR on the façade.

The other parameters have the same definition as in the ISO model in Eq. (10).

2.8.3.1. Exposure Factor (F_E)

In the ASHRAE model, the exposure factor F_E is equivalent to the combined effect of C_R and C_T as given in the ISO model (Defo et al., 2019). As shown in Table 2.10, three categories of exposure factors are suggested, given for different building heights and terrain types: severe, medium, and sheltered. Severe exposure includes hilltops, coastal areas, and funnelled wind (e.g., the wind tunnel effect caused by the proximity of two buildings). Sheltered exposure includes protection from nearby buildings or other permanent moderating features (e.g., trees).

Table 2.10. ASHRAE exposure factor (F_E) (ASHRAE Standard 160P, 2016)

Building height (m)	Type of terrain		
	Severe	Medium	Sheltered
<10	1.3	1.0	0.7
10 – 15	1.3	1.1	0.8
15 – 20	1.4	1.2	0.9
20 – 30	1.5	1.3	1.1
30 – 40	1.5	1.4	1.2
40 – 50	1.5	1.5	1.3
>50	1.5	1.5	1.5

2.8.3.2. Rain Deposition Factor (F_D)

The rain deposition factor (F_D) is equivalent to the wall factor (W) in the ISO standard.

To determine the wall factor, in the ISO standard six situations are provided (Figure 2.33),

whereas, only three situations are given in the ASHRAE standard: 0.35 for walls below a steep-slope roof, 0.5 for walls below a low-slope roof, and 1.0 for walls subject to rainfall runoff. The values of rain deposition factor (F_D) recommended by ASHRAE standard are shown in Table 2.11.

Table 2.11. Rain deposition factor (F_D) (ASHRAE Standard 160P, 2016)

Wall type	Deposition factor (F_D)
Walls below a steep-slope roof	0.35
Walls below a low-slope roof	0.5
Walls subject to rain runoff	1.0

2.9. Summary

This chapter focused on the research's foundation. First reviewed the freshwater availability and accessibility globally and in Malaysia, in the city of Kuala Lumpur. Key terminologies were defined. Rainwater harvesting (RWH) drivers, benefits, definitions, components, and implementation in Malaysia were explained. Tall building impacts on the domestic water network and rainfall-runoff distortion, plus the possibilities of collecting rainwater from the vertical façades, were discussed. Four Malaysian tropical seasons' classifications as the main divisive factor in dataset classifications in this research were explained at the basis of a complete tropical one-year. Information and related parameters to wind-driven rain (WDR) measurement, i.e., gauge's design principles, meteorological factors, and methods were reviewed. The literature review revealed that field measurements and semi-empirical methods have been primarily employed in WDR studies when the aim of research is collecting, calculating, and estimating the quantification of WDR loads on building walls. The two semi-empirical models, i.e., ISO standard 15927-3 and ASHRAE standard 160P, were employed for the

purpose of model validation by comparing the models' datasets with the in-situ dataset to predict WDR intensity values on tall building facades. This chapter concluded with definitions of the models' parameters, i.e., coefficients, and correction factors. The conceptual framework of the study is presented in Figure 2.34.

Universiti Malaya

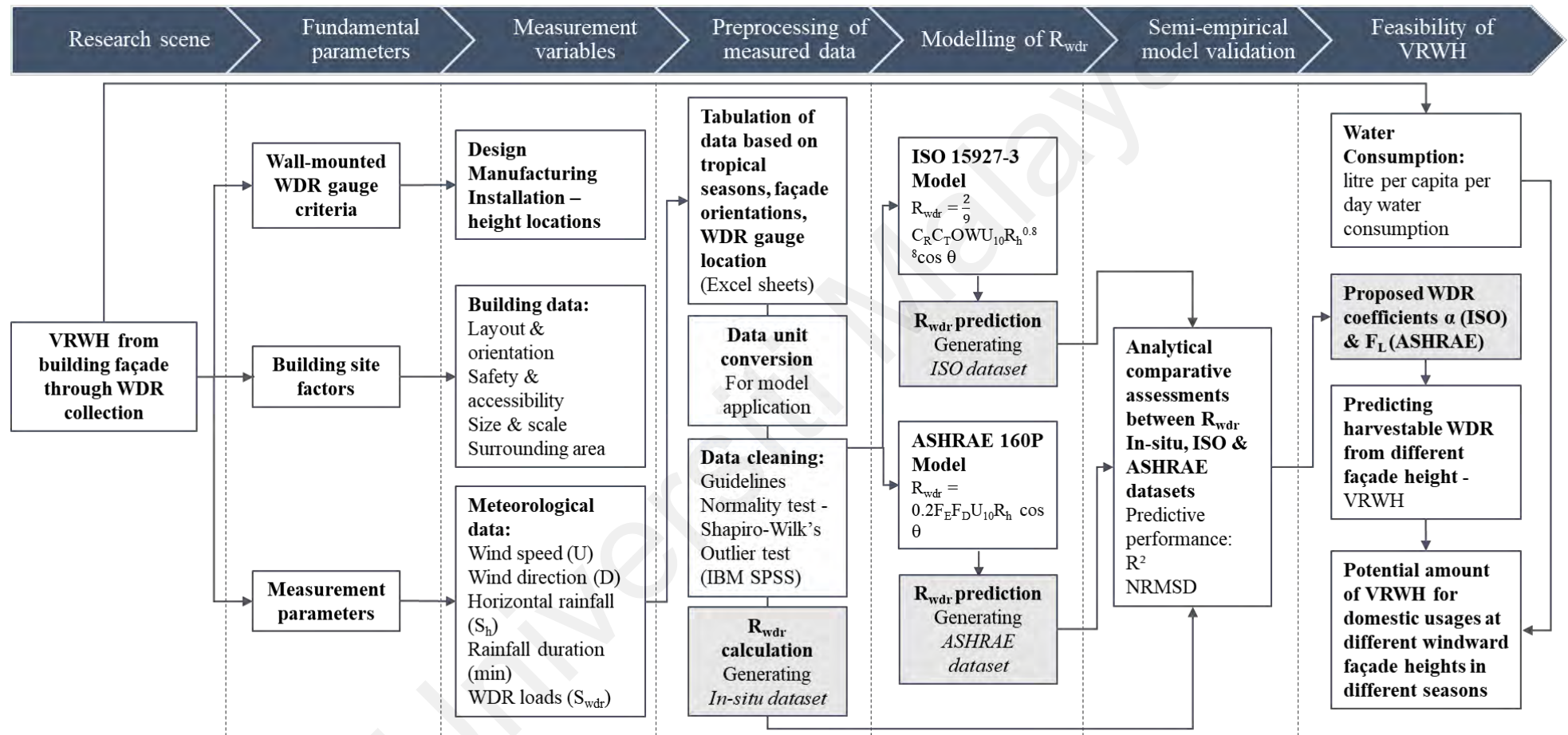


Figure 2.34. Conceptual research framework – Measurements and Modelling

CHAPTER 3: METHODOLOGY

This chapter outlines the methodology used for assessing the feasibility of vertical WDR harvesting from building façades as a new catchment area. This chapter consists of four sections; Section 3.1 presents the principles and guidelines used to design and manufacture the wall-mounted UM WDR gauge, Section 3.2 provides experimental measurement (in-situ) setup information, i.e., building, equipment, and surrounding areas, Section 3.3 describes the data cleaning process to generate in-situ dataset for model validation, and Section 3.4 is dedicated to the application of the semi-empirical models, i.e., ISO Standard 15927-3 and ASHRAE Standard 160P models, to predict R_{wdr} on tall building façades.

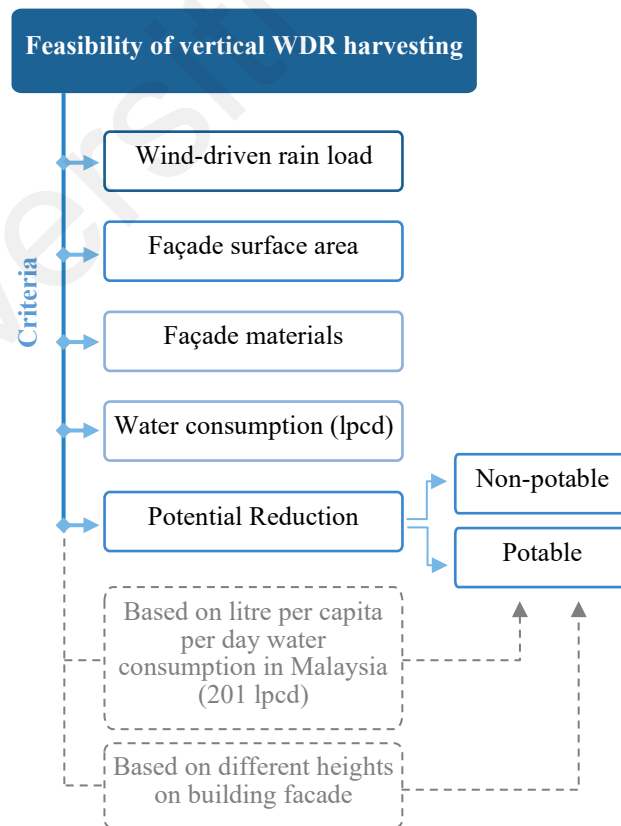


Figure 3.1. Feasibility framework of vertical WDR harvesting from building façade (modified from Chacha (2015) and Li et al. (2010))

In this study, the feasibility frameworks that were practiced by Li et al. (2010) and Chacha (2015) for RWH from roof surface areas were applied as the macro roadmap of the current research methodology with modifications for the façade surface areas of the buildings (Figure 3.1).

3.1. UM WDR Gauge

As previously stated, to date, wall-mounted WDR gauges have not been industrially produced; researchers design and manufacture the gauge according to their measurement purposes. The WDR gauge for this experimental study was designed and manufactured at the Universiti Malaya (UM), Kuala Lumpur, Malaysia, following the scientific guidelines and characteristics of the previous gauges described in detail in Chapter 2 (Section 2.6.3).

3.1.1. UM WDR Wall-Mounted Gauge Design

To adopt a material that has a better runoff property and minimum adhesion error for the UM WDR gauge, five materials were explored in Chapter 2 including regular glass sheet, acrylic (polymethyl-methacrylate), aluminium, stainless steel, and polished stainless steel. The absolute measurement errors due to adhesion for these five materials (Blocken & Carmeliet, 2005a) are listed in Table 3.1.

Table 3.1. Absolute adhesion water on five vertically placed plates made of different materials

	Glass	PMMA	Aluminium	Stainless steel	Polished stainless steel
Average adhesion water (mm or L/m²)	0.047	0.066	0.083	0.081	0.074

Glass with the minimum adhesion value has the best performance in terms of promoting rainwater runoff, and corresponding with the scope of this research, which is tall buildings' façades, which are typically glass curtain walls. However, it is heavy and more difficult to fabricate, install, and maintain for a long-term measurement period. With the consideration of durability (one-year measurement) and minimum adhesion, acrylic (PMMA) was adopted as the second-best option in Table 3.1 for the driving rain gauge material in this research. The height of the edge is chosen as 3 cm to minimise the influence of the rim in deforming the wind flow, the trajectory of raindrops, and splashing rain drops out. To minimise the adhesion of water, the connection tube from the collector to the tipping bucket is made as short as possible. The tipping bucket chosen as a reservoir has a volume of 15 Litres for the driving rain gauge with a collection area of 400 cm^2 (0.04 m^2).

Table 3.2 describes how the five major possible error sources that were identified during the literature review are addressed in the design of the UM gauge to minimise the biases in the measurement process in the present experimental research. Note that the EMPA wall-mounted gauge was considered the base model gauge with some modifications based on the local climate and lessons learned from the literature, which are described in Table 3.2.

A summary of the customisations and developments that were applied during the design and manufacturing stages of the UM gauge is as follows:

- i. All parts of the WDR gauge collector at UM were made of a 5 mm acrylic sheet and assembled by heat pressing to avoid any droplets leaking from the possible gaps. The material allows the rainwater to drip down into the tube with the least possibility of water adhesion on the surface compared with the materials that have been applied in the literature (aluminium, plate, polytetrafluoroethylene, stainless

steel, etc.), and the size of the collector area, according to the recommendation by (Blocken & Carmeliet, 2005a, 2005b, 2006b) was considered $20 \times 20 \text{ cm}^2$ to reduce the evaporation amount,

Table 3.2. Possible error sources and modifications to minimize in the gauge design stage

No.	Possible error sources	Modifications / Customizations
1	Adhesion-water evaporation	All parts of the gauge have been made of Acrylic (PMMA) sheets as an integrated device to promote water runoff
2	Evaporation from the reservoir	The bucket lid was covered with plastic between the upper cover and the bucket
3	Splashing of drops from the collection area	The catchment area is $20 \times 20 \text{ cm}^2$, and the rim around it has a height of 3 cm to minimize splashing from in and out of the gauge
4	Condensation on the collection area	Measurement has been done right after the rain stopped
5	Wind errors	The rim height around the gauge has been increased by 1 cm compared to the EMPA gauge
6	Droplet leakage	Whole gauge was assembled by heat pressing

- ii. To minimise evaporation from the reservoir, it was covered by two layers: (1) a plastic layer from inside to avoid water absorption and ventilation; and (2) a square shape plywood surface from outside to avoid solar radiation losses,
- iii. The collection area is $20 \times 20 \text{ cm}^2$ to reduce the rate of water splashing because the bigger the collector area, the more splashing errors occur. The height of the rim around the collector area was increased by 1 cm in comparison with the EMPA model to reach 3 cm in order to minimise rainwater splashing either inside or outside the catchment area and the possibility of entering water run-off from the surrounding area of the gauge,
- iv. The connector part of the gauge to the tube has the same material as the collector surface. It is integrated to the collector surface through two internal sloping

surfaces. These surfaces allow the effective shedding of runoff rainwater from the catchment area into the tube and the reservoir, respectively,

The tube is a rubber-hose sealed from both external sides to the connector and the reservoir cover, and the reservoir is an ordinary bucket with a volume of 15 litres (Table 3.3). The length of the tube is at the shortest possible length located outside the building on the façade, buckets are also located outside the building along with the WDR gauges; in a tropical climate, normally there is no water freezing possibility even in the rainy days,

- v. To reduce the wind error, (1) the area of the collector was designed at the practical minimum size based upon the previous studies, and (2) the height of the rim around the gauge has been considered 3 cm (Figure 3.2).

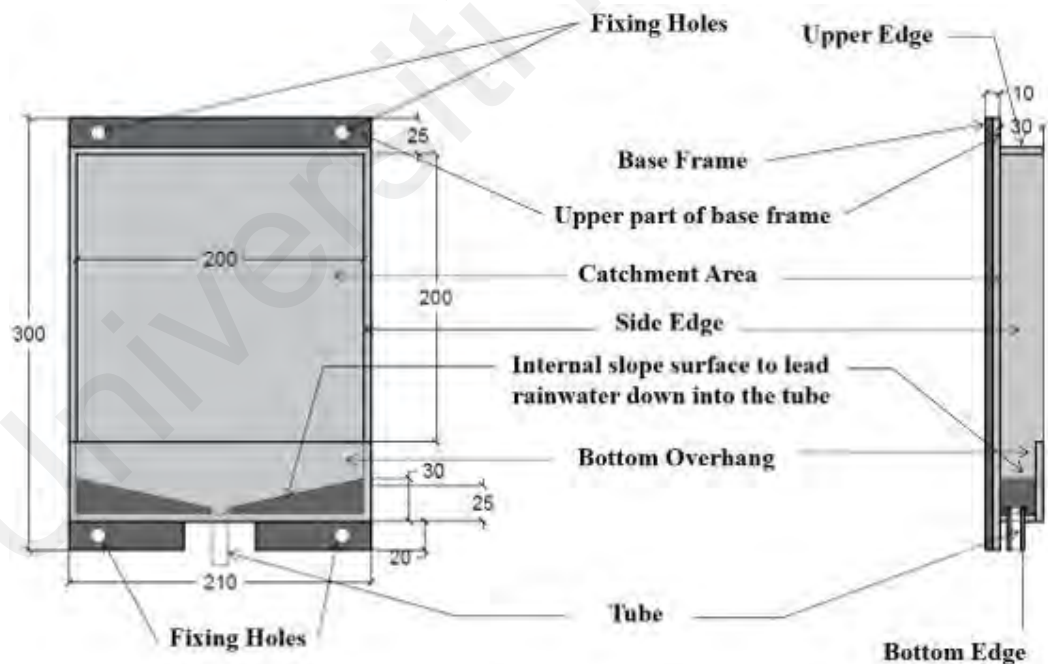
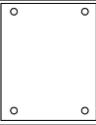




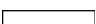






Figure 3.2. Elevation and section of the WDR gauge collector; dimensions in mm.

Table 3.3. The WDR gauge components list

	Components	Material	Quantity	Dimensions (mm)	Geometry
1	Base frame	PMMA	1	210 × 300	
2	Base part for collection area	PMMA	1	200 × 260	
3	Vertical side edges	PMMA	2	260 × 30	
4	Upper edge	PMMA	1	210 × 30	
5	Bottom edge	PMMA	1	210 × 30	
6	Front edge	PMMA	1	60 × 30	
7	Internal slope piece	PMMA	2	105 × 15	
8	Tube to reservoir	Plastic	1	10 Ø	
9	Reservoir	Plastic bucket	1	15 lit	
10	Screw	Metal	4	--	

3.2. Experimental Measurement (In-Situ)

3.2.1. Building Site

Figure 3.3 illustrates an aerial view of the measurement site. It is located on the main campus of Universiti Malaya in the city of Kuala Lumpur, Malaysia, at latitude 3°07'15" and longitude 101°39'23". The building has dimensions of $L \times W \times H = 18.60 \times 6.40 \times 3.50 \text{ m}^3$. The building's long side faces northeast and it is exposed to a downhill open space.

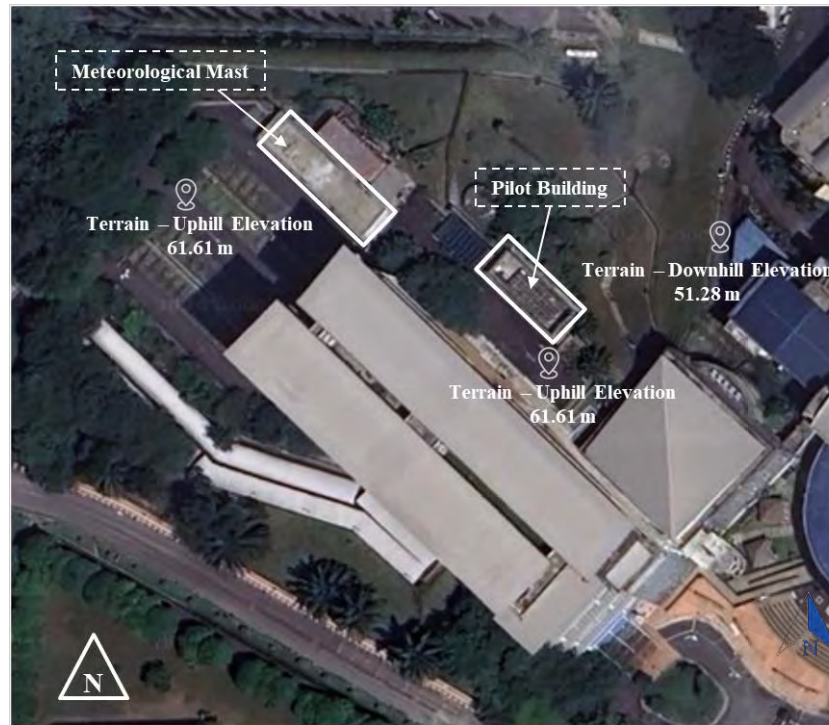


Figure 3.3. Aerial view of the building site

The southwest side is facing a pilot parking lot at a distance of 13 m, on its southeast and northwest sides are open parking areas, and the closest adjacent buildings are at a distance of 19.50 m and 25.70 m, respectively. Different types of adjacencies around the building and 24/7 accessibility have made it a suitable building for WDR measurement study at the campus in an urban area. Furthermore, the building's orientation, specifically NW-SE, is perfectly aligned with the predominant wind directions during monsoon seasons in Kuala Lumpur, ensuring that the windward façades were accurately positioned.

3.2.2. Measurement Setup

The parameters monitored by the sensors include local meteorological data, i.e., wind speed, wind direction, wind gust, wind pressure, temperature, relative humidity, horizontal rainfall, and WDR amount on the façade by the UM gauge.

The logging interval for which the experimental data are recorded is chosen to be 10-minute (Figure 2.19), following the guidelines by Van der Hoven (1957), Sumner (1981), Blocken and Carmeliet (2007a, 2008) and Kubilay et al. (2014a) in order to minimise the errors related to the time resolution of meteorological datasets. Since the horizontal

rainfall amount (S_h) and the WDR amount (S_{wdr}) are in event-based summed values, the corresponding meteorological data during rain events in the dataset are also presented in terms of event-based averaged values. The recorded 10-minute wind data (wind speed and wind direction) are averaged over event-based intervals.

3.2.2.1. Wind Speed (U) and Wind Direction (D)

According to the literature (Section 2.5.1), standard free-field wind speed and wind-direction measurements should be performed at a height of 10 m outside the constant flux layers around the buildings in an open area to obtain the actual data recorded. Accordingly, to minimise the effect of local turbulence induced by the building, a meteorological mast was installed on the rooftop of the adjacent building at a height of 3.50 m and sensors at a height of 4.50 m above the roof surface. Therefore, sensors were placed approximately 8 m above the ground to measure the approach-flow wind direction (D), wind speed (U), wind gust, and wind pressure. The wind speed at a height of 10 m (U_{10}) to fit in the model will be determined by employing equation Eq. (12) and extracting the proper exposure exponent α from Table 2.9.

Since the building site is located in a relatively open urban area, the recommended exponent $\alpha = 0.25$ for suburban terrain is used in this study to convert the wind speed measured at height h to height 10 m above the ground.

3.2.2.2. Horizontal Rainfall (S_h)

The daily recorded data of horizontal rainfall (S_h) in mm was collected from the nearest meteorological department (MMD) to the UM campus. It was logged in using the tipping bucket method (Figure 3.4). As stated in Section 2.5.2, the Malaysian Meteorological Department measures precipitation using the tipping bucket (Figure 3.4-a), automatic (Figure 3.4-b), and conventional methods (Figure 3.4-c). MMD (2024) outlined the

following principles and characteristics of the tipping bucket setup for the horizontal rainfall measurement that they are using:

- The standard instrument for measuring rainfall is the 203 mm rain gauge,
- This is essentially a circular funnel with a diameter of 203 mm that collects the rain into a graduated and calibrated cylinder,
- The measuring cylinder can record up to 25 mm of precipitation, any excess precipitation is captured in the outer metal cylinder,
- The top of the rain gauge is 0.3 m above the ground.



Figure 3.4. Meteorological instruments using by Malaysian Meteorological Department for horizontal rainfall (S_h) measurements, (a) tipping bucket, (b) automatic horizontal rain gauges, (c) conventional horizontal rain gauges (MMD, 2024)

A number of equipment, including a tipping bucket, a weighing gauge, and state-of-the-art gauges that use laser technology, have been designed for automatic observation. Tipping-buckets (Figure 3.4-a) are the most widely used because their technology has been around for a long time and the mechanism is simple and mechanical (MMD, 2024). Basically, a tipping-bucket gauge consists of a collector funnel that diverts water to a tipping bucket mechanism. An electronic pulse is generated each time the volume of water collected in one of the small brass buckets causes the bucket to tip. This is

equivalent to 0.2 mm of precipitation. The maximum detectable amount of rainwater is 200 mm/hour (MMD, 2024).

3.2.2.3. WDR (S_{wdr}) – Vertical WDR Harvesting

It was suggested in Sections 1.3 and 2.8.1 of the literature review to measure WDR on four building walls (all façade orientations) to enable correction of the WDR coefficient derived from ISO 15927-3 based on the local climate for the windward façades.

Following the previous research findings on the spatial distribution and wetting pattern of WDR on building façades, the highest catch ratio (η) values belonged to the top corners and the least values to the middle-lower two-third of the façade (Section 2.7.1). Accordingly, in the present study, eight UM WDR gauges were installed on the four façades of the pilot building at the campus of UM. Two gauges on each façade, one on the top corner edge (2.75 m height), and one on the middle two-third of the façade height (1 m height) to receive and measure the maximum and minimum accumulated WDR impinged on the gauge surface area (Figure 3.5 and Figure 3.6). During the measurement period, regular maintenance was taken to ensure the gauges' collection areas remained clean and unclogged.

The amount of rainwater collected by the wall-mounted WDR gauges was observed as event-based. The information including the beginning time, end time, and total rainfall volume was recorded. The amount of WDR (S_{wdr}) that was collected by the reservoirs was measured manually (hand-emptied) immediately after the rain stopped.

The WDR amount (S_{wdr}) measurement was carried out by eight wall-mounted gauges over the four tropical seasons of Malaysia; starting from April 2017 to March 2018. According to the annual report of the UNFCCC (2015), precipitation events in Kuala Lumpur occur mostly in the afternoons and evenings. Given this fact and the manual measurement of the WDR in this study, nocturnal precipitation (12 a.m. to 6 a.m.) was

not recorded. In addition, those diurnal accumulated precipitations (S_{wdr}) with an amount of less than 1 ml were excluded from the record.

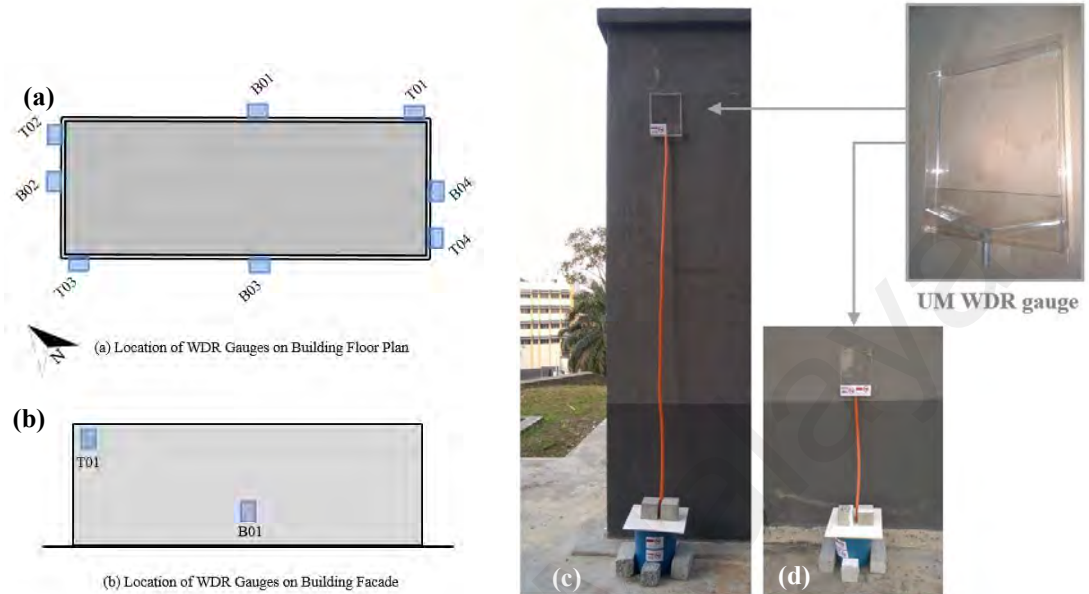


Figure 3.5. The orientation of the pilot building and locations of the WDR gauges on the building: (a) Floor plan, (b) the façade (not to scale), (c) location of gauge T02 (at 2.75 m height), (d) location of gauge B02 (at 1 m height).



Figure 3.6. The pilot building and position of the WDR gauges on the façades (a) South view (b) Meteorological mast on the rooftop of the building at the parking area.

3.2.2.4. Time Accuracy of the Data Logger

Once the Micro Station is logging, it keeps accurate time. However, according to the HOBO Micro Station Data Logger (H21-002) manual, there are three main sources of errors with time reporting. The following table lists the implementation considerations to address these errors:

Table 3.4. Time reporting possible errors of the data logger and the implementation considerations

No.	Possible error sources based on (H21-002) manual	Considerations in this study
1	Host clock error: A common source of error is an incorrect time in the computer used to launch the logger	Before launching the logger and after each read-out, the clock and date on the computer are checked and set to the correct time and date
2	Start-up error: The logger can lose as much as 2 seconds when it is launched	This is a one-time error that occurs as part of the start-up sequence and cannot be avoided, thus the initial logging and all read-out events are conducted in non-rainy moments
3	Clock drift: The long-term time accuracy is a function of temperature. The worst-case error is ± 8 parts per million (PPM) a week at 25°C, which is about 5 seconds per week. The error increases as the temperature deviates from 25°C (see the figure below). If the temperature were a constant -20°C, the logger time error could be as much as 35ppm (21 seconds per week).	Which can be disregarded in this study due to the KL weather condition with the mean annual temperature of 25.4°C

In compliance with the recommendations given by the data logger manual, additional periodic check-ups were performed during logging and read-out events to ensure the accuracy of recorded data, such as:

Performing a visual inspection – Fortnightly (once every two weeks), a visual inspection of the Micro Station tower and logger enclosure is conducted; reading out the logger and relaunching the system to reset the logger's clock. Additionally, in accordance with the manual's recommendations, the following matters were monitored too:

- Cables and wires are not damaged, cracked, cut, split, or broken,
- All the screws and bolts are tightly secured,
- The mast is still level,
- The ground attachments are fastened to the tripod and logger,
- There is no excess rust; replace rusty parts as necessary.

Verifying the sensor accuracy – All sensors were tested and recalibrated in the lab at the Faculty of Built Environment. A one-week pilot test was conducted on-site prior to performing the one-year measurement to verify the accuracy of all sensors.

3.3. Data Cleaning Process – Generating In-Situ Dataset

Correction of the measurements for errors is only possible in a limited number of situations. Therefore, carefully choosing precise and sufficient measurements from the overall amount of acquired data is essential for conducting the intended analysis and generating a valid in-situ dataset.

3.3.1. Preprocessing of In-Situ Measured Data

As the first step to prepare in-situ dataset comprising wind, horizontal rainfall, and WDR data for model validation, the following principles derived from the previous studies are taken into account (Abuku et al., 2009; Blocken & Carmeliet, 2004, 2005a, 2005b, 2006c; Kubilay et al., 2014a):

- Select rain events with large WDR sums to reduce the relative adhesion-water evaporation error,
- Select rain events for which WDR splashing errors will be absent or small; rain events characterised by reference wind-speed values U_{10} lower than 10 m/s and with horizontal rainfall intensities $R_h < 20$ mm/h,

- Select rain events for which the wind direction during rain is approximately perpendicular to the façade under study to limit the wind error in the WDR measurements on the façade. In this study, the wind direction D ($^{\circ}$) is assumed to be perpendicular to the corresponding façade orientation θ ($^{\circ}$) for each rain event,
- Nocturnal precipitation (12 a.m. to 6 a.m.) and diurnal precipitations with less than 1 ml were excluded from the record,
- Wind-driven rain bucket tips are filtered when wind speeds are less than 1 km/h and wind directions are lower than 22.5 degrees to the normal to the wall to avoid erroneous results when parameters such as the WDR catch ratio (η) are calculated. Otherwise, the delay between the horizontal rainfall and the tips of the wind-driven rain buckets produces erroneous results.

Tables of meteorological data (wind speed (U), wind direction (D), amount of horizontal rainfall (S_h)) and daily harvested WDR amounts (S_{wdr}) measured by the 8 wall-mounted gauges, Top (T01-T04) and Bottom (B01-B04), installed on all four building façades (NE, NW, SW, SE) for each tropical season are provided as the raw meteorological data and harvested WDR.

3.3.2. Data Units' Conversions

The wind speed (U) is logged in km/h, and the wind direction (D) in degrees ($^{\circ}$) measured clockwise from north. The horizontal rainfall amount (S_h) is logged in millimetres (mm), the harvested WDR amount (S_{wdr}) in millilitres (ml), and the spell duration in minutes. This study observed the WDR collection using the unit of rainfall event also known as event-based measurement. Accordingly, the meteorological data are transformed from a 10-minute averaging period to an event-based averaging period. Mean values for wind speed (U) and direction (D) are calculated over each rainfall event, adhering to the 'event-based averaged value' approach of this study (Section 2.8.2.7).

Accordingly, horizontal rainfall intensity (R_h) is calculated as the ratio of the total amount of horizontal rainfall (S_h) in mm falling during the rain event to the duration of the on-site recorded rainfall. It is expressed as mm per hour (mm/h) in this study.

The calculation steps for the conversion of units of accumulated WDR (S_{wdr}) (ml) from the reservoir to the WDR intensity value (R_{wdr}) (mm/h) are illustrated in Figure 3.7.

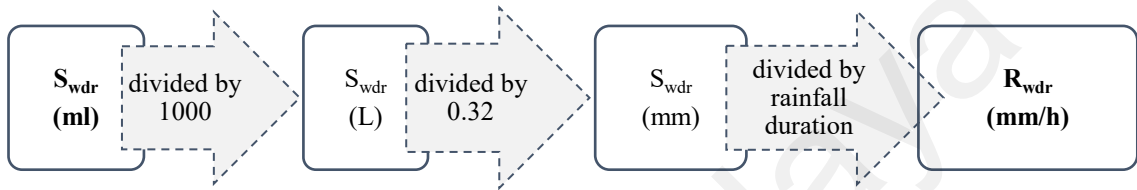


Figure 3.7. Unit conversion steps to calculate WDR intensity value (mm/h)

The wind speed (U_h) measured at the mast on-site is converted to a wind speed at the roof-line height (U_{10}) (m/s) as the reference wind speed (m/s) at 10 m height using Eq. (12) to determine the U_{10} value for each rain event to be fitted to the models:

The height of the mast (h) = 8 m, and the recommended exponent $\alpha = 0.25$ for a suburban terrain is used (see Table 2.9) because the building site is located in a relatively open urban area in the UM campus. Thus, the following equation is formulated for this study:

$$U_{10} = U_8/0.95$$

As discussed previously, due to the ever-changing wind direction (D) in reality (2.8.2.6), utilising the moderation method for the ‘event-based averaged’ approach of this study (2.8.2.7), and based on the evaluated and determined windward façades in each season (Section 4.1 (two façades in each season)), thus in the semi-empirical equations considered in this study:

- the wind direction D ($^{\circ}$) is assumed to be perpendicular to the corresponding façade orientation θ ($^{\circ}$) for each rain event, and the $\cos(D - \theta)$ value is calculated as one ($\cos 0^{\circ} = 1$),
- in WDR relationships, the ‘mean value’ of both façades’ top and bottom gauges will be used as one top and one bottom gauges of one windward façade in each season.

3.3.3. Spatial Distribution of WDR – Catch Ratio (η) Calculation

Definition and significance of catch ratio (η) have been discussed in Sections 2.6.1 and 2.7.1. Accordingly, the catch ratios (η) are calculated using equation Eq. (1) for each monitoring season to show the spatial distribution of WDR across the building façades. Subsequently, correlation analyses are performed to assess the influence of wind speed (U), height (top and bottom gauge locations), and horizontal rainfall intensity (R_h) on the catch ratio value (η).

3.3.4. Data Cleaning Process – Generating In-situ Dataset

This research followed the principles of the WDR field measurement method in building science, reviewed in Sections 2.6 and 2.7. In tropical regions, topography and monsoon winds are the main factors that influence the flow of the wind direction and velocity, and consequently, the WDR loads on the building façades. Therefore, considering the unique rainfall and wind patterns in the tropical climate, the analysis processes are conducted individually for each season because wind plays an important role in the applicability of the equation. It directly affects the WDR coefficient value. The following are the principles that govern the data cleaning process for each season dataset:

- i. To select accurate wind speed (U), horizontal rainfall intensity (R_h), and WDR intensity (R_{wdr}) datasets as in-situ dataset for model validation, the guidelines presented in Section 3.3.1 are followed for all rain events,

- ii. Normality Test and Outlier Test through IBM SPSS Statistic 26 software are conducted. There are two well-known tests of normality in SPSS, namely the Kolmogorov-Smirnov Test and the Shapiro-Wilk Test. The Shapiro-Wilk Test is more appropriate for small sample sizes (< 50 samples), but it can also handle sample sizes as large as 2000. For this reason, the Shapiro-Wilk's test is employed as the numerical means of assessing normality in this study.

3.4. Semi-Empirical Models

As stated in the literature, semi-empirical models for R_{wdr} prediction on building walls are partly or completely based on measurements that are conducted with WDR gauges (discussed in Section 2.8). Generally, these models incorporate parameters derived from WDR measurements. This section outlines the procedures that are undertaken for the models' application, validation, and R_{wdr} prediction.

The validated WDR measurement (in-situ) dataset derived from the data cleaning process is employed to validate the semi-empirical models, i.e., ISO 15927-3 (2009) and ASHRAE Standard 160P (2016).

3.4.1. Application of the Models – Generating the Models' Datasets

To apply ISO Standard 15927-3 and ASHRAE Standard 160P models:

Step 01: Determining validated in-situ R_{wdr} datasets derived from the data cleaning process for each rain event of each season that are tabulated separately.

Step 02: Determining correction factors and parameters for ISO standard 15927-3 and ASHRAE standard 160P models based on the given data in Sections 2.8.2 and 2.8.3.

Step 03: Calculation of R_{wdr} using ISO standard 15927-3 model Eq. (10) and ASHRAE standard 160P model Eq. (13) to create the models' datasets; ISO dataset and ASHRAE dataset.

3.4.2. Validation of the Models – Accuracy Performance Assessments

To validate ISO Standard 15927-3 and ASHRAE Standard 160P models:

Comparing the calculated datasets (ISO 15927-3 model and ASHRAE 160P model) with the corresponding measured dataset from the in-situ measurement of WDR under actual conditions allows an assessment of the accuracy and performance of these semi-empirical models (Kubilay et al., 2014a). Therefore, comparative graphs and tabulated values of the Mean R_{wdr} (mm/h) derived from the in-situ, ISO model, and ASHRAE model datasets on the windward façades of the pilot building (Top and Bottom gauges) will be conducted. They are followed by further analytical assessments to determine the degree of discrepancies (errors) and evaluate the predictive performance of the two semi-empirical models for top and bottom locations, i.e., calculation of difference (D), coefficient of determination (R^2) based on order 4 (quadratic) polynomial regression model, root mean square deviation (RMSD), and normalised root mean square deviation (NRMSD).

R^2 provides information about the correlation between two datasets, while NRMSD quantifies the normalised difference between them (error). In light of the purpose of the analysis section, which is the quantification of error between the experimental measurement (in-situ) dataset of the mean R_{wdr} and each model's (predicted), NRMSD is considered the right evaluation metric to proceed with to quantify the accuracy of the predictions. It is discussed further in Section 4.6.

3.4.3. Prediction of Mean R_{wdr} – Application of Proposed WDR Coefficients

To predict the mean R_{wdr} on the building wall for RWH:

To predict mean R_{wdr} values using WDR relationships (ISO and ASHRAE), Blocken and Carmeliet (2005b) have also specified the first two stages as follows:

Step 01: Determining the proposed WDR coefficient (α (ISO) and (F_L (ASHRAE)): It is determined from hourly measurements of wind speed (U), wind direction (D), horizontal rainfall intensity (R_h), and WDR intensity (R_{wdr}) at a certain position on a building façade.

Step 02: Application of the proposed WDR relationship (using the proposed WDR coefficient derived from the validated model): first the value of the WDR coefficients (α and F_L) are determined (for several positions on a building façade) through the cross-multiplication method process between the in-situ R_{wdr} dataset and the models' datasets. Then it is used for future R_{wdr} (mm/h) prediction with the models (ISO and ASHRAE), in which it is considered to be a value that is constant in time. Measured standard meteorological data (generally on an hourly basis) of wind speed (m/s), wind direction, and horizontal rainfall intensity (R_h) are used as input in WDR equations Eq. (10) and Eq. (13), namely the ISO standard 15927-3 model and the ASHRAE standard 160P model, respectively.

Step 03: Application of the Proposed WDR coefficients (α) and (F_L): The proposed WDR coefficients (α) for ISO standard 15927-3 and (F_L) for ASHRAE standard 160P are fitted into Eq. (10) and Eq. (13) respectively to predict the proposed R_{wdr} at different height locations on a building windward façade. Each season is subjected to the calculations separately.

Step 04: Based on the statistical data of the water consumption pattern in Malaysia (litres per capita per day) presented in 2.1.1 and the proposed harvestable mean R_{wdr} values (per square metre) as the representative constant for the windward façade for each model and each season, the possible percentage of harvested WDR for non-potable and potable usages (lpcd) is calculated.

3.5. Summary

This chapter presented the design, manufacturing, and installation principles of the UM WDR gauge for WDR collection from the facades of the pilot building. Basic information and characteristics of the measurement setup and meteorological factors were described. The measurement setup was composed of a one-storey rectangular building facing the prevailing wind direction at the main campus of the Universiti Malaya, Kuala Lumpur. The facades are equipped with WDR gauges, two gauges on each façade to generate WDR in-situ dataset. The in-situ dataset is used for correlation analysis to figure out the influence of meteorological parameters and surrounding areas on the spatial distribution of WDR (WDR catch ratio), as well as a prerequisite for model validation after verification through data cleaning process. The processes of data cleaning to generate three verified WDR datasets, i.e., in-situ, ISO, and ASHRAE were presented in detail. The chapter concluded by elaborating systematic (step-by-step) approaches taken for application and validation of the models, followed by the prediction of the Mean R_{wdr} on the building façade.

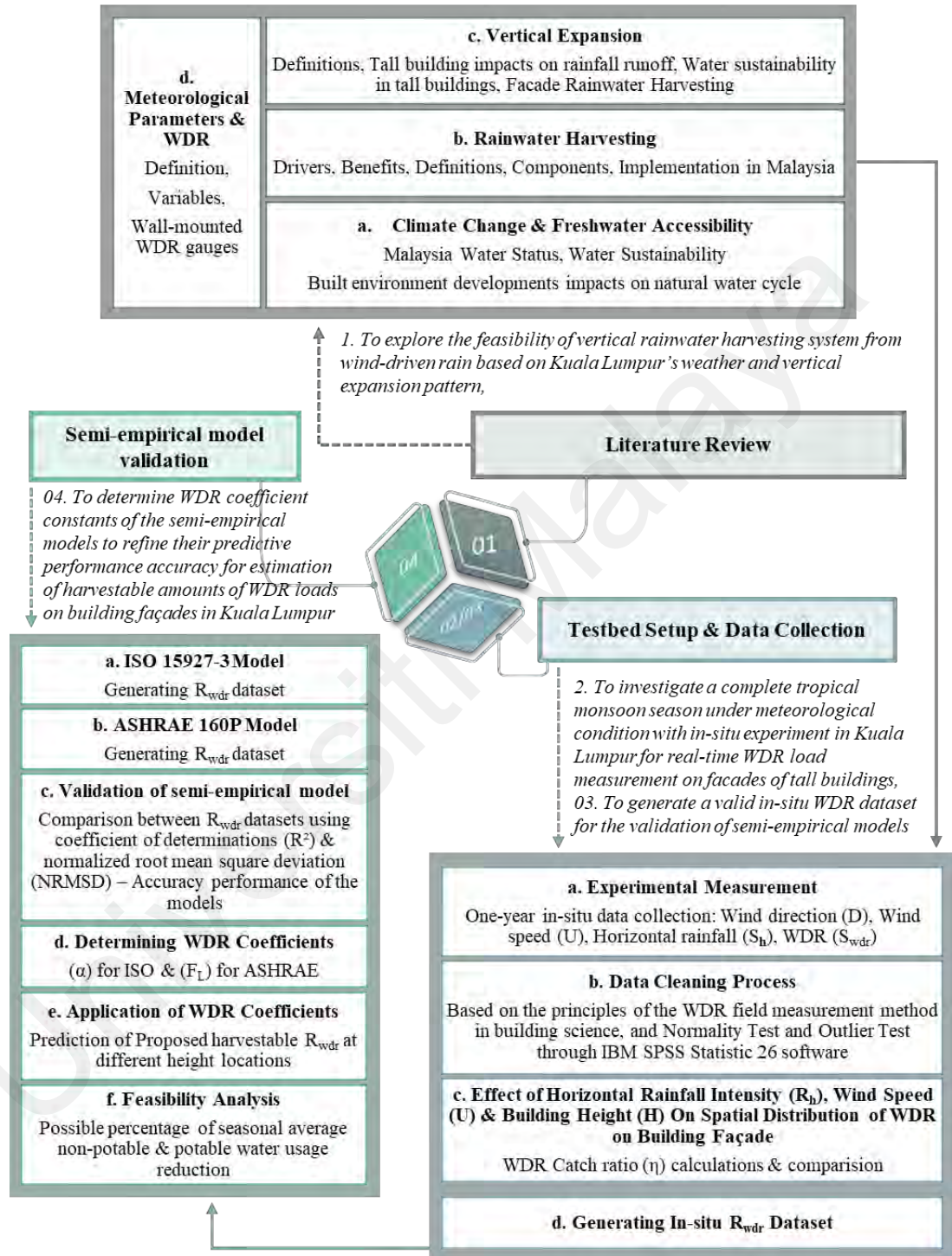
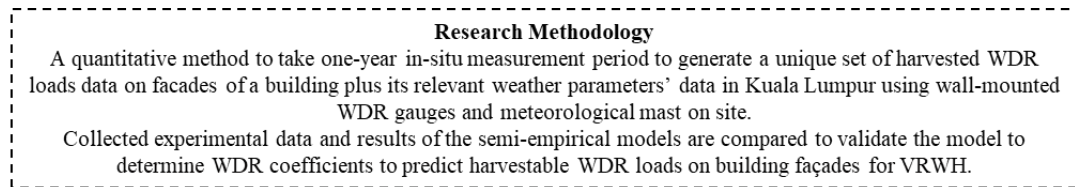


Figure 3.8. Research methodology diagram

CHAPTER 4: RESULTS AND ANALYSES

This chapter presents the results and analyses in eight sections, corresponding to the major steps in the process; Section 4.1 Preprocessing of in-situ measured data, Section 4.2 Data cleaning process – generating an in-situ dataset, Section 4.3 Spatial distribution of wind-driven rain – catch ratio (η) calculation, Section 4.4 Semi-empirical models, Section 4.5 R_{wdr} datasets of in-situ and predicted ISO standard 15927-3 and ASHRAE standard 160P models, Section 4.6 Validating the semi-empirical models, Section 4.7 Determining WDR coefficients for the semi-empirical models, and Section 4.8 Feasibility analysis of harvesting WDR.

In the final analysis step, the proposed WDR coefficients are applied to the models to predict R_{wdr} on tall building façades as the potential new catchment area for VRWH in the climatic condition of Kuala Lumpur.

4.1. Preprocessing of In-Situ Measured Data

A one-year in-situ measurement was conducted and categorised into four periods of tropical seasons experienced in Malaysia based on Table 4.1 in 2017. The first period was from April 1st to May 16th, 2017 as the First Monsoon Transitional Period. The second period of measurement was from May 17th to October 5th, 2017; the Southwest Monsoon season. The third period was from October 6th to November 12th, 2017 as the Second Monsoon Transitional Period. The fourth and last season of measurement was November 13th to March 27th, 2018 as the Northeast Monsoon season.

Table 4.1. Periods of seasons in Malaysia in 2017, data derived from Bahari et al. (2017)

	Seasons	Duration	Percentage of the year (%)
1	Monsoon Transitional Period	1 st April 2017 to 16 th May 2017	12.5
2	Southwest Monsoon	17 th May 2017 to 5 th October 2017	37.5
3	Monsoon Transitional Period	6 th October to 12 th November 2017	12.5
4	Northeast Monsoon	13 th November to 27 th March 2018	37.5

The raw data comprises all of the 10-minute mean data collected from April 1st, 2017 to March 27th, 2018. The first rain event was recorded on April 21st, 2017, from 16:45 to 19:15.

The total number of 93 WDR events was measured in total duration of 7,115 minutes (~119 hrs.) over the four seasonal periods in this experimental research.

The following subsections present results and analyses of temporal and frequency distributions of wind speed (U) and direction (D) and the temporal distribution of horizontal rainfall (S_h) and WDR amount (S_{wdr}) during a one-year measurement categorised into four tropical seasons.

Each season is presented with:

- i. Table of meteorological data: rainfall starting and ending time, rainfall duration (minute), wind speed mean (km/h), wind direction, and wind gust (km/h) measured by the meteorological mast installed at the site, and calculated horizontal rainfall intensity (mm/h),
- ii. Table of daily harvested WDR amounts (S_{wdr}) measured by the 8 wall-mounted gauges, Top (T01-T04) and Bottom (B01-B04), installed on all four building façades (NE, NW, SW, SE).

This data classification aims to further describe the dataset and to ensure that the preprocessing steps adequately exclude unwanted information.

4.1.1. Meteorological Raw Data and Harvested WDR - Season 1

The event-based mean meteorological data measured and recorded from April 1st to May 16th, 2017 is presented in APPENDIX A 1. The number of rainy days in this season is 14 days, with a total duration of 1,210 minutes. The total horizontal rainfall amount (S_h) is 660.2 mm, equivalent to 32.74 mm/h intensity (R_h). The mean wind speed varies between 1-6 km/h and the wind gust varies between 2-8 km/h; the highest values are in the NW (6 km/h) and SW (6 km/h). The wind direction is mainly from NW to SW; the prevailing direction is SW. All the rain events occurred in the afternoon and early evening with a minimum duration of 20 minutes and not to exceed 175 minutes without interruption, except one event (April 28) with a 45-minute short dry period. The longest duration of daily rainfall belongs to the events with the north direction.

The harvested precipitation measured by 8 WDR gauges over the first monsoon transitional period of the year is presented in APPENDIX A 2. Figure 4.1 illustrates the trend of collected WDR quantities by each gauge during each rain event and their distribution over the season; the gauges T03-SW (30,758 ml) among the top gauges and B02-NW (20,238 ml) among the bottom ones have received the highest amount of WDR, both facing the prevailing wind directions.

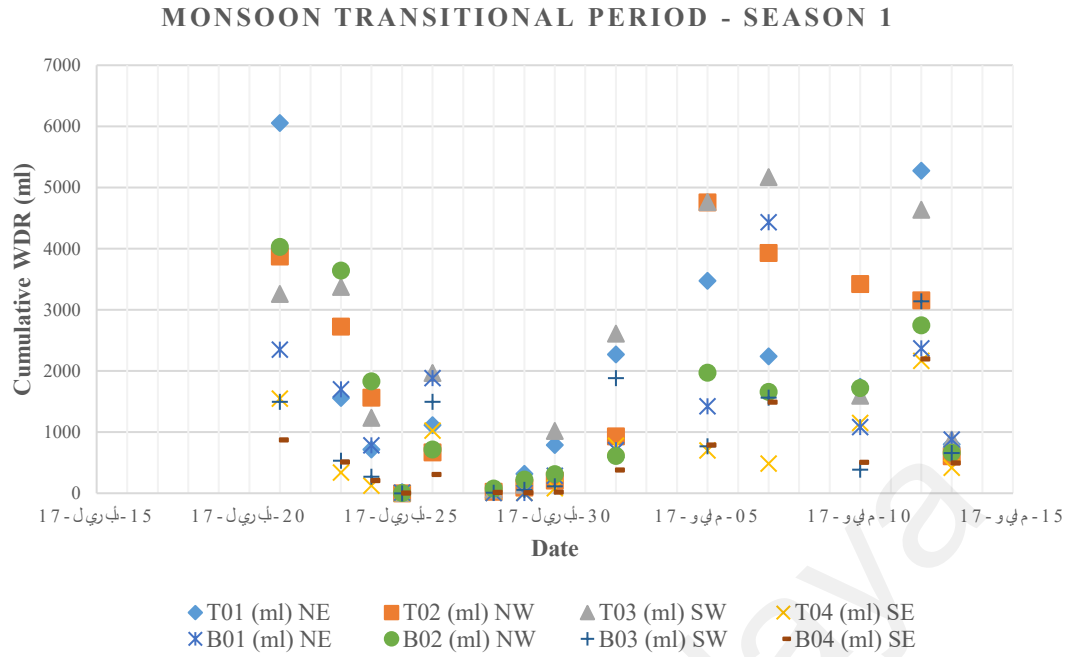


Figure 4.1. The daily harvested WDR amounts (S_{wdr}) measured by 8 WDR gauges during the Monsoon Transitional Period (Season 1)

4.1.2. Meteorological Raw Data and Harvested WDR - Season 2

The event-based mean meteorological data record for the rain events from May 17th to October 5th, 2017 is shown in APPENDIX A 3. The number of rainy days in this season is 22 with a precipitation duration of 1,495 minutes. The total horizontal rainfall amount (S_h) is 1,079.8 mm, which is equivalent to 43.34 mm/h intensity (R_h). This season has a mean wind speed and wind gust of more than 1.5 times the ones in the previous season; the mean wind speed is varied between 3 to 10 km/hr, the wind gust is between 4-12 km/hr. In general, the ESE (10 km/h) and SW (8 km/h) have the highest values. The prevailing wind direction in this season, as its name implies and the weather station recorded, is from SW more consistently in more than two-third of the season (July to September). All the rain events occurred in the afternoon and early evening, except one morning event, with a duration of minimum 20 and not exceeding 120 minutes without interruption, except one event (July 11) with a 30-minute short dry period. The longest duration of daily rainfall belongs to events with SW directions.

APPENDIX A 4 illustrates the harvested precipitation measured by 8 WDR gauges over Southwest Monsoon. Figure 4.2 shows the trend of collected WDR quantities by each gauge during each rain event and their distribution over the season; the gauges T03-SW (27,668 ml) among the top gauges and B03-SW (31,527 ml) among the bottom ones have received the highest amount of WDR, particularly during the second half of the season.

Note that the average daily rainfall duration of this season (67 min) is lower than that of season 1 (86 min), while its average horizontal rainfall (S_h) (49.45 mm) is higher than that of season 1 (35.72 mm), and also its accumulated WDR amount (S_{wdr}) (195,978 ml) is significantly higher than that of the season 1 (150,489 ml). Even though the average rainfall duration is lower than the previous season, the wind speed has been stronger with more consistent wind direction (SW), and consequently more accumulated horizontal rainfall (S_h) and WDR (S_{wdr}) over this season.

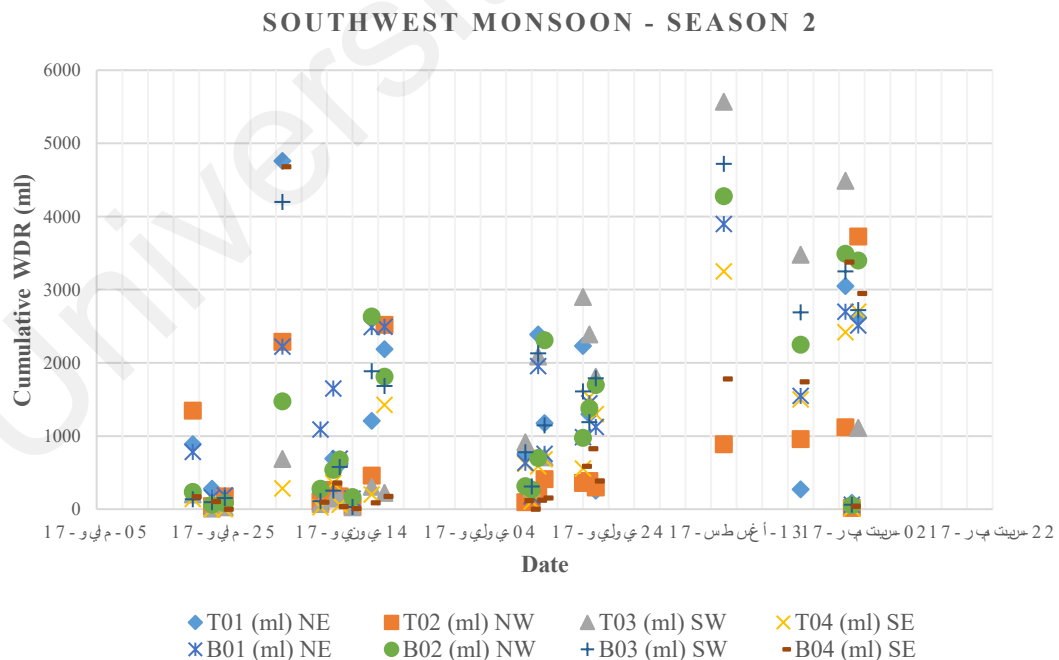


Figure 4.2. The daily harvested WDR amounts (S_{wdr}) measured by 8 WDR gauges during the Southwest Monsoon (Season 2)

4.1.3. Meteorological Raw Data and Harvested WDR - Season 3

The event-based mean meteorological data record for the rain events from October 6th to November 12th, 2017 is shown in APPENDIX A 5. The number of rainy days in this season is 13 and the precipitation duration is 1,090 minutes, which is shorter than both previous seasons. The total horizontal rainfall amount (S_h) is 395 mm, equivalent to 21.74 mm/h intensity. This rain event has a mean wind speed and wind gust even higher than in season 2; the mean wind speed is fluctuating between 2-14 km/hr, the wind gust is between 3-17 km/hr, but the horizontal rainfall amount is less than half of that in season 2. This season is shorter, and more homogeneous in terms of wind speed values and wind directions; wind direction fluctuations display a more isotropic distribution (APPENDIX A 5). During the first half (October), the wind speed is high and the daily rainfall duration is low. In the second half (November), wind speed decreases, daily rainfall duration increases, and rainfall intensity is relatively higher and homogeneous compared to the October ones. The highest mean wind speed values belong to the WNW (14 km/h) and NW (12 km/h). The prevailing wind direction is mostly West, fluctuating from NW in October to SW in November. All the rain events occurred in the afternoon and early evening, except one morning event, with a minimum duration of 30 minutes and not exceeding 195 minutes without interruption. The events in the second half in the SW direction have the longest durations of daily rainfall (except for one event in October, which lasted 195 minutes).

The harvested precipitation measured by 8 WDR gauges over the monsoon transitional period of the year is presented in APPENDIX A 6. Figure 4.3 indicates the trend of collected WDR quantities by each gauge during each rain event and their distribution over the season: the gauges T02-NW (17,360 ml) among the top gauges and the gauge B02-NW (13,970 ml) among the bottom gauges have collected the highest amount of WDR during this season, both facing the prevailing wind direction (NW).

The figure also indicates there are no noticeable sharp differences between the rest of the gauges in terms of the accumulated WDR amount (S_{wdr}) and the graph illustrates a homogeneous trend in all rain events over the season.

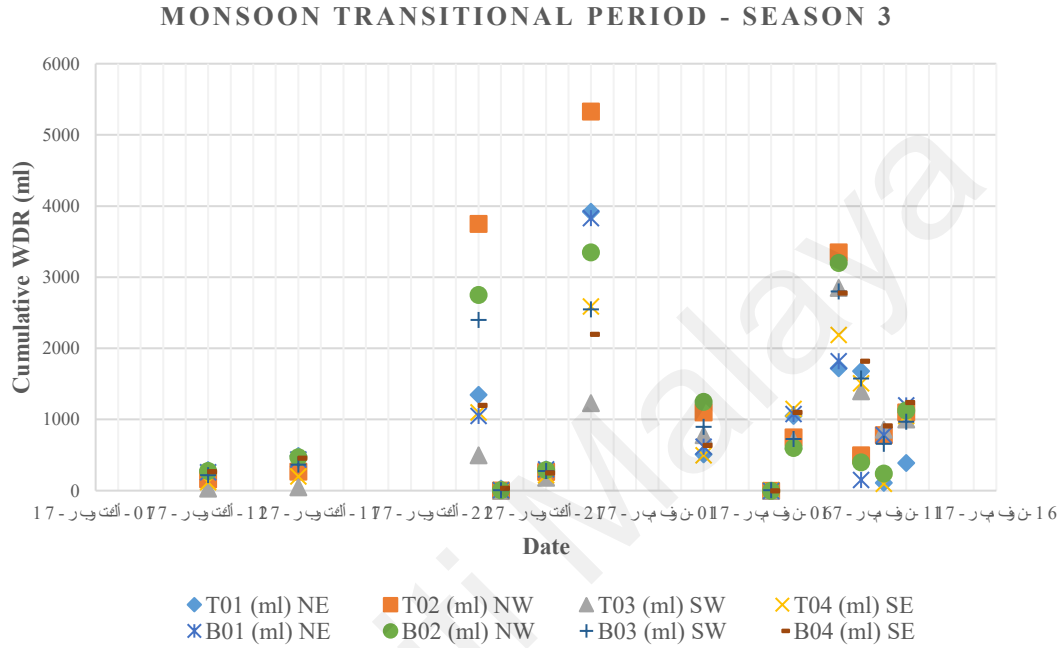


Figure 4.3. The daily harvested WDR amounts (S_{wdr}) measured by 8 WDR gauges during the Monsoon Transitional Period (Season 3)

4.1.4. Meteorological Raw Data and Harvested WDR - Season 4

The event-based mean meteorological data record for the rain events from November 13th to March 27th, 2018 is shown in APPENDIX A 7. The number of rainy days in this period is 44 and the precipitation duration is 3,845 minutes, which is the highest compared to the previous 3 seasons of the year.

The total horizontal rainfall amount (S_h) is 1,513.2 mm, equivalent to 23.61 mm/h intensity. Hence, this season consists of an average daily rainfall duration (87 min) almost the same as season 3 (83 min) but in the longest period (44 days and 3,845 min) which resulted in a sharp increase in the amount of horizontal rainfall.

This season has wind speed and wind gust of about the same values as season 3; the mean wind speed is fluctuating between 1-7 km/hr, and the wind gust is between 2-12 km/hr. The NE and W (7 km/h) have the highest values overall. The prevailing wind direction in this season, as its name implies and the weather station recorded, is mostly NE and NW, respectively and in short periods switches to the SW. All the rain events occurred mostly in the late afternoon and evening, with a minimum duration of 20 and not exceeding 180 minutes without interruption. The longest durations of daily rainfall belong to the events in the NW direction.

The harvested precipitation measured by eight WDR gauges during the northeast monsoon period is presented in APPENDIX A 8. The maximum precipitation duration along with the effective wind speed over this season resulted in the highest harvested WDR amount (S_{wdr}) with significant variations compared to all three previous seasons as the most heterogeneous season of the year. Note that during the last two months (February to March) of the season, rainfall duration and intensity have decreased significantly compared to the first four months of the season (November to January), and wind direction is mostly from NE.

As Figure 4.4 illustrates the trend of collected WDR quantities and their distribution over the season; the gauges T02-NW (74,159 ml) and B02-NW (65,394 ml), respectively from top and bottom, have harvested the highest amount of WDR during this season. However, the prevailing wind direction is NE (APPENDIX A 7). Two factors have influenced this outcome; (1) the precipitation duration, and (2) mean wind speed, which have been more variable in terms of their values (APPENDIX A 7) in this heterogeneous season and trend in the graph.

NORTHEAST MONSOON - SEASON 4

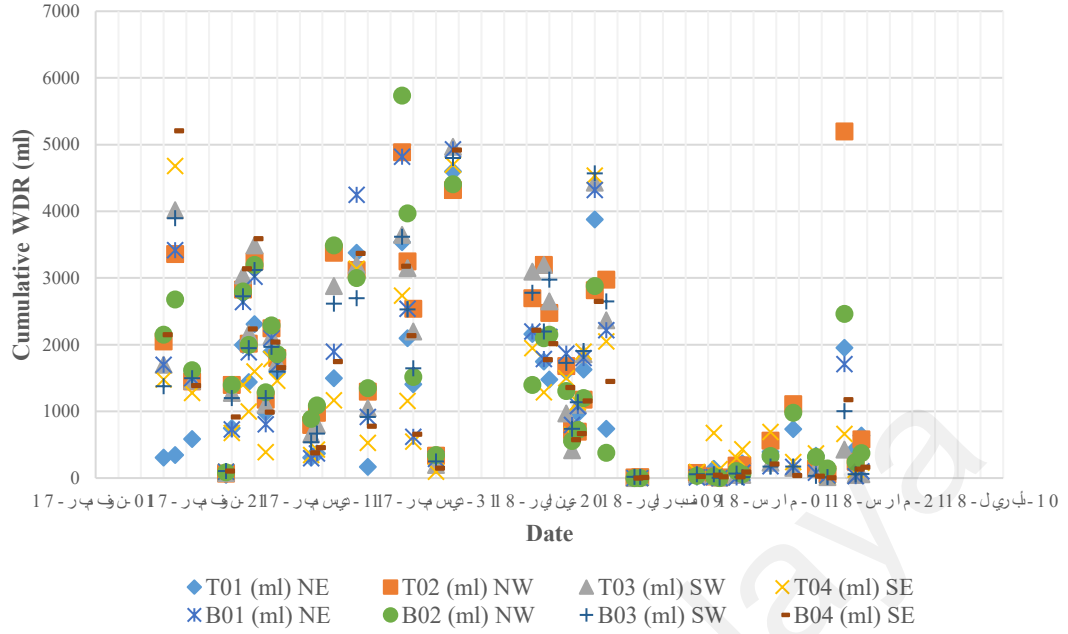


Figure 4.4. The daily harvested WDR amounts (S_{wdr}) measured by 8 WDR gauges during the Northeast Monsoon (Season 4)

4.1.5. Summary of Findings – In-Situ Measured Data

The building site enabled this research to experiment with three different adjacencies for the pilot building. The windward façades:

- NE façade: it faces a downhill and has no adjacent buildings, allows the wind to flow freely without any obstruction,
- SE façade: there is a one-storey adjacent building (same height as the pilot building) at a distance of 19.50 m,
- NW façade: there is a one-storey adjacent building (same height as the pilot building) at a distance of 25.70 m in an open parking area, wind flow is slightly obstructed by other buildings and trees,
- SW façade: there is a pilot parking of a 10-storey adjacent building at a distance of 13 m, wind flows with more obstruction in the presence of the tall building.

Since the aim of this study is to quantify WDR loads impinged on the vertical façades of urban buildings as an alternative water resource in the RWH system, this variety of surrounding areas provided a real scenario similar to an urban building location and orientation with different levels of adjacency of surrounding buildings and landscapes.

The WDR dataset that was extracted from this in-situ measurement gives a clear picture of the WDR quantification loads on building façades, which is what this study is all about (the scope of this study). It is also required to validate the semi-empirical models that will be addressed in Section 4.6.

The WDR was measured by 8 UM WDR gauges attached to the four walls of the pilot building in the campus area during one year. Each façade was equipped with two gauges; one on the top corner edge (2.75 m height) and one on the middle two-third of the façade height (1 m height), to receive and measure the maximum and minimum accumulated WDR. The total number of 93 WDR events was observed, with a total duration of 7,115 minutes. Figure 4.5 and Figure 4.6 illustrate the collected WDR amounts (ml) from all 8 gauges over each season and one-year measurements, respectively.

The comparison between WDR quantity and distribution on the building façades in all four seasons shows:

- i. Comparison between seasonal harvested WDR quantities shows that season 4 has received the highest, followed by seasons 2, 1, and 3 as the lowest receivers in general,
- ii. Season 1 comprises events with intense rainfalls of short durations, namely April 24th and May 13th, which contributed to a substantial amount of rainfall in total. On the contrary, season 3 has few events with long durations (e.g., November 11th) and a low amount of rainfall, which contributed to the farthest distance between rainfall duration and quantity of WDR impinged on the façades.,

- iii. The second transitional monsoon, season 3, with the minimum number of rainy days (13 days), and total horizontal rainfall (S_h) of 395 mm has harvested the lowest amount of WDR (101,428 ml). This season is the shortest event (1,090 min) with the most homogeneous wind flow in direction, velocity, and rainfall intensity,
- iv. Northeast monsoon, season 4, with the maximum number of rainy days (44 days), highest average daily rainfall duration time (87.38 min), and total horizontal rainfall (S_h) of 1,513.2 mm, has remarkably harvested the highest amount of WDR (493,065 ml), more than twice to five times each of the other three seasons,
- v. NW and SW are the façades with the highest WDR values (S_{wdr}) in almost all the seasons (except in season 2 for NW). These two directions face the prevailing wind directions, which have the highest wind speed values over the year,
- vi. The SE façade has received the minimum amount of WDR on top and bottom locations, with a significant difference, particularly in seasons 1 and 3,
- vii. The NE façade has received a noticeable amount of WDR even when the wind direction has not been aligned with the façade orientation, such as during seasons 1, 2, and 3. It has been one of the highest contributors to total WDR (S_{wdr}) collected in each season. The reason is the location and surrounding area of this façade, which is facing a downhill open space with no obstacle to distract or decrease the wind direction or speed value,
- viii. Comparison between total harvested WDR quantities of bottom and top gauges by each façade indicates that in several cases the quantities are almost equal or with slight differences, such as SE façade in seasons 1 and 2, NE façade in season 3, and SW façade in season 4. There are a few cases where the bottom gauges have received higher amounts than the top gauges, such as the NE, NW, and SW façades in season 2, the SW and SE in season 3, and the NE and SE in season 4.

In other cases, all the top gauges have significantly received more WDR than the bottom gauges, including the NE, NW, and SW in season 1, the NW in seasons 3 and 4, and the SW in seasons 1 and 4 (Figure 4.5 and Figure 4.6),

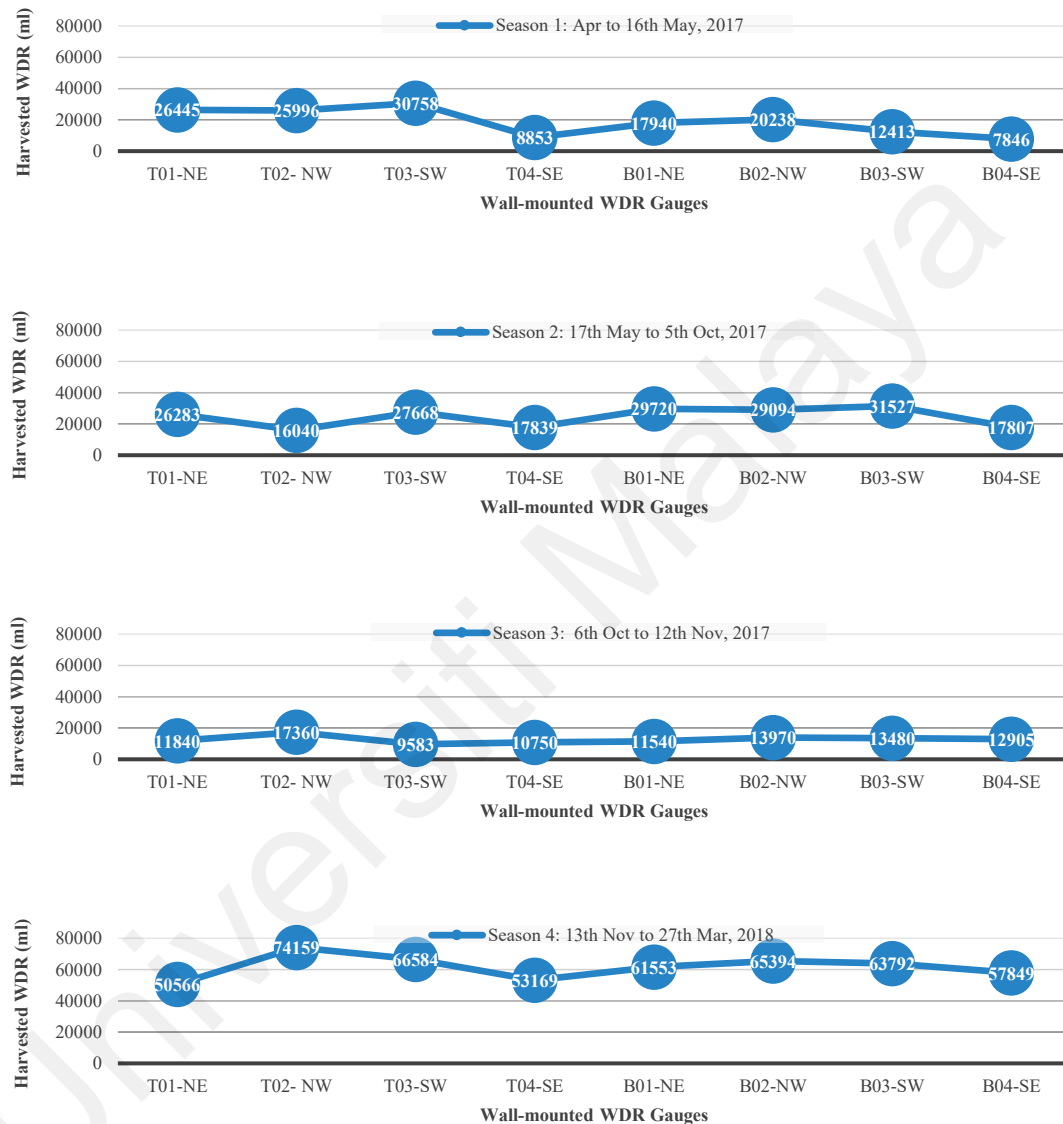


Figure 4.5. Measurements of WDR (ml) by 8 wall-mounted gauges installed on the Top Corner (T01-T04) and Bottom Middle (B01-B04) of the façades over each tropical season (April 2017 – March 2018)

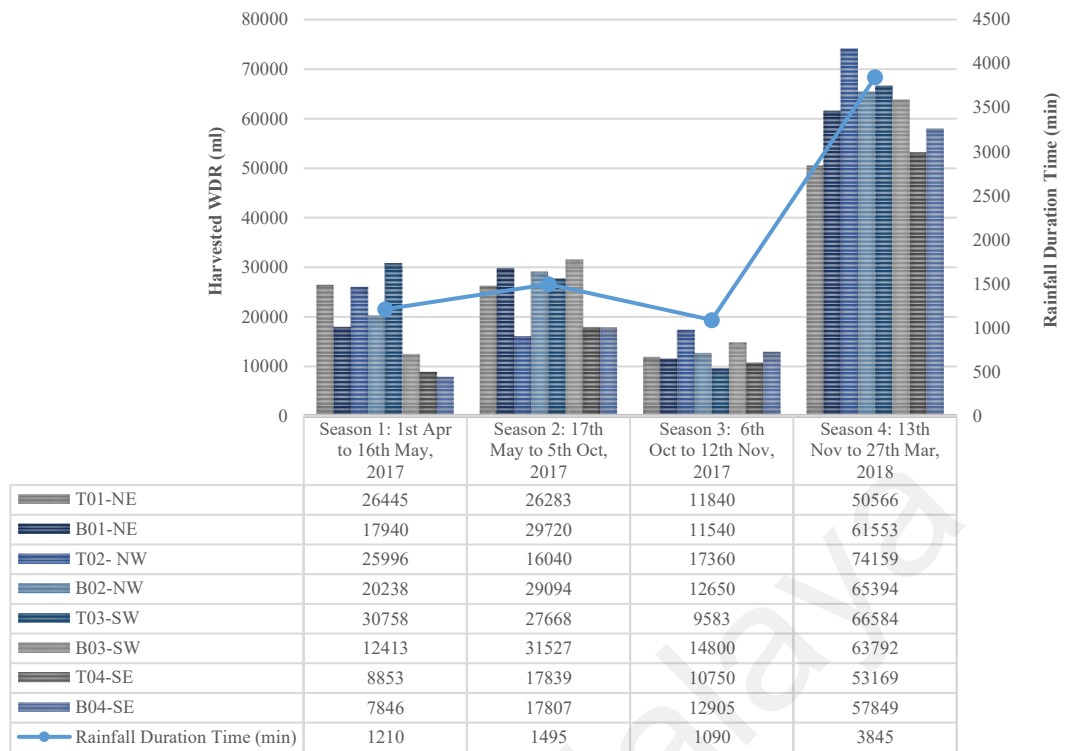


Figure 4.6. Harvested WDR (ml) by 8 wall-mounted gauges (collector area of each gauge is $20 \times 20 \text{ cm}^2$) installed two (Top and Bottom) on each façade (NE, NW, SW, SE) during each tropical season (April 2017 – March 2018)

- ix. Comparison between the total harvested WDR quantities (S_{wdr}) of the top and bottom gauges from the same façade in each season shows that in season 1, the top gauges received 33,615 ml more than the bottom gauges (61%), as stated in the literature. In season 2, all the bottom gauges have received more WDR. In seasons 3 and 4, two façades received higher amounts in top gauges and two façades in bottom gauges. Over seasons 2, 3, and 4, the bottom gauges received, respectively 20,318 ml (55%), 2,368 ml (51%), and 4,109 ml (50%) more than the top gauges (Figure 4.5).

Table 4.2. Maximum and minimum WDR receiver event (in total) in each season and the maximum and minimum WDR receiver gauge in each respective event (*Trace \leq 1 ml WDR amounts (S_{wdr}))

		T01 (ml) NE	T02 (ml) NW	T03 (ml) SW	T04 (ml) SE	B01 (ml) NE	B02 (ml) NW	B03 (ml) SW	B04 (ml) SE	Total (ml)
Season 1										
Min	25-Apr-17	23	2	7	Trace	9	7	3	5	56
Max	12-May-17	5280	3158	4641	2167	2370	2750	3142	2200	25708
Season 2										
Min	31-Aug-17	90	20	60	15	60	55	60	40	400
Max	11-Aug-17	890	890	5570	3250	3900	4280	4720	1780	25280
Season 3										
Min	6-Nov-17	Trace	Trace	Trace	10	Trace	Trace	10	Trace	20
Max	29-Oct-17	3920	5330	1230	2590	3830	3350	2550	2200	25000
Season 4										
Min	4-Feb-18	*Trace	10	3	Trace	Trace	Trace	19	2	34
Max	3-Jan-18	4600	4320	4970	4700	4930	4410	4800	4920	37650

Among the 93 rainfall events in each season, the largest amounts of WDR were recorded as 25,708; 25,280; 25,000; and 37,650 ml; and the lowest ones as 56, 400, 20, and 34 ml by events in seasons 1, 2, 3, and 4 respectively (Table 4.2).

4.1.6. WDR Intensity (R_{wdr}) (mm/h)

On each façade, two gauges were installed. Each gauge has a collector surface area of 0.04 m^2 , so the surface collector area on each façade is 0.08 m^2 and on all façades is 0.32 m^2 . Figure 3.7 illustrated the mathematical processes for converting the accumulated WDR amount (S_{wdr}) from millilitres to millimetres per hour (mm/h) of WDR intensity (R_{wdr}).

Figure 4.7 compares WDR intensity values (R_{wdr}) for each façade orientation in each tropical season. It is observed that the NW façade has the highest value in 3 out of 4 seasons, followed by the SW façade. It indicates a strong impact of building façade orientation (see also Figure 4.6 (8 gauges)) on the WDR intensity (R_{wdr}). Façades facing the prevailing wind direction have received the highest amounts in all seasons.

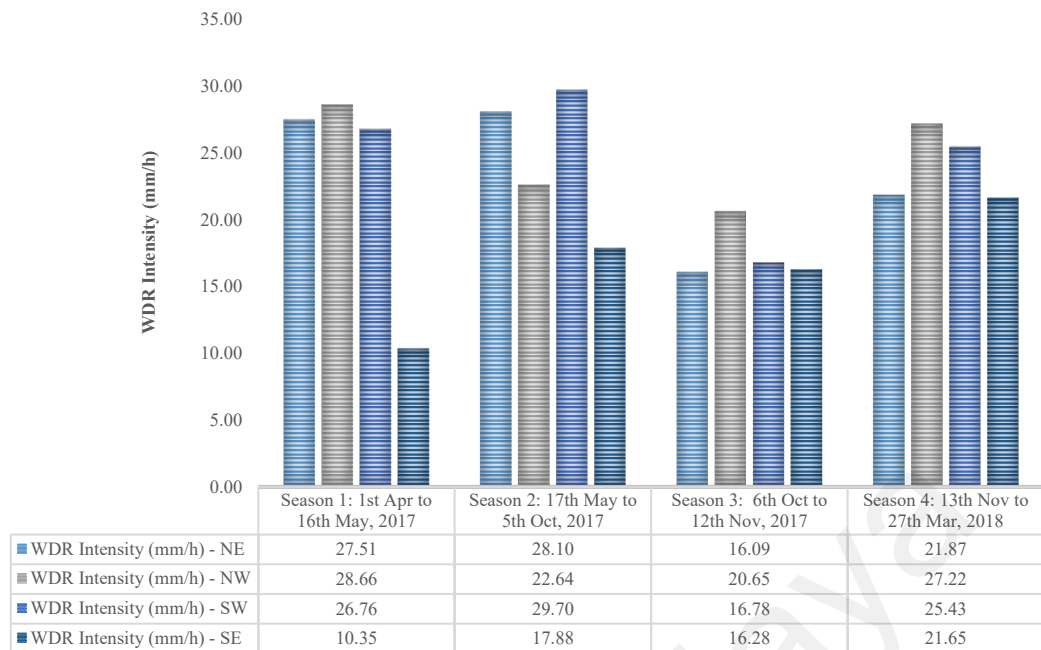


Figure 4.7. Seasonal calculated WDR intensity (R_{wdr}) for each façade (two WDR gauges on each façade) during 4 tropical seasons. (Rainfall intensity is determined as the average rainfall rate in mm/h for specific rainfall duration and a selected frequency. One millimetre (mm) of rainfall is the equivalent of one litre of water per square metre).

4.1.7. Impact of Horizontal Rainfall Intensity (R_h) and Wind Speed (U) on the WDR Intensity (R_{wdr})

In this section, the effect of the horizontal rainfall intensity (R_h) and wind speed (U) on the amount of harvested WDR (S_{wdr}) at a particular time, also known as WDR intensity (R_{wdr}), is evaluated.

The total annual harvested WDR amounts (S_{wdr}) by 8 gauges for 93 events were recorded through in-situ measurements as 940,960 ml, which is equivalent to an average 22.35 mm/h WDR intensity (R_{wdr}).

Average seasonal WDR intensity was calculated as 23.32, 24.58, 17.45, and 24.04 mm/h for seasons 1 to 4, respectively.

Figure 4.8 illustrates trends of average wind speed (km/h), average wind gust (km/h), horizontal rainfall intensity (mm/h), average rainfall duration time (hr), and WDR intensity (mm/h) recorded via in-situ measurements over the four tropical seasons.

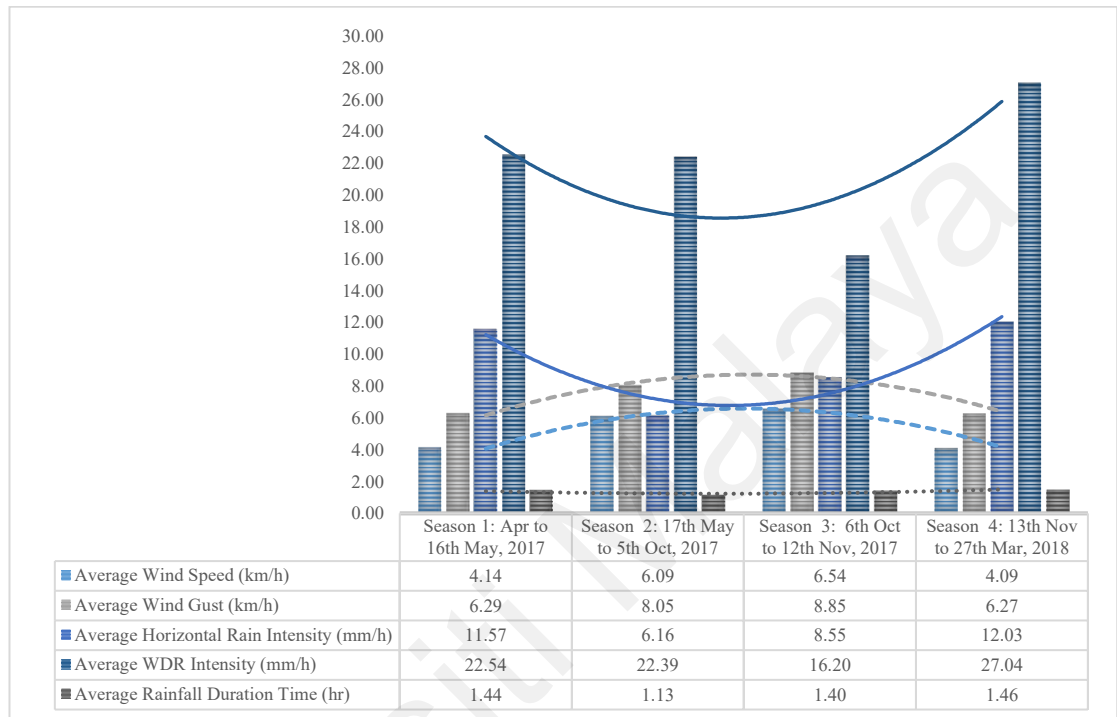


Figure 4.8. Impact of seasonal meteorological data on WDR intensity (R_{wdr}) parameter during 4 tropical seasons (April 2017 – March 2018).

To start with, this figure declares that the WDR intensity (R_{wdr}) value is significantly affected by the total horizontal rainfall intensity (R_h). The amount of WDR intensity (R_{wdr}) is simply proportional to its horizontal rainfall intensity (R_h). The seasonal average data with a greater R_h (mm/h), showed greater R_{wdr} (mm/h); such as seasons 1 and 4 (Figure 4.8), horizontal rainfall intensities (R_h) of 11.57 mm/h and 12.03 mm/h, has led to 22.54 mm/h and 27.04 mm/h R_{wdr} , respectively.

In addition, Figure 4.8 illustrates the role of wind speed in WDR intensity values. It should be emphasised that one of the main characteristics of monsoon winds is their high temporal variations. Wind speeds can double or triple within seconds in tropical climates;

sharp fluctuations as wind gust occurs in several events are clearly visible in the measurement results. Seasons 1 and 4 with the highest average R_{wdr} and R_h have almost same average wind speed of 4 km/h. The average wind speed throughout the year does not show high fluctuation; it is between 4 to 6 km/h.

Figure 4.9 shows the degree of relevancy between WDR intensity (R_{wdr}), wind speed (U), and horizontal rainfall intensity (R_h) based on rain events in each season. The overall trend of WDR intensity with respect to horizontal rainfall intensity and wind speed in all seasons coincides well with each other. However, some mismatches, i.e., sharp ascending or descending, were also detected, which can be further explained as follows:

- The reason behind events with sharp ascending or descending single points of WDR intensity can be addressed by wind gust speed and rainfall duration at that particular event. For example, in season 1, events April 21st and May 12th both have a long rainfall duration (150 min and 105 min), and a high wind gust of 8 km/h compared to the normal wind speed of 5 km/h and 4 km/h, respectively. Event October 24th in season 3, and January 3rd in season 4, have a similar reason for their significant jump; wind gust of 10 km/h and 11 km/h respectively, and wind speed of 5 km/h for both events.
- The sudden descending points in events with relevant high wind speed, such as season 1, April 25th (5 km/h); and season 3, October 25th (11 km/h), are resulted from the short duration of rainfall of 20 min and 30 min, respectively.

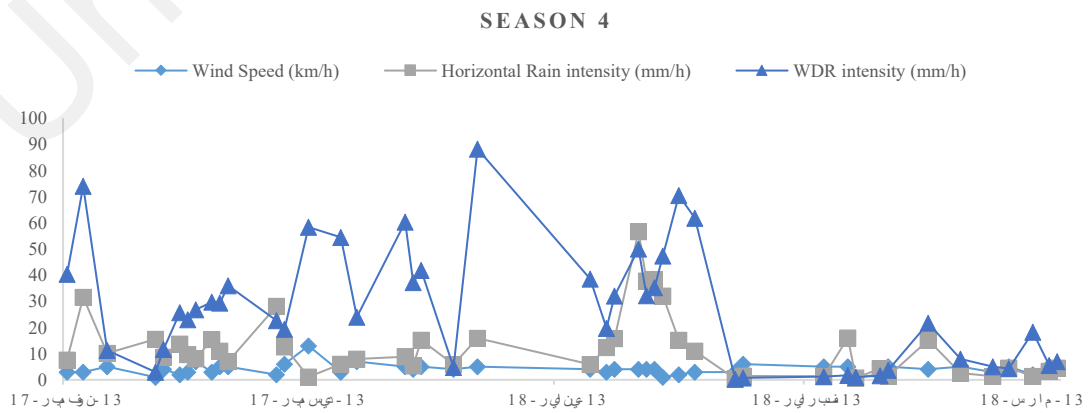
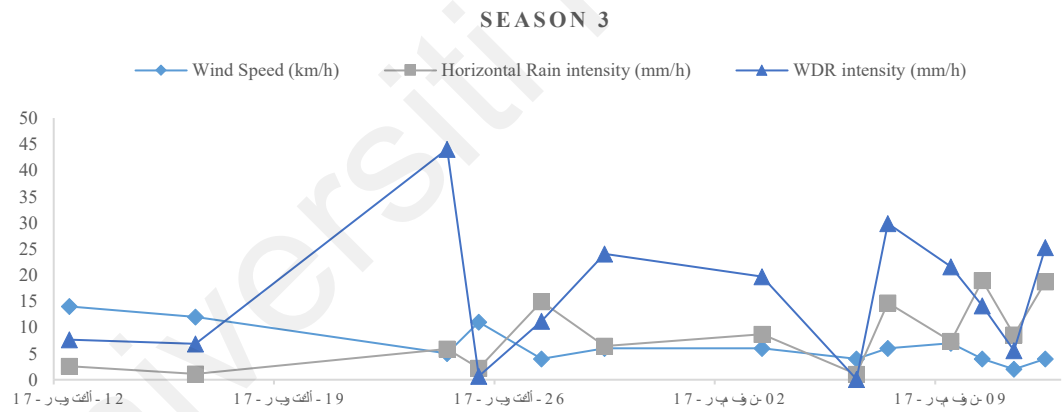
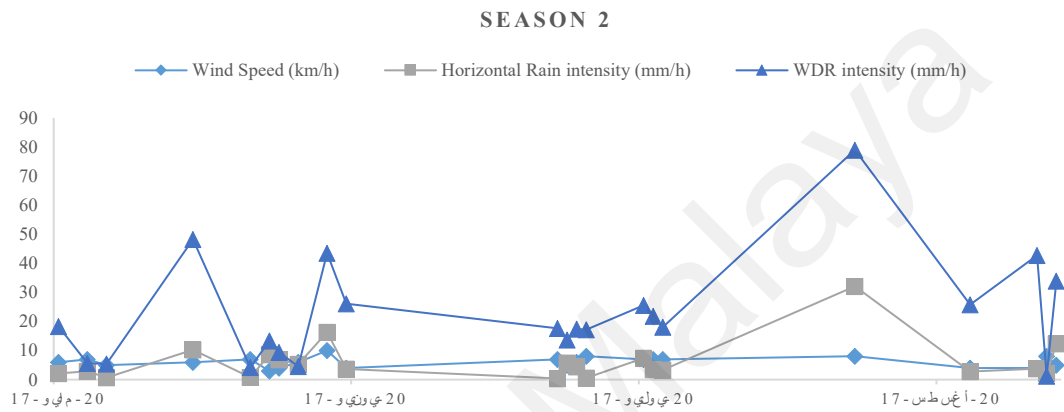
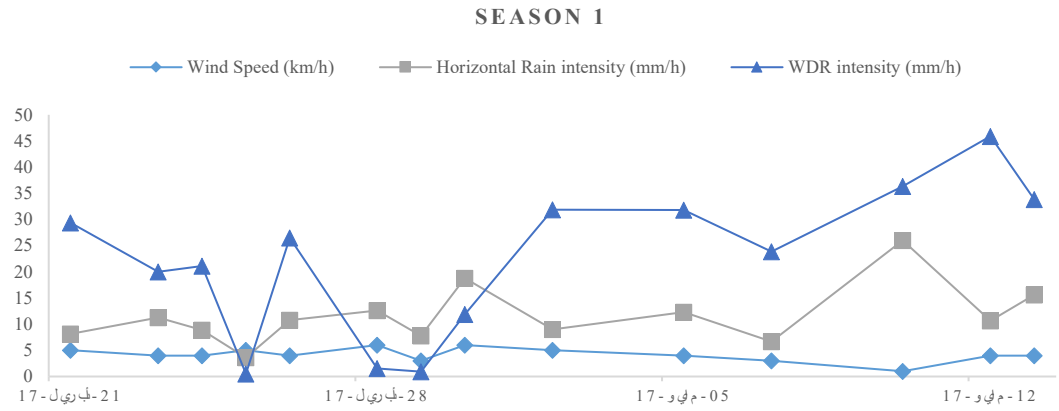


Figure 4.9. Daily meteorological data; wind speed (U) (km/h), horizontal rainfall intensity (R_h) (mm/h), and WDR intensity (R_{wdr}) (mm/h) for each season

4.2. Data Cleaning Process – Generating In-Situ Dataset

As previously mentioned in Section 3.3.4, principles derived from the literature review as well as the Normality test and Outlier test are performed as the primary data cleaning approach of this research.

Below are the principles that govern the process:

- i. To select reliable meteorological data, the guidelines presented in Section 3.3.1 are followed for all 93 rain events. In compliance with the guideline:
 - No rain events characterised by reference wind-speed values greater than 10 m/s were recorded to be excluded,
 - There are 8 events with horizontal rainfall intensities greater than 20 mm/h to be excluded, including: May 10th (season 1); August 11th (season 2); November 15th, December 9th, January 23rd 24th 25th, 26th (season 4).
- ii. Normality Test and Outlier Test through IBM SPSS Statistic 26 software – It was observed that WDR intensity values (R_{wdr}) less than 1 mm/h were among the detected outliers by the software. Therefore, all the measurements below this detection threshold were disregarded. Consequently, the results are as follows:
 - in total, 19 events as outliers were detected and excluded from the datasets as April 25th, 29th, 30th of (season 1); June 17th (season 2); October 12th, 16th, 24th, 25th, November 6th (season 3); November 24th, December 13th, January 3rd, February 4th, 5th, 15th, 18th, 19th, 22nd, 23rd (season 4). Figure 4.10 to Figure 4.13 show graphs of the normal distribution of datasets (after eliminating the outliers) through the Normal Q-Q (quantile-quantile) plot, the box plot, and the Shapiro-Wilk Test of variables including wind speed (U), rainfall intensity (R_h), and WDR intensity (R_{wdr}) analysis for each season, respectively (see Table 4.3 to Table 4.6).

4.2.1. Data Cleaning Process – Season 1

In Shapiro-Wilk's test ($\text{Sig} > 0.05$), the p-values of 0.045 (~ 0.05), 0.93, and 0.47 for U, R_h , and R_{wdr} are equal to or greater than 0.05, which implies that it is acceptable to assume that the distribution of variables is approximately normal in the season 1 dataset (Table 4.3). A visual inspection of their normal Q-Q plot and box plot graphs (Figure 4.10) shows that the variables were approximately normally distributed with a skewness ($-2 < \text{Sk} (0.806 \& 0.456 \& -0.747) < 2$) and kurtosis ($-4 < K (1.237 \& 0.426 \& 2.322) < 4$) within the acceptable range.

Table 4.3. Normality tests processing and standard error summary of validated cases in season one (10 out of 14 cases (71%) were accepted)

Case Processing Summary – Season 1

	Valid		Missing		Total	
	N	Percent	N	Percent	N	Percent
U	10	100.0%	0	0.0%	10	100.0%
R_h	10	100.0%	0	0.0%	10	100.0%
R_{wdr}	10	100.0%	0	0.0%	10	100.0%

Description

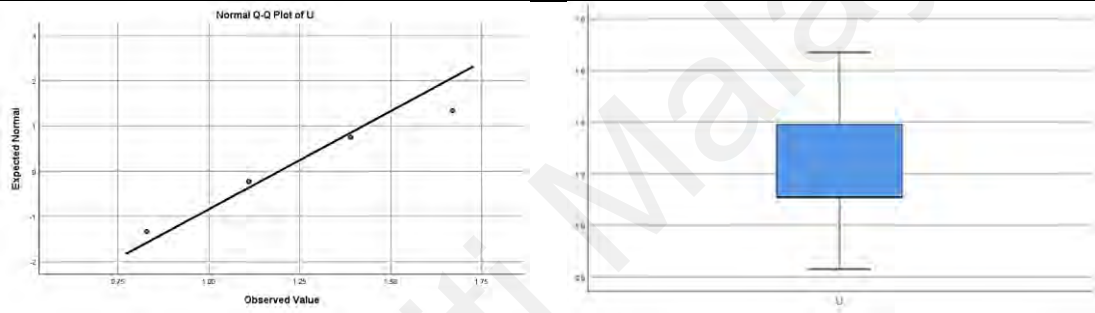
		Statistic	Std. Error
U	Mean	1.1940	0.07290
	Std. Deviation	0.23052	
	Minimum	0.83	
	Maximum	1.67	
	Skewness	0.806	0.687
	Kurtosis	1.237	1.334
R_h	Mean	10.5850	0.81133
	Std. Deviation	2.56565	
	Minimum	6.65	
	Maximum	15.60	
	Skewness	0.456	0.687
	Kurtosis	0.426	1.334
R_{wdr}	Mean	26.5850	3.64508
	Std. Deviation	11.52675	
	Minimum	1.56	
	Maximum	45.91	
	Skewness	-0.747	0.687
	Kurtosis	2.322	1.334

Tests of Normality – Shapiro-Wilk

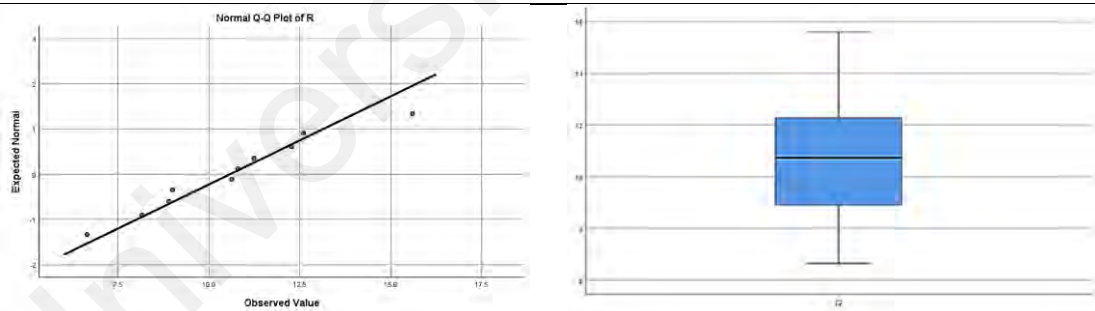
	Statistic	df	Sig.
U	0.841	10	0.045
R_h	0.975	10	0.932
R_{wdr}	0.932	10	0.470

The standard error ($-1.96 < SE (0.07 \text{ \& } 0.81) < 1.96$) values of variables U and R_h are in the acceptable range, and the higher value for R_{wdr} (3.6) in this test can be explained as the result of a small sample size, a high statistic mean of 26.5, and a standard deviation of 11.5. Thus, it is practically convincible to have a higher SE of 3.6 because it is inversely proportional to the sample size, meaning that smaller samples tend to produce greater standard errors. Here, it only shows the sample mean distribution is barely symmetrical around the population mean, but normally distributed, as the test results declare.

U



R_h



R_{wdr}

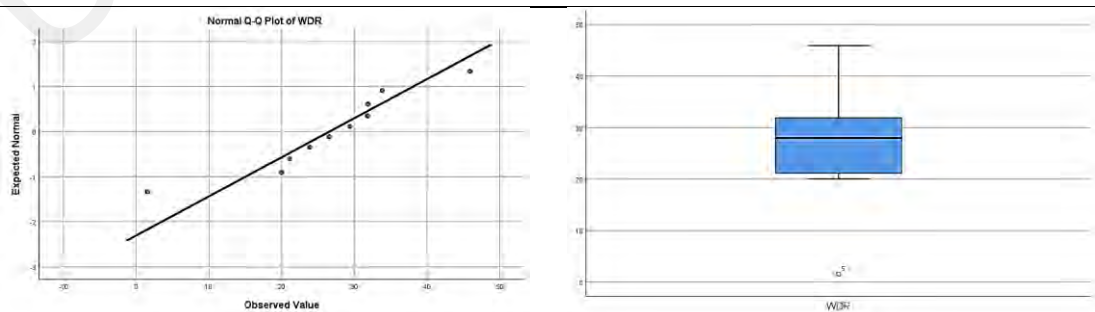


Figure 4.10. Q-Q plot and box plot graphs of wind (U), horizontal rainfall intensity (R_h), and WDR intensity (R_{wdr}) in season one

SPSS marks any outlier with a circle. Far outliers or extreme outliers, which are more likely to be true outliers, it marks with a star.

In this study, all the extreme outliers are excluded, but the outliers with circle marks remained on the condition that the Q-Q plot, skewness and kurtosis, Shapiro-Wilk's test, and standard errors are within the acceptable range to keep the sample size as large as possible for the model validation. Accordingly, here case number 5 (April 28th) is retained for model validation purposes (see Figure 4.10).

4.2.2. Data Cleaning Process – Season 2

Table 4.4. Normality tests processing and standard error summary of validated cases in season two (20 out of 22 cases (90%) were accepted)

Case Processing Summary – Season 2

	Valid		Missing		Total	
	N	Percent	N	Percent	N	Percent
U	20	100.0%	0	0.0%	20	100.0%
R _h	20	100.0%	0	0.0%	20	100.0%
R _{wdr}	20	100.0%	0	0.0%	20	100.0%

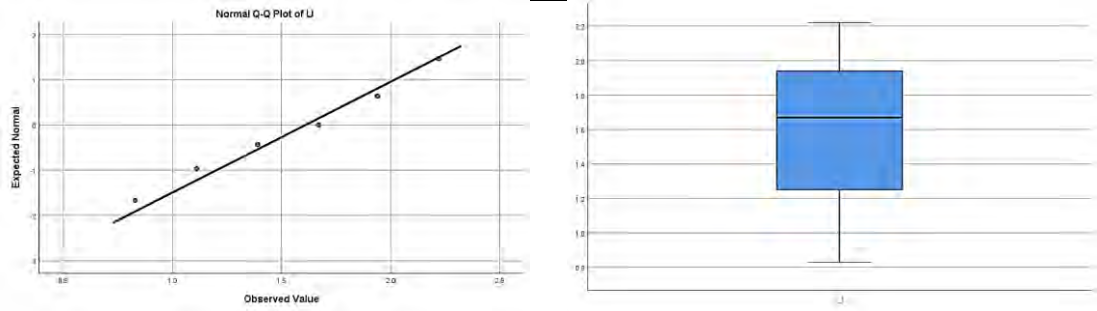
Description

		Statistic	Std. Error
U	Mean	1.6100	0.09127
	Std. Deviation	0.40818	
	Minimum	0.83	
	Maximum	2.22	
	Skewness	-0.289	0.512
	Kurtosis	-1.001	0.992
R _h	Mean	4.3570	0.74047
	Std. Deviation	3.31150	
	Minimum	0.40	
	Maximum	12.35	
	Skewness	0.947	0.512
	Kurtosis	0.408	0.992
R _{wdr}	Mean	18.5060	2.83512
	Std. Deviation	12.67906	
	Minimum	1.25	
	Maximum	48.29	
	Skewness	0.839	0.512
	Kurtosis	0.454	0.992

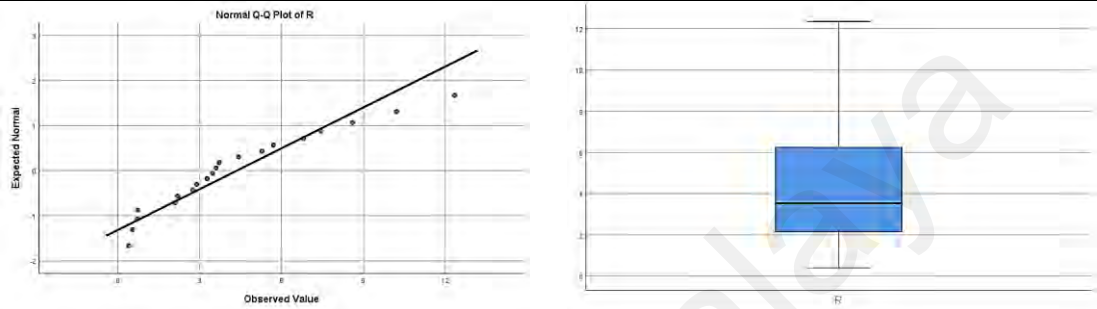
Tests of Normality - Shapiro-Wilk

	Statistic	df	Sig.
U	0.922	20	0.110
R _h	0.918	20	0.090
R _{wdr}	0.929	20	0.150

U



R_h



R_{wdr}

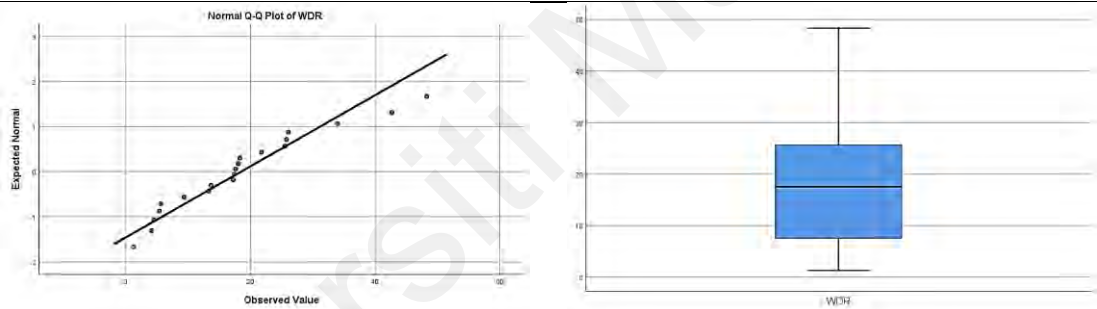


Figure 4.11. Q-Q plot and box plot graphs of wind (U), horizontal rainfall intensity (R_h), and WDR intensity (R_{wdr}) in season two

In Shapiro-Wilk's test ($\text{Sig} > 0.05$), the p-values of 0.11, 0.09, and 0.15 for U, R_h, and R_{wdr} are greater than 0.05, which implies that it is acceptable to assume that the distribution of variables is approximately normal in the season 2 dataset (Table 4.4).

A visual inspection of their normal Q-Q plot and box plot graphs (Figure 4.11) shows that the variables were approximately normally distributed with a skewness ($-2 < \text{Sk} (-0.289 \text{ \& } 0.947 \text{ \& } 0.839) < 2$) and kurtosis ($-4 < K (-1.001 \text{ \& } 0.408 \text{ \& } 0.454) < 4$) within the acceptable range (Table 4.4). The standard error ($-1.96 < \text{SE} (0.09 \text{ \& } 0.7) < 1.96$) values of variables U and R_h are in the acceptable range, and the higher value for R_{wdr} (2.8) in

this test can be explained as the result of a small sample size, a high statistic mean of 18.5, and a standard deviation of 12.6. It is practically convincible to have a higher SE of 2.8 because it is inversely proportional to the sample size, meaning that smaller samples tend to produce greater standard errors. Here, it only shows the sample mean distribution is barely symmetrical around the population mean, but normally distributed, as the test results declare.

4.2.3. Data Cleaning Process – Season 3

Table 4.5. Normality tests processing and standard error summary of validated cases in season three (8 out of 13 cases (61%) were accepted)

Case Processing Summary – Season 3

	Valid		Missing		Total	
	N	Percent	N	Percent	N	Percent
U	8	100.0%	0	0.0%	8	100.0%
R _h	8	100.0%	0	0.0%	8	100.0%
R _{wdr}	8	100.0%	0	0.0%	8	100.0%

Description

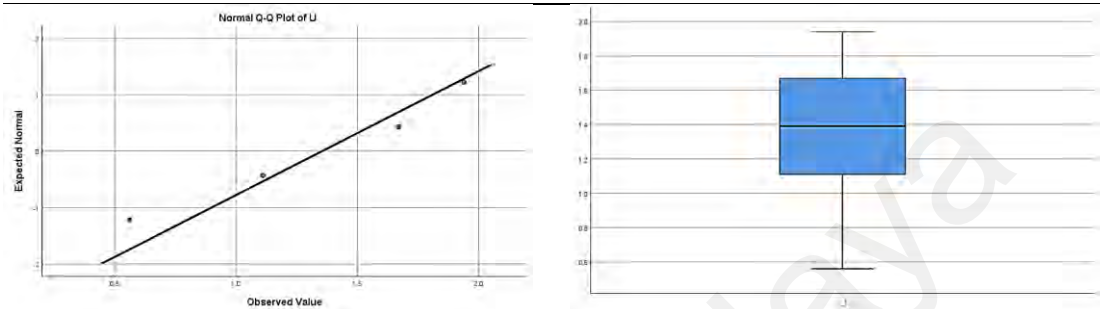
		Statistic	Std. Error
U	Mean	1.3550	0.16102
	Std. Deviation	0.45544	
	Minimum	0.56	
	Maximum	1.94	
	Skewness	-0.509	0.752
	Kurtosis	-0.462	1.481
R _h	Mean	12.2862	1.80978
	Std. Deviation	5.11884	
	Minimum	6.43	
	Maximum	18.95	
	Skewness	0.245	0.752
	Kurtosis	-1.967	1.481
R _{wdr}	Mean	18.9063	2.84849
	Std. Deviation	8.05676	
	Minimum	5.55	
	Maximum	29.83	
	Skewness	-0.451	0.752
	Kurtosis	-0.629	1.481

Tests of Normality - Shapiro-Wilk

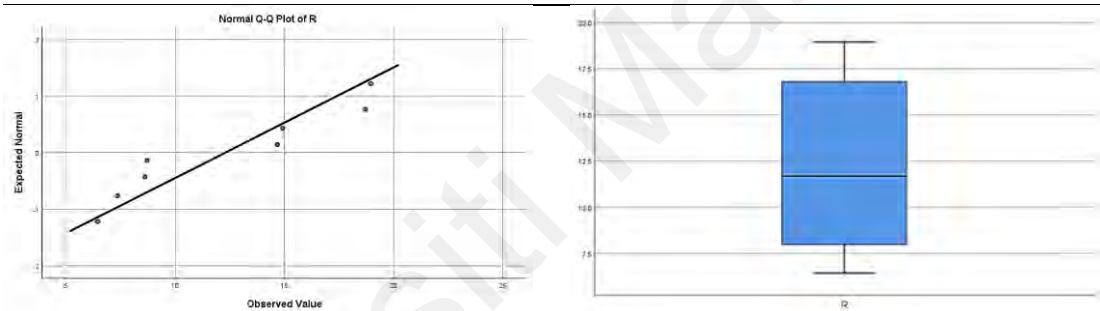
	Statistic	df	Sig.
U	0.898	8	0.276
R _h	0.867	8	0.142
R _{wdr}	0.969	8	0.887

In Shapiro-Wilk's test ($\text{Sig} > 0.05$), the p-values of 0.27, 0.14, and 0.88 for U, R_h , and R_{wdr} are greater than 0.05, which implies that it is acceptable to assume that the distribution of variables is normal in the season 3 dataset (Table 4.5).

U



R_h



R_{wdr}

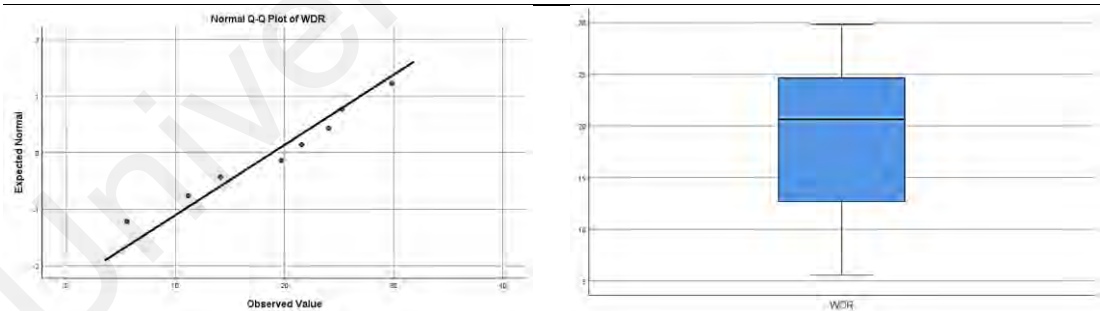


Figure 4.12. Q-Q plot and box plot graphs of wind (U), horizontal rainfall intensity (R_h), and WDR intensity (R_{wdr}) in season three

A visual inspection of their normal Q-Q plot and box plot graphs (Figure 4.12) shows that the variables were normally distributed with a skewness ($-2 < Sk (-0.509 \text{ \& } 0.245 \text{ \& } -0.451) < 2$) and kurtosis ($-4 < K (-0.462 \text{ \& } -1.967 \text{ \& } -0.629) < 4$) within the acceptable range (Table 4.5). The standard error ($-1.96 < SE (0.16 \text{ \& } 1.8) < 1.96$) values of variables

U and R_h are in the acceptable range. The higher value for R_{wdr} (2.8) in this test can be explained as the result of a small sample size, a high statistic mean of 18.9, and standard deviation of 8.05. It is practically convincible to have a higher SE of 2.8 because it is inversely proportional to the sample size, meaning that smaller samples tend to produce greater standard errors.

Here, it only shows the sample mean distribution is barely symmetrical around the population mean, but normally distributed, as the test results declare.

4.2.4. Data Cleaning Process – Season 4

Table 4.6. Normality tests processing and standard error summary of validated cases in season four (28 out of 44 cases (63%) were accepted)

Case Processing Summary – Season 4

	Valid		Missing		Total	
	N	Percent	N	Percent	N	Percent
U	28	100.0%	0	0.0%	28	100.0%
R_h	28	100.0%	0	0.0%	28	100.0%
R_{wdr}	28	100.0%	0	0.0%	28	100.0%

Description

		Statistic	Std. Error
U	Mean	1.1504	0.07097
	Std. Deviation	0.37553	
	Minimum	0.56	
	Maximum	1.94	
	Skewness	0.302	0.441
	Kurtosis	-0.298	0.858
R_h	Mean	8.8104	0.84300
	Std. Deviation	4.46074	
	Minimum	1.32	
	Maximum	15.83	
	Skewness	0.068	0.441
	Kurtosis	-1.037	0.858
R_{wdr}	Mean	27.4386	3.48290
	Std. Deviation	18.42977	
	Minimum	4.31	
	Maximum	70.52	
	Skewness	0.715	0.441
	Kurtosis	-0.095	0.858

Tests of Normality - Shapiro-Wilk

	Statistic	df	Sig.
U	0.922	28	0.040
R_h	0.953	28	0.233
R_{wdr}	0.931	28	0.064

In Shapiro-Wilk's test ($\text{Sig} > 0.05$), the p-values of 0.04 (~ 0.05), 0.23, and 0.06 for U , R_h , and R_{wdr} are almost equal or greater than 0.05, which implies that it is acceptable to assume that the distribution of variables is approximately normal in the season 4 dataset (Table 4.6). A visual inspection of their normal Q-Q plot and box plot graphs (Figure 4.13) shows that the variables were approximately normally distributed with a skewness ($-2 < \text{Sk}$ (0.302 & 0.068 & 0.715) < 2) and kurtosis ($-4 < K$ (-0.298 & -1.037 & -0.095) < 4) within the acceptable range (Table 4.6).

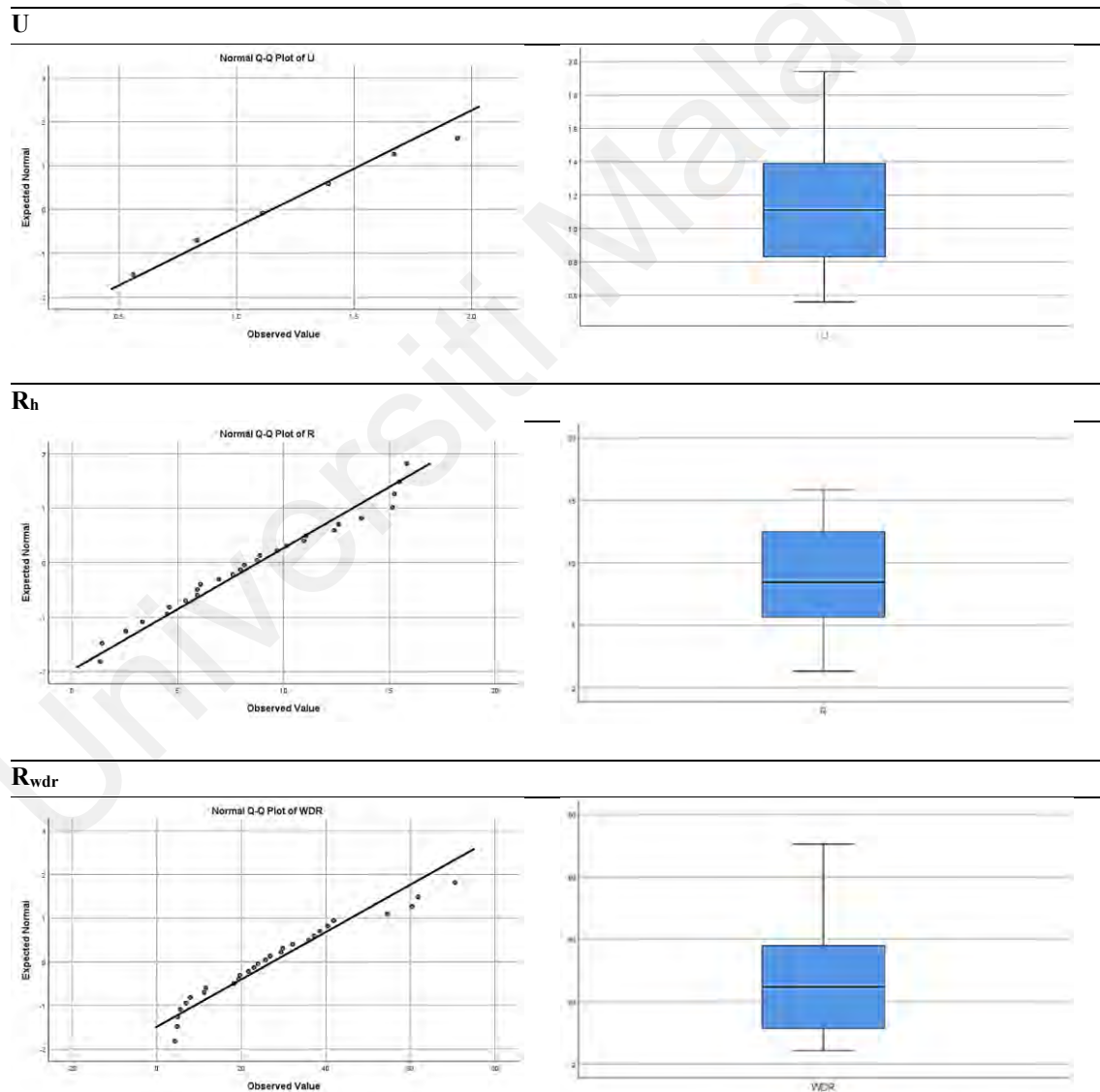


Figure 4.13. Q-Q plot and box plot graphs of wind (U), horizontal rainfall intensity (R_h), and WDR intensity (R_{wdr}) in season four

The standard error ($-1.96 < SE (0.07 \text{ \& } 0.84) < 1.96$) values of variables U and R_h are in the acceptable range, and the higher value for WDR (3.4) in this test can be explained as the result of a small sample size, a high statistic mean of 27.4, and a standard deviation of 18.4. It is practically convincible to have a higher SE of 3.4 because it is inversely proportional to the sample size, meaning that smaller samples tend to produce greater standard errors. Here, it only shows the sample mean distribution is barely symmetrical around the population mean, but normally distributed, as the test results declare.

4.3. Spatial Distribution of Wind-Driven Rain – Catch Ratio (η) Calculation

The spatial distribution of WDR on the building façade is analysed in this section, taking into account the catch ratio (η) values and building height factors. The plots of spatial WDR distribution during the one-year monitoring period on the pilot building walls at UM campus, are shown in Figure 4.14,

Figure 4.16, Figure 4.18, and Figure 4.20. A combined graph illustrating the average daily WDR catch ratio (η) by each WDR gauge and average daily horizontal rainfall intensity (R_h) during each tropical season is presented in Figure 4.15, Figure 4.17, Figure 4.19, and Figure 4.21, respectively.

4.3.1. WDR Catch Ratio (η) – Season 1

During season 1, as mentioned in Section 4.1.1, the wind direction is mainly from NW to SW. As illustrated in Figure 4.15 and Table 4.7, the catch ratio values on windward façades are on average higher at the top gauges, which indicates that the corners and edges receive the higher amount of rain. The values of average catch ratio vary from 1.43 to 3.64, and 1.14 to 4.40, at the top and bottom locations, respectively. The catch ratio values and hence the amount of harvested WDR from the building façade (Section 4.1.1) vary with locations (Figure 4.14). The spatial distribution of WDR on windward façades follows the classical wetting pattern of building façades, however, the total average daily

catch ratio values for the top and bottom gauges on all façades are almost equal; 10.29 for the top and 10.94 for the bottom gauges in the season 1 (Table 4.7).

Universiti Malaya

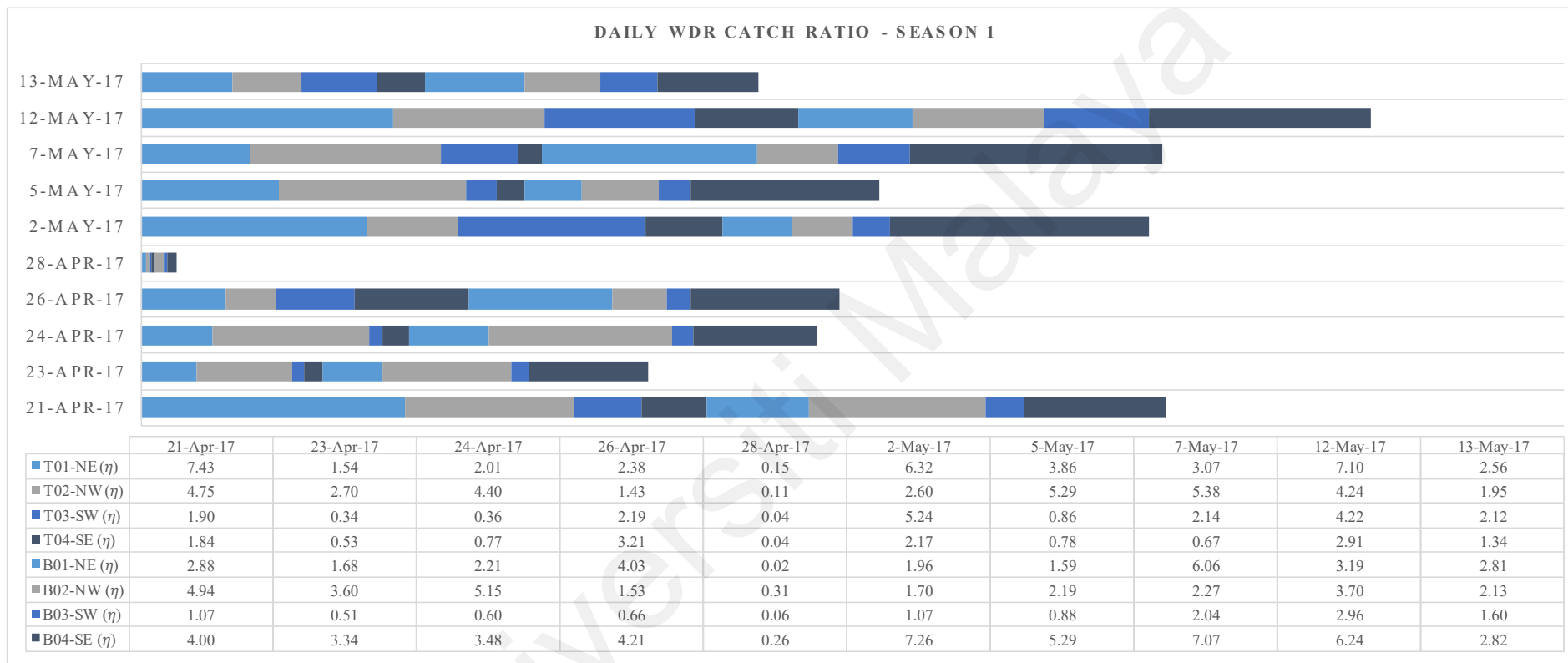


Figure 4.14. Catch ratio values (η) at WDR gauge locations for the entire monitoring period of season 1

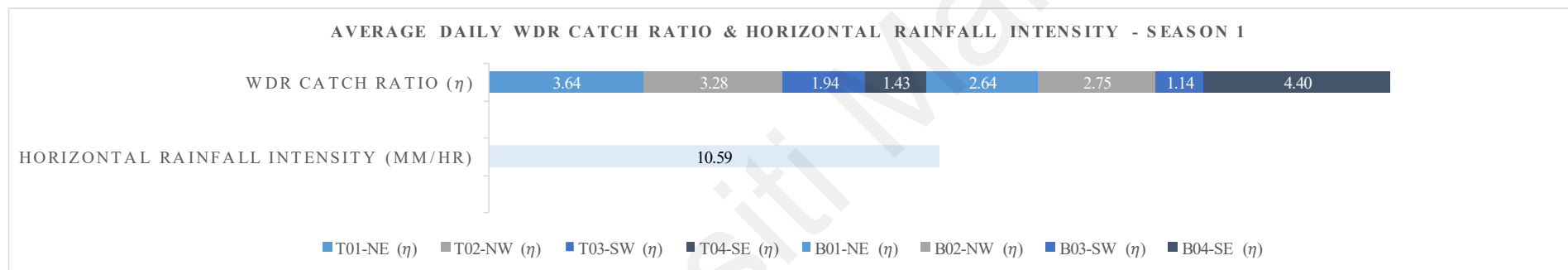


Figure 4.15. Average daily WDR catch ratio (η) and horizontal rainfall intensity (R_h) values at driving rain gauge locations based on the entire monitoring period of season 1

Table 4.7. Average daily WDR catch ratio values (η) at driving rain gauge locations based on the entire monitoring period of season 1

	NE	NW	SW	SE	TOTAL
Top	3.64	3.28	1.94	1.43	10.29
Bottom	2.64	2.75	1.14	4.40	10.94
TOTAL	6.29	6.04	3.08	5.82	21.23

4.3.2. WDR Catch Ratio (η) – Season 2

During Season 2, as mentioned in Section 4.1.2, the wind direction is mainly from NW to SW.

Figure 4.16 and Figure 4.17 illustrate the catch ratio values (η) of all eight WDR gauges for the entire monitoring period of season 2 in daily and average daily distribution patterns. On the windward façade NW, the average daily catch ratio value (η) for the top gauge (11.99) is the highest among all top gauges and higher than the bottom gauge value (10.04) on the façade, which indicates that the corners and edges receive the higher amount of rain. Taking into account excluding two large rain events of this season during data cleaning process, the lower average value of the catch ratio (η) for SW façade is explainable (Table 4.8).

The values of average catch ratio (η) vary from 2.56 to 11.99, and 3.34 to 10.39, at the top and the bottom locations, respectively. The catch ratio values (η) and hence the amount of harvested WDR from the building façade (Section 4.1.2) vary with locations (Figure 4.16). The spatial distribution of WDR on NW as windward façade and also NE and SE façades follows the classical wetting pattern of building façades. However, the total average values are slightly against the classical pattern; 31.12 for the top and 33.82 for the bottom gauges (Table 4.8), which is justifiable based on the data cleaning exclusions as interpreted in the previous paragraph.

Table 4.8. Average daily WDR catch ratio (η) values at driving rain gauge locations based on the entire monitoring period of season 2

	NE	NW	SW	SE	TOTAL
Top	10.21	11.99	2.56	6.36	31.12
Bottom	10.39	10.04	10.05	3.34	33.82
TOTAL	20.60	22.03	12.61	9.70	64.94

Universiti Malaya

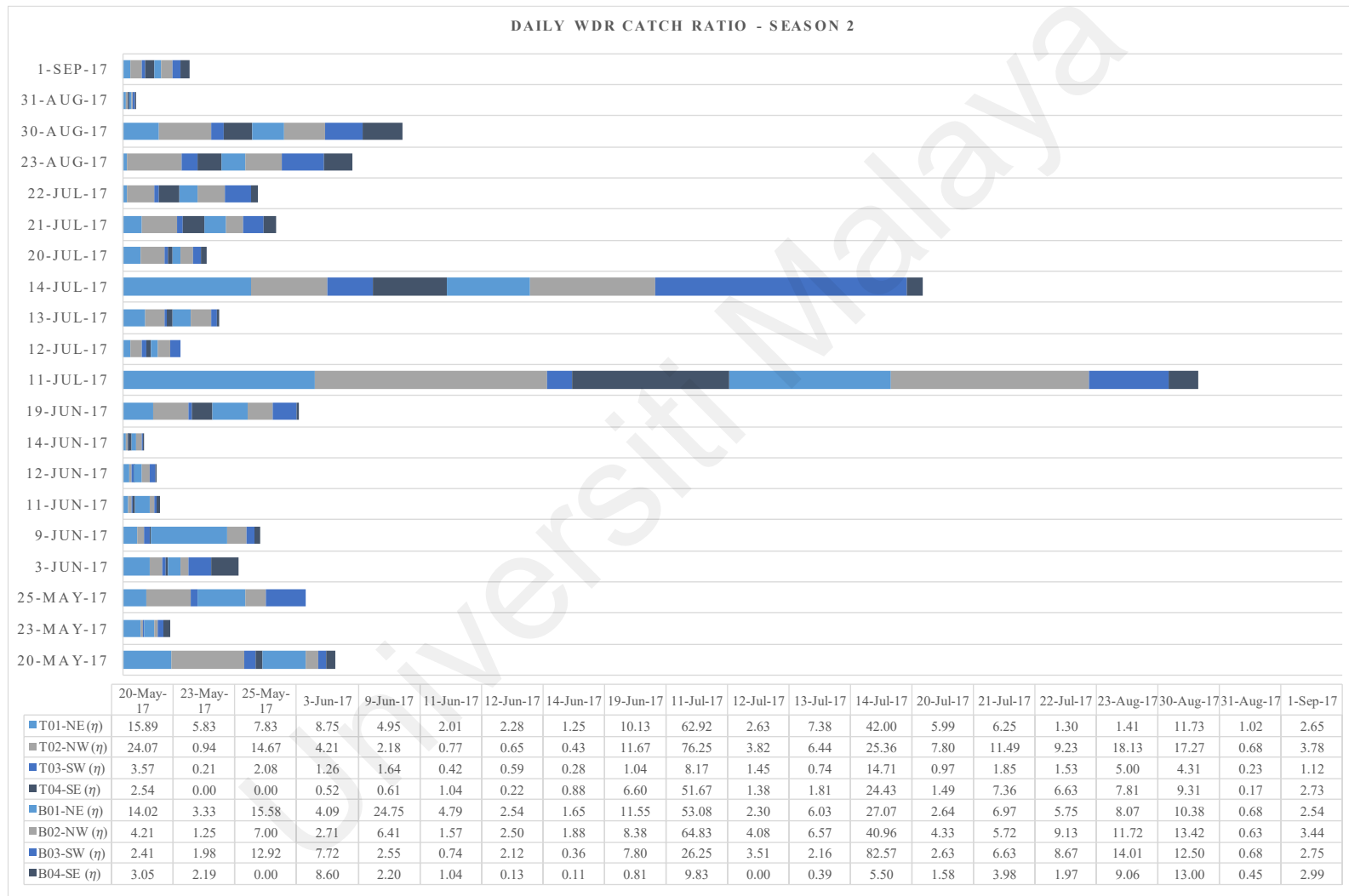


Figure 4.16. Catch ratio values (η) at WDR gauge locations for the entire monitoring period of season 2

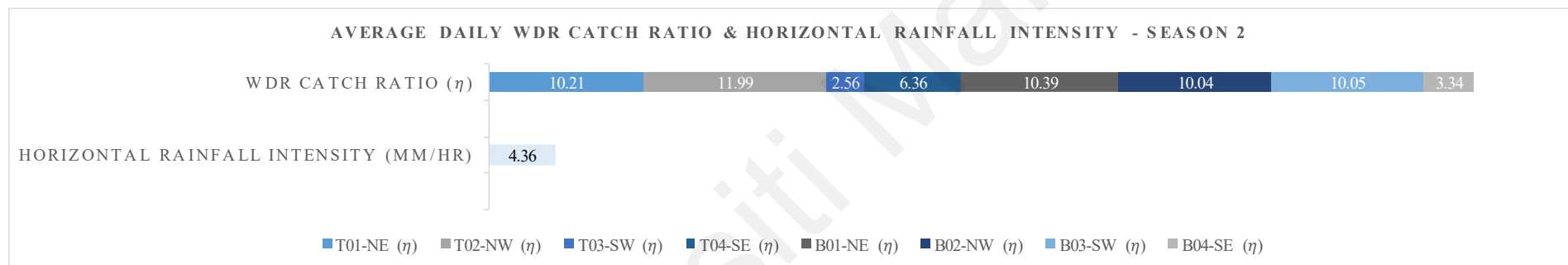


Figure 4.17. Average daily WDR catch ratio (η) and horizontal rainfall intensity (R_h) values at driving rain gauge locations based on the entire monitoring period of season 2

4.3.3. WDR Catch Ratio (η) – Season 3

Season 3 is the shortest season with the lowest rain events. As mentioned in Section 4.1.3, its prevailing wind direction is mostly from the West fluctuating from NW to SW. Figure 4.18 and Figure 4.19 illustrate the catch ratio values (η) of all eight WDR gauges for the entire monitoring period of season 3 in daily and average daily distribution patterns. On the windward façade NW, the average daily catch ratio value (η) for the top gauge (2.31) is the highest compared to the values of the top gauges on other façades. It is also higher than the bottom gauge value (1.81). The SW façade, as the second highest catch ratio value (η), has almost equal values for both the top (1.54) and the bottom (1.92) on the façade.

As illustrated in Figure 4.19 and Table 4.9, the values of average catch ratio (η) vary from 1.54 to 2.31, and 1.79 to 1.92, at the top and bottom locations respectively. The catch ratio values (η) and hence the amount of harvested WDR from the building façade (Section 4.1.3) vary with locations (Figure 4.18). The spatial distribution of WDR on windward façade NW follows the classical wetting pattern of building façades, however, the total average catch ratio values (η) for the top (7.09) and the bottom (7.37) gauges on all façades are almost equal, with a slight difference, do not follow the classical pattern in this season, same as in season 1 (Table 4.9).

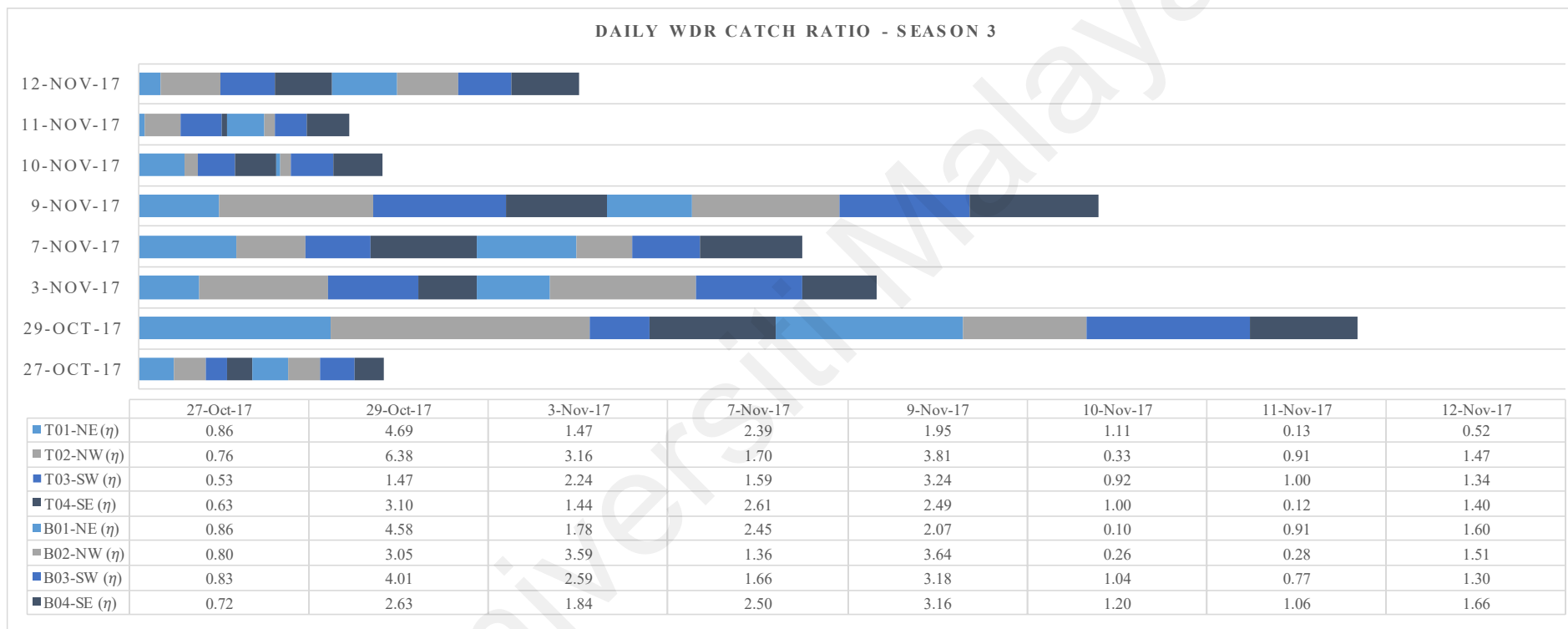


Figure 4.18. Catch ratio values (η) at WDR gauge locations for the entire monitoring period of season 3

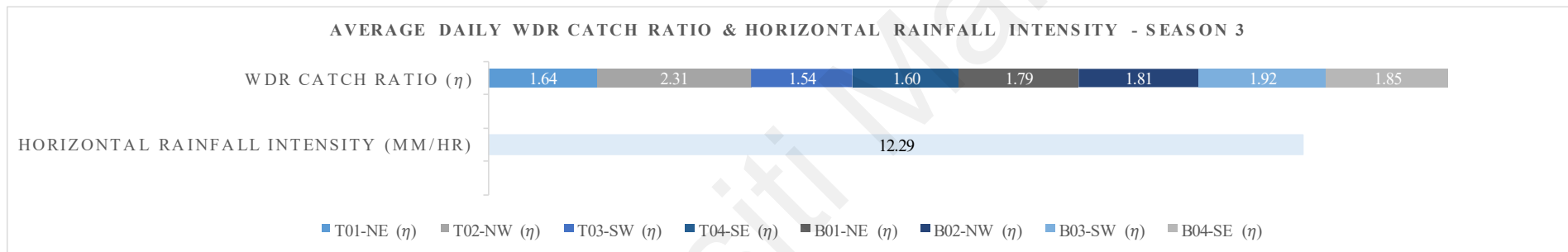


Figure 4.19. Average daily WDR catch ratio (η) and horizontal rainfall intensity (R_h) values at driving rain gauge locations based on the entire monitoring period of season 3

Table 4.9. Average daily WDR catch ratio values (η) at driving rain gauge locations based on the entire monitoring period of season 3

	NE	NW	SW	SE	TOTAL
Top	1.64	2.31	1.54	1.60	7.09
Bottom	1.79	1.81	1.92	1.85	7.37
TOTAL	3.43	4.13	3.46	3.44	14.47

4.3.4. WDR Catch Ratio (η) – Season 4

Season 4 is the longest season with the largest rain events. As mentioned in Section 4.1.4, its prevailing wind direction is mostly NE and NW, and in short periods, it switches to the SW. Figure 4.20 and Figure 4.21 illustrate the catch ratio values (η) of all eight WDR gauges for the entire monitoring period of season 4 in daily and average daily distribution patterns. Table 4.10 shows that windward façades NW (9.68), NE (6.96), and SW (6.70) have the highest average daily catch ratio values (η), respectively. On all of these façades, the catch ratio values (η) for the top gauges are higher or equal to the bottom values.

As illustrated in Figure 4.21 and Table 4.10, the values of average catch ratio (η) vary from 2.84 to 5.36, and 3.04 to 4.32, at the top and bottom locations, respectively. The catch ratio values (η) and hence the amount of harvested WDR from the building façade (Section 4.1.4) vary with locations (Figure 4.20). The spatial distribution of WDR on all windward façades follows the classical wetting pattern of building façades (Table 4.10).

Table 4.10. Average daily WDR catch ratio values (η) at driving rain gauge locations based on the entire monitoring period of season 4

	NE	NW	SW	SE	TOTAL
Top	3.48	5.36	3.43	2.84	15.10
Bottom	3.48	4.32	3.27	3.04	14.12
TOTAL	6.96	9.68	6.70	5.88	29.22

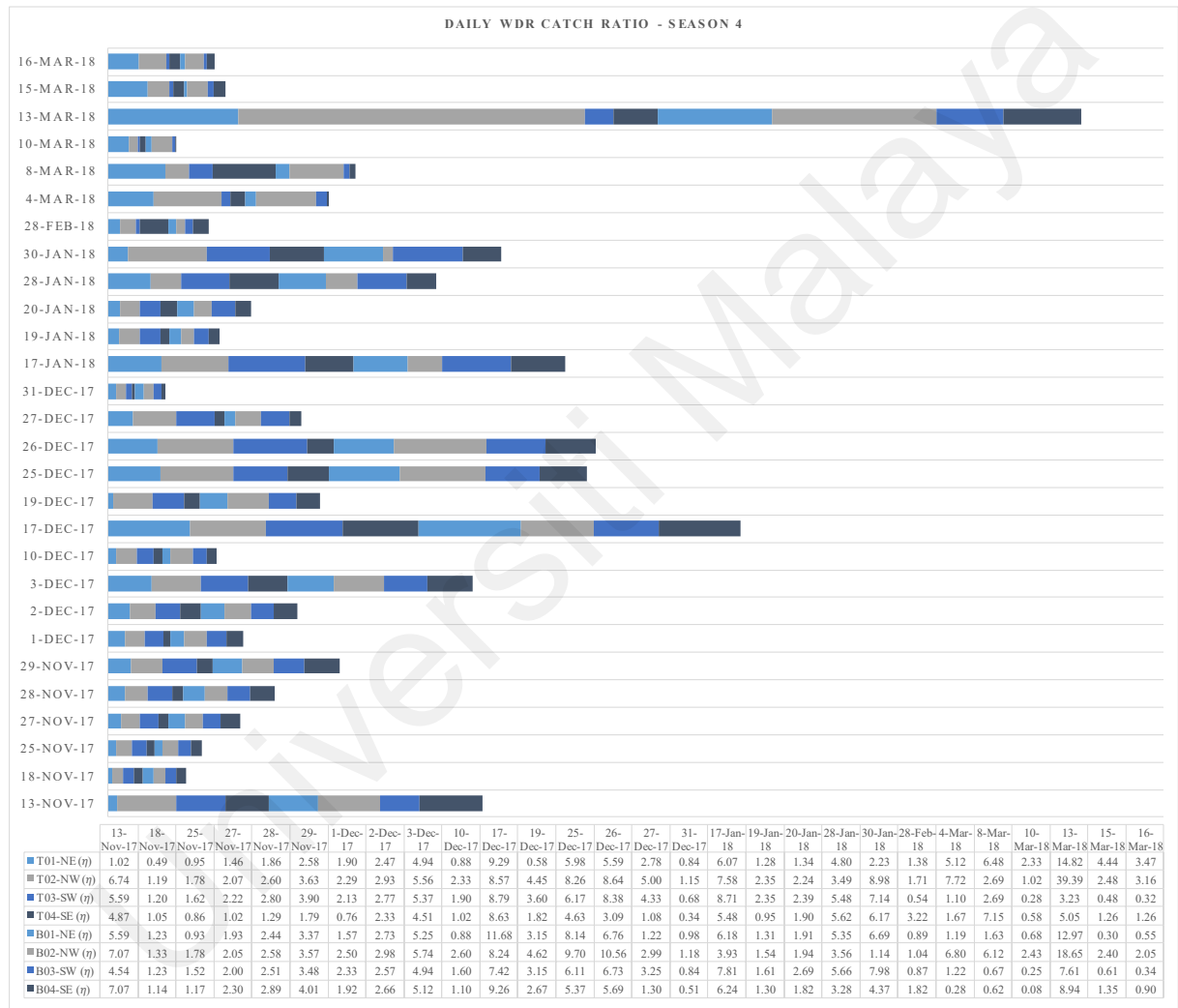


Figure 4.20. Catch ratio values (η) at WDR gauge locations for the entire monitoring period of season 4

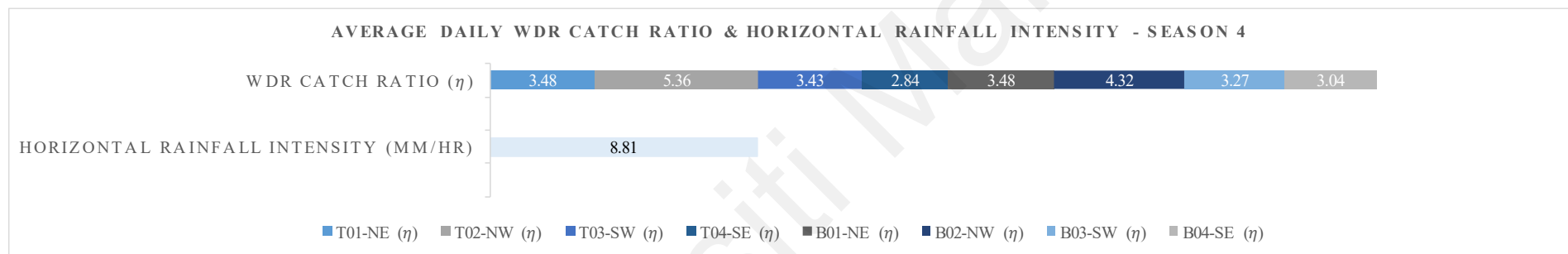


Figure 4.21. Average daily WDR catch ratio (η) and horizontal rainfall intensity (R_h) values at driving rain gauge locations based on the entire monitoring period of season 4

4.3.5. WDR Catch Ratio (η) As a Function of Wind Speed (U) and Height (H)

The comparative analyses of WDR catch ratio showed that the distribution of WDR catch ratios on building façades is significantly influenced by wind speed (U). In this section, correlation analysis is conducted between catch ratio value (η) and wind speed for all windward façades that were calculated and discussed during catch ratio analyses (Sections 4.3.1 to 4.3.4) for each season and different height locations; one for windward top gauges and one for windward bottom gauges. The coefficient of determination (R-squared (R^2)) between wind speed (U) and catch ratio (η) of top and bottom locations is generated to explore how catch ratio value (η) varies with wind speed.

Figure 4.22 illustrates the correlation results, including R^2 values and trendlines. The relationships between variables R^2 and U were analysed using third-order polynomial (cubic polynomial) regressions.

When values rise or fall at increasingly higher rates and the straight line is unable to capture the patterns in the data (standard linear regression), a higher order equation by adding powers of the original features as new features is generated, i.e., a linear polynomial regression model. A polynomial regression fits a curved relationship between the response variable and predictors using higher-order predictor values, but it is linear in terms of the parameters [it involves multiple powers of an initial predictor] (Huang & He, 2024) Eq. (14).

$$Y = \beta_0 + \beta_1 X + \beta_2 X^2 + \dots + \beta_n X^n + b \quad \text{Eq. (14)}$$

This is still considered a linear model, as the coefficients associated with the features are still linear; x^2 is only a feature. However, the curve that we are fitting is quadratic in nature. Selecting the optimum degree for a polynomial regression comes down to

balancing the model's complexity with its explanatory power. The best model is one that accomplishes the desired level of explanation or prediction with as few predictor variables as possible (Kiernan, 2014). In this section, third-order (third-degree) describes the optimum order with the fewest variables among other regression relationships (up to 6th order).

The main advantages of polynomial regression models include interpretability, parsimony, and prediction (Bates, 1988). In general, these models are capable of accommodating various mean functions and are easily interpretable due to the fact that the parameters can be associated with meaningful factors.

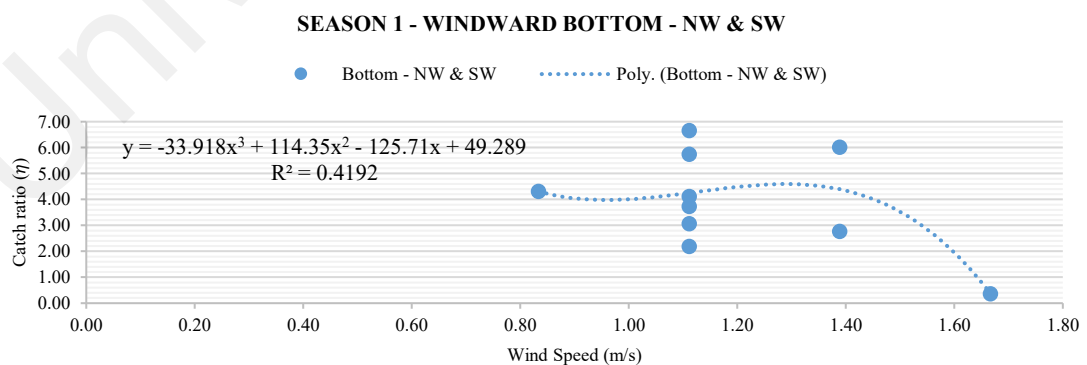
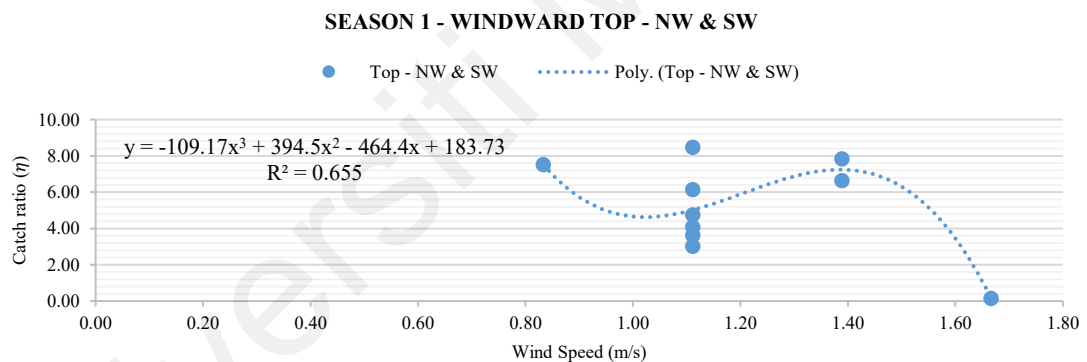
To choose an optimal model to generate reliable R^2 , different orders from 2 to 6 were tested. It was quite clear from the plots that the quadratic curve (order 2) was able to fit the data better than the linear line, and by fitting a cubic curve (order 3) to the dataset, it was seen that it passes through more data points than the quadratic and the linear plots. However, the higher-order model (up to 6) could pass through most of the data points but was generating insignificant differences with the cubic curve model in terms of R^2 value. Thus, in order to prevent over-fitting of the model that leads to failure to generalise on unseen data, in this section, a cubic curve (degree 3) was chosen to generate the coefficient of determination (R^2) to evaluate the correlation between wind (U) and WDR catch ratio (η).

The coefficient of determination (R^2) results (effect of wind (U) on WDR catch ratio (η)) and trendlines as shown in Figure 4.22 indicate that:

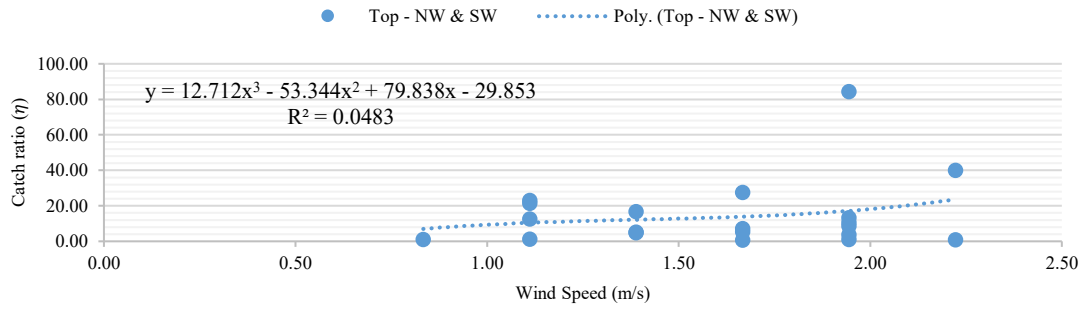
- i. In season 1, gauges on the windward façades of NW and SW have strong and moderate R^2 values for the top (0.65) and bottom (0.42) locations, respectively.

The variation in wind speed is more steady between 1 m/s to 1.2 m/s, and the catch ratio values are more fluctuating between 2 to 6,

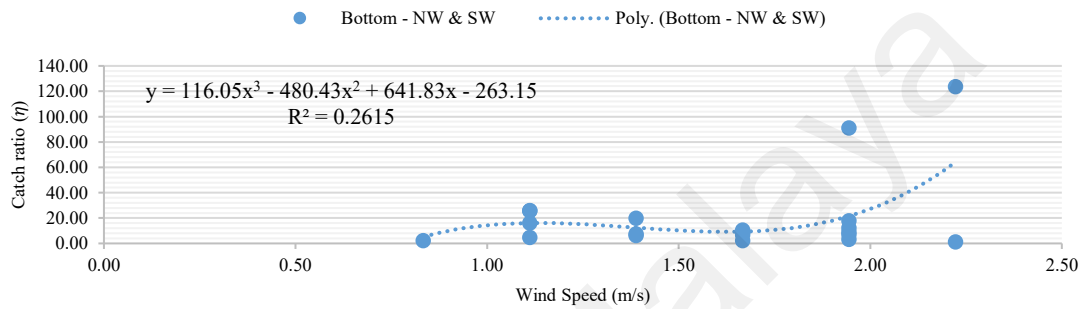
- ii. In season 2, the top gauges on the windward façades of NW and SW have the lowest R^2 value (0.04) among all the seasons, and the bottom gauges have a weak value (0.26). Wind speed in the majority of rain events is mostly between 1 m/s to 2 m/s and catch ratio values are under 20,
- iii. In season 3, gauges on the windward façades of NW and SW have the highest and relatively equal R^2 values for top (0.75) and bottom (0.77) locations among all the seasons, with a strong harmonic correlation. Wind speed and catch ratio values have the steadiest pattern with an ascending trendline. Same as in season 2, wind speed in the majority of rain events is mostly between 1 m/s to 2 m/s, but catch ratio values fluctuate between 1 to 8,



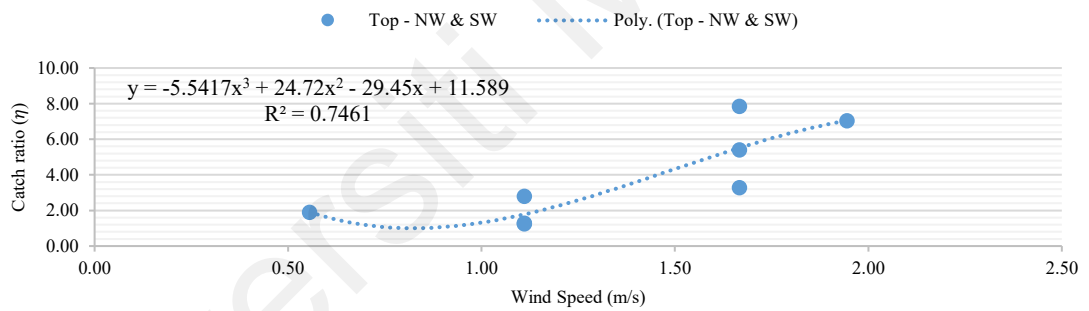
SEASON 2 - WINDWARD TOP - NW & SW



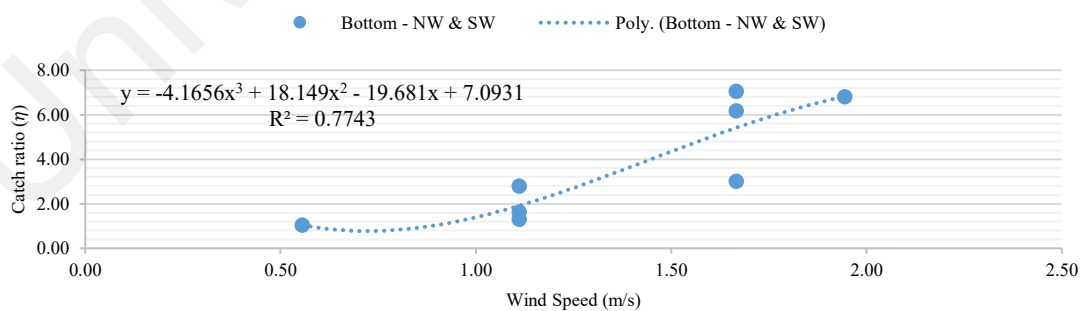
SEASON 2 - WINDWARD BOTTOM - NW & SW



SEASON 3 - WINDWARD TOP - NW & SW



SEASON 3 - WINDWARD BOTTOM - NW & SW



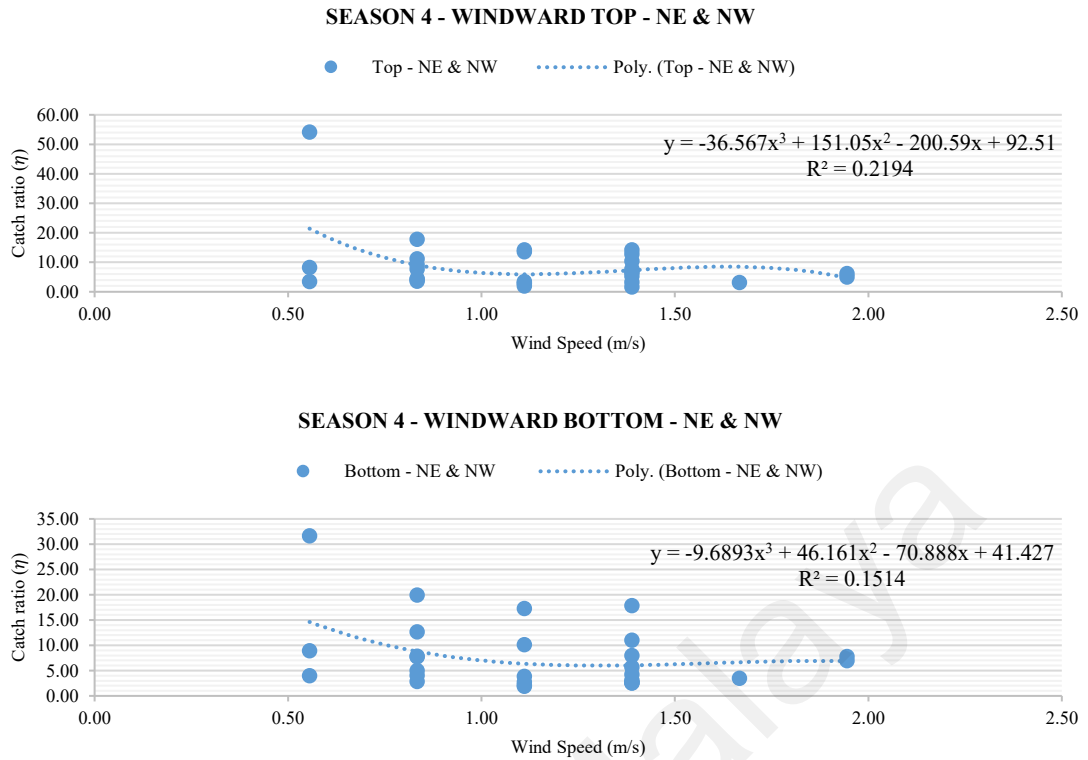


Figure 4.22. Coefficient of determination (R^2) analysis results between WDR catch ratio (η) on windward façades and wind speed (m/s) during season 1 to season 4 (The R^2 shown is based on cubic polynomial regression; $0.2 < \text{Value} < 0.4$ is weak, $0.4 < \text{Value} < 0.6$ is moderate, and $0.6 < \text{Value} < 0.8$ means strong effect on the catch ratio variable).

- iv. In season 4, the top gauges on the windward façades of NE and NW have a slightly higher R^2 value (0.22) than the bottom gauges (0.15), with a weak correlation in the opposite direction (descending trendline). Having the greatest number of rain events among all seasons, the majority of rain events have wind speed between 1 m/s to 2 m/s, the same as in seasons 2 and 3, and catch ratio values are mostly under 30.

4.3.6. WDR Catch Ratio (η) As a Function of Horizontal Rainfall Intensity (R_h) and Height (H)

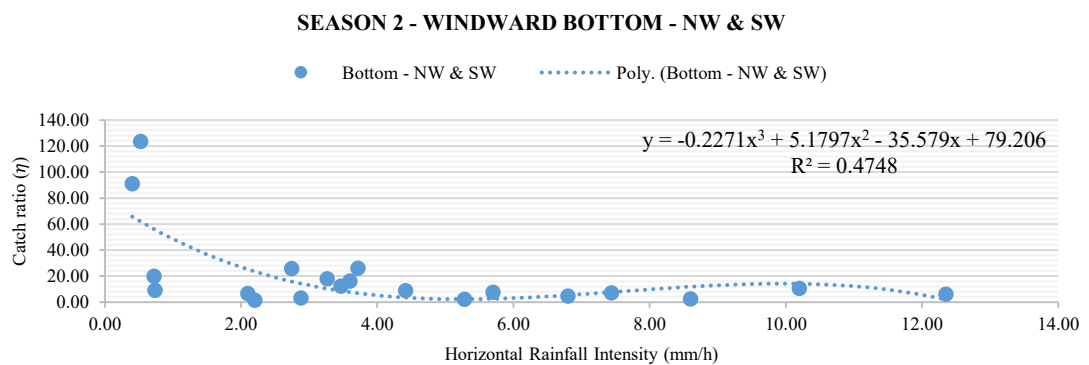
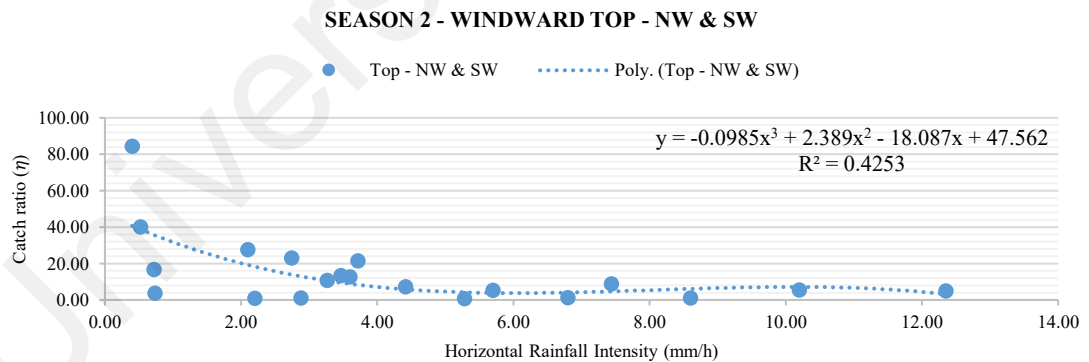
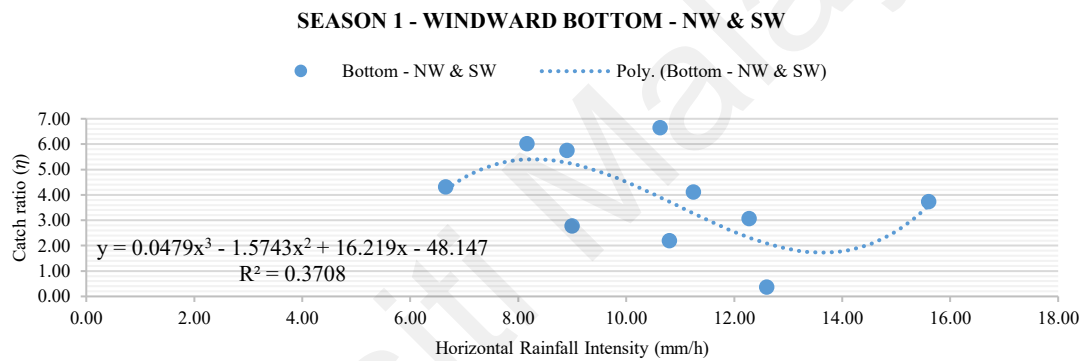
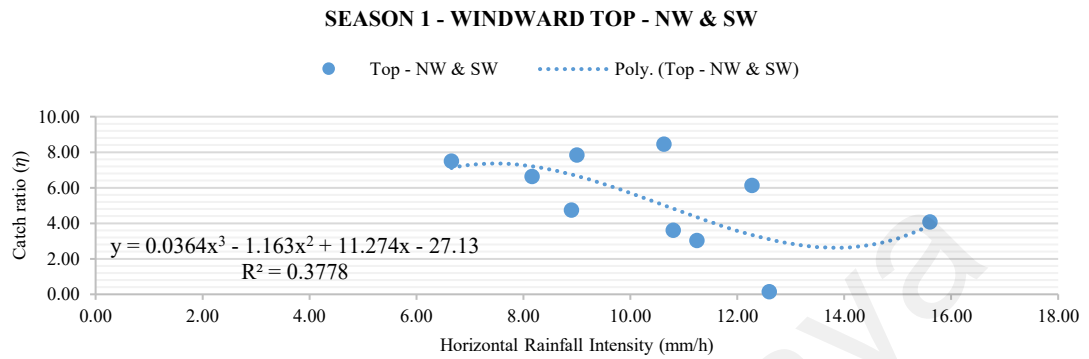
In this section, correlation analyses are conducted between catch ratio value (η) and horizontal rainfall intensity (R_h) to investigate how catch ratio value varies with horizontal rainfall intensity at different heights (top and bottom locations). Correlation

analysis is conducted between these two variables for all windward façades that were examined in the previous section (Section 4.3.5) for each season and in two parts; one for windward top gauges and one for windward bottom gauges, to compare the coefficient of determination, R-squared, between R_h and the catch ratio of top and bottom locations.

The coefficient of determination results, which show the effect of horizontal rainfall (R_h) on WDR catch ratio (η), along with the trendlines displayed in Figure 4.23, indicate the following:

- i. In season 1, the top gauges on the windward façades of NW and SW have almost equal R^2 values for the top (0.38) and the bottom gauges (0.37), with a relatively weak correlation. The variation in horizontal rainfall intensity is more steady between 8 to 12 mm/h, and catch ratio values are more fluctuating up to 8,
- ii. In season 2, gauges on the windward façades of NW and SW have almost equal R^2 values for the top (0.43) and bottom (0.47) locations, with a moderate correlation. Horizontal rainfall intensity in the majority of rain events is mostly between 2 mm/h to 6 mm/h, and catch ratio values are under 30,
- iii. In season 3, gauges on the windward façades of NW and SW have the highest R^2 values for top (0.77) and bottom (0.62) locations among all seasons, with a strong correlation. Horizontal rainfall intensities and catch ratio values have the steadiest pattern with a descending trendline. Both parameters show a fluctuating pattern throughout the season in a great range of 5 mm/h to 10 mm/h and up to 8 for horizontal rainfall intensity and catch ratio value, respectively, with the least number of rain events among all seasons,
- iv. In season 4, the top gauges on the windward façades of NE and NW have twice the R^2 value (0.39) of the bottom gauges (0.20), with a relatively weak correlation. Having the greatest number of rain events among all seasons, the majority of rain

events have horizontal rainfall intensity between 5 mm/h to 15 mm/h, and catch ratio values are mostly under 20.



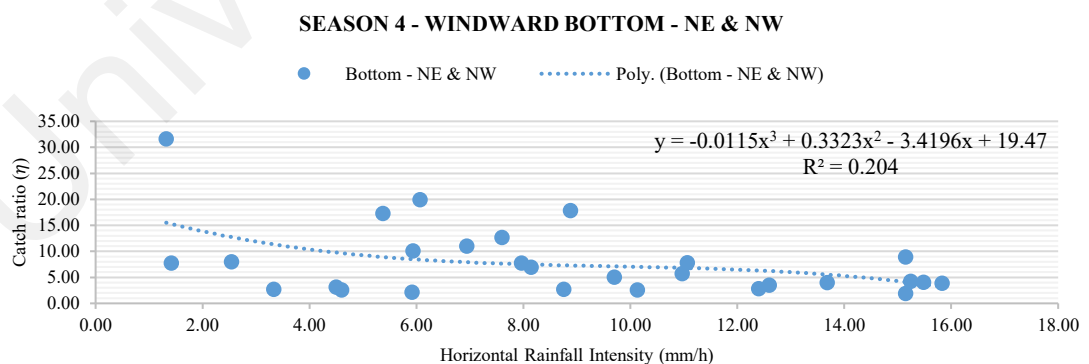
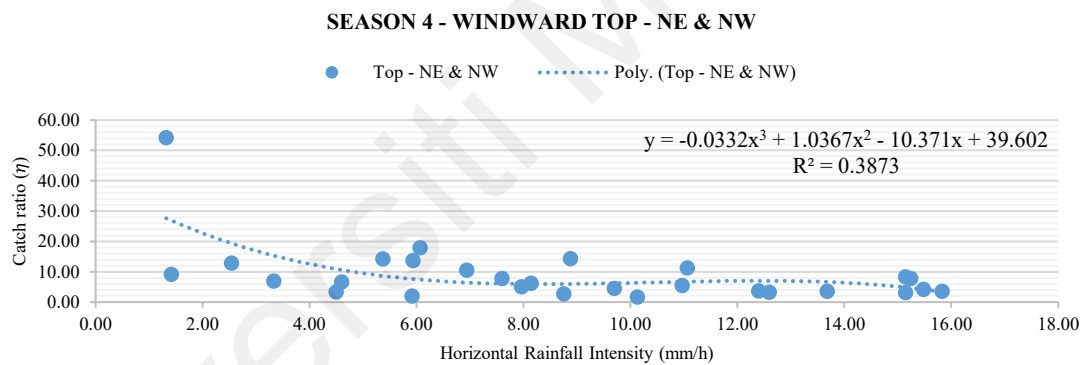
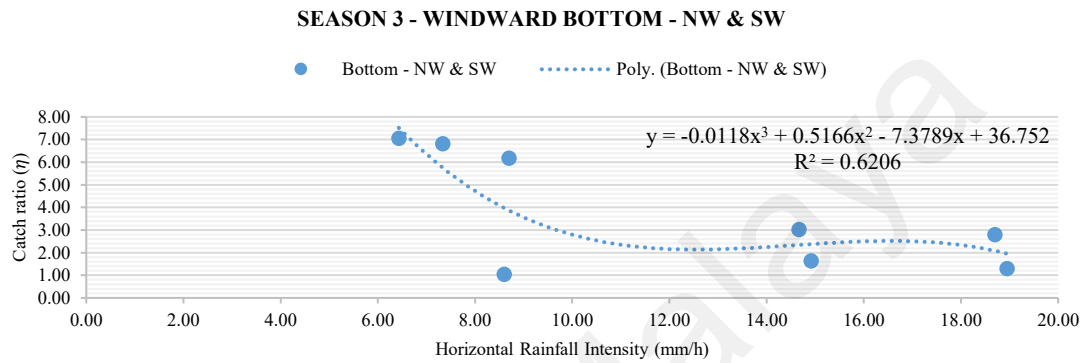
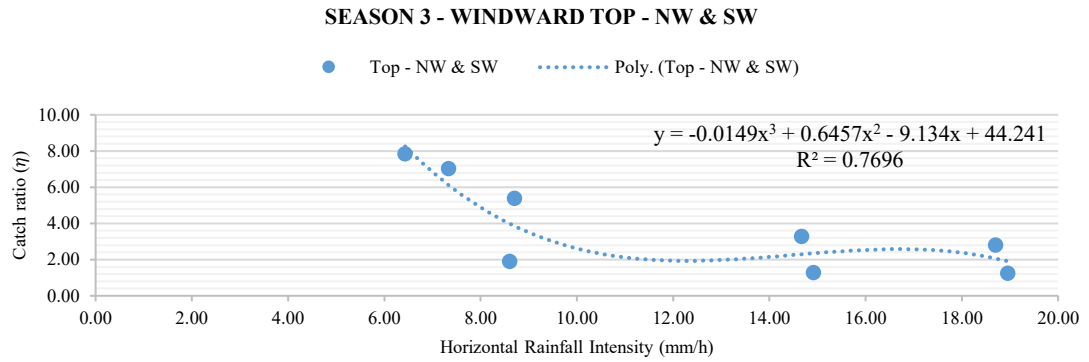


Figure 4.23. Coefficient of determination (R^2) analysis results between WDR catch ratio (η) on windward façades and horizontal rainfall intensity (mm/h) during season 1 to season 4 (The R^2 shown is based on cubic polynomial regression; $0.2 < \text{Value} < 0.4$ is weak, $0.4 < \text{Value} < 0.6$ is moderate, and $0.6 < \text{Value} < 0.8$ means strong effect on the catch ratio variable).

4.3.7. Summary of Findings – WDR Catch Ratio (η)

As Figure 4.22 showed, wind speed (U) and catch ratio value (η) were correlated in all seasons. In seasons 2 and 3, lower wind speed resulted in a lower catch ratio (an ascending trendline), and values increased with the increase of wind speed in a harmonic pattern; in seasons 1 and 4 they were correlated in an inverse relationship; catch ratio increased when wind speed decreased. Such descending trendlines can be resulted from diverse rise and fall data values at increasingly high and low rates throughout these two seasons as heterogeneous data trends compared with other two seasons with more homogeneous data and harmonic ascending trends.

Horizontal rainfall intensity (R_h) as another main factor affecting catch ratio value (η) was analysed (Figure 4.23), and results demonstrated that the frequency of rainfall intensity is largely greater than 5 mm/h and the catch ratio value is vastly fluctuating at the pilot building façades throughout the year. The correlation between catch ratio value and horizontal rainfall intensity in all 4 seasons followed a descending trend pattern in general; lower horizontal rainfall intensity resulted in a higher catch ratio, and values decreased with the increase in horizontal rainfall intensity.

Note that theoretically, with the increase in rainfall intensity, terminal drop velocity increases, and WDR and hence WDR catch ratio decreases, which justifies the descending trend pattern of catch ratio with increasing rainfall intensity.

From wind speed (U) and horizontal rainfall intensity (R_h) analyses, it is found that catch ratio values (η) are mainly higher in the rain events that satisfy the conditions of high wind speed and low horizontal rainfall intensity simultaneously. For instance:

- i. in the rain event July 14th, with the highest amount of catch ratio for the top (40.07) and bottom (123.54) gauges, wind speed was as high as 2.22 m/s and horizontal

rainfall intensity was as low as 0.53 mm/h among other rain event data in season 2,

- ii. in the rain event October 29th, with the highest amount of catch ratio for the top (7.85) and bottom (7.06) gauges, wind speed was as high as 1.67 m/s and horizontal rainfall intensity was as low as 6.43 mm/h among other rain event data in season 3.

4.4. Semi-Empirical Models

In this section, after the data cleaning process (Section 4.2) and correlation analyses, the 66 out of 93 rain events that were assessed and verified as in-situ dataset, are used for the model validation process. This study employs semi-empirical models of ISO 15927-3 (2009) and ASHRAE Standard 160P (2016), as mentioned in the previous chapter.

The values of WDR intensity (R_{wdr}) on the vertical façade of a building is calculated using the ISO standard 15927-3 and ASHRAE standard 160P models. The calculated values are then compared with the measured WDR to evaluate the predictive performance of the models to determine the WDR coefficients α (ISO) and F_L (ASHRAE)), values that are constant in time. The proposed coefficients will be used to predict WDR quantity on the building façade in the future.

4.4.1. Application of the Models

In this section, to calculate the WDR intensity values (R_{wdr}) by the ISO and ASHRAE models to generate the models' datasets for each season, two steps are taken:

- i. To convert and categorise event-based data derived from the validated meteorological data obtained from one-year in-situ measurement, i.e., wind speed (U) (m/s), horizontal rainfall intensity (R_h) (mm/h), wind direction (D°), and determined wind-driven rain intensity (R_{wdr}) values,

- ii. To determine and categorise correction factors and parameters derived from the models' guidelines presented in Sections 2.8.2 and 2.8.3, i.e., terrain roughness coefficient (C_R), topography coefficient (C_T), obstruction factor (O), wall factor (W), rain exposure factor (E_F), and rain deposition factor (F_D).

4.4.1.1. Step One: Determining Validated In-Situ R_{wdr} Dataset

The experimental measured data (in-situ dataset) for each rain event of each season are tabulated as validated dataset for model validation in this section; see APPENDIX B 1 (season one), APPENDIX B 2 (season two), APPENDIX B 3 (season three), and APPENDIX B 4 (season four). Tables demonstrate meteorological parameters (wind speed (U) (m/s), horizontal rainfall intensity (R_h) (mm/h), and wind direction (D°)) and determined wind-driven rain intensity (R_{wdr}) values (mm/h) for windward façades that were assessed and validated through the data cleaning process in Section 4.2.

The assessment process was comprised of three main steps:

1. To select data based on conformity with principles and guidelines derived from the literature review (section 4.2),
2. To select data based on statistic assessment tests (section 4.2.1 to section 4.2.4):
 - i. Normality Test – Shapiro-Wilk Test
 - ii. Outlier Test
3. The analytical comparative assessment to evaluate the correlation analysis between the parameters (section 4.3.5 to section 4.3.6):
 - i. Polynomial regression model – The coefficient of determination (R^2)

4.4.1.2. Step Two: Determining Correction Factors and Parameters for ISO

Standard 15927-3 and ASHRAE Standard 160P Models

The terrain roughness coefficient (C_R) is calculated by the ISO-suggested equation Eq. (11); Table 2.7 for the terrain category and corresponding values of K_R , y_0 and y_{min} , Table 2.8 for the obstruction factor (O), and Figure 2.33 for the wall factor (W) are used for the R_{wdr} calculation.

The wind speed (U_h) measured at the mast at 8 m height is converted to a reference wind speed at the roof-line height (U_{10}) (m/s) using Eq. (12) to determine the U_{10} value for each rain event (explained in Section 3.3.2).

Table 4.11. Parameters used for calculation of R_{wdr} by semi-empirical models ISO 15927-3 (2009) and ASHRAE Standard 160P (2016) in this study

Correction Factors	Values	
C_R - Terrain category IV – Urban areas in which at least 15% of the surface is covered with buildings of average height exceeding 15 m	$K_R = 0.24$ $y_0 = 1.00$ $y_{min} = 16$ (Table 2.7)	Eq. (11) for $y < y_{min}$ $C_R = 0.24 \times \ln(16/1) = 0.66$
C_T - For upstream slopes	1.00 (Section 2.8.2)	
O - Distance to obstacle; 15 to 25 m	0.40 (Table 2.8)	
W - One-storey building with flat roof	Top = 0.50; Bottom = 0.30 (Figure 2.33)	
F_L - Empirical constant	0.20 (Section 2.8.3)	
F_E - Sheltered exposure, height < 10 m medium exposure, height < 10 m	0.70 (NW&SW façade orientation) 1.00 (NE&NW façade orientation) (Table 2.10)	
F_D – Walls subject to rain runoff / Flat roof building	1.00 Table 2.11 / (Figure 2.33)	

The pilot building was assumed to be located in terrain category IV, which, according to ISO Standard, relates to urban areas ($K_R = 0.24$, $y_0 = 1$, and $y_{min} = 16$). The corresponding exposure category in the ASHRAE standard 160P is that of sheltered exposure (Table 2.10).

Table 4.11 represents the parameters and coefficients values taken into consideration when each model in this study calculates R_{wdr} .

The final step towards the calculation of wind-driven rain intensity (R_{wdr}) by the ISO standard 15927-3 and ASHRAE standard 160P models is to apply:

- a) Eq. (10) and Eq. (13) respectively for each model using the validated experimental data (Section 4.4.1.1) presented in APPENDIX B 1 (season one), APPENDIX B 2 (season two), APPENDIX B 3 (season three), and APPENDIX B 4 (season four),
- b) corresponding determined correction factors and parameters presented in Table 4.12 (season one), Table 4.13 (season two), Table 4.14 (season three), and Table 4.15 (season four).

Table 4.12. Determined parameters for ISO standard 15927-3 and ASHRAE standard 160P models - Season One

Rain Event	α	C_R	C_T	O	W		U_{10}	R_h	$R_h^{0.88}$	$\cos(D-\theta)$	F_L	F_E	F_D
					Top	Bottom							
21-Apr-17	0.222	0.66	1.00	0.40	0.50	0.30	1.46	8.16	6.34	1.00	0.20	0.70	1.00
23-Apr-17	0.222	0.66	1.00	0.40	0.50	0.30	1.17	11.24	8.41	1.00	0.20	0.70	1.00
24-Apr-17	0.222	0.66	1.00	0.40	0.50	0.30	1.17	8.90	6.85	1.00	0.20	0.70	1.00
26-Apr-17	0.222	0.66	1.00	0.40	0.50	0.30	1.17	10.80	8.12	1.00	0.20	0.70	1.00
02-May-17	0.222	0.66	1.00	0.40	0.50	0.30	1.46	9.00	6.91	1.00	0.20	0.70	1.00
05-May-17	0.222	0.66	1.00	0.40	0.50	0.30	1.17	12.27	9.08	1.00	0.20	0.70	1.00
07-May-17	0.222	0.66	1.00	0.40	0.50	0.30	0.88	6.65	5.30	1.00	0.20	0.70	1.00
12-May-17	0.222	0.66	1.00	0.40	0.50	0.30	1.17	10.63	8.00	1.00	0.20	0.70	1.00
13-May-17	0.222	0.66	1.00	0.40	0.50	0.30	1.17	15.60	11.22	1.00	0.20	0.70	1.00

Table 4.13. Determined parameters for ISO standard 15927-3 and ASHRAE standard 160P models – Season Two

Rain Event	α	C_R	C_T	O	W		U_{10}	R_h	$R_h^{0.88}$	$\cos(D-\theta)$	F_L	F_E	F_D
					Top	Bottom							
20-May-17	0.222	0.66	1.00	0.40	0.50	0.30	1.75	2.10	1.92	1.00	0.20	0.70	1.00
23-May-17	0.222	0.66	1.00	0.40	0.50	0.30	2.05	2.88	2.54	1.00	0.20	0.70	1.00
25-May-17	0.222	0.66	1.00	0.40	0.50	0.30	1.46	0.72	0.75	1.00	0.20	0.70	1.00
03-Jun-17	0.222	0.66	1.00	0.40	0.50	0.30	1.75	10.20	7.72	1.00	0.20	0.70	1.00
09-Jun-17	0.222	0.66	1.00	0.40	0.50	0.30	2.05	0.73	0.76	1.00	0.20	0.70	1.00
11-Jun-17	0.222	0.66	1.00	0.40	0.50	0.30	0.88	8.60	6.64	1.00	0.20	0.70	1.00
12-Jun-17	0.222	0.66	1.00	0.40	0.50	0.30	1.17	6.80	5.40	1.00	0.20	0.70	1.00
14-Jun-17	0.222	0.66	1.00	0.40	0.50	0.30	1.75	5.28	4.32	1.00	0.20	0.70	1.00
19-Jun-17	0.222	0.66	1.00	0.40	0.50	0.30	1.17	3.60	3.09	1.00	0.20	0.70	1.00
11-Jul-17	0.222	0.66	1.00	0.40	0.50	0.30	2.05	0.40	0.45	1.00	0.20	0.70	1.00
12-Jul-17	0.222	0.66	1.00	0.40	0.50	0.30	1.46	5.70	4.63	1.00	0.20	0.70	1.00
13-Jul-17	0.222	0.66	1.00	0.40	0.50	0.30	1.75	4.42	3.70	1.00	0.20	0.70	1.00
14-Jul-17	0.222	0.66	1.00	0.40	0.50	0.30	2.34	0.53	0.57	1.00	0.20	0.70	1.00
20-Jul-17	0.222	0.66	1.00	0.40	0.50	0.30	2.05	7.44	5.85	1.00	0.20	0.70	1.00
21-Jul-17	0.222	0.66	1.00	0.40	0.50	0.30	2.05	3.47	2.99	1.00	0.20	0.70	1.00
22-Jul-17	0.222	0.66	1.00	0.40	0.50	0.30	2.05	3.27	2.83	1.00	0.20	0.70	1.00
23-Aug-17	0.222	0.66	1.00	0.40	0.50	0.30	1.17	2.74	2.43	1.00	0.20	0.70	1.00
30-Aug-17	0.222	0.66	1.00	0.40	0.50	0.30	1.17	3.71	3.17	1.00	0.20	0.70	1.00
31-Aug-17	0.222	0.66	1.00	0.40	0.50	0.30	2.34	2.20	2.00	1.00	0.20	0.70	1.00
01-Sep-17	0.222	0.66	1.00	0.40	0.50	0.30	1.46	12.35	9.13	1.00	0.20	0.70	1.00

Table 4.14. Determined parameters for ISO standard 15927-3 and ASHRAE standard 160P models – Season Three

Rain Event	α	C_R	C_T	O	W		U_{10}	R_h	$R_h^{0.88}$	$\cos(D-\theta)$	F_L	F_E	F_D
					Top	Bottom							
27-Oct-17	0.222	0.66	1.00	0.40	0.50	0.30	1.17	14.91	10.78	1.00	0.20	0.70	1.00
29-Oct-17	0.222	0.66	1.00	0.40	0.50	0.30	1.75	6.43	5.14	1.00	0.20	0.70	1.00
03-Nov-17	0.222	0.66	1.00	0.40	0.50	0.30	1.75	8.70	6.71	1.00	0.20	0.70	1.00
07-Nov-17	0.222	0.66	1.00	0.40	0.50	0.30	1.75	14.67	10.63	1.00	0.20	0.70	1.00
09-Nov-17	0.222	0.66	1.00	0.40	0.50	0.30	2.05	7.33	5.77	1.00	0.20	0.70	1.00
10-Nov-17	0.222	0.66	1.00	0.40	0.50	0.30	1.17	18.95	13.31	1.00	0.20	0.70	1.00
11-Nov-17	0.222	0.66	1.00	0.40	0.50	0.30	0.58	8.60	6.64	1.00	0.20	0.70	1.00
12-Nov-17	0.222	0.66	1.00	0.40	0.50	0.30	1.17	18.70	13.16	1.00	0.20	0.70	1.00

Table 4.15. Determined parameters for ISO standard 15927-3 and ASHRAE standard 160P models – Season Four

Rain Event	α	C_R	C_T	O	W		U_{10}	R_h	$R_h^{0.88}$	$\cos(D-\theta)$	F_L	F_E	F_D
					Top	Bottom							
13-Nov-17	0.222	0.66	1.00	0.40	0.50	0.30	0.88	7.60	5.96	1.00	0.20	1.00	1.00
18-Nov-17	0.222	0.66	1.00	0.40	0.50	0.30	1.46	10.13	7.67	1.00	0.20	1.00	1.00
25-Nov-17	0.222	0.66	1.00	0.40	0.50	0.30	1.17	8.76	6.75	1.00	0.20	1.00	1.00
27-Nov-17	0.222	0.66	1.00	0.40	0.50	0.30	0.58	13.68	9.99	1.00	0.20	1.00	1.00
28-Nov-17	0.222	0.66	1.00	0.40	0.50	0.30	0.88	9.70	7.39	1.00	0.20	1.00	1.00
29-Nov-17	0.222	0.66	1.00	0.40	0.50	0.30	2.05	8.15	6.33	1.00	0.20	1.00	1.00
01-Dec-17	0.222	0.66	1.00	0.40	0.50	0.30	0.88	15.48	11.14	1.00	0.20	1.00	1.00
02-Dec-17	0.222	0.66	1.00	0.40	0.50	0.30	1.46	10.97	8.23	1.00	0.20	1.00	1.00
03-Dec-17	0.222	0.66	1.00	0.40	0.50	0.30	1.46	6.94	5.50	1.00	0.20	1.00	1.00
10-Dec-17	0.222	0.66	1.00	0.40	0.50	0.30	1.75	12.60	9.30	1.00	0.20	1.00	1.00
17-Dec-17	0.222	0.66	1.00	0.40	0.50	0.30	0.88	6.07	4.89	1.00	0.20	1.00	1.00
19-Dec-17	0.222	0.66	1.00	0.40	0.50	0.30	2.05	7.96	6.21	1.00	0.20	1.00	1.00
25-Dec-17	0.222	0.66	1.00	0.40	0.50	0.30	1.46	8.88	6.83	1.00	0.20	1.00	1.00
26-Dec-17	0.222	0.66	1.00	0.40	0.50	0.30	1.17	5.37	4.39	1.00	0.20	1.00	1.00
27-Dec-17	0.222	0.66	1.00	0.40	0.50	0.30	1.46	15.24	10.99	1.00	0.20	1.00	1.00
31-Dec-17	0.222	0.66	1.00	0.40	0.50	0.30	1.17	5.92	4.78	1.00	0.20	1.00	1.00
17-Jan-18	0.222	0.66	1.00	0.40	0.50	0.30	1.17	5.93	4.79	1.00	0.20	1.00	1.00
19-Jan-18	0.222	0.66	1.00	0.40	0.50	0.30	0.88	12.40	9.17	1.00	0.20	1.00	1.00
20-Jan-18	0.222	0.66	1.00	0.40	0.50	0.30	1.17	15.83	11.36	1.00	0.20	1.00	1.00
28-Jan-18	0.222	0.66	1.00	0.40	0.50	0.30	0.58	15.15	10.93	1.00	0.20	1.00	1.00
30-Jan-18	0.222	0.66	1.00	0.40	0.50	0.30	0.88	11.07	8.29	1.00	0.20	1.00	1.00
28-Feb-18	0.222	0.66	1.00	0.40	0.50	0.30	1.17	15.15	10.93	1.00	0.20	1.00	1.00
04-Mar-18	0.222	0.66	1.00	0.40	0.50	0.30	1.46	2.54	2.27	1.00	0.20	1.00	1.00
08-Mar-18	0.222	0.66	1.00	0.40	0.50	0.30	0.88	1.42	1.36	1.00	0.20	1.00	1.00
10-Mar-18	0.222	0.66	1.00	0.40	0.50	0.30	1.46	4.50	3.76	1.00	0.20	1.00	1.00
13-Mar-18	0.222	0.66	1.00	0.40	0.50	0.30	0.58	1.32	1.28	1.00	0.20	1.00	1.00
15-Mar-18	0.222	0.66	1.00	0.40	0.50	0.30	1.46	3.33	2.88	1.00	0.20	1.00	1.00
16-Mar-18	0.222	0.66	1.00	0.40	0.50	0.30	1.46	4.60	3.83	1.00	0.20	1.00	1.00

4.5. R_{wdr} Datasets of In-Situ and Predicted ISO Standard 15927-3 and ASHRAE STANDARD 160P Models

In this section, R_{wdr} (mm/h) values on the windward façades of the pilot building (Top and Bottom gauges) are calculated using ISO standard 15927-3 and ASHRAE standard 160P models' equations to generate the predicted datasets and compare them with the experimental measured (in-situ) dataset to examine the level of differences/discrepancies between them as the pre-processing step for the models' validation process.

A total of 93 rain events generated 65 validated sets of WDR data (Exp.) to conduct models' calculations (ISO and ASHRAE). Every dataset was carried out according to the 'event-based averaged value' approach as described in Section 2.8.2.7. A detection threshold of $R_{\text{wdr}} < 1$ mm/h was also applied for the WDR intensity on each façade (top and bottom gauges) in the previous section, and measurements below this detection threshold were disregarded, such as the rain event April 28 in season one.

The amount of R_{wdr} (mm/h) was then calculated by the corresponding equations of the ISO standard 15927-3 and ASHRAE standard 160P models. Each rain event includes two windward façades, and each windward façade includes two WDR gauges (TOP and Bottom). The calculation processes were carried out for each gauge on each windward façade; there were a total of 4 gauges for each rain event. In line with the 'event-based averaged value' approach, and as can be seen in Table 4.16 to Table 4.19, the amount of R_{wdr} (mm/h) top gauges for each rain event is calculated as 'Mean value of top gauge' (mean of both top gauges of both windward façades) and 'Mean value of bottom gauge' for each rain event. These determined Mean values of top and bottom gauges, as illustrated in Section 4.4.1.1, will then be applied to the models' equations to determine the WDR coefficients for each season.

4.5.1. In-situ and Predicted R_{wdr} Datasets – Season 1

Figure 4.24 (Mean R_{wdr} top (a) and Mean R_{wdr} bottom (b)) presents the comparison between the in-situ Mean measured (Exp.) WDR intensity (R_{wdr}) and calculated Mean R_{wdr} using semi-empirical models, i.e., ISO standard 15927-3 and ASHRAE standard 160P, for season one (monsoon transitional period – April 1st to May 16th 2017) on windward façades (NW-SW). Table 4.16 shows the Mean R_{wdr} measured (top and bottom) (mm/h) and calculated models' values for all 9 validated rain events (derived from APPENDIX B 1) over the façade for the entire monitoring period of season one.

- **ISO and ASHRAE** – It is observed that the trends of the ISO and ASHRAE models are parallel to each other, with almost high discrepancies (ASHRAE has lower values) in the top location and almost no discrepancies in the bottom location of the façade during the entire season one.
- **ISO and Measured (Exp.)** – The ISO model underestimates the Mean R_{wdr} measured values for the majority of the rain events at the top and bottom locations. The discrepancies during the entire season at the top location are relatively low or almost zero in one rain event, i.e., April 21st and 24th, except for May 12th with a high discrepancy. It has a relatively good agreement with the bottom location, with almost zero discrepancy in one rain event, May 5th, except for April 24th and May 12th.
- **ASHRAE and Measured (Exp.)** – The ASHRAE model also underestimates the Mean R_{wdr} measured values at the top location for the entire season, and the majority of the bottom location values. It shows a larger discrepancy at the top location in general; only two rain events have almost equal values with the measured values, i.e., April 23rd and 26th. It has a relatively good agreement with

the Mean R_{wdr} bottom location, with almost zero discrepancy in one rain event, May 5th.

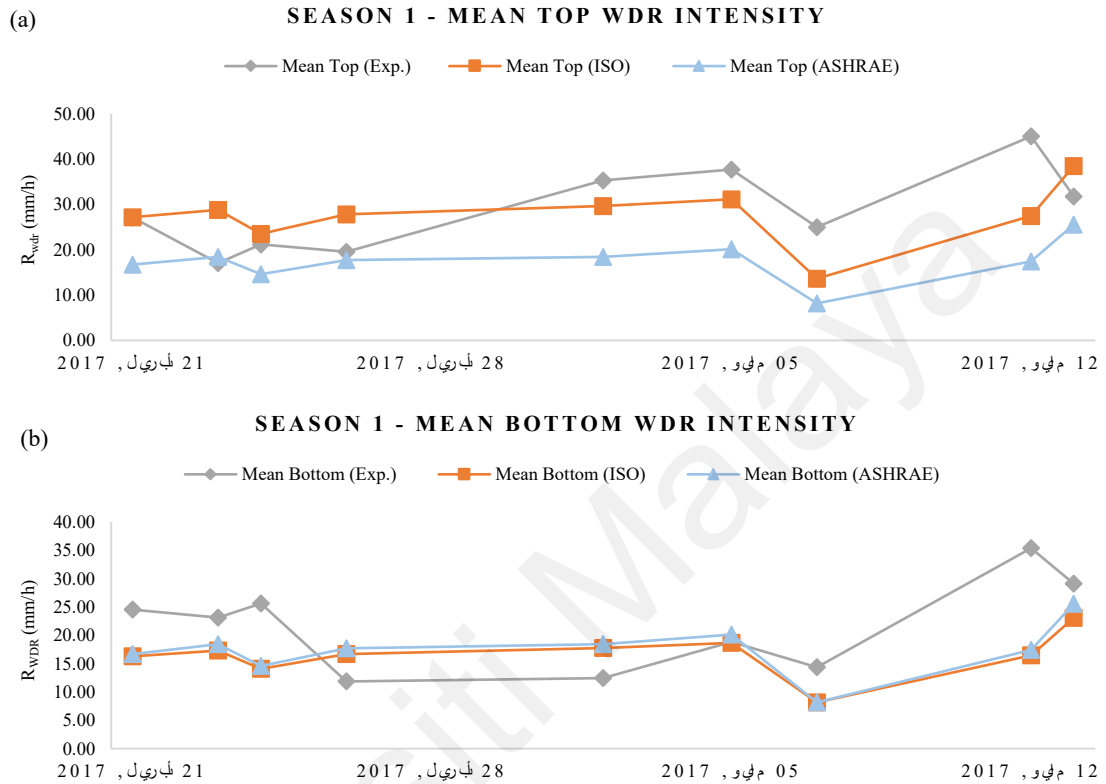


Figure 4.24. Comparison of the Mean R_{wdr} (mm/h) between Experimental measurement, predicted ISO and ASHRAE models for two positions (Top and Bottom) on the windward façade (NW-SW) – Season One

Table 4.16. R_{wdr} (WDR intensity) (mm/h) on windward façades - Experimental measurement / ISO model / ASHRAE model – Season One

Rain Event	Mean Top (Exp.)	Mean Bottom (Exp.)	Mean Top (ISO)	Mean Bottom (ISO)	Mean Top (ASHRAE)	Mean Bottom (ASHRAE)
21-Apr-17	27.11	24.54	27.17	16.30	16.70	16.70
23-Apr-17	17.05	23.11	28.83	17.30	18.41	18.41
24-Apr-17	21.16	25.59	23.47	14.08	14.57	14.57
26-Apr-17	19.55	11.85	27.82	16.69	17.68	17.68
02-May-17	35.28	12.46	29.62	17.77	18.42	18.42
05-May-17	37.69	18.83	31.13	18.68	20.10	20.10
07-May-17	25.00	14.34	13.63	8.18	8.17	8.17
12-May-17	45.00	35.36	27.43	16.46	17.40	17.40
13-May-17	31.78	29.10	38.45	23.07	25.54	25.54

4.5.2. In-situ and Predicted R_{wdr} Datasets – Season 2

Figure 4.25 (Mean R_{wdr} top (a) and Mean R_{wdr} bottom (b)) presents the comparison between the in-situ Mean measured (exp.) WDR intensity (R_{wdr}) and calculated Mean R_{wdr} using semi-empirical models, i.e., ISO standard 15927-3 and ASHRAE standard 160P for season two (Southwest monsoon – 17th May to 5th October 2017) on windward façades (NW-SW). Table 4.17 shows the Mean R_{wdr} measured (top and bottom) (mm/h) and calculated models' values for all 20 validated rain events (derived from APPENDIX B 2) over the façade for the entire monitoring period of season two.

- **ISO and ASHRAE** – It is observed that the trends of the ISO and ASHRAE models are basically parallel to each other, with low discrepancies in the top location and almost no discrepancies in the bottom location of the façade during the entire season two.
- **ISO and Measured (Exp.)** – The ISO model generally underestimates the Mean R_{wdr} measured values for the majority of the rain events at top and bottom locations during season two. It provides good agreement for some cases, i.e., May 25th, June 9th, July 12th, 13th, and 20th at the top location. The discrepancies in overestimation (i.e., May 23rd, June 11th, 12th, 14th, August 31st) and underestimation (i.e., July 11th, 14th, August 23rd, 30th) cases are mostly high during the season two at the top location. For the bottom location on the façade, ISO tends to underestimate the majority of the Mean R_{wdr} measured values with large discrepancies, i.e., June 3rd, 19th, July 14th, 23rd, August 30th. It provides good agreement for some cases, i.e., May 20th, 23rd, 25th, June 9th, 11th, and July 20th at a lower location.
- **ASHRAE and Measured (Exp.)** – The ASHRAE model prediction trendline resembles the ISO trendline with a larger distance from and mostly

underestimating the Mean R_{wdr} measured values at the top location for the entire season two, except for June 3rd and 9th, in good agreement. The differences in underestimation cases, i.e., May 20th, June 19th, July 11th, August 23rd, and 30th, are mostly high during season two at higher locations of the building façade. For the lower location, the ASHRAE prediction is almost equal to ISO's for season two with the same trendline and discrepancy; underestimating the majority of the Mean R_{wdr} measured values with large differences, i.e., June 3rd, 19th, July 14th, August 23rd, and 30th. It provides good agreement for some cases, i.e., May 20th, 23rd, 25th, June 9th, 11th, and July 20th.

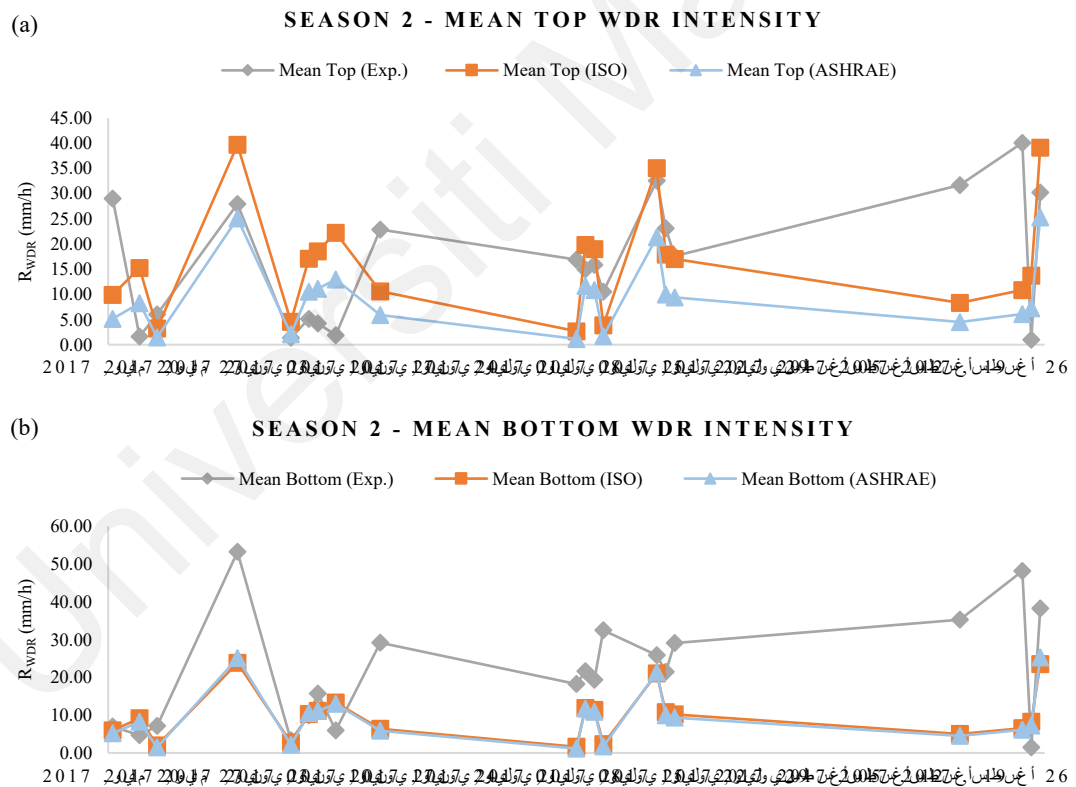


Figure 4.25. Comparison of the Mean R_{wdr} (mm/h) between Experimental measurement, predicted ISO and ASHRAE models for two positions (Top and Bottom) on the windward façade (NW-SW) – Season Two

Table 4.17. R_{wdr} (WDR intensity) (mm/h) on windward façades - Experimental measurement / ISO model / ASHRAE model – Season Two

Rain Event	Mean Top (Exp.)	Mean Bottom (Exp.)	Mean Top (ISO)	Mean Bottom (ISO)	Mean Top (ASHRAE)	Mean Bottom (ASHRAE)
20-May-17	29.03	6.96	9.88	5.93	5.16	5.16
23-May-17	1.65	4.65	15.21	9.13	8.25	8.25
25-May-17	6.03	7.17	3.21	1.93	1.47	1.47
03-Jun-17	27.91	53.20	39.68	23.81	25.05	25.05
09-Jun-17	1.40	3.28	4.57	2.74	2.10	2.10
11-Jun-17	5.13	9.95	17.08	10.25	10.56	10.56
12-Jun-17	4.23	15.71	18.52	11.11	11.13	11.13
14-Jun-17	1.89	5.91	22.23	13.34	12.97	12.97
19-Jun-17	22.88	29.12	10.58	6.35	5.89	5.89
11-Jul-17	16.88	18.22	2.68	1.61	1.15	1.15
12-Jul-17	15.00	21.64	19.82	11.89	11.67	11.67
13-Jul-17	15.87	19.30	19.00	11.40	10.85	10.85
14-Jul-17	10.52	32.43	3.89	2.33	1.72	1.72
20-Jul-17	32.60	25.88	35.07	21.04	21.32	21.32
21-Jul-17	23.13	21.42	17.91	10.75	9.93	9.93
22-Jul-17	17.58	29.08	17.00	10.20	9.36	9.36
23-Aug-17	31.71	35.29	8.33	5.00	4.49	4.49
30-Aug-17	40.07	48.14	10.88	6.53	6.08	6.08
31-Aug-17	1.00	1.44	13.72	8.23	7.20	7.20
01-Sep-17	30.25	38.25	39.13	23.48	25.28	25.28

4.5.3. In-situ and Predicted R_{wdr} Datasets – Season 3

Figure 4.26 (Mean R_{wdr} top (a) and Mean R_{wdr} bottom (b)) presents the comparison between the in-situ Mean measured (exp.) WDR intensity (R_{wdr}) and calculated Mean R_{wdr} using semi-empirical models, i.e., ISO standard 15927-3 and ASHRAE standard 160P, for season three (Monsoon Transitional Period – October 6th to November 12th, 2017) on windward façades (NW-SW). Table 4.18 shows the Mean R_{wdr} measured (top and bottom) (mm/h) and calculated models' values for all 8 validated rain events (derived from APPENDIX B 3) over the façade for the entire monitoring period of season three.

- **ISO and ASHRAE** – It is observed that the trends of the ISO and ASHRAE models are harmoniously parallel to each other, with almost high discrepancies (ASHRAE has lower values), in the top location and low discrepancies in the bottom location of the façade during the entire season three.
- **ISO and Measured (Exp.)** – The ISO model overestimates the Mean R_{wdr} measured values during the entire season three at the top location of the façade.

The discrepancy is slightly high for all the rain events except for October 29th, November 9th, and 11th, which has a good agreement. For the lower location, the model prediction discrepancies with the Mean R_{wdr} measured values are generally lower. It has a relatively good agreement with the lower location except for October 27th, November 7th, and 10th, and one case has almost zero discrepancy, i.e., November 11th.

- **ASHRAE and Measured (Exp.)** – The ASHRAE model overestimates the majority of the Mean R_{wdr} measured values at the top and bottom locations for the entire season. It has a good agreement with November 3rd, 9th, 11th, and 12th at the higher location of the façade. For the lower location, the ASHRAE prediction trendline resembles ISO’s trendline. It has a relatively good agreement with the lower location except for October 27th, November 7th, and 10th, and one case has almost zero discrepancy, i.e., November 11th.

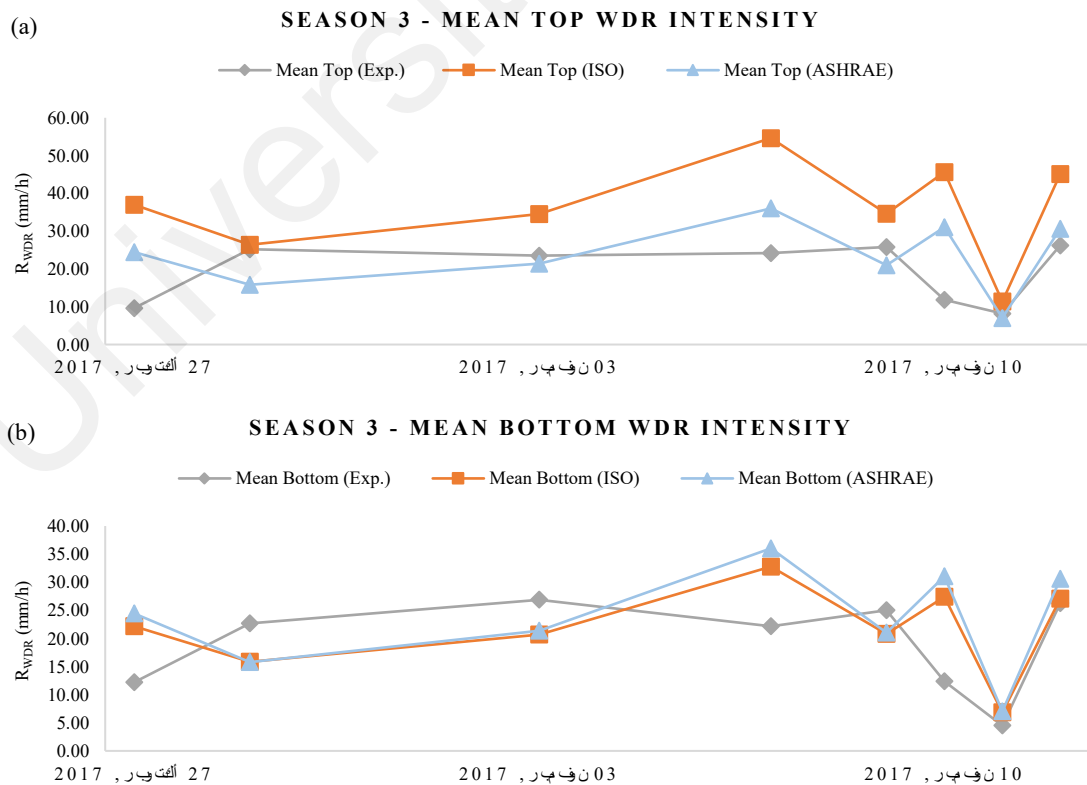


Figure 4.26. Comparison of the Mean R_{wdr} (mm/h) between Experimental measurement, predicted ISO and ASHRAE models for two positions (Top and Bottom) on the windward façade (NW-SW) – Season Three

Table 4.18. R_{wdr} (WDR intensity) (mm/h) on windward façades - Experimental measurement / ISO model / ASHRAE model – Season Three

Rain Event	Mean Top (Exp.)	Mean Bottom (Exp.)	Mean Top (ISO)	Mean Bottom (ISO)	Mean Top (ASHRAE)	Mean Bottom (ASHRAE)
27-Oct-17	9.60	12.21	36.96	22.18	24.42	24.42
29-Oct-17	25.23	22.69	26.44	15.87	15.79	15.79
03-Nov-17	23.50	26.88	34.50	20.70	21.37	21.37
07-Nov-17	24.17	22.17	54.63	32.78	36.02	36.02
09-Nov-17	25.83	25.00	34.63	20.78	21.01	21.01
10-Nov-17	11.88	12.38	45.63	27.38	31.03	31.03
11-Nov-17	8.20	4.50	11.38	6.83	7.04	7.04
12-Nov-17	26.25	26.25	45.10	27.06	30.62	30.62

4.5.4. In-situ and Predicted R_{wdr} Datasets – Season 4

Figure 4.27 (Mean R_{wdr} top (a) and Mean R_{wdr} bottom (b)) presents the comparison between the in-situ Mean measured (exp.) WDR intensity (R_{wdr}) and calculated Mean R_{wdr} using semi-empirical models, i.e., ISO standard 15927-3 and ASHRAE standard 160P for season four (Northeast Monsoon – November 13th to March 27th, 2018) on windward façades (NE-NW). Table 4.19 shows the Mean R_{wdr} measured (top and bottom) (mm/h) and calculated models' values for all 28 validated rain events (derived from APPENDIX B 4) over the façade for the entire monitoring period of season four.

- **ISO and ASHRAE** – It is observed that the trendlines of the ISO and ASHRAE models are relatively identical at the top and bottom locations, particularly the higher location, of the façade during the entire season four, which is the longest season with the largest rain events.
- **ISO and Measured (Exp.)** – The ISO model trendline in season four generally shows underestimation with the Mean R_{wdr} measured values at the top and bottom locations of the façade. The discrepancy is relatively low during the entire season for all the rain events (in relatively good agreement), except for November 13th, 18th, December 10th, 17th, 25th, January 17th, 28th, 30th, and March 13th. For the lower location on the façade, ISO prediction values show smaller discrepancies compared with the higher location. Almost all the predicted values are in good

agreement with the Mean R_{wdr} measured values, except for November 13th, December 17th, 25th, January 28th, and 30th.

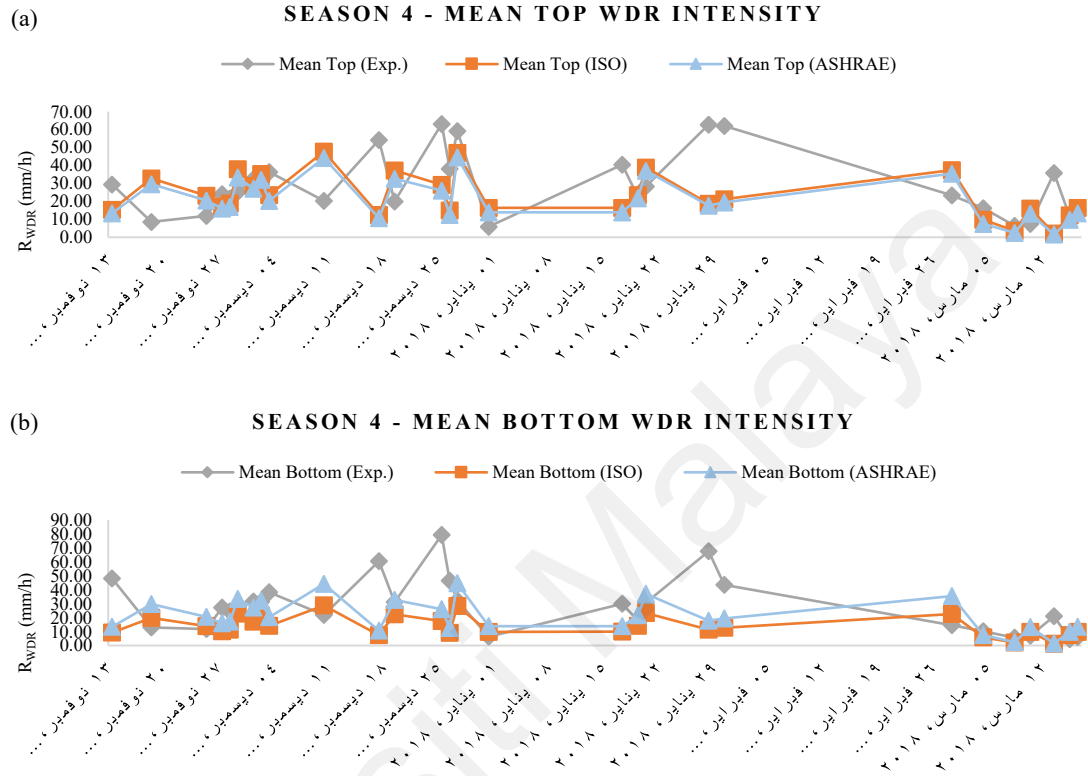


Figure 4.27. Comparison of the Mean R_{wdr} (mm/h) between Experimental measurement, predicted ISO and ASHRAE models for two positions (Top and Bottom) on the windward façade (NE-NW) – Season Four

- **ASHRAE and Measured (Exp.)** – The ASHRAE model prediction trendline in season four is almost identical to the ISO model's at the top location for the entire season. It has a slight difference with the ISO model's for the lower location on the façade, closer to the Mean R_{wdr} measured values, which is mainly attributed to the fact that the F_D factor in ASHRAE has a constant value for all façade heights, as mentioned in Section 4.5.1.

Table 4.19. R_{wdr} (WDR intensity) (mm/h) on windward façades - Experimental measurement / ISO model / ASHRAE model – Season Four

Rain Event	Mean Top (Exp.)	Mean Bottom (Exp.)	Mean Top (ISO)	Mean Bottom (ISO)	Mean Top (ASHRAE)	Mean Bottom (ASHRAE)
13-Nov-17	29.50	48.13	15.32	9.19	13.33	13.33
18-Nov-17	8.50	13.00	32.88	19.73	29.63	29.63
25-Nov-17	11.94	11.83	23.13	13.88	20.48	20.48
27-Nov-17	24.15	27.20	17.13	10.28	16.00	16.00
28-Nov-17	21.63	24.31	18.98	11.39	17.02	17.02
29-Nov-17	25.27	28.27	37.98	22.79	33.34	33.34
01-Dec-17	32.40	31.50	28.64	17.19	27.16	27.16
02-Dec-17	29.64	31.36	35.26	21.16	32.08	32.08
03-Dec-17	36.43	38.14	23.57	14.14	20.30	20.30
10-Dec-17	20.25	21.90	47.79	28.68	44.21	44.21
17-Dec-17	54.17	60.42	12.56	7.54	10.64	10.64
19-Dec-17	20.05	30.95	37.24	22.34	32.60	32.60
25-Dec-17	63.23	79.20	29.27	17.56	25.96	25.96
26-Dec-17	38.21	46.50	15.05	9.03	12.56	12.56
27-Dec-17	59.25	32.10	47.09	28.25	44.56	44.56
31-Dec-17	5.90	6.40	16.39	9.83	13.85	13.85
17-Jan-18	40.50	30.00	16.42	9.85	13.88	13.88
19-Jan-18	22.50	17.68	23.56	14.14	21.75	21.75
20-Jan-18	28.29	30.50	38.95	23.37	37.03	37.03
28-Jan-18	62.81	67.50	18.74	11.24	17.72	17.72
30-Jan-18	62.00	43.33	21.32	12.79	19.42	19.42
28-Feb-18	23.46	14.61	37.47	22.48	35.44	35.44
04-Mar-18	16.31	10.15	9.73	5.84	7.43	7.43
08-Mar-18	6.50	5.50	3.50	2.10	2.49	2.49
10-Mar-18	7.54	7.01	16.10	9.66	13.16	13.16
13-Mar-18	35.78	20.87	2.19	1.31	1.54	1.54
15-Mar-18	11.53	4.50	12.36	7.42	9.75	9.75
16-Mar-18	15.26	5.99	16.41	9.85	13.45	13.45

4.5.5. Summary of Findings – Comparative Analyses of In-Situ and Predicted

R_{wdr} Datasets

In season 1, the ISO model generally shows better agreement with the Mean R_{wdr} measured values, with lower discrepancies for both top and bottom locations compared with the ASHRAE model during the entire season one. Generally, the ASHRAE model underestimates the values of Mean R_{wdr} at higher locations and has higher discrepancies, due to the fact that the F_D factor in ASHRAE has a constant value for all façade heights, which seems to be higher for the higher location. Both models have a relatively good agreement with the Mean R_{wdr} measured values of the lower location; May 5th has almost zero discrepancy in both models.

In season 2, the ISO model tends to show mostly underestimation for the Mean R_{wdr} measured values, with lower discrepancies for both top and bottom locations compared with the ASHRAE model during the entire season two. Generally, the ASHRAE model also tends to show underestimation for the values of Mean R_{wdr} at both locations, particularly for the lower location, due to the fact that F_D factor in ASHRAE has a constant value for all façade heights, which seems to be higher for the higher location. Both models have a relatively good agreement with some Mean R_{wdr} measured values at high and low locations on the façade, i.e., June 9th for the top, and May 20th, 23rd, 25th, June 9th, 11th and July 20th for the bottom locations.

In season 3, the ASHRAE model shows better agreement with the Mean R_{wdr} measured values, with a lower discrepancy for both top and bottom locations compared with the ISO model during the entire season three. Generally, the ISO model overestimates the values of Mean R_{wdr} at higher locations and has higher discrepancies compared with ASHRAE in season three. In season three, both models have more or less a good agreement with the Mean R_{wdr} measured values at high and low locations on the façade, and two cases have a considerably low discrepancy, i.e., November 9th and 11th.

In season 4, both ISO and ASHRAE models show better agreement with the Mean R_{wdr} measured values, with a lower discrepancy for both top and bottom locations for the entire season four. It can be said that the semi-empirical models in this season are more successful at predicting the Mean R_{wdr} for the high and low locations of the building façade compared with seasons one, two, and three.

4.6. Validating the Semi-Empirical Models

The comparison between the calculated R_{wdr} by the semi-empirical models' equations, i.e., ISO standard 15927-3 and ASHRAE standard 160P, was conducted in the previous section through comparative graphs and tables demonstrating the values of the predicted

Mean R_{wdr} (mm/h) and the experimental measured (in-situ) on the windward façades of the pilot building (Top and Bottom gauges).

In this section, further analytical assessments i.e., calculation of difference (D), coefficient of determination (R^2), root mean square deviation (RMSD), and normalised root mean square deviation (NRMSD), are carried out to evaluate the predictive performance of the two models. Analyses are performed between the in-situ and the predicted models' datasets of the R_{wdr} for the top and bottom locations.

In this section, the performance of different coefficients of determination (R^2) by the polynomial regression analyses is calculated and evaluated to find the optimum order (degree) value with as few predictor variables as possible to avoid overestimation of the proposed model and R^2 by choosing higher-ordered values. After this, the best-fit line (regression curve) for the predicted R_{wdr} values is determined based on the Eq. (14) explanations and as discussed in Section 4.3.5. Table 4.20 gives a comparison of fitting order 3 (cubic), order 4 (quadratic), and order 5 (quantic) curves on the datasets. In some cases, the degree of improvement between order 3 and order 4 can be seen as significant (i.e., season 2 and season 4), but between order 4 and order 5, the difference is negligible. Thus, order 4 was chosen to generate R^2 to assess the validity of the predictive performance of the semi-empirical models. In statistics, the coefficient of determination, R^2 , is used as a measure of the proportion of the variance in observed (experimental measurement) values that is explained by the predicted (model) values (Piñeiro et al., 2008).

Piñeiro et al. (2008) have provided empirical evidence and presented analytical proof that when evaluating a model using linear regressions, it is advisable to place the observed values on the y-axis and the predicted values on the x-axis. They further clarified that model evaluation using opposite regression leads to incorrect estimations of both the

slope and the y-intercept; the underestimation of the slope, the overestimation of the y-intercept, and declining R^2 values.

Table 4.20. Performance of different coefficient of determinations (R^2) values by the polynomial regression analyses

Semi-empirical models		Coefficient of Determinations (R^2)					
		ISO standard 15927-3			ASHRAE 160P		
Season	Location	Order 3	Order 4	Order 5	Order 3	Order 4	Order 5
One	Top	0.16	0.17	0.32	0.15	0.15	0.26
	Bottom	0.35	0.37	0.47	0.33	0.33	0.40
Two	Top	0.27	0.45	0.45	0.23	0.45	0.45
	Bottom	0.39	0.39	0.40	0.35	0.37	0.37
Three	Top	0.45	0.46	0.60	0.50	0.53	0.68
	Bottom	0.56	0.56	0.68	0.60	0.60	0.72
Four	Top	0.03	0.09	0.10	0.05	0.13	0.13
	Bottom	0.07	0.09	0.09	0.09	0.12	0.12

Piñeiro et al. (2008) have provided empirical evidence and presented analytical proof that when evaluating a model using linear regressions, it is advisable to place the observed values on the y-axis and the predicted values on the x-axis. They further clarified that model evaluation using opposite regression leads to incorrect estimations of both the slope and the y-intercept; the underestimation of the slope, the overestimation of the y-intercept, and declining R^2 values.

The root mean square deviation (RMSD) represents the mean deviation of predicted values of 'n' number of the rain events in each season with respect to the observed (Exp.) ones. It is measured in the same units as the model variable being looked at in Eq. (15).

$$RMSD = \sqrt{\frac{1}{n} \sum_{i=1}^n (\hat{y}_i - y_i)^2} \quad \text{Eq. (15)}$$

In fluid dynamics model-generated research areas (parameters such as wind speed, precipitation, and temperature) to quantify the uniformity of flow behaviour, the

normalised root mean square deviation (NRMSD) is used instead of RMSD. The lower the value of the NRMSD, the higher the accuracy of the model. Low NRMSD values indicate that the model fits the data well and has more precise predictions for unseen/tested data. Higher levels, on the other hand, imply fewer accurate forecasts of the model. The values between 0.2 and 0.5 show that the model can relatively accurately predict the data.

$$\text{NRMSD} = \frac{\text{RMSD}}{|y_{\max} - y_{\min}|} \quad \text{Eq. (16)}$$

where;

y_{\max} is maximum value of mean R_{wdr} in the corresponding season dataset and y_{\min} as the minimum value.

Table 4.21 to Table 4.24 show all the calculated aforementioned parameters, i.e., SD, R^2 , RMSD, and NRMSD, for each season to evaluate the accuracy of the predicted R_{wdr} (mm/h) by the semi-empirical models, ISO standard 15927-3 and ASHRAE standard 160P.

4.6.1. Accuracy of the Predicted R_{wdr} Dataset – Season 1

The coefficient of determinations (R^2) and regression line of the measured (exp.) against the predicted (ISO and ASHRAE models) mean wind-driven rain intensity (R_{wdr}) on the windward façades (NW-SW) of the pilot building for the top and bottom locations during season one (monsoon transitional period – April 1st to May 16th, 2017) are shown in Figure 4.28 (datasets derived from Table 4.16). Table 4.21 also represents error estimations for each location and each model, allowing for a more accurate evaluation of

the models' performance. Referring to the scatter plot (Figure 4.28) and statistical parameters (Table 4.21), it is observed that:

- **ISO (top location)** – Insignificant R^2 ($0.17 < 0.20$); Relatively accurate NRMSD ($0.37 < 0.50$).

The reason behind simultaneously low R-squared and NRMSD is that R^2 only gives information about model fit, 'correlation' between two datasets (Measured and ISO), but no information about the model's predictive performance. However, NRMSD indicates how well the model will perform on unseen data. In other words, it is about scale. The scale of R^2 values can vary significantly, while NRMSD is the normalised error distance.

The R^2 result indicates an insignificant correlation between the two datasets R_{wdr} (Measured and ISO) (R^2 of 17%), and the NRMSD result indicates relatively accurate prediction values of the R_{wdr} , on average, from the measured (actual) values in the dataset; the error in prediction performance is low (37%).

- The ISO model predictive performance for the top location in season one is statistically relatively accurate, with an insignificant correlation.
- **ASHRAE (top location)** – Insignificant R^2 ($0.15 < 0.20$); Low NRMSD ($0.82 > 0.50$).

The R^2 result indicates an insignificant correlation between the two datasets R_{wdr} (Measured and ASHRAE) (R^2 of 15%), and the NRMSD result indicates large discrepancies in prediction values of the R_{wdr} , on average, from the measured (actual) values in the dataset; the error in prediction performance is high (82%).

- The ASHRAE model predictive performance for the top location in season one is statistically low, with an insignificant correlation.

- **ISO (bottom location)** – Weak R^2 ($0.20 < 0.37 < 0.40$); Low NRMSD ($0.60 > 0.50$).

The R^2 result indicates a weak correlation between the two datasets R_{wdr} (Measured and ISO) (R^2 of 37%), and the NRMSD result indicates relatively large discrepancies in prediction values of the R_{wdr} , on average, from the measured (actual) values in the dataset; the error in prediction performance is relatively high (60%).

- The ISO model predictive performance for the bottom location in season one is statistically relatively low, with a weak correlation.
- **ASHRAE (bottom location)** – Weak R^2 ($0.20 < 0.33 < 0.40$); Relatively accurate NRMSD ($0.49 < 0.50$).

The R^2 result indicates a weak correlation between the two datasets R_{wdr} (Measured and ASHRAE) (R^2 of 33%), and the NRMSD result indicates relatively accurate prediction values of the R_{wdr} , on average, from the measured (actual) values in the dataset; the error in prediction performance is relatively low (49%).

- The ASHRAE model predictive performance for the bottom location in season one is statistically relatively accurate, with a weak correlation.

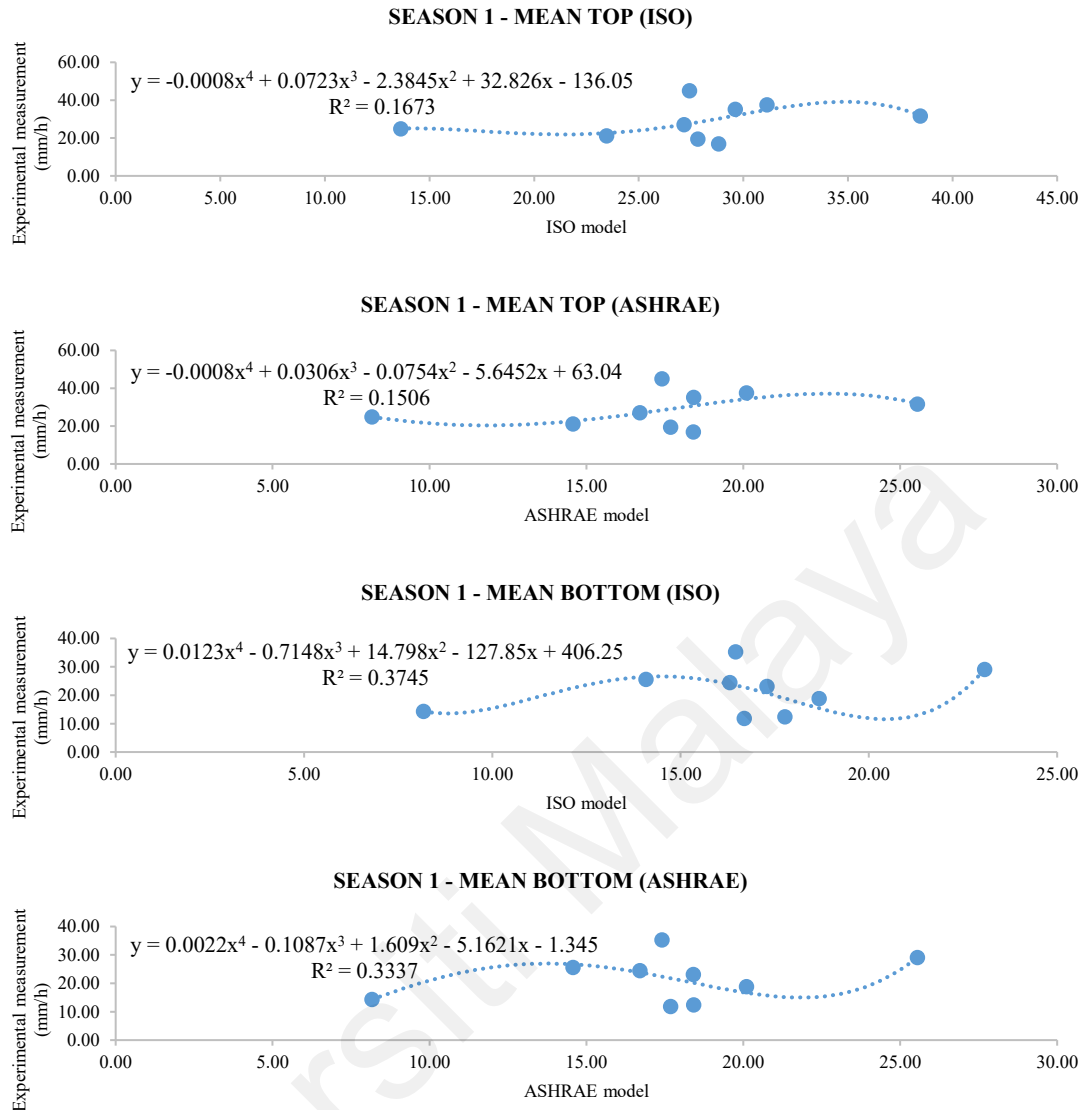


Figure 4.28. Experimental measurement vs. Predicted ISO and ASHRAE models' regression scatter plots of datasets Mean R_{wdr} (mm/h) for two positions (Top and Bottom) at the windward façade (NW-SW) during season One (The R^2 shown is based on order 4 (quadratic) polynomial regression; $0.2 < \text{Value} < 0.4$ is weak, $0.4 < \text{Value} < 0.6$ is moderate, and $0.6 < \text{Value} < 0.8$ means strong effect on the catch ratio variable).

4.6.2. Accuracy of the Predicted R_{wdr} Dataset – Season 2

The coefficient of determinations (R^2) and regression line of the measured (exp.) against the predicted (ISO and ASHRAE models) mean wind-driven rain intensity (R_{wdr}) on the windward façades (NW-SW) of the pilot building for the top and bottom locations during season two (Southwest monsoon – May 17th to October 5th, 2017) are shown in Figure 4.29 (datasets derived from Table 4.17). Table 4.22 also represents error estimations for

each location and each model, allowing for a more accurate evaluation of the models' performance. Referring to the scatter plot (Figure 4.29) and statistical parameters (Table 4.22), it is observed that:

- **ISO (top location)** – Moderate R^2 ($0.40 < 0.45 < 0.60$); Relatively accurate NRMSD ($0.36 < 0.50$).

The R^2 result indicates a moderate correlation between the two datasets R_{wdr} (Measured and ISO) (R^2 of 45%), and the NRMSD result indicates relatively accurate prediction values of the R_{wdr} deviate, on average, from the measured (actual) values in the dataset; the error in prediction performance is low (36%).

- The ISO model predictive performance for the top location in season two is statistically relatively accurate, with a moderate correlation.

- **ASHRAE (top location)** – Moderate R^2 ($0.40 < 0.45 < 0.60$); Relatively low NRMSD ($0.57 > 0.50$).

The R^2 result indicates a moderate correlation between the two datasets R_{wdr} (Measured and ASHRAE) (R^2 of 45%), and the NRMSD result indicates slightly large differences in prediction values of the R_{wdr} , on average, from the measured (actual) values in the dataset; the error in prediction performance is slightly high (57%).

- The ASHRAE model predictive performance for the top location in season two is statistically relatively low, with a moderate correlation.

- **ISO (bottom location)** – Weak / relatively moderate R^2 ($0.20 < 0.39 < 0.40$); Low NRMSD ($0.80 > 0.50$).

The R^2 result indicates a relatively moderate correlation between the two datasets R_{wdr} (Measured and ISO) (R^2 of 39%), and the NRMSD result indicates large

differences in prediction values of the R_{wdr} , on average, from the measured (actual) values in the dataset; the error in prediction performance is high (80%).

- The ISO model predictive performance for the bottom location in season two is statistically low, with a relatively moderate correlation.
- **ASHRAE (bottom location)** – Weak R^2 ($0.20 < 0.37 < 0.40$); Low NRMSD ($0.74 > 0.50$).

The R^2 result indicates a weak correlation between the two datasets R_{wdr} (Measured and ASHRAE) (R^2 of 37%), and the NRMSD result indicates large differences in prediction values of the R_{wdr} , on average, from the measured (actual) values in the dataset; the error in prediction performance is relatively large (74%).

- The ASHRAE model predictive performance for the bottom location in season two is statistically low, with a weak correlation.

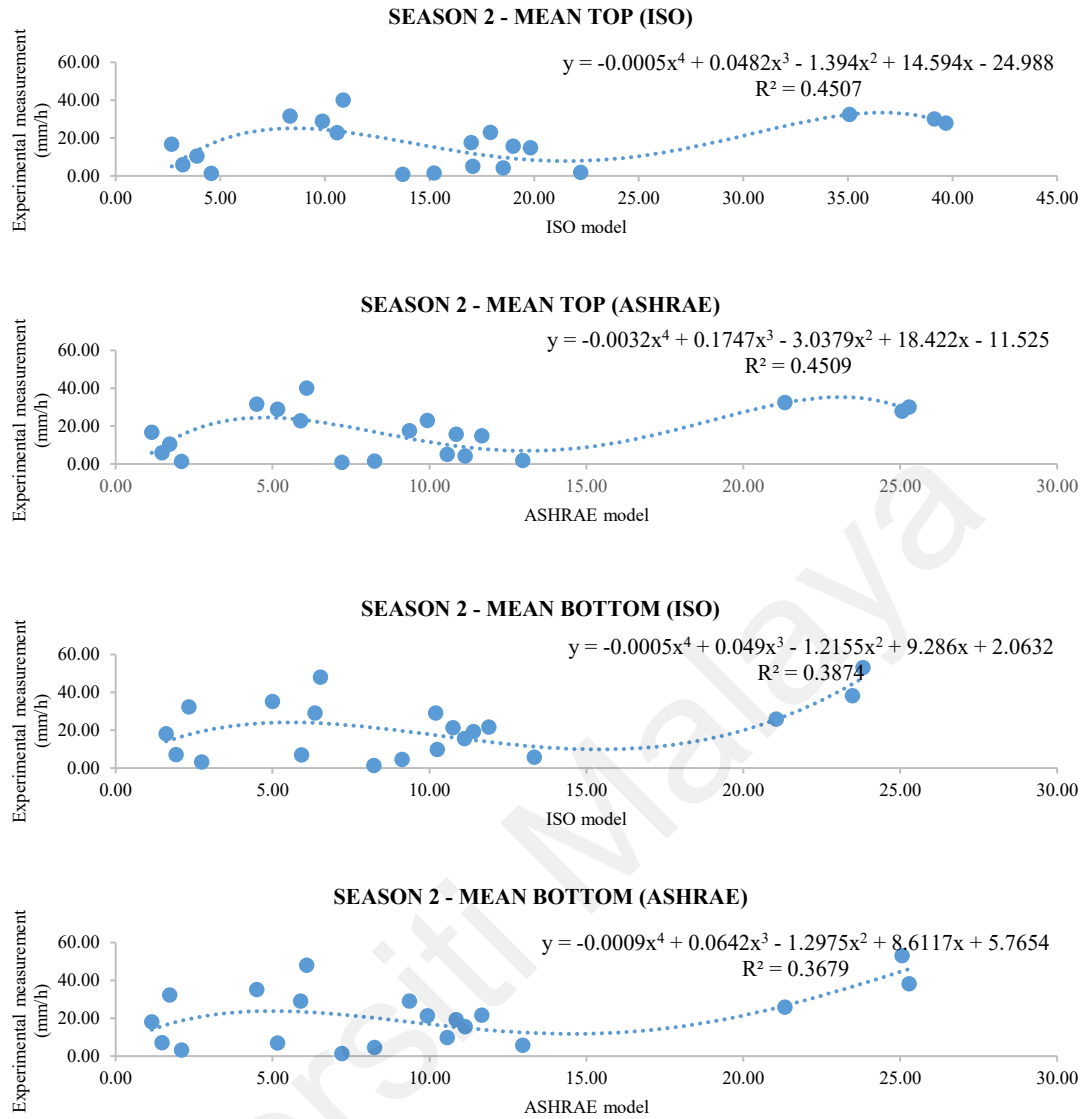


Figure 4.29. Experimental measurement vs. Predicted ISO and ASHRAE models' regression scatter plots of datasets Mean R_{wdr} (mm/h) for two positions (Top and Bottom) at the windward façade (NW-SW) during season Two (The R^2 shown is based on order 4 (quadratic) polynomial regression; $0.2 < \text{Value} < 0.4$ is weak, $0.4 < \text{Value} < 0.6$ is moderate, and $0.6 < \text{Value} < 0.8$ means strong effect on the catch ratio variable).

4.6.3. Accuracy of the Predicted R_{wdr} Dataset – Season 3

The coefficient of determinations (R^2) and regression line of the in-situ measured (exp.) against the predicted (ISO and ASHRAE models) mean wind-driven rain intensity (R_{wdr}) on the windward façades (NW-SW) of the pilot building for the top and bottom locations during season three (Monsoon Transitional Period – 6th October to 12th November 2017) are shown in Figure 4.30 (datasets derived from Table 4.18). Table 4.23 also represents

error estimations for each location and each model, allowing for a more accurate evaluation of the models' performance. Referring to the scatter plot (Figure 4.30) and statistical parameters (Table 4.23), it is observed that:

- **ISO (top location)** – Moderate R^2 ($0.40 < 0.46 < 0.60$); Relatively accurate NRMSD ($0.48 < 0.50$).

The R^2 result indicates a moderate correlation between the two datasets R_{wdr} (Measured and ISO) (R^2 of 46%), and the NRMSD result indicates relatively accurate prediction values of the R_{wdr} deviate, on average, from the measured (actual) values in the dataset; the error in prediction performance is low (48%).

- The ISO model predictive performance for the top location in season three is statistically relatively accurate, with a moderate correlation.

- **ASHRAE (top location)** – Moderate R^2 ($0.40 < 0.53 < 0.60$); Relatively accurate NRMSD ($0.36 < 0.50$).

The R^2 result indicates a moderate correlation between the two datasets R_{wdr} (Measured and ASHRAE) (R^2 of 53%), and the NRMSD result indicates low differences in prediction values of the R_{wdr} , on average, from the measured (actual) values in the dataset; the error in prediction performance is low (36%).

- The ASHRAE model predictive performance for the top location in season three is statistically relatively accurate, with a moderate correlation.

- **ISO (bottom location)** – Moderate R^2 ($0.40 < 0.56 < 0.60$); Relatively accurate NRMSD ($0.32 < 0.50$).

The R^2 result indicates a moderate correlation between the two datasets R_{wdr} (Measured and ISO) (R^2 of 56%), and the NRMSD result indicates low differences in prediction values of the R_{wdr} , on average, from the measured (actual) values in the dataset; the error in prediction performance is low (32%).

- The ISO model predictive performance for the bottom location in season three is statistically relatively accurate, with a moderate correlation.
- **ASHRAE (bottom location)** – Relatively strong R^2 ($0.60 < 0.60 < 0.80$); Relatively accurate NRMSD ($0.35 < 0.50$).

The R^2 result indicates a relatively strong correlation between the two datasets R_{wdr} (Measured and ASHRAE) (R^2 of 60%), and the NRMSD result indicates relatively accurate prediction values of the R_{wdr} , on average, from the measured (actual) values in the dataset; the error in prediction performance is low (35%).

- The ASHRAE model predictive performance for the bottom location in season three is statistically relatively accurate, with a relatively strong correlation.

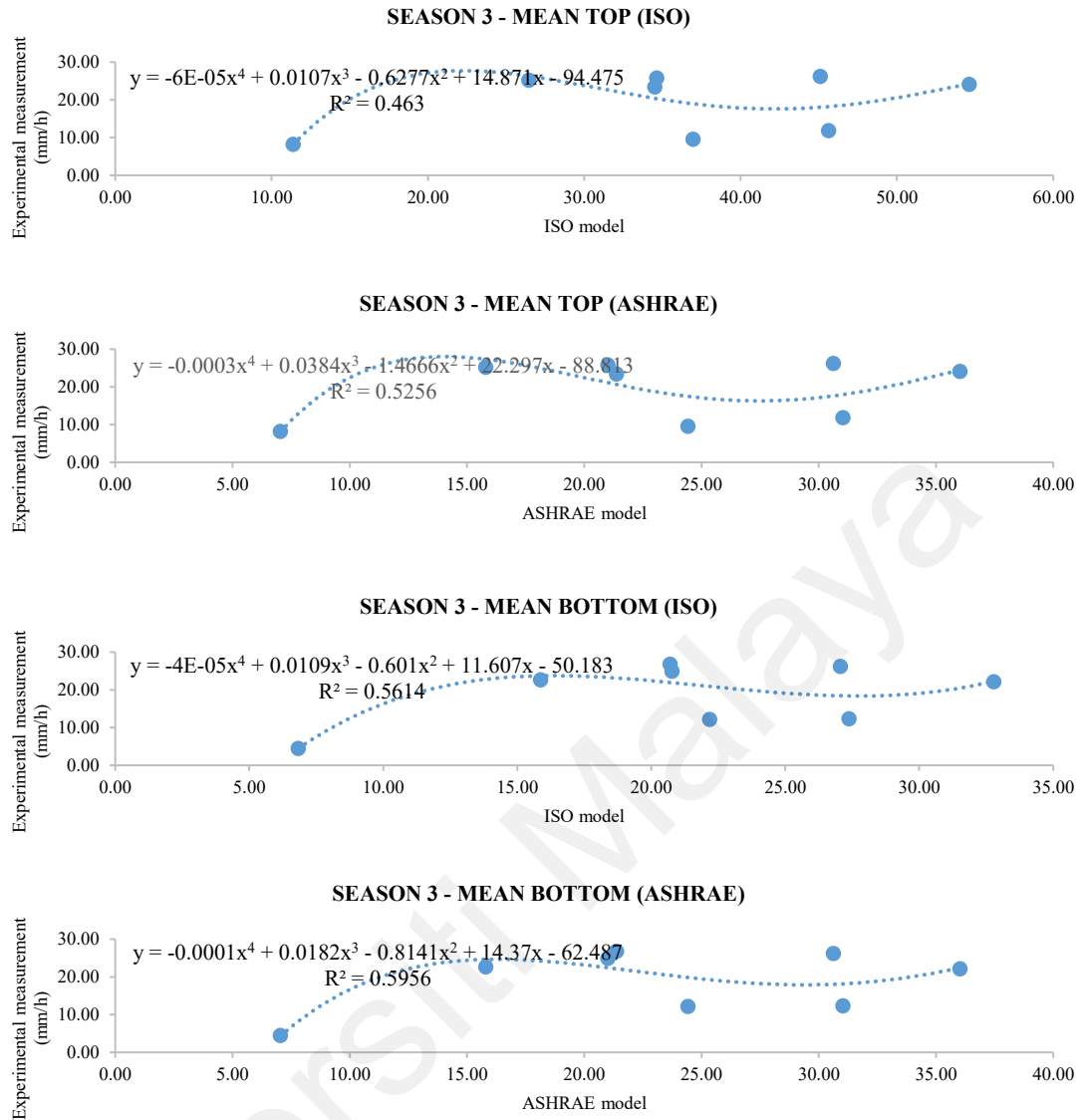


Figure 4.30. Experimental measurement vs. Predicted ISO and ASHRAE models' regression scatter plots of datasets Mean R_{wdr} (mm/h) for two positions (Top and Bottom) at the windward façade (NW-SW) during season Three (The R^2 shown is based on order 4 (quadratic) polynomial regression; $0.2 < \text{Value} < 0.4$ is weak, $0.4 < \text{Value} < 0.6$ is moderate, and $0.6 < \text{Value} < 0.8$ means strong effect on the catch ratio variable).

4.6.4. Accuracy of the Predicted R_{wdr} Dataset – Season 4

The coefficient of determinations (R^2) and regression line of the measured (exp.) against the predicted (ISO and ASHRAE models) mean wind-driven rain intensity (R_{wdr}) on the windward façades (NE-NW) of the pilot building for the top and bottom locations during season four (Northeast Monsoon – November 13th to March 27th, 2018) are shown in Figure 4.31 (datasets derived from Table 4.19). Table 4.24 also represents error

estimations for each location and each model, allowing for a more accurate evaluation of the models' performance. Referring to the scatter plot (Figure 4.31) and statistical parameters (Table 4.24), it is observed that:

- **ISO (top location)** – Insignificant R^2 ($0.09 < 0.20$); Relatively accurate NRMSD ($0.45 < 0.50$).

The reason behind simultaneously low R-squared and NRMSD can be similarly explained, as in Section 4.6.1 for season one; R^2 only gives information about model fit; 'correlation' between the two datasets (Measured and ISO), NRMSD indicates how well the model will perform on unseen data.

The R^2 result indicates an insignificant correlation between the two datasets R_{wdr} (Measured and ISO) (R^2 of 9%), and the NRMSD result indicates relatively accurate prediction values of the R_{wdr} , on average, from the measured (actual) values in the dataset; the error in prediction performance is low (45%).

- The ISO model predictive performance for the top location in season four is statistically relatively accurate, with an insignificant correlation.
- **ASHRAE (top location)** – Insignificant R^2 ($0.13 < 0.20$); Relatively accurate NRMSD ($0.49 < 0.50$).

The R^2 result indicates an insignificant correlation between the two datasets R_{wdr} (Measured and ASHRAE) (R^2 of 13%), and the NRMSD result indicates relatively accurate prediction values of the R_{wdr} , on average, from the measured (actual) values in the dataset; the error in prediction performance is relatively low (49%).

- The ASHRAE model predictive performance for the top location in season four is statistically relatively accurate, with an insignificant correlation.

- **ISO (bottom location)** – Insignificant R^2 ($0.09 < 0.20$); Low NRMSD ($0.88 > 0.50$).

The R^2 result indicates an insignificant correlation between the two datasets R_{wdr} (Measured and ISO) (R^2 of 9%), and the NRMSD result indicates large differences in prediction values of the R_{wdr} , on average, from the measured (actual) values in the dataset; the error in prediction performance is high (88%).

- The ISO model predictive performance for the bottom location in season four is statistically low, with an insignificant correlation.
- **ASHRAE (bottom location)** – Insignificant R^2 ($0.12 < 0.20$); Relatively accurate NRMSD ($0.51 > 0.50$).

The R^2 result indicates an insignificant correlation between the two datasets R_{wdr} (Measured and ASHRAE) (R^2 of 12%), and the NRMSD result indicates relatively low differences in prediction values of the R_{wdr} , on average, from the measured (actual) values in the dataset; the error in prediction performance is relatively low (51%).

- The ASHRAE model predictive performance for the bottom location in season four is statistically relatively accurate, with an insignificant correlation.

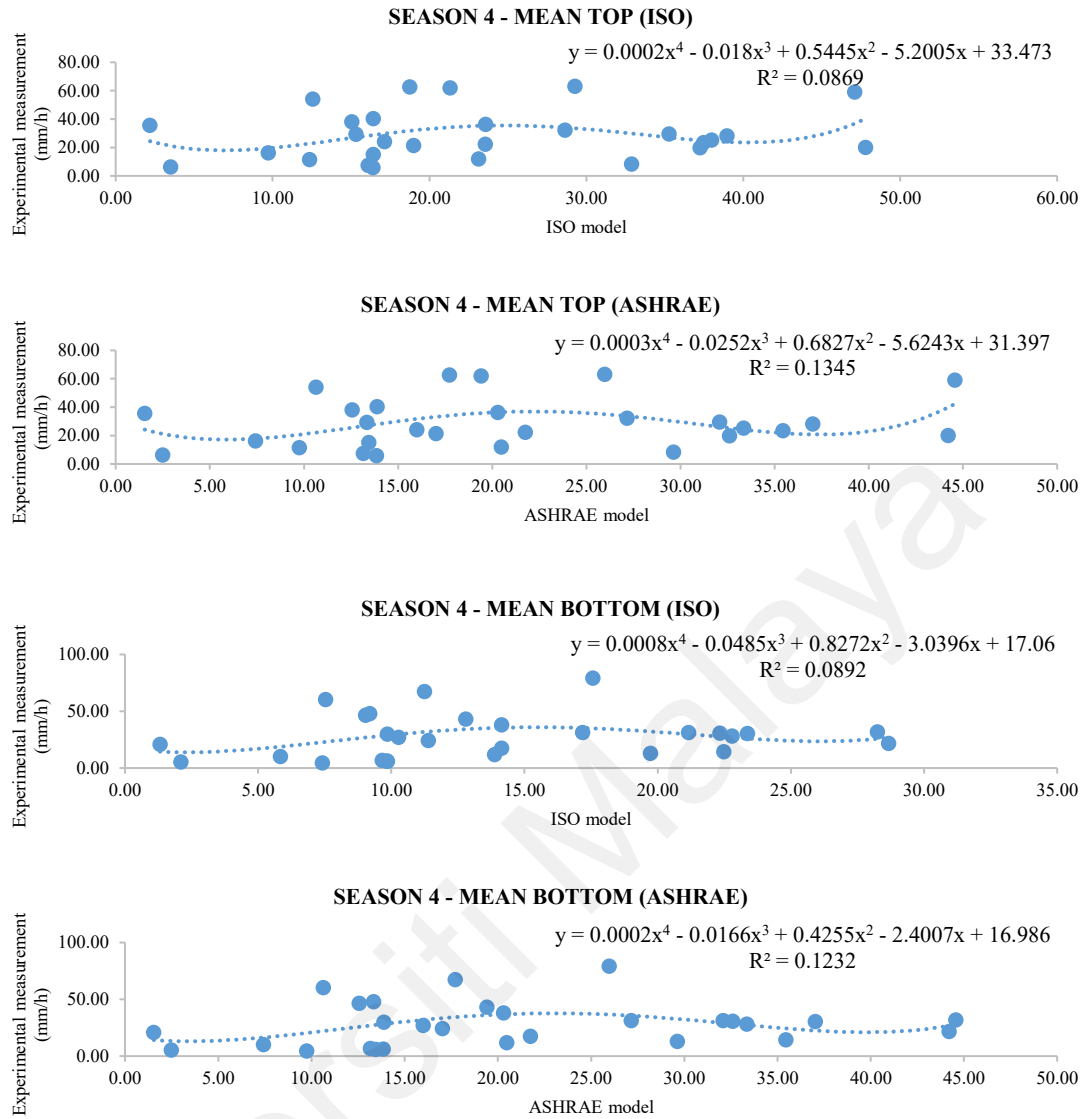


Figure 4.31. Experimental measurement vs. Predicted ISO and ASHRAE Models' regression scatter plots of datasets Mean R_{wdr} (mm/h) for two positions (Top and Bottom) at the windward façade (NE-NW) during season Four (The R^2 shown is based on order 4 (quadratic) polynomial regression; $0.2 < \text{Value} < 0.4$ is weak, $0.4 < \text{Value} < 0.6$ is moderate, and $0.6 < \text{Value} < 0.8$ means strong effect on the catch ratio variable).

Table 4.21. Difference (D) (Negative D value shows underestimation, Positive D value shows overestimation), coefficient of determination (R^2), root mean square deviation (RMSD), and normalised root mean square deviation (NRMSD) for predicted R_{wdr} (WDR intensity) (mm/h) by ISO model and ASHRAE model – Season One

Rain Event	Experimental Measurement		ISO Model										ASHRAE Model									
	Top	Bottom	Top					Bottom					Top					Bottom				
	Mean	Mean	Mean	D	R^2	RMSD	NRMSD	Mean	D	R^2	RMSD	NRMSD	Mean	D	R^2	RMSD	NRMSD	Mean	D	R^2	RMSD	NRMSD
21-Apr-17	27.11	24.54	27.17	-0.07	0.17	9.25	0.37	16.30	8.24	0.37	8.93	0.60	16.70	10.40	0.15	14.28	0.82	16.70	7.84	0.33	8.49	0.49
23-Apr-17	17.05	23.11	28.83	-11.78				17.30	5.82				18.41	-1.36				18.41	4.70			
24-Apr-17	21.16	25.59	23.47	-2.30				14.08	11.51				14.57	6.59				14.57	11.01			
26-Apr-17	19.55	11.85	27.82	-8.27				16.69	-4.84				17.68	1.86				17.68	-5.83			
02-May-17	35.28	12.46	29.62	5.65				17.77	-5.31				18.42	16.85				18.42	-5.96			
05-May-17	37.69	18.83	31.13	6.56				18.68	0.15				20.10	17.60				20.10	-1.26			
07-May-17	25.00	14.34	13.63	11.37				8.18	6.16				8.17	16.82				8.17	6.16			
12-May-17	45.00	35.36	27.43	17.57				16.46	18.90				17.40	27.60				17.40	17.95			
13-May-17	31.78	29.10	38.45	-6.68				23.07	6.03				25.54	6.23				25.54	3.56			

Table 4.22. Difference (D) (Negative D value shows underestimation, Positive D value shows overestimation), coefficient of determination (R^2), root mean square deviation (RMSD), and normalised root mean square deviation (NRMSD) for predicted R_{wdr} (WDR intensity) (mm/h) by ISO model and ASHRAE model – Season Two

Rain Event	Experimental Measurement		ISO Model										ASHRAE Model									
	Top	Bottom	Top					Bottom					Top					Bottom				
	Mean	Mean	Mean	D	R^2	RMSD	NRMSD	Mean	D	R^2	RMSD	NRMSD	Mean	D	R^2	RMSD	NRMSD	Mean	D	R^2 Value	RMSD	NRMSD
20-May-17	29.03	6.96	9.88	19.15	0.45	13.36	0.36	5.93	1.03	0.39	17.68	0.80	5.16	23.87	0.45	13.82	0.57	5.16	1.80	0.37	17.77	0.74
23-May-17	1.65	4.65	15.21	-13.56				9.13	-4.48				8.25	-6.60				8.25	-3.60			
25-May-17	6.03	7.17	3.21	2.82				1.93	5.24				1.47	4.56				1.47	5.70			
03-Jun-17	27.91	53.20	39.68	-11.78				23.81	29.39				25.05	2.86				25.05	28.15			
09-Jun-17	1.40	3.28	4.57	-3.17				2.74	0.54				2.10	-0.70				2.10	1.18			
11-Jun-17	5.13	9.95	17.08	-11.95				10.25	-0.30				10.56	-5.44				10.56	-0.61			
12-Jun-17	4.23	15.71	18.52	-14.29				11.11	4.60				11.13	-6.91				11.13	4.58			
14-Jun-17	1.89	5.91	22.23	-20.34				13.34	-7.43				12.97	-11.08				12.97	-7.06			
19-Jun-17	22.88	29.12	10.58	12.29				6.35	22.77				5.89	16.98				5.89	23.22			
11-Jul-17	16.88	18.22	2.68	14.21				1.61	16.61				1.15	15.74				1.15	17.07			
12-Jul-17	15.00	21.64	19.82	-4.82				11.89	9.75				11.67	3.33				11.67	9.97			
13-Jul-17	15.87	19.30	19.00	-3.14				11.40	7.89				10.85	5.01				10.85	8.44			
14-Jul-17	10.52	32.43	3.89	6.63				2.33	30.10				1.72	8.80				1.72	30.71			
20-Jul-17	32.60	25.88	35.07	-2.47				21.04	4.84				21.32	11.28				21.32	4.56			
21-Jul-17	23.13	21.42	17.91	5.21				10.75	10.67				9.93	13.19				9.93	11.48			
22-Jul-17	17.58	29.08	17.00	0.58				10.20	18.88				9.36	8.22				9.36	19.72			
23-Aug-17	31.71	35.29	8.33	23.39				5.00	30.29				4.49	27.22				4.49	30.79			
30-Aug-17	40.07	48.14	10.88	29.20				6.53	41.62				6.08	33.99				6.08	42.06			
31-Aug-17	1.00	1.44	13.72	-12.72				8.23	-6.79				7.20	-6.20				7.20	-5.77			
01-Sep-17	30.25	38.25	39.13	-8.88				23.48	14.77				25.28	4.97				25.28	12.97			

Table 4.23. Difference (D) (Negative D value shows underestimation, Positive D value shows overestimation), coefficient of determination (R^2), root mean square deviation (RMSD), and normalised root mean square deviation (NRMSD) for predicted R_{wdr} (WDR intensity) (mm/h) by ISO model and ASHRAE model – Season Three

Rain Event	Experimental Measurement		ISO Model										ASHRAE Model									
	Top	Bottom	Top					Bottom					Top					Bottom				
	Mean	Mean	Mean	D	R^2	RMSD	NRMSD	Mean	D	R^2	RMSD	NRMSD	Mean	D	R^2	RMSD	NRMSD	Mean	D	R^2	RMSD	NRMSD
27-Oct-17	9.60	12.21	36.96	-27.36	0.46	20.56	0.48	22.18	-9.96	0.56	8.26	0.32	24.42	-14.82	0.53	10.39	0.36	24.42	-12.21	0.60	10.05	0.35
29-Oct-17	25.23	22.69	26.44	-1.21				15.87	6.83				15.79	9.44				15.79	6.90			
03-Nov-17	23.50	26.88	34.50	-11.00				20.70	6.17				21.37	2.13				21.37	5.51			
07-Nov-17	24.17	22.17	54.63	-30.46				32.78	-10.61				36.02	-11.86				36.02	-13.86			
09-Nov-17	25.83	25.00	34.63	-8.80				20.78	4.22				21.01	4.82				21.01	3.99			
10-Nov-17	11.88	12.38	45.63	-33.76				27.38	-15.00				31.03	-19.15				31.03	-18.65			
11-Nov-17	8.20	4.50	11.38	-3.18				6.83	-2.33				7.04	1.16				7.04	-2.54			
12-Nov-17	26.25	26.25	45.10	-18.85				27.06	-0.81				30.62	-4.37				30.62	-4.37			

Table 4.24. Difference (D) (Negative D value shows underestimation, Positive D value shows overestimation), coefficient of determination (R^2), root mean square deviation (RMSD), and normalised root mean square deviation (NRMSD) for predicted R_{wdr} (WDR intensity) (mm/h) by ISO model and ASHRAE model – Season Four

Rain Event	Experimental Measurement		ISO Model										ASHRAE Model									
	Top	Bottom	Top					Bottom					Top					Bottom				
	Mean	Mean	Mean	D	R^2	RMSD	NRMSD	Mean	D	R^2	RMSD	NRMSD	Mean	D	R^2	RMSD	NRMSD	Mean	D	R^2	RMSD	NRMSD
13-Nov-17	29.50	48.13	15.32	14.18	0.09	20.55	0.45	9.19	38.94	0.09	24.02	0.88	13.33	16.17	0.13	20.92	0.49	13.33	34.79	0.12	22.03	0.51
18-Nov-17	8.50	13.00	32.88	-24.38				19.73	-6.73				29.63	-21.13				29.63	-16.63			
25-Nov-17	11.94	11.83	23.13	-11.19				13.88	-2.04				20.48	-8.54				20.48	-8.65			
27-Nov-17	24.15	27.20	17.13	7.02				10.28	16.92				16.00	8.15				16.00	11.20			
28-Nov-17	21.63	24.31	18.98	2.64				11.39	12.92				17.02	4.61				17.02	7.29			
29-Nov-17	25.27	28.27	37.98	-12.71				22.79	5.48				33.34	-8.07				33.34	-5.07			
01-Dec-17	32.40	31.50	28.64	3.76				17.19	14.31				27.16	5.24				27.16	4.34			
02-Dec-17	29.64	31.36	35.26	-5.62				21.16	10.20				32.08	-2.44				32.08	-0.72			
03-Dec-17	36.43	38.14	23.57	12.86				14.14	24.00				20.30	16.13				20.30	17.84			
10-Dec-17	20.25	21.90	47.79	-27.54				28.68	-6.78				44.21	-23.96				44.21	-22.31			
17-Dec-17	54.17	60.42	12.56	41.61				7.54	52.88				10.64	43.52				10.64	49.77			
19-Dec-17	20.05	30.95	37.24	-17.19				22.34	8.61				32.60	-12.55				32.60	-1.65			
25-Dec-17	63.23	79.20	29.27	33.95				17.56	61.64				25.96	37.26				25.96	53.24			
26-Dec-17	38.21	46.50	15.05	23.17				9.03	37.47				12.56	25.65				12.56	33.94			
27-Dec-17	59.25	32.10	47.09	12.16				28.25	3.85				44.56	14.69				44.56	-12.46			
31-Dec-17	5.90	6.40	16.39	-10.49				9.83	-3.43				13.85	-7.95				13.85	-7.45			
17-Jan-18	40.50	30.00	16.42	24.08				9.85	20.15				13.88	26.62				13.88	16.12			
19-Jan-18	22.50	17.68	23.56	-1.06				14.14	3.54				21.75	0.75				21.75	-4.07			
20-Jan-18	28.29	30.50	38.95	-10.66				23.37	7.13				37.03	-8.74				37.03	-6.53			
28-Jan-18	62.81	67.50	18.74	44.08				11.24	56.26				17.72	45.09				17.72	49.78			
30-Jan-18	62.00	43.33	21.32	40.68				12.79	30.54				19.42	42.58				19.42	23.92			
28-Feb-18	23.46	14.61	37.47	-14.02				22.48	-7.88				35.44	-11.98				35.44	-20.83			
04-Mar-18	16.31	10.15	9.73	6.57				5.84	4.31				7.43	8.88				7.43	2.72			
08-Mar-18	6.50	5.50	3.50	3.01				2.10	3.40				2.49	4.02				2.49	3.01			
10-Mar-18	7.54	7.01	16.10	-8.56				9.66	-2.64				13.16	-5.62				13.16	-6.15			
13-Mar-18	35.78	20.87	2.19	33.59				1.31	19.56				1.54	34.23				1.54	19.33			
15-Mar-18	11.53	4.50	12.36	-0.83				7.42	-2.92				9.75	1.79				9.75	-5.25			
16-Mar-18	15.26	5.99	16.41	-1.15				9.85	-3.86				13.45	1.81				13.45	-7.46			

4.6.5. Summary of Findings – Accuracy of the Predictive Performance of the Models

A dataset of mean wind-driven rain intensity (R_{wdr}) from a total of 65 validated rain events through one-year experimental measurement was validated in Section 4.4 to generate calculated datasets by the semi-empirical models, i.e., ISO standard 15927-3 and ASHRAE standard 160P in Section 4.5. The three datasets were compared to determine the degree of discrepancies (errors) and evaluate the validity of the models' predictive performances in Section 4.6. Two main statistical criteria, namely coefficient of determination (R^2) (based on the order 4 (quadratic) polynomial regression model), and normalised root mean square deviation (NRMSD) (based on Eq. (16)), were applied to evaluate the correlation between two datasets and the accuracy of predicting R_{wdr} on the windward façade of the pilot building by the models. R^2 provides information about the correlation between two datasets, while NRMSD quantifies the normalised difference between them (error). In light of the aim of the current analysis section, quantification of error between the experimental measurement dataset of the mean R_{wdr} and each model's, NRMSD is considered the right evaluation metrics to proceed with to quantify the accuracy of the predictions.

The results indicated a mixed perspective on the models' performances throughout the year. The inherent complexity of WDR load prediction on building walls, however, anticipated this outcome.

A summary of comparison analyses (Section 4.5) and accuracy evaluations (validation) of the models against the experimental dataset, predictive performance (Section 4.6), is presented as follows:

- **Season One – ISO model** – The overall trends of the predicted mean R_{wdr} (mm/h) for the 9 validated rain events at top and bottom locations on the windward façades

(NW-SW) are quite similar (Figure 4.24). The discrepancy during the entire season one is relatively low (majority underestimating) or almost zero from the Exp. measured values for some cases.

- The ISO model for season one shows statistically relatively accurate prediction values for higher locations (NRMSD 0.37) and relatively low values for lower locations (NRMSD 0.60) (Table 4.21) on the façade.
- **Season One – ASHRAE model** – The trends of the predicted mean R_{wdr} (mm/h) for the 9 validated rain events at top and bottom locations on the windward façades (NW-SW) are identical (Figure 4.24) because the F_D factor in ASHRAE remains constant across all façade heights. The discrepancy during the entire season one is relatively large (mostly underestimating) from the Exp. measured values, except for a few cases.
- The ASHRAE model for season one shows statistically low prediction values for higher locations (NRMSD 0.82) and relatively accurate values for lower locations (NRMSD 0.49) (Table 4.21) on the façade.
- **Season Two – ISO model** – The overall trends of the predicted mean R_{wdr} (mm/h) for the 20 validated rain events at top and bottom locations on the windward façades (NW-SW) are quite similar (Figure 4.25). The discrepancy during the entire season two is relatively low (majority underestimating) for the higher location and relatively large (majority underestimating) for the lower location on the façade, with several cases in good agreement.
- The ISO model for season two shows statistically relatively accurate prediction values for higher locations (NRMSD 0.36) and low values for lower locations (NRMSD 0.80) (Table 4.22) on the façade.

- **Season Two – ASHRAE model** – The trends of the predicted mean R_{wdr} (mm/h) for the 20 validated rain events at top and bottom locations on the windward façades (NW-SW) are identical (Figure 4.25) because the F_D factor in ASHRAE remains constant across all façade heights. The discrepancy during the entire season two is relatively large (mostly underestimating) from the Exp. measured values, except for some cases in good agreement.
- The ASHRAE model for season two shows statistically relatively low prediction values for higher locations (NRMSD 0.57) and low values for lower locations (NRMSD 0.74) (Table 4.22) on the façade.
- **Season Three – ISO model** – The overall trends of the predicted mean R_{wdr} (mm/h) for the 8 validated rain events at top and bottom locations on the windward façades (NW-SW) are quite similar (Figure 4.26). The discrepancy during the entire season three is generally slightly moderate (majority overestimating) from the Exp. measured values, with several cases in good agreement.
- The ISO model for season three shows statistically relatively accurate prediction values for higher locations (NRMSD 0.48) and lower locations (NRMSD 0.32) (Table 4.23) on the façade.
- **Season Three – ASHRAE model** – The trends of the predicted mean R_{wdr} (mm/h) for the 8 validated rain events at top and bottom locations on the windward façades (NW-SW) are identical (Figure 4.26) because the F_D factor in ASHRAE remains constant across all façade heights. The discrepancy during the entire season three is low (mostly overestimated) from the Exp. measured values, and the calculated cases are mostly in good agreement.

- The ASHRAE model for season three shows statistically relatively accurate prediction values for higher locations (NRMSD 0.36) and lower locations (NRMSD 0.35) (Table 4.23) on the façade.
- **Season Four – ISO model** – The overall trends of the predicted mean R_{wdr} (mm/h) for the 28 validated rain events at top and bottom locations on the windward façades (NE-NW) are quite similar (Figure 4.27). The discrepancy during the entire season four is relatively low (majority underestimating) from the Exp. measured values, with nearly all cases in good agreement.
- The ISO model for season four shows statistically relatively accurate prediction values for higher locations (NRMSD 0.45) and low values for lower locations (NRMSD 0.88) (Table 4.24) on the façade.
- **Season Four – ASHRAE model** – The trends of the predicted mean R_{wdr} (mm/h) for the 28 validated rain events at top and bottom locations on the windward façades (NE-NW) are identical (Figure 4.26) because the F_D factor in ASHRAE remains constant across all façade heights. The discrepancy during the entire season four is relatively low (majority underestimating) from the Exp. measured values, with nearly all cases in good agreement.
- The ASHRAE model for season four shows statistically a relatively accurate prediction values for higher locations (NRMSD 0.49) and lower locations (NRMSD 0.51) (Table 4.24) on the façade.

Table 4.25 provides a summary of the predictive performance of the semi-empirical models, i.e., ISO standard 15927-3 and ASHRAE standard 160P models, in estimating R_{wdr} (mm/h) for both locations on the building façade for each season separately.

Table 4.25. Predictive performance of the ISO and ASHRAE models for the top and bottom locations on the building façade for each season (0.20 < NRMSD < 0.50 is relatively accurate)

Seasons	ISO Standard 15927-3 Model	NRMSD value	ASHRAE STANDARD 160P Model	NRMSD value
01 (Top / Bottom)	Relatively Accurate / Relatively Low	0.37 / 0.60	Low / Relatively Accurate	0.82 / 0.42
02 (Top / Bottom)	Relatively Accurate / Low	0.36 / 0.80	Relatively Low / Low	0.57 / 0.74
03 (Top / Bottom)	Relatively Accurate	0.48 / 0.32	Relatively Accurate	0.36 / 0.35
04 (Top / Bottom)	Relatively Accurate / Low	0.45 / 0.88	Relatively Accurate	0.49 / 0.51

4.7. Determining WDR Coefficients for the Semi-Empirical Models

In the previous section, the accuracy performance of the two semi-empirical models, i.e., ISO standard 15927-3 and ASHRAE standard 160P, were evaluated by comparison with the experimental results. Table 4.25 shows the level of predictive performance of each model. It was observed that the ASHARE in general suffers more in relatively accurately predicting R_{wdr} on the windward façade of the pilot building. In this section, WDR coefficients for the ISO model (α) and the ASHRAE model (F_L) are calculated using the experimental measured R_{wdr} and semi-empirical parameters extracted from Table 4.12 to Table 4.15 for each location (top and bottom) and season separately.

4.7.1. Application of the Proposed WDR Coefficients (α) and (F_L)

Eq. (10) and Eq. (13) are respectively used to determine (α) for ISO standard 15927-3 and (F_L) for ASHRAE standard 160P. The results are presented in Table 4.26 to Table 4.29 for each season for top and bottom locations individually, as well as the Mean value (top and bottom) of the WDR coefficients. The mean value will be used as the representative constant for the windward façade for each model to be generalised as the proposed WDR coefficient.

Table 4.26. Determined WDR Coefficient - Season One

Rain Event	α (ISO)		F _L (ASHRAE)	
	Top	Bottom	Top	Bottom
21-Apr-17	0.221	0.334	0.325	0.294
23-Apr-17	0.131	0.297	0.185	0.251
24-Apr-17	0.200	0.403	0.290	0.351
26-Apr-17	0.156	0.158	0.221	0.134
02-May-17	0.264	0.156	0.383	0.135
05-May-17	0.269	0.224	0.375	0.187
07-May-17	0.407	0.389	0.612	0.351
12-May-17	0.364	0.477	0.517	0.406
13-May-17	0.183	0.280	0.249	0.228
Average	0.244	0.302	0.351	0.260
Mean (Top & Bottom)	0.273		0.305	

Table 4.27. Determined WDR Coefficient – Season Two

Rain Event	α (ISO)		F _L (ASHRAE)	
	Top	Bottom	Top	Bottom
20-May-17	0.652	0.261	1.125	0.270
23-May-17	0.024	0.113	0.040	0.113
25-May-17	0.417	0.827	0.818	0.973
03-Jun-17	0.156	0.496	0.223	0.425
09-Jun-17	0.068	0.266	0.133	0.312
11-Jun-17	0.067	0.216	0.097	0.188
12-Jun-17	0.051	0.314	0.076	0.282
14-Jun-17	0.019	0.098	0.029	0.091
19-Jun-17	0.480	1.018	0.776	0.988
11-Jul-17	1.400	2.517	2.946	3.179
12-Jul-17	0.168	0.404	0.257	0.371
13-Jul-17	0.185	0.376	0.292	0.356
14-Jul-17	0.601	3.086	1.224	3.772
20-Jul-17	0.206	0.273	0.306	0.243
21-Jul-17	0.287	0.442	0.466	0.431
22-Jul-17	0.230	0.633	0.376	0.621
23-Aug-17	0.845	1.568	1.412	1.571
30-Aug-17	0.818	1.638	1.318	1.583
31-Aug-17	0.016	0.039	0.028	0.040
01-Sep-17	0.172	0.362	0.239	0.303
Average	0.343	0.747	0.609	0.806
Mean (Top & Bottom)	0.545		0.707	

Table 4.28. Determined WDR Coefficient – Season Three

Rain Event	α (ISO)		F _L (ASHRAE)	
	Top	Bottom	Top	Bottom
27-Oct-17	0.058	0.122	0.079	0.100
29-Oct-17	0.212	0.318	0.319	0.287
03-Nov-17	0.151	0.288	0.220	0.252
07-Nov-17	0.098	0.150	0.134	0.123
09-Nov-17	0.166	0.267	0.246	0.238
10-Nov-17	0.058	0.100	0.077	0.080
11-Nov-17	0.160	0.146	0.233	0.128
12-Nov-17	0.129	0.215	0.171	0.171
Average	0.129	0.201	0.185	0.172
Mean (Top & Bottom)	0.165		0.179	

Table 4.29. Determined WDR Coefficient – Season Four

Rain Event	α (ISO)		F_L (ASHRAE)	
	Top	Bottom	Top	Bottom
13-Nov-17	0.428	1.163	0.443	0.722
18-Nov-17	0.057	0.146	0.057	0.088
25-Nov-17	0.115	0.189	0.117	0.116
27-Nov-17	0.313	0.588	0.302	0.340
28-Nov-17	0.253	0.474	0.254	0.286
29-Nov-17	0.148	0.275	0.152	0.170
01-Dec-17	0.251	0.407	0.239	0.232
02-Dec-17	0.187	0.329	0.185	0.195
03-Dec-17	0.343	0.599	0.359	0.376
10-Dec-17	0.094	0.170	0.092	0.099
17-Dec-17	0.957	1.780	1.018	1.135
19-Dec-17	0.120	0.308	0.123	0.190
25-Dec-17	0.479	1.001	0.487	0.610
26-Dec-17	0.564	1.143	0.608	0.740
27-Dec-17	0.279	0.252	0.266	0.144
31-Dec-17	0.080	0.144	0.085	0.092
17-Jan-18	0.547	0.676	0.584	0.432
19-Jan-18	0.212	0.278	0.207	0.163
20-Jan-18	0.161	0.290	0.153	0.165
28-Jan-18	0.744	1.333	0.709	0.762
30-Jan-18	0.646	0.752	0.639	0.446
28-Feb-18	0.139	0.144	0.132	0.082
04-Mar-18	0.372	0.386	0.439	0.273
08-Mar-18	0.413	0.582	0.523	0.442
10-Mar-18	0.104	0.161	0.115	0.107
13-Mar-18	3.630	3.529	4.634	2.704
15-Mar-18	0.207	0.135	0.237	0.092
16-Mar-18	0.206	0.135	0.227	0.089
Average	0.430	0.620	0.478	0.403
Mean (Top & Bottom)	0.525		0.441	

The proposed WDR coefficients α and F_L derived from Table 4.26 to Table 4.29 are categorised and applied to each model, ISO standard 15927-3 (Eq. (10) and ASHRAE standard 160P Eq. (13), to predict R_{wdr} for each tropical season in Kuala Lumpur, Malaysia (Table 4.30). The accuracy and predictive performance of the semi-empirical models using these proposed constants will then be evaluated in the following section.

Table 4.30. Proposed WDR coefficients for ISO Standard 15927-3 model (α) and ASHRAE STANDARD 160P model (F_L) to predict R_{wdr} for each tropical season in Kuala Lumpur, Malaysia

Seasons	ISO Standard 15927-3 Model	ASHRAE STANDARD 160P Model
01	$R_{wdr} = 0.273 C_R C_T O W U_{10} R_h^{0.88} \cos (D - \theta)$	$R_{wdr} = 0.305 F_E F_D U_{10} R_h \cos \theta$
02	$R_{wdr} = 0.545 C_R C_T O W U_{10} R_h^{0.88} \cos (D - \theta)$	$R_{wdr} = 0.707 F_E F_D U_{10} R_h \cos \theta$
03	$R_{wdr} = 0.165 C_R C_T O W U_{10} R_h^{0.88} \cos (D - \theta)$	$R_{wdr} = 0.179 F_E F_D U_{10} R_h \cos \theta$
04	$R_{wdr} = 0.525 C_R C_T O W U_{10} R_h^{0.88} \cos (D - \theta)$	$R_{wdr} = 0.441 F_E F_D U_{10} R_h \cos \theta$

4.7.2. Comparison between R_{wdr} In-situ, Predicted ISO Standard 15927-3 and ASHRAE Standard 160P Models Using Proposed WDR Coefficients

To evaluate the predictive performance of the semi-empirical models (ISO Standard 15927-3 and ASHRAE 160P) by using the proposed WDR coefficients, determined in the previous section, the same procedures as in Section 4.5 are followed, i.e., comparison chart of the Mean R_{wdr} (mm/h), R^2 value, and NRMSD.

R_{wdr} (mm/h) values on the windward façades of the pilot building (Top and Bottom gauges) are calculated using the proposed WDR coefficients and compared with the experimental measurement values to determine the level of discrepancies. To confirm the validity of the proposed WDR coefficients of the semi-empirical equations based on the literature and as discussed in Section 4.6, Eq. (16) of the NRMSD method will be applied as the main statistical assessment approach for this purpose in this section.

4.7.2.1. Proposed R_{wdr} Dataset – Season 1

- **Proposed ISO and Proposed ASHRAE** – Figure 4.32 shows that the trendlines of the proposed predicted R_{wdr} (mm/h) by ISO and ASHRAE models are more compatible with each other and show a similar behaviour for both top and bottom locations compared with Figure 4.24. ASHRAE has lower values for the top location and higher values for the bottom location compared with ISO during the entire season one.

- **Proposed ISO and Measured (Exp.)** – Table 4.31 indicates the amount of discrepancies calculated for the basic model suggested by the standard and the corresponding proposed one. The minimum R_{wdr} (min) and maximum R_{wdr} (max) values (irrespective of sign (positive or negative)), as well as their difference (max – min) as a statistical indicator are illustrated in the table to evaluate the level of improvement in predictive performance of the proposed WDR coefficients for the models.

Figure 4.32 and Table 4.31 show the proposed ISO has almost no changes in predicting R_{wdr} (mm/h) for the top location ($17.81 > 17.50$) and good improvement for the bottom location ($14.39 < 18.75$) on the façade compared with the basic model results in season one (Figure 4.24).

Comparing the statistical parameters, i.e., R^2 and NRMSD, in Table 4.35 (proposed) with Table 4.21 (basic standard), indicates that R^2 values for both locations have remained constant (Top 0.17, bottom 0.37), and NRMSD values have improved particularly for the lower location (top $0.36 < 0.37$, bottom $0.42 < 0.60$). It declares an accuracy enhancement in the predictive performance of the proposed ISO model in season one.

- **Proposed ASHRAE and Measured (Exp.)** – The discrepancies show that proposed ASHRAE has significant improvement in predicting R_{wdr} (mm/h) for the top location ($17.40 < 26.24$) and good improvement for the bottom location ($14.70 < 16.69$) on the façade compared with the basic model suggested by the standard results in season one (Figure 4.24).

Comparing the statistical parameters, i.e., R^2 and NRMSD, in Table 4.35 (proposed) with Table 4.21 (basic standard), indicates that R^2 values for both locations have remained constant (Top 0.15, bottom 0.33), and NRMSD values

have improved significantly (top $0.36 < 0.82$, bottom $0.36 < 0.49$). It declares a significant accuracy enhancement in the predictive performance of the proposed ASHRAE model in season one.

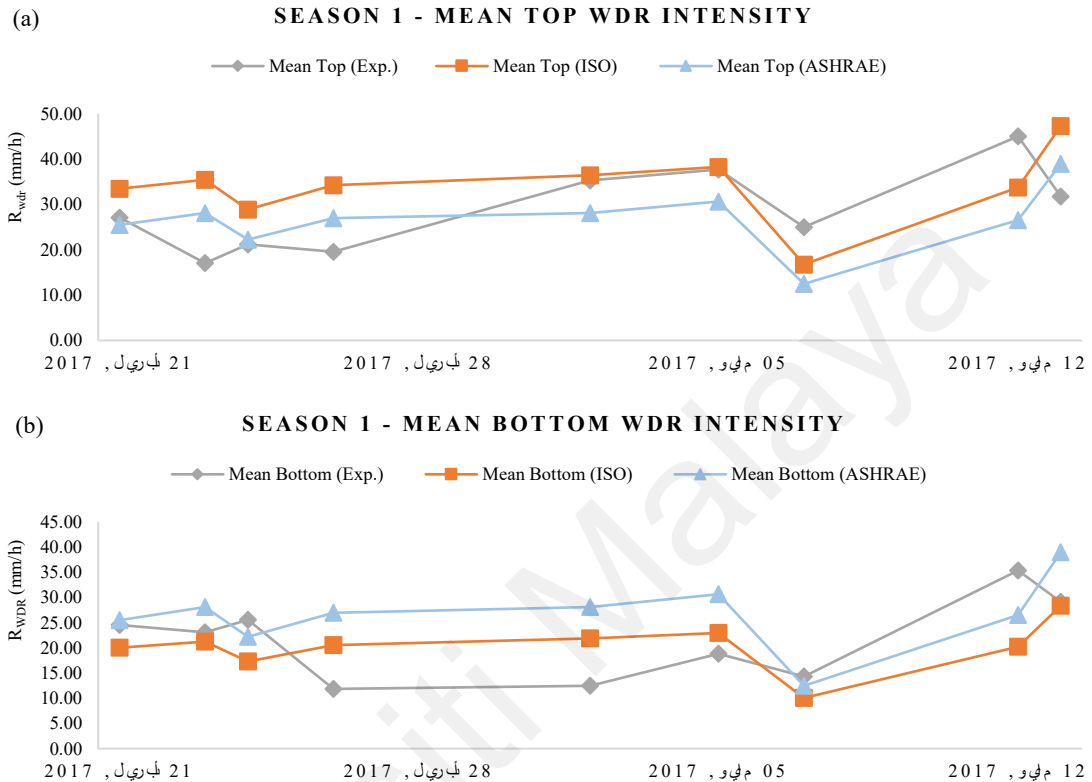


Figure 4.32. Comparison of the Mean R_{wdr} (mm/h) between Experimental measurement and Predicted values using the Proposed WDR coefficients for two positions (Top (a) and Bottom (b)) on the windward façade (NW-SW) – Season One

Table 4.31. R_{wdr} (WDR intensity) (mm/h) discrepancies (D) using the WDR coefficients of the Standard Models (ISO Standard 15927-3 and ASHRAE 160P) and the Proposed WDR Coefficients on windward façades (NW-SW) – Season One

Rain Event	ISO		Proposed ISO		ASHRAE		Proposed ASHRAE	
	D - Top	D - Bottom	D - Top	D - Bottom	D - Top	D - Bottom	D - Top	D - Bottom
21-Apr-17	0.07	8.24	6.31	4.49	10.40	7.84	1.63	0.93
23-Apr-17	11.78	5.82	18.40	1.84	1.36	4.70	11.03	4.97
24-Apr-17	2.30	11.51	7.69	8.27	6.59	11.01	1.06	3.36
26-Apr-17	8.27	4.84	14.67	8.68	1.86	5.83	7.42	15.12
02-May-17	5.65	5.31	1.15	9.39	16.85	5.96	7.18	15.63
05-May-17	6.56	0.15	0.59	4.14	17.60	1.26	7.04	11.81
07-May-17	11.37	6.16	8.24	4.28	16.82	6.16	12.53	1.87
12-May-17	17.57	18.90	11.27	15.12	27.60	17.95	18.46	8.82
13-May-17	6.68	6.03	15.51	0.73	6.23	3.56	7.18	9.85
Min (mm/h)	0.07	0.15	0.59	0.73	1.36	1.26	1.06	0.93
Max (mm/h)	17.57	18.90	18.40	15.12	27.60	17.95	18.46	15.63
Max – Min (mm/h)	17.50	18.75	17.81	14.39	26.24	16.69	17.40	14.70

4.7.2.2. Proposed R_{wdr} Dataset – Season 2

- **Proposed ISO and Proposed ASHRAE** – Figure 4.33 shows that the trendlines of the proposed predicted R_{wdr} (mm/h) by the ISO and ASHRAE models are more compatible with each other and show a similar behaviour for both top and bottom locations compared with Figure 4.25. ASHRAE has lower values for the top location and higher values for the bottom location compared with ISO during the entire season two.
- **Proposed ISO and Measured (Exp.)** – Figure 4.33 and Table 4.32 show the proposed ISO has a large regression (failing) in predicting R_{wdr} (mm/h) for the top location ($68.54 > 28.62$), and a significant improvement for the bottom location ($29.68 < 41.32$) on the façade compared with the basic model results in season two (Figure 4.25).

Comparing the statistical parameters, i.e., R^2 and NRMSD, in Table 4.36 (proposed) with Table 4.22 (basic standard), indicates that R^2 values for both locations have remained constant (Top 0.45, bottom 0.39), and NRMSD values have remained almost constant for the higher location ($0.38 > 0.36$), and improved significantly for the lower location ($0.31 < 0.80$). The values declare an accuracy enhancement in the predictive performance of the proposed ISO model in season two.

- **Proposed ASHRAE and Measured (Exp.)** – The discrepancies demonstrated in Figure 4.33 and Table 4.32 show that the proposed ASHRAE has a large regression (failing) in predicting R_{wdr} (mm/h) for the top location ($59.83 > 33.29$) and a lower regression (failing) for the bottom location ($49.15 > 41.45$) on the façade compared with the basic model results in season two (Figure 4.25).

Comparing the statistical parameters, i.e., R^2 and NRMSD, in Table 4.36 (proposed) with Table 4.22 (basic standard), indicates that R^2 values for both locations have remained constant (Top 0.45, bottom 0.37), and NRMSD values have improved significantly (top $0.34 < 0.57$, bottom $0.31 < 0.74$). It declares a significant accuracy enhancement in the predictive performance of the proposed ASHRAE model in season two.

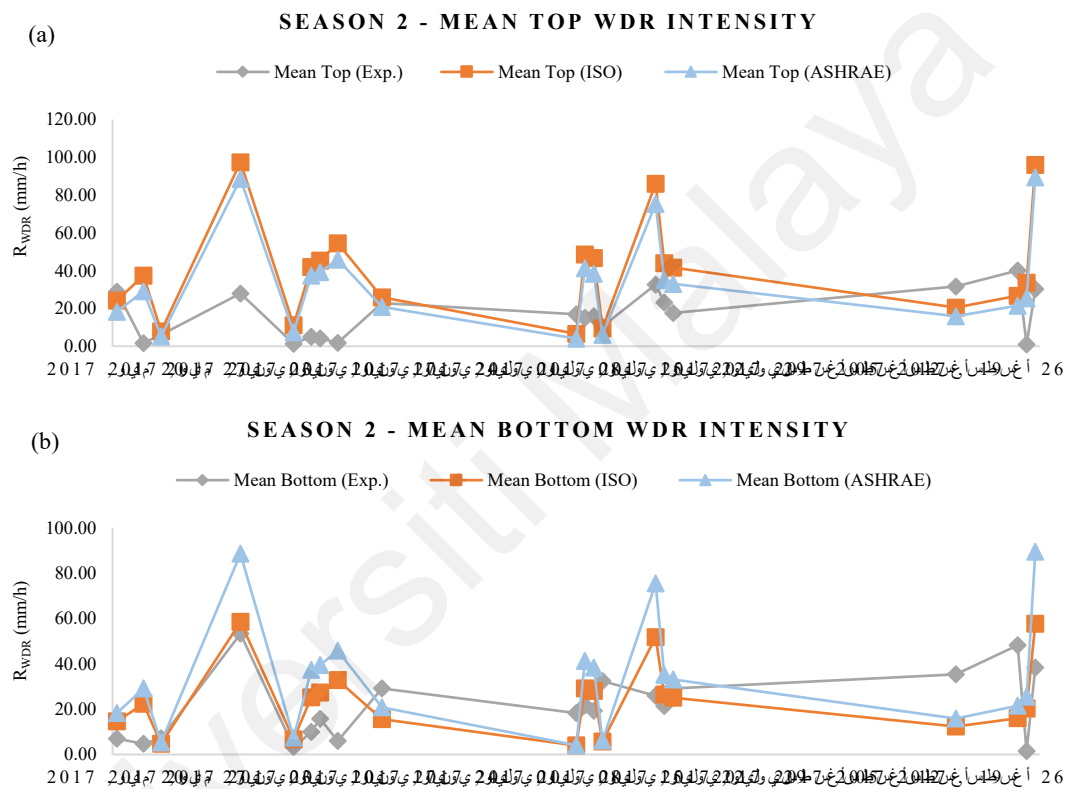


Figure 4.33. Comparison of the Mean R_{wdr} (mm/h) between Experimental measurement and Predicted values using the Proposed WDR coefficients for two positions (Top (a) and Bottom (b)) on the windward façade (NW-SW) – Season Two

Table 4.32. R_{wdr} (WDR intensity) (mm/h) discrepancies (D) using the WDR coefficients of the Standard Models (ISO Standard 15927-3 and ASHRAE 160P) and the Proposed WDR Coefficients on windward façades (NW-SW) – Season Two

Rain Event	ISO		Proposed ISO		ASHRAE		Proposed ASHRAE	
	D - Top	D - Bottom	D - Top	D - Bottom	D - Top	D - Bottom	D - Top	D - Bottom
20-May-17	19.15	1.03	4.78	7.59	23.87	1.80	10.79	11.28
23-May-17	13.56	4.48	35.70	17.76	6.60	3.60	27.52	24.52
25-May-17	2.82	5.24	1.85	2.44	4.56	5.70	0.82	1.96
03-Jun-17	11.78	29.39	69.51	5.25	2.86	28.15	60.65	35.36
09-Jun-17	3.17	0.54	9.81	3.44	0.70	1.18	6.03	4.14
11-Jun-17	11.95	0.30	36.80	15.20	5.44	0.61	32.21	27.38
12-Jun-17	14.29	4.60	41.23	11.56	6.91	4.58	35.14	23.65
14-Jun-17	20.34	7.43	52.69	26.84	11.08	7.06	43.95	39.93
19-Jun-17	12.29	22.77	3.10	13.53	16.98	23.22	2.04	8.28
11-Jul-17	14.21	16.61	10.31	14.27	15.74	17.07	12.83	14.16
12-Jul-17	4.82	9.75	33.65	7.55	3.33	9.97	26.24	19.60
13-Jul-17	3.14	7.89	30.79	8.70	5.01	8.44	22.49	19.07
14-Jul-17	6.63	30.10	0.97	26.70	8.80	30.71	4.44	26.35
20-Jul-17	2.47	4.84	53.50	25.78	11.28	4.56	42.76	49.48
21-Jul-17	5.21	10.67	20.85	4.97	13.19	11.48	11.99	13.70
22-Jul-17	0.58	18.88	24.15	4.04	8.22	19.72	15.51	4.01
23-Aug-17	23.39	30.29	11.27	23.02	27.22	30.79	15.84	19.41
30-Aug-17	29.20	41.62	13.37	32.12	33.99	42.06	18.57	26.64
31-Aug-17	12.72	6.79	32.68	18.77	6.20	5.77	24.47	24.03
01-Sep-17	8.88	14.77	65.82	19.39	4.97	12.97	59.11	51.11
Min (mm/h)	0.58	0.30	0.97	2.44	0.70	0.61	0.82	1.96
Max (mm/h)	29.20	41.62	69.51	32.12	33.99	42.06	60.65	51.11
Max - Min (mm/h)	28.62	41.32	68.54	29.68	33.29	41.45	59.83	49.15

4.7.2.3. Proposed R_{wdr} Dataset – Season 3

- **Proposed ISO and Proposed ASHRAE** – Figure 4.34 shows that the trendlines of the proposed predicted R_{wdr} (mm/h) by ISO and ASHRAE models are more compatible with each other and show a similar behaviour for both top and bottom locations compared with Figure 4.26. ASHRAE has lower values for the top location and higher values for the bottom location compared with ISO during the entire season three.
- **Proposed ISO and Measured (Exp.)** – Figure 4.34 and Table 4.33 show that the proposed ISO has significant improvement in predicting R_{wdr} (mm/h) for the top location ($21.95 < 32.55$), and good improvement for the bottom location ($10.91 < 14.19$) on the façade compared with the basic model results in season three (Figure 4.26).

Comparing the statistical parameters, i.e., R^2 and NRMSD, in Table 4.37 (proposed) with Table 4.23 (basic standard), indicates that R^2 values for both locations have remained constant (Top 0.46, bottom 0.56), and NRMSD values have improved for the higher location ($0.38 < 0.48$), and slightly increased for the lower location ($0.40 > 0.32$). The values declare an accuracy enhancement in the predictive performance of the proposed ISO model in season three.

- ***Proposed ASHRAE and Measured (Exp.)*** – The discrepancies demonstrated in Figure 4.34 and Table 4.33 show that the proposed ASHRAE has made good improvements in predicting R_{wdr} (mm/h) for both the top location ($14.75 < 17.99$) and the bottom location ($14.25 > 16.11$) on the façade compared with the basic model results in season three (Figure 4.26).

Comparing the statistical parameters, i.e., R^2 and NRMSD, in Table 4.37 (proposed) with Table 4.23 (basic standard), indicates that R^2 values for both locations have remained constant (Top 0.53, bottom 0.60), and NRMSD values have slightly improved and are still relatively accurate (top $0.35 < 0.36$, bottom $0.34 < 0.35$). The values declare accuracy in the predictive performance of the proposed ASHRAE model in season three.

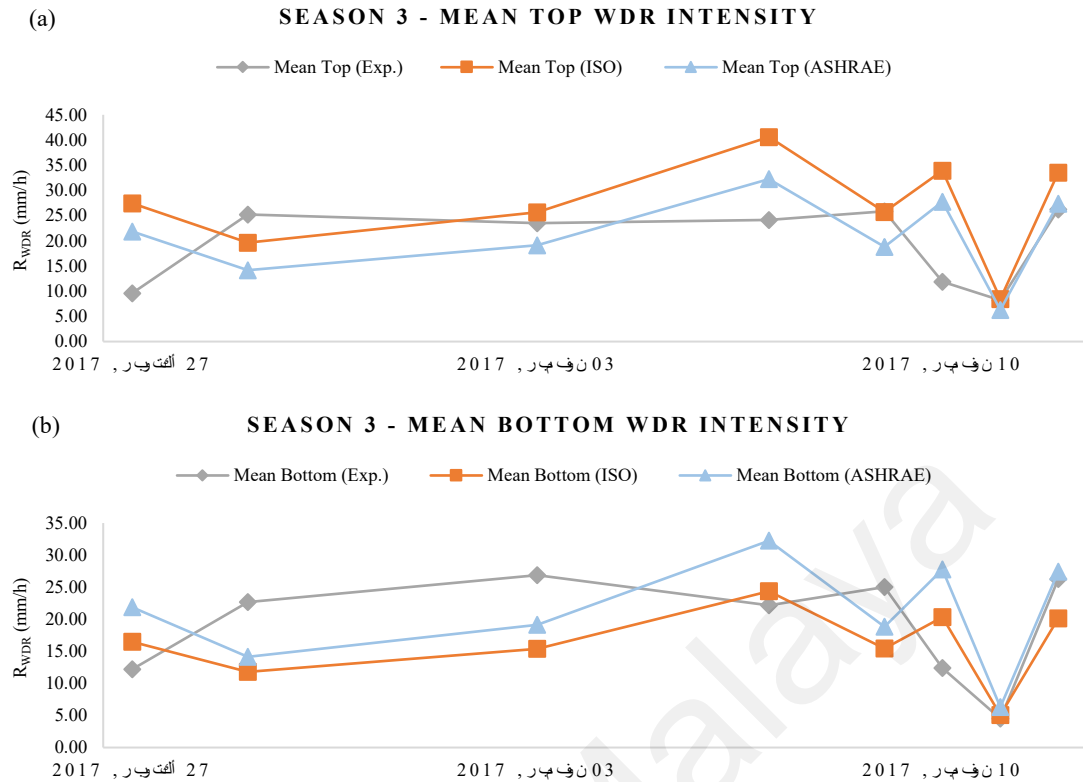


Figure 4.34. Comparison of the Mean R_{wdr} (mm/h) between Experimental measurement and Predicted values using the Proposed WDR coefficients for two positions (Top (a) and Bottom (b)) on the windward façade (NW-SW) – Season Three

Table 4.33. R_{wdr} (WDR intensity) (mm/h) discrepancies (D) using the WDR coefficients of the Standard Models (ISO Standard 15927-3 and ASHRAE 160P) and the Proposed WDR Coefficients on windward façades (NW-SW) – Season Three

Rain Event	ISO		Proposed ISO		ASHRAE		Proposed ASHRAE	
	D - Top	D - Bottom	D - Top	D - Bottom	D - Top	D - Bottom	D - Top	D - Bottom
27-Oct-17	27.36	9.96	17.87	4.27	14.82	12.21	12.26	9.64
29-Oct-17	1.21	6.83	5.58	10.90	9.44	6.90	11.09	8.56
03-Nov-17	11.00	6.17	2.14	11.49	2.13	5.51	4.38	7.75
07-Nov-17	30.46	10.61	16.44	2.19	11.86	13.86	8.07	10.07
09-Nov-17	8.80	4.22	0.09	9.56	4.82	3.99	7.03	6.19
10-Nov-17	33.76	15.00	22.04	7.97	19.15	18.65	15.90	15.40
11-Nov-17	3.18	2.33	0.26	0.58	1.16	2.54	1.90	1.80
12-Nov-17	18.85	0.81	7.27	6.14	4.37	4.37	1.15	1.15
Min (mm/h)	1.21	0.81	0.09	0.58	1.16	2.54	1.15	1.15
Max (mm/h)	33.76	15.00	22.04	11.49	19.15	18.65	15.90	15.40
Max - Min (mm/h)	32.55	14.19	21.95	10.91	17.99	16.11	14.75	14.25

4.7.2.4. Proposed R_{wdr} Dataset – Season 4

- **Proposed ISO and Proposed ASHRAE** – Figure 4.35 shows that the trendlines of the proposed predicted R_{wdr} (mm/h) by ISO and ASHRAE models are more compatible with each other and show a similar behaviour for both top and bottom locations compared with Figure 4.27. ASHRAE has lower values for the top location and higher values for the bottom location compared with ISO during the entire season four.
- **Proposed ISO and Measured (Exp.)** – Figure 4.35 and Table 4.34 show the proposed ISO has a large regression (failing) in predicting R_{wdr} (mm/h) for the top location ($91.12 > 43.25$), and a significant improvement for the bottom location ($45.38 < 59.60$) on the façade compared with the basic model results in season four (Figure 4.27).

Comparing the statistical parameters, i.e., R^2 and NRMSD, in Table 4.38 (proposed) with Table 4.24 (basic standard), indicates that R^2 values for both locations have remained constant (Top 0.09, bottom 0.09), and NRMSD values have improved significantly for the higher location ($0.38 < 0.45$) and for the lower location ($0.38 < 0.88$). The values declare significant accuracy enhancements in the predictive performance of the proposed ISO model in season four.

- **Proposed ASHRAE and Measured (Exp.)** – The discrepancies demonstrated in Figure 4.35 and Table 4.34 show that the proposed ASHRAE has a large regression (failing) in predicting R_{wdr} (mm/h) for both the top location ($77.15 > 44.34$) and the bottom location ($75.57 > 52.52$) on the façade compared with the basic model results in season four (Figure 4.27).

Comparing the statistical parameters, i.e., R^2 and NRMSD, in Table 4.38 (proposed) with Table 4.24 (basic standard), indicates that R^2 values for both

locations have remained constant (Top 0.13, bottom 0.12), and NRMSD values have improved significantly (top $0.35 < 0.49$, bottom $0.36 < 0.51$). It declares a significant accuracy enhancement in the predictive performance of the proposed ASHRAE model in season four.



Figure 4.35. Comparison of the Mean R_{wdr} (mm/h) between Experimental measurement and Predicted values using the Proposed WDR coefficients for two positions (Top (a) and Bottom (b)) on the windward façade (NE-NW) – Season Four

Table 4.34. R_{wdr} (WDR intensity) (mm/h) discrepancies (D) using the WDR coefficients of the Standard Models (ISO Standard 15927-3 and ASHRAE 160P) and the Proposed WDR Coefficients on windward façades (NE-NW) – Season Four

Rain Event	ISO		Proposed ISO		ASHRAE		Proposed ASHRAE	
	D - Top	D - Bottom	D - Top	D - Bottom	D - Top	D - Bottom	D - Top	D - Bottom
13-Nov-17	14.18	38.94	6.72	26.39	16.17	34.79	0.10	18.73
18-Nov-17	24.38	6.73	69.26	33.65	21.13	16.63	56.83	52.33
25-Nov-17	11.19	2.04	42.75	20.99	8.54	8.65	33.22	33.33
27-Nov-17	7.02	16.92	16.35	2.90	8.15	11.20	11.13	8.08
28-Nov-17	2.64	12.92	23.27	2.62	4.61	7.29	15.90	13.21
29-Nov-17	12.71	5.48	64.56	25.62	8.07	5.07	48.25	45.25
01-Dec-17	3.76	14.31	35.34	9.14	5.24	4.34	27.48	28.38
02-Dec-17	5.62	10.20	53.75	18.68	2.44	0.72	41.09	39.38
03-Dec-17	12.86	24.00	19.32	4.69	16.13	17.84	8.33	6.62
10-Dec-17	27.54	6.78	92.78	45.92	23.96	22.31	77.23	75.58
17-Dec-17	41.61	52.88	24.46	42.59	43.52	49.77	30.70	36.95
19-Dec-17	17.19	8.61	68.02	21.88	12.55	1.65	51.84	40.93
25-Dec-17	33.95	61.64	6.00	37.66	37.26	53.24	5.97	21.95
26-Dec-17	23.17	37.47	2.63	25.15	25.65	33.94	10.51	18.79
27-Dec-17	12.16	3.85	52.10	34.71	14.69	12.46	39.01	66.16
31-Dec-17	10.49	3.43	32.86	16.86	7.95	7.45	24.63	24.13
17-Jan-18	24.08	20.15	1.66	6.70	26.62	16.12	9.90	0.60
19-Jan-18	1.06	3.54	33.22	15.75	0.75	4.07	25.47	30.29
20-Jan-18	10.66	7.13	63.82	24.76	8.74	6.53	53.36	51.14
28-Jan-18	44.08	56.26	18.50	40.91	45.09	49.78	23.74	28.43
30-Jan-18	40.68	30.54	11.58	13.08	42.58	23.92	19.19	0.52
28-Feb-18	14.02	7.88	65.16	38.57	11.98	20.83	54.69	63.54
04-Mar-18	6.57	4.31	6.71	3.67	8.88	2.72	0.08	6.24
08-Mar-18	3.01	3.40	1.76	0.54	4.02	3.01	1.02	0.01
10-Mar-18	8.56	2.64	30.53	15.83	5.62	6.15	21.48	22.00
13-Mar-18	33.59	19.56	30.60	17.77	34.23	19.33	32.37	17.47
15-Mar-18	0.83	2.92	17.70	13.04	1.79	5.25	9.96	16.99
16-Mar-18	1.15	3.86	23.54	17.30	1.81	7.46	14.40	23.67
Min (mm/h)	0.83	2.04	1.66	0.54	0.75	0.72	0.08	0.01
Max (mm/h)	44.08	61.64	92.78	45.92	45.09	53.24	77.23	75.58
Max - Min (mm/h)	43.25	59.60	91.12	45.38	44.34	52.52	77.15	75.57

Table 4.35. Proposed difference (D), coefficient of determination (R^2), root mean square deviation (RMSD), and normalised root mean square deviation (NRMSD) for predicted R_{wdr} (WDR intensity) (mm/h) by Proposed WDR coefficients for ISO Standard 15927-3 model (α) and ASHRAE standard 160P model (F_L) – Season One

Rain Event	Experimental Measurement		Proposed ISO Model										Proposed ASHRAE Model									
	Top	Bottom	Top					Bottom					Top					Bottom				
	Mean	Mean	Mean	D	R^2	RMSD	NRMSD	Mean	D	R^2	RMSD	NRMSD	Mean	D	R^2	RMSD	NRMSD	Mean	D	R^2	RMSD	NRMSD
21-Apr-17	27.11	24.54	33.42	-6.31	0.17	11.00	0.36	20.05	4.49	0.37	7.60	0.42	25.47	1.63	0.15	9.61	0.36	25.47	-0.93	0.33	9.59	0.36
23-Apr-17	17.05	23.11	35.45	-18.40				21.27	1.84				28.08	-11.03				28.08	-4.97			
24-Apr-17	21.16	25.59	28.86	-7.69				17.31	8.27				22.22	-1.06				22.22	3.36			
26-Apr-17	19.55	11.85	34.21	-14.67				20.53	-8.68				26.97	-7.42				26.97	-15.12			
02-May-17	35.28	12.46	36.43	-1.15				21.86	-9.39				28.09	7.18				28.09	-15.63			
05-May-17	37.69	18.83	38.29	-0.59				22.97	-4.14				30.65	7.04				30.65	-11.81			
07-May-17	25.00	14.34	16.76	8.24				10.05	4.28				12.46	12.53				12.46	1.87			
12-May-17	45.00	35.36	33.73	11.27				20.24	15.12				26.54	18.46				26.54	8.82			
13-May-17	31.78	29.10	47.28	-15.51				28.37	0.73				38.95	-7.18				38.95	-9.85			

Table 4.36. Proposed difference (D), coefficient of determination (R^2), root mean square deviation (RMSD), and normalised root mean square deviation (NRMSD) for predicted R_{wdr} (WDR intensity) (mm/h) by Proposed WDR coefficients for ISO Standard 15927-3 model (α) and ASHRAE standard 160P model (F_L) – Season Two

Rain Event	Experimental Measurement		Proposed ISO Model										Proposed ASHRAE Model									
	Top	Bottom	Top					Bottom					Top					Bottom				
	Mean	Mean	Mean	D	R^2	RMSD	NRMSD	Mean	D	R^2	RMSD	NRMSD	Mean	D	R^2	RMSD	NRMSD	Mean	D	R^2 Value	RMSD	NRMSD
20-May-17	29.03	6.96	24.25	4.78	0.45	34.53	0.38	14.55	-7.59	0.39	16.93	0.31	18.23	10.79	0.45	29.22	0.34	18.23	-11.28	0.37	26.02	0.31
23-May-17	1.65	4.65	37.35	-35.70				22.41	-17.76				29.17	-27.52				29.17	-24.52			
25-May-17	6.03	7.17	7.88	-1.85				4.73	2.44				5.21	0.82				5.21	1.96			
03-Jun-17	27.91	53.20	97.42	-69.51				58.45	-5.25				88.56	-60.65				88.56	-35.36			
09-Jun-17	1.40	3.28	11.21	-9.81				6.72	-3.44				7.43	-6.03				7.43	-4.14			
11-Jun-17	5.13	9.95	41.92	-36.80				25.15	-15.20				37.33	-32.21				37.33	-27.38			
12-Jun-17	4.23	15.71	45.46	-41.23				27.27	-11.56				39.36	-35.14				39.36	-23.65			
14-Jun-17	1.89	5.91	54.58	-52.69				32.75	-26.84				45.84	-43.95				45.84	-39.93			
19-Jun-17	22.88	29.12	25.97	-3.10				15.58	13.53				20.84	2.04				20.84	8.28			
11-Jul-17	16.88	18.22	6.57	10.31				3.94	14.27				4.05	12.83				4.05	14.16			
12-Jul-17	15.00	21.64	48.65	-33.65				29.19	-7.55				41.24	-26.24				41.24	-19.60			
13-Jul-17	15.87	19.30	46.66	-30.79				27.99	-8.70				38.36	-22.49				38.36	-19.07			
14-Jul-17	10.52	32.43	9.54	0.97				5.73	26.70				6.08	4.44				6.08	26.35			
20-Jul-17	32.60	25.88	86.10	-53.50				51.66	-25.78				75.36	-42.76				75.36	-49.48			
21-Jul-17	23.13	21.42	43.97	-20.85				26.38	-4.97				35.12	-11.99				35.12	-13.70			
22-Jul-17	17.58	29.08	41.73	-24.15				25.04	4.04				33.09	-15.51				33.09	-4.01			
23-Aug-17	31.71	35.29	20.45	11.27				12.27	23.02				15.88	15.84				15.88	19.41			
30-Aug-17	40.07	48.14	26.70	13.37				16.02	32.12				21.50	18.57				21.50	26.64			
31-Aug-17	1.00	1.44	33.68	-32.68				20.21	-18.77				25.47	-24.47				25.47	-24.03			
01-Sep-17	30.25	38.25	96.07	-65.82				57.64	-19.39				89.36	-59.11				89.36	-51.11			

Table 4.37. Proposed difference (D), coefficient of determination (R^2), root mean square deviation (RMSD), and normalised root mean square deviation (NRMSD) for predicted R_{wdr} (WDR intensity) (mm/h) by Proposed WDR coefficients for ISO 15927-3 model (α) and ASHRAE 160p model (F_L) – Season Three

Rain Event	Experimental Measurement		Proposed ISO Model										Proposed ASHRAE Model									
	Top	Bottom	Top					Bottom					Top					Bottom				
	Mean	Mean	Mean	D	R^2	RMSD	NRMSD	Mean	D	R^2	RMSD	NRMSD	Mean	D	R^2	RMSD	NRMSD	Mean	D	R^2	RMSD	NRMSD
27-Oct-17	9.60	12.21	27.47	-17.87	0.46	12.06	0.38	16.48	-4.27	0.56	7.64	0.40	21.86	-12.26	0.53	9.11	0.35	21.86	-9.64	0.60	8.72	0.34
29-Oct-17	25.23	22.69	19.65	5.58				11.79	10.90				14.14	11.09				14.14	8.56			
03-Nov-17	23.50	26.88	25.64	-2.14				15.39	11.49				19.12	4.38				19.12	7.75			
07-Nov-17	24.17	22.17	40.60	-16.44				24.36	-2.19				32.24	-8.07				32.24	-10.07			
09-Nov-17	25.83	25.00	25.74	0.09				15.44	9.56				18.81	7.03				18.81	6.19			
10-Nov-17	11.88	12.38	33.91	-22.04				20.35	-7.97				27.77	-15.90				27.77	-15.40			
11-Nov-17	8.20	4.50	8.46	-0.26				5.08	-0.58				6.30	1.90				6.30	-1.80			
12-Nov-17	26.25	26.25	33.52	-7.27				20.11	6.14				27.40	-1.15				27.40	-1.15			

Table 4.38. Proposed difference (D), coefficient of determination (R^2), root mean square deviation (RMSD), and normalised root mean square deviation (NRMSD) for predicted R_{wdr} (WDR intensity) (mm/h) by Proposed WDR coefficients for ISO Standard 15927-3 model (α) and ASHRAE STANDARD 160P model (F_L) – Season Four

Rain Event	Experimental Measurement		Proposed ISO Model										Proposed ASHRAE Model									
	Top	Bottom	Top					Bottom					Top					Bottom				
	Mean	Mean	Mean	D	R^2	RMSD	NRMSD	Mean	D	R^2	RMSD	NRMSD	Mean	D	R^2	RMSD	NRMSD	Mean	D	R^2	RMSD	NRMSD
13-Nov-17	29.50	48.13	36.22	-6.72	0.09	40.76	0.38	21.73	26.39	0.09	24.37	0.38	29.40	0.10	0.13	33.14	0.35	29.40	18.73	0.12	34.58	0.36
18-Nov-17	8.50	13.00	77.76	-69.26				46.65	-33.65				65.33	-56.83				65.33	-52.33			
25-Nov-17	11.94	11.83	54.70	-42.75				32.82	-20.99				45.16	-33.22				45.16	-33.33			
27-Nov-17	24.15	27.20	40.50	-16.35				24.30	2.90				35.28	-11.13				35.28	-8.08			
28-Nov-17	21.63	24.31	44.89	-23.27				26.94	-2.62				37.52	-15.90				37.52	-13.21			
29-Nov-17	25.27	28.27	89.83	-64.56				53.90	-25.62				73.52	-48.25				73.52	-45.25			
01-Dec-17	32.40	31.50	67.74	-35.34				40.64	-9.14				59.88	-27.48				59.88	-28.38			
02-Dec-17	29.64	31.36	83.39	-53.75				50.03	-18.68				70.74	-41.09				70.74	-39.38			
03-Dec-17	36.43	38.14	55.75	-19.32				33.45	4.69				44.76	-8.33				44.76	-6.62			
10-Dec-17	20.25	21.90	113.03	-92.78				67.82	-45.92				97.48	-77.23				97.48	-75.58			
17-Dec-17	54.17	60.42	29.70	24.46				17.82	42.59				23.47	30.70				23.47	36.95			
19-Dec-17	20.05	30.95	88.06	-68.02				52.84	-21.88				71.88	-51.84				71.88	-40.93			
25-Dec-17	63.23	79.20	69.23	-6.00				41.54	37.66				57.25	5.97				57.25	21.95			
26-Dec-17	38.21	46.50	35.58	2.63				21.35	25.15				27.71	10.51				27.71	18.79			
27-Dec-17	59.25	32.10	111.35	-52.10				66.81	-34.71				98.26	-39.01				98.26	-66.16			
31-Dec-17	5.90	6.40	38.76	-32.86				23.26	-16.86				30.53	-24.63				30.53	-24.13			
17-Jan-18	40.50	30.00	38.84	1.66				23.30	6.70				30.60	9.90				30.60	-0.60			
19-Jan-18	22.50	17.68	55.72	-33.22				33.43	-15.75				47.97	-25.47				47.97	-30.29			
20-Jan-18	28.29	30.50	92.10	-63.82				55.26	-24.76				81.64	-53.36				81.64	-51.14			
28-Jan-18	62.81	67.50	44.31	18.50				26.59	40.91				39.07	23.74				39.07	28.43			
30-Jan-18	62.00	43.33	50.42	11.58				30.25	13.08				42.81	19.19				42.81	0.52			
28-Feb-18	23.46	14.61	88.62	-65.16				53.17	-38.57				78.14	-54.69				78.14	-63.54			
04-Mar-18	16.31	10.15	23.02	-6.71				13.81	-3.67				16.38	-0.08				16.38	-6.24			
08-Mar-18	6.50	5.50	8.27	-1.76				4.96	0.54				5.49	1.02				5.49	0.01			
10-Mar-18	7.54	7.01	38.06	-30.53				22.84	-15.83				29.01	-21.48				29.01	-22.00			
13-Mar-18	35.78	20.87	5.17	30.60				3.10	17.77				3.40	32.37				3.40	17.47			
15-Mar-18	11.53	4.50	29.23	-17.70				17.54	-13.04				21.49	-9.96				21.49	-16.99			
16-Mar-18	15.26	5.99	38.81	-23.54				23.28	-17.30				29.66	-14.40				29.66	-23.67			

4.7.2.5. Summary of Findings – Accuracy of the Predictive Performance of the Semi-empirical Models Using Proposed WDR Coefficients

Table 4.39 provides a summary of the predictive performance of the semi-empirical models, i.e., ISO standard 15927-3 and ASHRAE standard 160P models, using proposed WDR coefficients in estimating R_{wdr} (mm/h) based on the values of NRMSD derived from Table 4.35 to Table 4.38.

The predictive performance accuracy of the semi-empirical models for the top and bottom locations on the windward façade of the building during each season was compared using the basic WDR coefficients (Table 4.25) and the proposed WDR coefficients (Table 4.39). The NRMSD values decreased when the proposed WDR coefficients were applied by the semi-empirical models. As a result, the semi-empirical models exhibited significantly improved accuracy in predictive performance in estimating R_{wdr} (mm/h) for both locations on the building façade during the entire year.

Table 4.39. Predictive performance of the ISO and ASHRAE models using Proposed WDR coefficients for the top and bottom locations on the building façade for each season (0.20 < NRMSD < 0.50 is relatively accurate)

Seasons	ISO Standard 15927-3 Model	NRMSD value	ASHRAE standard 160P Model	NRMSD value
01 (Top / Bottom)	Relatively Accurate	0.36 / 0.42	Relatively Accurate	0.36 / 0.36
02 (Top / Bottom)	Relatively Accurate	0.38 / 0.31	Relatively Accurate	0.34 / 0.31
03 (Top / Bottom)	Relatively Accurate	0.38 / 0.40	Relatively Accurate	0.35 / 0.34
04 (Top / Bottom)	Relatively Accurate	0.38 / 0.38	Relatively Accurate	0.35 / 0.36

The spatial distribution of the WDR on the building façade is complex, as it is a function of inherently transient parameters, such as horizontal rainfall intensity (R_h), wind speed (U), and wind direction (D). The results given in Table 4.39 can justify reliability of the proposed WDR coefficients to predict the possible harvestable R_{wdr} on the windward

façades using the real-time meteorological data for each tropical season in Kuala Lumpur, Malaysia.

4.8. Feasibility Analysis of Possible Vertical Harvestable WDR on Building Façade

The height classification in exposure factor (F_E) of the ASHRAE Standard 160P Standard model (2.8.3.1) allows for more elaborate classification and analysis of building height in comparison with the wall factor (W) in the ISO Standard 15927-3 model (0). Hence, in the current section, the ASHRAE exposure factor (F_E) classification is used to demonstrate the variation of potential WDR harvesting (vertical rainwater harvesting) from tall building façades. The proposed predicted R_{wdr} on the building façade by both semi-empirical models is calculated, and each season is subjected to the calculations individually.

The models' correction factors and parameters are determined based on the information provided in Section 4.4.1. Proposed WDR coefficients are derived from semi-empirical equations presented in Table 4.30.

Table 4.40 shows all the proposed WDR coefficients and parameters based on the different heights to predict the potential harvestable R_{wdr} (mm/h) per square metre (m^2) on the windward façade of a tall building located in Kuala Lumpur, Malaysia.

Table 4.41 illustrates the seasonal variation of R_{wdr} (mm/h), wind-driven rain intensity, for each building height category. The monitoring period for season one includes 9 rain events, and for seasons 2, 3, and 4, there are 20, 8, and 28 rain events, respectively. In total, the dataset includes 65 rain events for the entire tropical year. The quantification of the predicted loads is based on the daily average amount of R_{wdr} (Mean values).

Table 4.40. Determined parameters for Proposed ISO 15927-3 and ASHRAE standard 160P models at different heights (m) on building windward façade

Season 1 – Total 9 Rain events												
Building Height (m)	α	C_R	C_T	O	W	U_{10}	R_h	$R_h^{0.88}$	cos (D-0)	F_L	F_E	F_D
<10	0.273	0.66	1.00	0.40	0.40	1.20	10.36	7.83	1.00	0.305	0.70	1.00
10 – 15	0.273	0.66	1.00	0.40	0.50	1.20	10.36	7.83	1.00	0.305	0.80	1.00
15 – 20	0.273	0.66	1.00	0.40	0.50	1.20	10.36	7.83	1.00	0.305	0.90	1.00
20 – 30	0.273	0.66	1.00	0.40	0.50	1.20	10.36	7.83	1.00	0.305	1.10	1.00
30 -40	0.273	0.66	1.00	0.40	0.50	1.20	10.36	7.83	1.00	0.305	1.20	1.00
40 – 50	0.273	0.66	1.00	0.40	0.50	1.20	10.36	7.83	1.00	0.305	1.30	1.00
>50	0.273	0.66	1.00	0.40	0.50	1.20	10.36	7.83	1.00	0.305	1.50	1.00
Season 2 – Total 20 Rain events												
Building Height (m)	α	C_R	C_T	O	W	U_{10}	R_h	$R_h^{0.88}$	cos (D-0)	F_L	F_E	F_D
<10	0.545	0.66	1.00	0.40	0.40	1.70	4.36	3.65	1.00	0.707	0.70	1.00
10 – 15	0.545	0.66	1.00	0.40	0.50	1.70	4.36	3.65	1.00	0.707	0.80	1.00
15 – 20	0.545	0.66	1.00	0.40	0.50	1.70	4.36	3.65	1.00	0.707	0.90	1.00
20 – 30	0.545	0.66	1.00	0.40	0.50	1.70	4.36	3.65	1.00	0.707	1.10	1.00
30 -40	0.545	0.66	1.00	0.40	0.50	1.70	4.36	3.65	1.00	0.707	1.20	1.00
40 – 50	0.545	0.66	1.00	0.40	0.50	1.70	4.36	3.65	1.00	0.707	1.30	1.00
>50	0.545	0.66	1.00	0.40	0.50	1.70	4.36	3.65	1.00	0.707	1.50	1.00
Season 3 – Total 8 Rain events												
Building Height (m)	α	C_R	C_T	O	W	U_{10}	R_h	$R_h^{0.88}$	cos (D-0)	F_L	F_E	F_D
<10	0.165	0.66	1.00	0.40	0.40	1.43	12.29	9.10	1.00	0.179	0.70	1.00
10 – 15	0.165	0.66	1.00	0.40	0.50	1.43	12.29	9.10	1.00	0.179	0.80	1.00
15 – 20	0.165	0.66	1.00	0.40	0.50	1.43	12.29	9.10	1.00	0.179	0.90	1.00
20 – 30	0.165	0.66	1.00	0.40	0.50	1.43	12.29	9.10	1.00	0.179	1.10	1.00
30 -40	0.165	0.66	1.00	0.40	0.50	1.43	12.29	9.10	1.00	0.179	1.20	1.00
40 – 50	0.165	0.66	1.00	0.40	0.50	1.43	12.29	9.10	1.00	0.179	1.30	1.00
>50	0.165	0.66	1.00	0.40	0.50	1.43	12.29	9.10	1.00	0.179	1.50	1.00
Season 4 – Total 28 Rain events												
Building Height (m)	α	C_R	C_T	O	W	U_{10}	R_h	$R_h^{0.88}$	cos (D-0)	F_L	F_E	F_D
<10	0.525	0.66	1.00	0.40	0.40	1.21	8.81	6.79	1.00	0.441	1.00	1.00
10 – 15	0.525	0.66	1.00	0.40	0.50	1.21	8.81	6.79	1.00	0.441	1.10	1.00
15 – 20	0.525	0.66	1.00	0.40	0.50	1.21	8.81	6.79	1.00	0.441	1.20	1.00
20 – 30	0.525	0.66	1.00	0.40	0.50	1.21	8.81	6.79	1.00	0.441	1.30	1.00
30 -40	0.525	0.66	1.00	0.40	0.50	1.21	8.81	6.79	1.00	0.441	1.40	1.00
40 – 50	0.525	0.66	1.00	0.40	0.50	1.21	8.81	6.79	1.00	0.441	1.50	1.00
>50	0.525	0.66	1.00	0.40	0.50	1.21	8.81	6.79	1.00	0.441	1.50	1.00

Results in Table 4.41 and Figure 4.36 reveal that the semi-empirical models have predicted WDR loads (lit/m²) in an ascending trend. Note that the ISO model has the

same value for heights higher than 10 m, and it is attributed to the constant wall factor (W), which has less sensitivity to the building height (Figure 2.33), lacks variation across tall building façades. However, as previously stated, the ASHRAE model is capable of predicting for a more variety of height categories on building walls exceeding 10 m height. Therefore, as Table 4.41 indicates, the model has statistically performed a rational constant ascending trend from 10 m (the least value) up to >50 m (the highest value) height on the windward façade of a tall building.

Table 4.41. Spatial distribution of Mean (daily average) R_{wdr} (WDR intensity) (mm/h) (annual and seasonal (S01, S02, S03, S04)) at different heights (m) on building windward façade (per square metre) based on Proposed ISO 15927-3 and ASHRAE standard 160P models' WDR coefficients

Building Height (m)	Season 1 Mean R_{wdr} (mm/h) of 9 Rain events		Season 2 Mean R_{wdr} (mm/h) of 20 Rain events		Season 3 Mean R_{wdr} (mm/h) of 8 Rain events		Season 4 Mean R_{wdr} (mm/h) of 28 Rain events		Year (mm/h) Mean of 65 Rain events	
	Proposed ISO - Mean NW&SW	Proposed ASHRAE - Mean NW&SW	Proposed ISO - Mean NW&SW	Proposed ASHRAE - Mean NW&SW	Proposed ISO - Mean NW&SW	Proposed ASHRAE - Mean NW&SW	Proposed ISO - Mean NE&NW	Proposed ASHRAE - Mean NE&NW	Proposed ISO - Mean	Proposed ASHRAE - Mean
<10	27.08	26.55	35.64	36.57	22.66	22.02	45.52	47.01	32.72	33.04
10 – 15	33.85	30.34	44.55	41.79	28.33	25.17	56.90	51.71	40.91	37.25
15 – 20	33.85	34.13	44.55	47.01	28.33	28.31	56.90	56.41	40.91	41.47
20 – 30	33.85	41.72	44.55	57.46	28.33	34.60	56.90	61.11	40.91	48.73
30 – 40	33.85	45.51	44.55	62.69	28.33	37.75	56.90	65.82	40.91	52.94
40 – 50	33.85	49.30	44.55	67.91	28.33	40.90	56.90	70.52	40.91	57.16
>50	33.85	56.89	44.55	78.36	28.33	47.19	56.90	70.52	40.91	63.24

The better predictive performance of ISO 15927-3 is found for buildings less than 3 storey, given more constant values for the wall factor (W) less than 10 m in height. Whereas the ASHRAE standard 160P has only one value for heights less than 10 m. But when it comes to tall building façades to predict WDR load, the ISO model has only one constant value for multi-storey buildings (Figure 2.33), and ASHRAE performs better by providing a wider range of constant values for exposure factor (F_E) for different higher heights, as can be observed in Table 4.41 and Figure 4.36. This implies that to improve

the predictive performance of the ISO model for tall buildings, more wall factor (W) values are required along the façade height.

Over and above, the quantity of harvestable WDR predicted by the proposed WDR coefficients on the vertical surface of the façade in each season, shows that the higher the height, the greater the harvested WDR would be. However, the façade area at the lowest height (<10 m) also harvests a substantial amount of WDR to supply non-potable or potable water.

As stated in Section 2.1.1, the report by the Malaysian Water Association has declared a high level of water consumption in the country (201 lpcd) and the urgency to reduce it by 18% in conformity with the recommended water usage by the WHO, i.e, 165 liters per capita per day (lpcd). It was also specified by the aforementioned survey (2.1.1) that 29% of household water usage accounts for non-potable usage, which is equivalent to 58 lpcd. Based on these statistical data and the predicted harvestable yearly average R_{wdr} values (per square metre) that have been illustrated in Table 4.41 and Figure 4.36, the possible percentage of harvested WDR for non-potable and potable usages (lpcd) is calculated. The results are given in Table 4.42 and Figure 4.37.

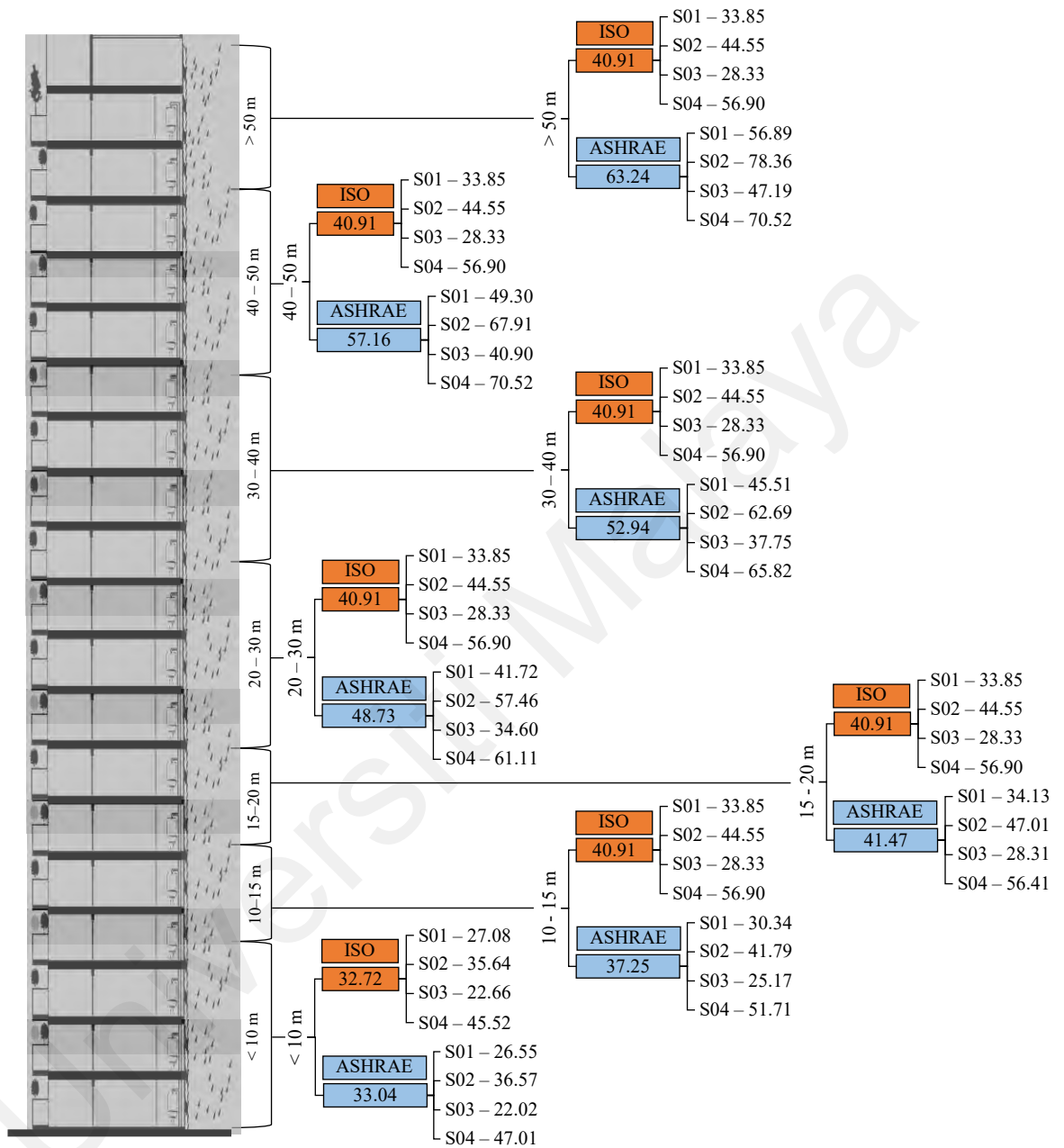


Figure 4.36. Illustration of spatial distribution of Mean (daily average) R_{wdr} (WDR intensity) (mm/h) (annual (65 Rain events) and seasonal (S01, S02, S03, S04)) at different heights (m) on building windward façade (per square metre) based on the Proposed ISO 15927-3 and ASHRAE 160P models' WDR coefficients

Table 4.42. Potential reduction non-potable (%) and potable (%) water usages based on Proposed model prediction of harvestable R_{wdr} (per square metre) at different heights (m) on building windward façade derived from Table 4.41

Building Height (m)	Proposed Model Prediction - annual average R_{wdr} (mm/h OR lit/m ²)	Potential Reduction Non-potable (%)	Potential Reduction Potable (%)
<10	ISO - 32.72	56	23
	ASHRAE - 33.04	57	23
10 – 15	ISO - 40.91	70	29
	ASHRAE - 37.25	64	26
15 – 20	ISO - 40.91	70	29
	ASHRAE - 41.47	71	29
20 – 30	ISO - 40.91	70	29
	ASHRAE - 48.73	84	34
30 -40	ISO - 40.91	70	29
	ASHRAE - 52.94	91	37
40 – 50	ISO - 40.91	70	29
	ASHRAE - 57.16	98	40
>50	ISO - 40.91	70	29
	ASHRAE - 63.24	109	44

The ISO model predicted 23% to 29% for potable usage and 56% to 70% for non-potable usage reduction per square metre harvesting WDR from the vertical façade at heights less than 10 metres to greater than 10 metres, respectively. The ASHRAE model prediction generated a wide range of values for each height category, i.e., 23% to 44% for potable usage and 57% to 109% for non-potable usage reduction per square metre harvesting WDR from the vertical façade at heights less than 10 metres to greater than 50 metres, respectively. Note that the annual average R_{wdr} accounts for the average of 65 rain events derived from all four tropical seasons.

Note that during the preprocessing and data cleaning phases (Section 4.2), a number of WDR events, including high-quantity accumulated ones, were excluded as outliers (28 out of 93 rain events). It indicates that, in reality, the quantity of harvested WDR from the building façade was even higher than what the measured dataset represented. Moreover, in Section 4.7.2.5, the relatively accuracy of the predictive performance of the semi-empirical models was validated. Based on these facts and findings, the feasibility of harvesting WDR from tall building façades from the viewpoint of availability and

accessibility of sufficient quantity loads, particularly at higher locations, can be confidently justified to be implemented as a new alternative catchment area in rainwater harvesting practices.

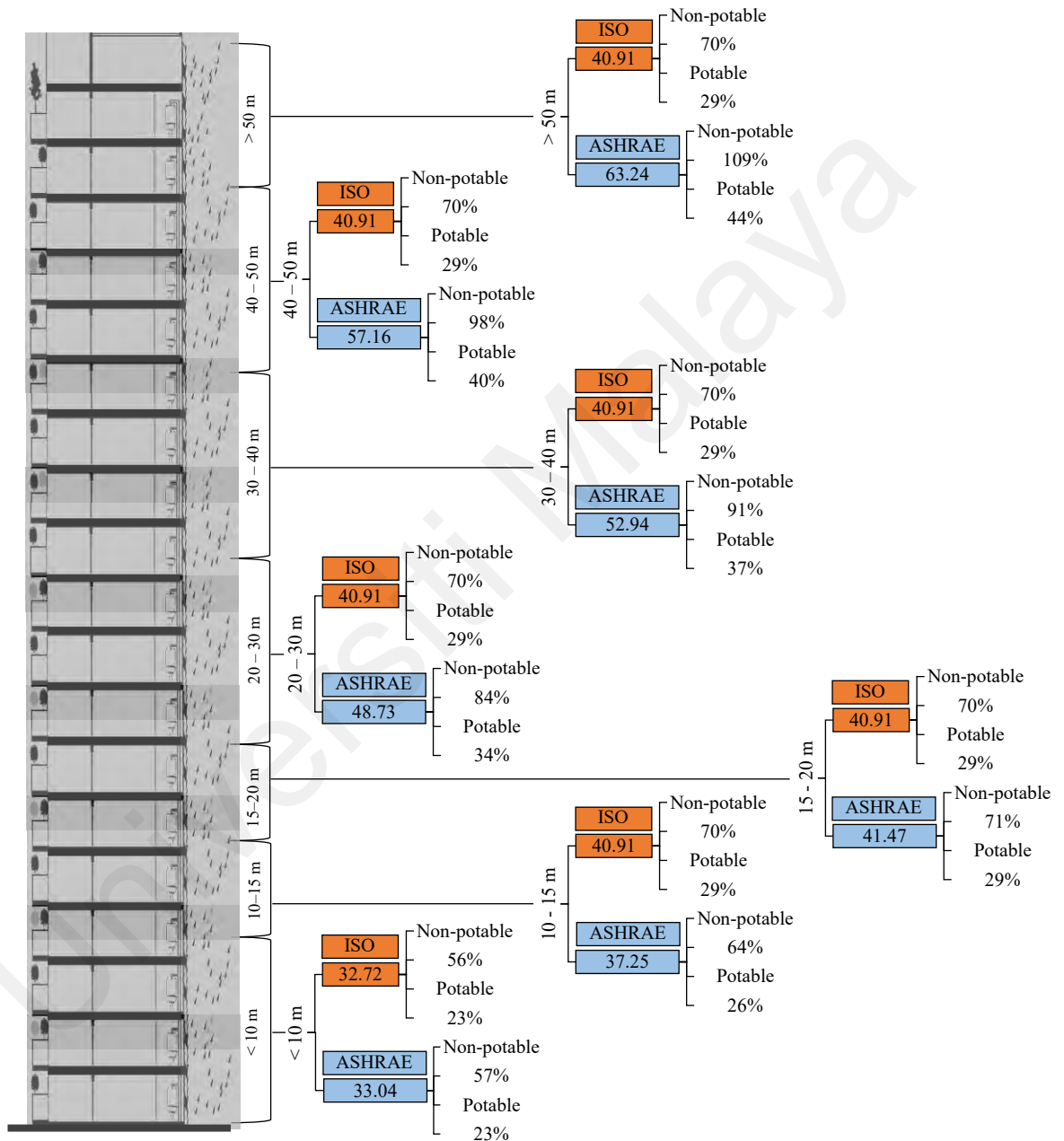


Figure 4.37. Illustration of potential reduction non-potable (%) and potable (%) water usages based on Proposed model prediction of harvestable R_{wdr} (per square metre) at different heights (m) on building windward façade

4.9. Summary

This chapter presented the data findings of in-situ measurement, which were categorized into four tropical seasons of Malaysia. Harvested WDR load (S_{wdr}) and related meteorological data, i.e., horizontal rainfall amount (S_h), wind speed (U), and wind direction (D), were measured on-site as raw data. S_{wdr} amounts were collected from eight wall-mounted WDR on four façades of the pilot building. WDR intensity (R_{wdr}) for each season and each WDR gauge was calculated. The correlation analyses between R_{wdr} and the related meteorological data were conducted to understand the impact of parameters on the R_{wdr} . This step was carried out to respond to the second research objective. The WDR catch ratio was calculated to identify the spatial distribution of the WDR on the building façade. After the Data Unit Conversion process, the raw data were verified first through the guidelines derived from the literature review and then the Normality test and Outlier test (Shapiro-Wilk's test and Q-Q plot and box plot graphs). The former step omitted 9 rain events and the latter step 19 rain events. Total 65 rain events out of 93 were verified as the in-situ dataset for the model validation process.

After the data cleaning process of the in-situ raw data, the impact of dominant meteorological factors on the spatial distribution of the WDR, catch ratio (η), was analysed. The results showed that horizontal rainfall intensity (R_h) and wind speed (U) influenced the catch ratio values significantly on the windward facades. The catch ratio value (η) was mainly higher in the rain events that satisfy the conditions of low R_h and high U simultaneously, such as rain events 14th July and 29th October.

In the next step, the Mean R_{wdr} in-situ dataset was compared with the semi-empirical models' datasets generated from the two standard equations, namely, ISO Standard 15927-3 and ASHRAE Standard 160P. The cross-comparison analysis was carried out to evaluate the accuracy performance of the models. Analytical comparative assessments to

evaluate the predictive performance of the models were conducted through the coefficient of determination (R^2), Normalised root mean square deviation (NRMSD), and 'Polynomial regression analyses – order 4' to generate the best-fit line (regression curve) for the predicted R_{wdr} values. Results showed relatively low (value > 0.5) to relatively accurate ($0.2 < \text{value} < 0.5$) predictive performance of the models. The WDR coefficients were refined through the cross-multiplication method. The models incorporated the proposed WDR coefficients for ISO Standard 15927-3 and ASHRAE Standard 160P. The proposed predicted Mean R_{wdr} datasets showed significant improvements in accuracy of predictive performance of the models in all seasons. It was found that the application of the refined coefficients to the ISO Standard 15927-3 model (α) and the ASHRAE Standard 160P model (F_L) could relatively accurately predict WDR intensity on tall building facades. The ISO model illustrated better performance for building heights less than 10 m, providing more constant values for the wall factor (W) within this range, and fixed value for greater than 10 m height. The ASHRAE model on the other hand, illustrated better performance for building height more than 10 m height up to 50 m by providing a wider range of constant values for exposure factor (F_E).

The ISO model predicted 23% to 29% reduction for potable usage and 56% to 70% reduction for non-potable usage at heights less than 10 meters to greater than 10 meters. The ASHRAE model predicted 23% to 44% reduction for potable usage and 57% to 109% reduction for non-potable usage at heights less than 10 meters to greater than 50 meters.

CHAPTER 5: CONCLUSION

This chapter provides a summary of research findings addressing each research question through the corresponding research objective. Afterwards, the overall contribution of the study, limitations, and recommendations are provided.

5.1. Summary of Findings

The research presented in this thesis aimed to evaluate the possibility of vertical RWH through measurement and predictive modelling of the R_{wdr} impinging on the curtain wall façades of the tall buildings, as a new catchment area. To achieve this goal, this thesis first reviewed the challenges and potential that tall buildings have offered to urban areas in terms of their impacts on rainfall-runoff pattern changes and RWH possibilities (Objective 1). Then in-situ measurements of WDR and related meteorological factors were carried out (Objective 2), to generate WDR dataset (Objective 3) to validate semi-empirical models and determine the WDR coefficients for the estimation of the harvestable R_{wdr} based on the spatial distribution on tall building façade (Objective 4).

In the following, the main research findings through this thesis are summarised in the order of each research objective.

5.1.1. Research Objective 1

To explore the feasibility of vertical rainwater harvesting system from wind-driven rain based on Kuala Lumpur's weather and vertical expansion pattern.

In the literature review, it was declared that in Malaysia, about 97% of raw water supply is derived primarily from rivers and in highly developed and populated areas such as Federal Territory of Kuala Lumpur, the river resources have been fully exploited and 25 out of 189 rivers in Malaysia were announced dead rivers (Section 2.1.1). The Malaysian

government acts and strategic plans related to sustainable water management, and the implementation status of RWH in the country were explored and presented in Section 2.2.5. The review showed that nationally, there is an urgency to reduce high level of water consumption (209 to 228 lpcd) by 18% in conformity with the recommended water usage by the WHO (165 lpcd).

In Section 2.3, it was revealed that apart from the extra pressure that tall buildings put on the domestic water network (increased demand by residents), their vast vertical façade areas create negative impacts on the rainfall-runoff patterns in urban avenues. Distortion of the runoff process, 3D flow path, and sub-basin division, were addressed as pivotal challenges created by these tall structures in urban areas. It was learnt that developing upstream areas without upgrading stormwater infrastructure in downstream areas in Kuala Lumpur, was resulted in experiencing increasing avenue flooding.

The review also cited that the conventional (2D) horizontal RWH, as the most available alternative water resource at building scale, in tall buildings as the scope of this research, has been left on the sidelines due to the unavailability or inadequacy of the rooftop areas (preferable green roof or recreational functions).

On the other hand, the availability of a great portion (Figure 1.1) of glass curtain walls, non-absorbent materials (Figure 2.6), in tall buildings as the prospect factor, was brought to light and explored in this research as a new possible catchment area for VRWH in tropical climate of Kuala Lumpur with ample annual rainfall.

5.1.2. Research Objective 2

To investigate a complete tropical monsoon season under meteorological condition with in-situ experiment in Kuala Lumpur for real-time WDR load measurement on facades of tall buildings.

In Section 1.3, it was stated that among the three scientific approaches in the field of building science, i.e., (1) measurements, (2) semi-empirical methods, and (3) numerical simulations, for WDR load determination on building façades, the first two methods are used mainly and frequently together. It was revealed that globally there is a deficiency in WDR dataset, particularly those derived from long-term in-situ measurements on building façade. The prerequisite steps to generate a WDR dataset for semi-empirical models validation were found out to be:

- i. wall-mounted WDR gauge design and manufacturing,
- ii. experimental measurements; including WDR (S_{wdr}) collection and related meteorological factors, i.e., horizontal rainfall (S_h), wind direction (D), and wind speed (U).

Acrylic (polymethyl-methacrylate) was chosen for the UM gauge material, because it has the closest average adhesion water value (0.066 mm) to the glass (0.047 mm) (curtain walls of tall buildings), which was identified heavy, difficult to fabricate, and most importantly, not recommended for long-term measurement due to fragility. The pilot building at UM campus was equipped with 8 WDR gauges, 2 gauges on each façade; one on the Top edge and one on the middle (two-third) bottom, to collect the highest and lowest amounts of WDR loads based on the findings on spatial distribution of the WDR on building wall (Section 2.7.1). A meteorological mast was installed in the vicinity of the building. During the one-year measurements, 93 WDR events, equivalent to 119 hours, over 4 tropical seasons were recorded as the in-situ measurement dataset (raw data). This study conducted the horizontal rainfall (S_h) and WDR (S_{wdr}) measurements by the unit of rainfall event namely ‘event-based’, and wind direction (D) and wind speed (U) by ‘10-minute’ interval logging. The set-up was exposed to different adjacencies, provided a real scenario similar to a building located in an urban area with an orientation facing local prevailing wind (windward facades).

Seasonal harvested S_{wdr} indicated that season 4 was the highest and season 3 the lowest receivers. NW and SW, facing the prevailing wind direction, in almost all the seasons have collected the highest amount of WDR. The NE façade which was not considered windward façade in this study, but has received noticeable amount of WDR due to its exposure to open surrounding area. It reaffirms the effect of surrounding area on the harvested amount of S_{wdr} .

The total annual harvested WDR amounts (S_{wdr}) by 8 gauges were recorded as 940,960 ml, which is equivalent to an average 22.35 mm/h WDR intensity (R_{wdr}). Out of this amount of accumulated S_{wdr} , the largest amounts were recorded as 25,708; 25,280; 25,000; and 37,650 ml; and the lowest ones as 56, 400, 20, and 34 ml by events in seasons 1, 2, 3, and 4 respectively (Table 4.2).

Annual comparison between the top and bottom gauges based on the façade orientation, showed different accumulation patterns, not necessarily all followed the traditional wetting pattern indicated in the literature review:

- several cases have shown equal amounts,
- a few cases collected higher in bottom gauges,
- several cases have followed the traditional pattern, higher amounts in the top gauges, i.e., the NE, NW, and SW in season 1, the NW in seasons 3 and 4, and the SW in seasons 1 and 4 (Figure 4.6).

Thus, it can be reaffirmed that the windward facades have had tendency to follow the traditional patterns; the higher location, the greater amount of S_{wdr} .

The degree of relevancy analysis between seasonal average data of WDR intensity (R_{wdr}), wind speed (U), and horizontal rainfall intensity (R_h) showed an overall coincide trend between the parameters. Regardless of rain event duration, the rainfall events (Figure 4.8) with a greater amount of R_h (mm/h), had greater R_{wdr} (mm/h); such as seasons 1 and 4

(Figure 4.8), R_h of 11.57 mm/h and 12.03 mm/h produced R_{wdr} of 22.54 mm/h and 27.04 mm/h, respectively. As the figure showed the average wind speed (U) over the year has been approximately steady (4 - 6 km/h), for instance for these two seasons it was the same 4 km/h.

However, the degree of relevancy analysis between daily average data of R_{wdr} , U , and R_h showed a few sharp rises and falls which can be explained as presence of:

- i. wind gust speed,
- ii. duration of rainfall, at that particular rain event.

These two real-time factors have significant influence on the R_{wdr} quantity. For instance, a long rainfall duration accompanied with a high wind gust resulted in a peak ascension, or a short rainfall duration resulted in a sudden descension (Figure 4.9).

The comparison analyses of WDR data (raw data) were performed to explore the local characteristics and impact of meteorological factors, as the dominant factors, on the WDR intensity (R_{wdr}) on the building walls during each tropical seasons. Moreover, the raw WDR data including the meteorological data provided the primary prerequisite for the model validation; raw in-situ dataset.

5.1.3. Research Objective 3

To generate a valid in-situ WDR dataset for the validation of semi-empirical models.

To meet the third research objective, two steps were taken:

- i. the preprocessing of the raw dataset extracted from WDR in-situ measurements,
- ii. the data cleaning process of the raw dataset for each tropical season.

During the first step:

- all the meteorological data extracted from the excel files of the data logger, were categorised into 4 seasons and converted from '10-minute' mean intervals to

‘event-based’ mean values (unit conversions) to proceed with event-based S_h and S_{wdr} values,

- the harvested WDR amounts measured by 8 wall-mounted gauges on each façade (NE, NW, SW, SE) were categorised into Top (T01-T04) and Bottom (B01-B04) locations to explore the impact of the ‘height parameter’.

During the second step:

- conformity of data values with the principles and guidelines studied in the literature review; excluding events with wind speed (U) values greater than 10 m/s and horizontal rainfall (R_h) intensities greater than 20 mm/h, 8 events were excluded,
- conducting Normality Test (Shapiro-Wilk Test) and Outlier Test. It was found that WDR intensity values (R_{wdr}) less than 1 mm/h were among the detected outliers by the software, 20 events were excluded.

The validity of the seasons 1, 2, 3, and 4 datasets was evaluated through the normality test as 71%, 90%, 61%, and 63%, respectively.

In total, 28 out of 93 rain events were detected as outliers and excluded from the WDR raw datasets of all 4 seasons in this study. The validated WDR dataset included 65 rain events for the model validation process. In fulfilling the objective three requirements, the analyses were followed by determining the windward façades and calculation of catch ratios (η).

A summary of correlation analyses between catch ratio value (η) as a function of wind speed (U) and horizontal rainfall intensity (R_h), to evaluate the impact of U and R_h on spatial distribution of the WDR on the building wall, are as follows:

- as illustrated in Figure 4.22, the correlation between catch ratio value (η) and wind speed (U) in all seasons showed that the wind speed is approximately steady

throughout the year (1 - 2 m/s). In seasons 2 and 3 (homogenous seasons), the correlation showed an ascending trendline, means the parameters are in a harmonic pattern (lower U resulted in lower η). In seasons 1 and 4 (heterogeneous seasons), they were correlated in an inverse relationship; a descending trendline, which was resulted from diverse rise and fall data values at high rates of fluctuations in wind speed,

- as illustrated in Figure 4.23, the correlation between catch ratio value (η) and horizontal rainfall intensity (R_h) in all seasons showed that the frequency of rainfall intensity was greater than 5 mm/h throughout the year. In all four seasons, the correlation showed a descending trendline. It theoretically, occurs because when R_h increases, terminal drop velocity increases, consequently the WDR catch ratio (η) decreases, which justifies the descending trend pattern of catch ratio with increasing rainfall intensity,
- catch ratio (η) as a function of wind speed (U) and horizontal rainfall intensity (R_h) was mainly higher in the rain events that satisfy the conditions of high U and low R_h simultaneously.

5.1.4. Research Objective 4

To determine WDR coefficient constants of the semi-empirical models to refine their predictive performance accuracy for estimation of harvestable amounts of WDR loads on building façades in Kuala Lumpur.

After data transformation (ETL) process, two semi-empirical models, i.e., ISO standard 15927-3 and ASHRAE standard 160P, were employed. The validated in-situ dataset were transformed into ‘event-based averaged value’ to moderate the predicted outputs of the models (due to involving real-time fluid dynamic parameters). R_{wdr} (mm/h) was predicted

by two models and the predicted datasets were compared with the in-situ dataset of R_{wdr} for each season.

Analytical comparative assessments to evaluate the predictive performance of the two models for top and bottom locations in each season mainly included:

- i. the coefficient of determination (R^2),
- ii. normalised root mean square deviation (NRMSD) between the in-situ dataset and the predicted datasets of the R_{wdr} (WDR intensity) (mm/h),
- iii. 'polynomial regression analyses – order 4' to generate the best-fit line (regression curve) for the predicted R_{wdr} values.

The accuracy of the predictive performance of the standard models for each location in each season indicated that ISO and ASHRAE models' prediction results:

- for heterogeneous season 1 were relatively accurate to low,
- for homogenous season 2 were relatively accurate to low,
- for homogenous season 3 were relatively accurate,
- for heterogeneous season 4 were relatively accurate to low,
- for the top locations in general, were relatively accurate,
- for the bottom locations, were mostly low accurate.

Following the predictive performance analysis, the in-situ WDR intensity (R_{wdr}) values were applied to each model equation in the cross-multiplication method to determine the WDR coefficients for the ISO (α) and the ASHRAE (F_L) models. The coefficients were determined for top and bottom locations separately and then converted to the mean (top and bottom) value as the representative value for the windward façade to proceed further. This thesis determined the proposed WDR coefficients for the ISO (0.273, 0.545, 0.165, and 0.525) and ASHRAE (0.305, 0.707, 0.179, and 0.441) models for the tropical seasons

1, 2, 3, and 4. Then, the proposed R_{wdr} using the proposed coefficients by the semi-empirical models was predicted, and the accuracy of the predictive performance of the proposed models was analysed through the same procedures carried out earlier for the basic semi-empirical models.

Comparing the accuracy of the predictive performance of the ‘basic’ semi-empirical models and the ‘proposed’ models using the ‘proposed WDR coefficients’ indicated that:

- the proposed α for the ISO model and the proposed F_L for the ASHRAE model provided relatively accurate results for both top and bottom locations on the building façade during the entire year, all four seasons (Table 4.39).

The spatial distribution of the WDR in real-time condition on the building façade is a complex phenomenon as a function of inherently transient parameters, i.e., R_h and U . Thus, the achieved results can be considered as representatives of sufficiently promising WDR coefficients for the semi-empirical models to predict the value of R_{wdr} for each tropical season in Kuala Lumpur, Malaysia.

Finally, the harvestable WDR loads on tall building façades were predicted following the height classifications in exposure factor (F_E) of ASHRAE standard 160P model. The result showed that the higher the building façade height, the greater the harvested amount of R_{wdr} would be.

The ISO model predicted 23% to 29% for potable usage and 56% to 70% for non-potable usage reduction per square meter at heights less than 10 metres to greater than 10 metres, respectively. The ASHRAE model predicted 23% to 44% for potable usage and 57% to 109% for non-potable usage reduction per square metre at heights less than 10 metres to greater than 50 metres, respectively.

Given the fact that only 65 out of 93 rain events could be processed as a valid dataset, (some excluded data comprised high quantities of WDR), it was declared that in reality,

the ‘quantity of harvestable WDR’ from building façades was even higher in this region and climate condition. Moreover, considering the relatively accuracy of the predictive performance of the semi-empirical models, it can be concluded that the possibility of harvesting VWDR from tall building façades as a new catchment area, particularly at higher locations, ‘can be confidently justified and predicted’ by the semi-empirical models.

5.2. Research Contributions

This thesis includes the following overall contributions:

- Six modifications and customizations were applied (section 3.1.1) in design and manufacturing the UM wall-mounted WDR gauge to minimise the possible measurement errors learnt from the literature review.
- This is the first in-situ experimental measurement conducted for a one-year period to measure WDR loads on the vertical surface of building façades in the tropical climate of Kuala Lumpur, Malaysia,
- The research generated a unique WDR dataset derived from real-time in-situ measurement with high resolution; this dataset will be crucial for the semi-empirical model’s improvements as well as the CFD model’s validation,
- In-situ measurements of wind speed (U), wind direction (D), and horizontal rainfall intensity (R_h), as well as their effects on catch ratios (η) and WDR intensity (R_{wdr}), are the basis of this investigation on the spatial distribution of wind-driven rain on building façades. Correlation analyses of the impact of meteorological data on the WDR catch ratio revealed that rain events with lower horizontal rainfall intensity (R_h) and higher wind velocity (U) have higher catch ratio value (η).

- Correlation analyses of seasons' datasets showed seasons two and three as the homogenous seasons with harmonic pattern, and seasons one and four as the heterogeneous seasons with high rate of fluctuations.
- This research compared the amount of WDR predicted by two semi-empirical models, i.e., the ASHRAE Standard 160 and the ISO Standard 15927-3, with the amount of WDR harvested during one year in real-time from the building façade, followed by a cross-multiplication method to determine the WDR coefficients for the ISO (α) and ASHRAE (F_L) models. The results showed that in order to enhance the accuracy performance of the semi-empirical models to predict the harvestable amount of WDR on a building façade, it is necessary to refine the WDR coefficients values using long-term in-situ measurements – real-time meteorological data – for any particular weather condition that falls under the purview of the study,
- To predict the quantity of harvestable WDR on tall building façades, the ASHRAE standard 160P model showed higher practicality compared with the ISO standard 15927-3 model due to offering more classifications in exposure factor (F_E) at different ranges of heights (> 10 m) on the building façade,
- The quantity of harvestable WDR predicted by the proposed WDR coefficients confidently justified the possibility of VRWH from the building façade as a new sustainable alternative catchment area to be implemented in rainwater harvesting practices, particularly for non-potable water usage to manage the domestic water supply and the freshwater resources.
- This study constructed a systematic methodology for collecting WDR, generating valid in-situ WDR dataset, validating semi-empirical models, refining WDR

coefficients to predict harvestable amount of R_{wdr} on windward façade of tall buildings.

5.3. Research Implications

The main outcomes of this research highlighted the promising potential of the study aim.

As such, this work yields the following implications:

- The availability of a great portion of glass curtain walls, non-absorbent materials, in tall buildings as the prospect factor, was brought to light and explored in this research as a new catchment area for VRWH (via WDR) in the tropical climate of KL with ample annual rainfall.
- To design and manufacture UM WDR wall-mounted gauge as the prerequisite steps for in-situ WDR measurement. This gauge can be useful for the future research on WDR measurement in building science as an optimised wall-mounted WDR gauge.
- To generate first in-situ WDR intensity (R_{wdr}) dataset derived from one-year real-time measurement in the tropical climate of Kuala Lumpur. It can be applied for model validations to estimate the amount of harvestable WDR from building facades in both academia and industry as façade design criteria for VRWH practices.
- To identify two real-time factors, i.e., ‘wind gust speed’ and ‘duration of rainfall’, as the main common factors representing the outliers through the degree of relevancy analysis between daily average data of R_{wdr} , U , and R_h . It can be included in the data cleaning process assessments prior to generating WDR datasets.

- To refine WDR coefficient constants of two frequently used semi-empirical models; F_L for ASHRAE standard 160P and α for ISO standard 15927-3. It significantly enhanced accuracy of the predictive performance of the models to estimate the spatial distribution of the R_{wdr} on tall building facades to harvest in the tropical climate of Kuala Lumpur.
- Application of the proposed WDR coefficients to the models and determining the harvestable amounts of WDR on tall building façade based on the ASHRAE range of constant values for exposure factor (F_E). The proposed predicted WDR dataset can be used for reference meteorological conditions, e.g. as boundary conditions, this set of results can be used for any number of further analyses.
- To justify possibility of harvesting WDR from tall building façades particularly at higher locations as vertical rainwater harvesting (VRWH) practice.

5.4. Recommendations and Future Works

- Research on WDR loads on building façades has a dearth of experimental datasets. It is necessary to conduct more in-situ measurements on actual building façades with different geometries and architectural features in different climates in order to validate CFD models and refine semi-empirical models,
- ASHRAE standard 160P and ISO standard 15927-3 models, two of the most frequently used semi-empirical models, have been developed based on a limited number of building geometries and façade locations via experimental measurements. Thus, significant discrepancies between in-situ measurements and the predicted WDR by these semi-empirical models are inevitable. Due to this fact, it is essential to refine a number of correction factors used in the models to enhance the accuracy of predictive performance of the model based on the scope of the research, geographically or geometrically. In this thesis, WDR coefficient

factors were studied and refined based on the geography (weather condition) and orientation of the building (windward façade). As the results revealed, for instance, the ISO standard needs to develop wall factor values for different heights, particularly when it comes to tall building façades, and also needs to consider façade orientation,

- This study assumed a perpendicular wind direction ($\cos 0^\circ = 1$) to the corresponding façade orientation for each rain event. In cases where more accurate model's prediction for WDR is required, it is recommended to apply the measured in-situ wind direction to the WDR relationships,
- It should also be noted that, in order to put the findings of this study into practice, further experimental investigations are required. One of the study's limitations is that it did not use a real-size tall building façade for measurement. Therefore, there may be constraints when it comes to adapting this study's methods to real-size structures. Future research can address these shortcomings of the current one. Furthermore, in real-practice scenarios, the quantity of precipitation intercepted by the building façade could vary with respect to the adjacent building density and height. To determine how surrounding areas affect the façade's ability to collect rainwater, further experiments are necessary,
- The in-situ measurement dataset that has been generated in this study can be subjected to computational fluid dynamic analysis to assess the accuracy of the predictive performance of the CFD model in estimating the amount of harvestable WDR at different heights of tall building façades.

REFERENCES

- 12MP. (2021). *Twelfth Malaysia Plan (2021-2025) A Prosperous, Inclusive, Sustainable Malaysia*. Director General, Economic Planning Unit, Prime Minister's Department, Putrajaya, Malaysia: Percetakan Nasional Malaysia Berhad Retrieved from <https://pulse.icdm.com.my/wp-content/uploads/2021/09/Twelfth-Plan-Documents-compressed-1.pdf>
- Abbas, M., Zhao, L., & Wang, Y. (2022). Perspective Impact on Water Environment and Hydrological Regime Owing to Climate Change: A Review. *Hydrology*, 9(11), 203.<https://doi.org/10.3390/hydrology9110203>
- Abdulla, F., Abdulla, C., & Eslamian, S. (2021). Concept and technology of rainwater harvesting. *Handbook of water harvesting and conservation: basic concepts and fundamentals*, 1-16.<https://doi.org/10.1002/9781119478911.ch1>
- Abu-Zidan, Y. (2019). *Verification and validation framework for computational fluid dynamics simulation of wind loads on tall buildings*. The University of Melbourne.
- Abu-Zidan, Y., Mendis, P., Gunawardena, T., Mohotti, D., & Fernando, S. (2022). Wind design of tall buildings: The state of the art. *Electronic Journal of Structural Engineering*, 22(01), 53-71.<https://doi.org/10.56748/ejse.2233101>
- Abuku, M., Blocken, B., Nore, K., Thue, J. V., Carmeliet, J., & Roels, S. (2009). On the validity of numerical wind-driven rain simulation on a rectangular low-rise building under various oblique winds. *Building and Environment*, 44(3), 621-632.<https://doi.org/10.1016/j.buildenv.2008.05.003>
- Adl-Zarrabi, B., & Hogberg, A. (2001). *Microclimate: field measurements, driving rain analyses*. Paper presented at the Proceedings of Performance of the Exterior Envelopes of Whole Buildings VIII: integration of Building Envelopes, Florida, US. Retrieved from https://web.ornl.gov/sci/buildings/conf-archive/2001%20B8%20papers/034_Adl_Zarrabi.pdf
- Adnan, A., Ahmad, A. C., & Teriman, S. (2020). Rainwater Harvesting (RWH) installation for buildings: A systematic review and meta-analysis approach. *Malaysian Journal of Sustainable Environment*, 6(1), 89-108.<https://doi.org/10.24191/myse.v6i1.8681>
- Ahmadian, E., Sodagar, B., Bingham, C., Elnokaly, A., & Mills, G. (2021). Effect of urban built form and density on building energy performance in temperate climates. *Energy and Buildings*, 236, 110762.<https://doi.org/10.1016/j.enbuild.2021.110762>
- Al-Kodmany, K. (2012). The logic of vertical density: tall buildings in the 21st century city.<https://doi.org/10.21022/IJHRB.2012.1.2.131>
- Alamerew, E., Fentaw, B., & Ali, S. (2002). Traditional rainwater harvesting systems for food production: The case of Kobo Wereda, Northern Ethiopia. *Addis Abeba: ERHA*. Retrieved from <https://citeseerx.ist.psu.edu/document?repid=rep1&type=pdf&doi=d922d2be6de56c0ffbf6b4fc4fa1a21b71e6aea1>
- Ali, A. A. (2017). *Evaluating rainwater harvesting systems in arid and semi-arid regions*. (PhD). Wageningen University. Retrieved from <https://www.proquest.com/docview/2521532474?pq-origsite=gscholar&fromopenview=true>
- Ali, M. M., & Al-Kodmany, K. (2012). Tall Buildings and Urban Habitat of the 21st Century: A Global Perspective. *Buildings*, 2(4), 384-423.<https://doi.org/10.3390/buildings2040384>

- Almeida, A. P., Liberalesso, T., Silva, C. M., & Sousa, V. (2021). Dynamic modelling of rainwater harvesting with green roofs in university buildings. *Journal of Cleaner Production*, 312, 127655. <https://doi.org/10.1016/j.jclepro.2021.127655>
- Amoloye, T. O. (2012). *Wind Engineering: A Review of the Eurocode provisions for the Wind Loading on Low-rise Buildings*. Cranfield University. Retrieved from <https://kwasuspace.kwasu.edu.ng/handle/123456789/297>
- ASHRAE Standard 160P. (2016). ASHRAE standard 160P - Criteria for moisture control design analysis in buildings. In (Vol. 114). ASHRAE, Atlanta, USA.
- Auerbach, J., & Wan, P. (2020). Forecasting the urban skyline with extreme value theory. *International Journal of Forecasting*, 36(3), 814-828. <https://doi.org/10.1016/j.ijforecast.2019.09.004>
- Back, L. E., & Bretherton, C. S. (2005). The relationship between wind speed and precipitation in the Pacific ITCZ. *Journal of climate*, 18(20), 4317-4328. <https://doi.org/10.1175/JCLI3519.1>
- Bahari, Y. A. b., Pengarah, K., & Malaysia, J. M. (2017). *Jabatan Meteorologi Malaysia, Annual Report 2017*. Malaysia: Jabatan Meteorologi Malaysia Retrieved from <https://www.met.gov.my/content/pdf/penerbitan/laporantahunan/laporantahunan2017.pdf>
- Barron, J., & Salas, J. C. (2009). *Rainwater harvesting: a lifeline for human well-being*: UNEP/Earthprint.
- Basart, A. (1946). Verhandeling inzake de regenval op het verticale vlak met betrekking tot de bouwconstructie. *Tech-nical report, Instituut voor warmte-economie TNO, Keramisch Instituut TNO, The Netherlands (in Dutch)*.
- Bates, D. (1988). Nonlinear Regression Analysis and Its Applications. *John Wiley and Sons: New York google schola*, 2, 379-416.
- Beijer, O. (1977). *Concrete walls and weathering*. Paper presented at the RILEM/ASTM/CIB symposium on evaluation of the performance of external vertical surfaces of buildings. doi:<https://doi.org/10.1007/BF02473802>
- Beorkrem, C., & Damiano, A. (2018). A Tool for Optimizing Conceptual Mass Design and Orientation for Rainwater Harvesting Facades. In *Humanizing Digital Reality* (pp. 603-612): Springer. https://doi.org/10.1007/978-981-10-6611-5_50
- Best, A. (1950). The size distribution of raindrops. *Quarterly Journal of the Royal Meteorological Society.*, 76, 16-36. <https://doi.org/10.1002/qj.49707632704>
- Biloria, N. (2021). From smart to empathic cities. *Frontiers of Architectural Research*, 10(1), 3-16. <https://doi.org/10.1016/j.foar.2020.10.001>
- Bisht, D. S., Chatterjee, C., Kalakoti, S., Upadhyay, P., Sahoo, M., & Panda, A. (2016). Modeling urban floods and drainage using SWMM and MIKE URBAN: a case study. *Natural Hazards*, 84, 749-776. <https://doi.org/10.1007/s11069-016-2455-1>
- Biswas, B. K., & Mandal, B. H. (2014). Construction and evaluation of rainwater harvesting system for domestic use in a remote and rural area of Khulna, Bangladesh. *International Scholarly Research Notices*, 2014. <http://dx.doi.org/10.1155/2014/751952>
- Blocken, B. (2010). *CFD in Building Engineering - Fundamentals and applications in urban physics and wind engineering*: Building Physics and Systems, Faculty of Architecture, Building and Planning Eindhoven University of Technology, The Netherlands. Retrieved from https://www.academia.edu/3984861/CFD_in_Building_Engineering_Course_Book
- Blocken, B., Abuku, M., Nore, K., Briggen, P., Schellen, H., Thue, J., . . . Carmeliet, J. (2011). Intercomparison of wind-driven rain deposition models based on two case studies with full-scale measurements. *Journal of Wind Engineering and*

- Industrial Aerodynamics*, 99(4), 448-459. <https://doi.org/10.1016/j.jweia.2010.11.004>
- Blocken, B., & Carmeliet, J. (2002). Spatial and temporal distribution of driving rain on a low-rise building. *Wind and Structures*, 5(5), 441-462. <https://doi.org/10.12989/was.2002.5.5.441>
- Blocken, B., & Carmeliet, J. (2004). A review of wind-driven rain research in building science. *Journal of Wind Engineering and Industrial Aerodynamics* 92, 1079–1130. <https://doi.org/10.1016/j.jweia.2004.06.003>
- Blocken, B., & Carmeliet, J. (2005a). *Guidelines for wind, rain and wind-driven rain measurements at test-building sites*. Paper presented at the Proceedings of the 7th Symposium on Building Physics in the Nordic Countries: Reykjavik. <https://research.tue.nl/en/publications/guidelines-for-wind-rain-and-wind-driven-rain-measurements-at-test-building-sites>
- Blocken, B., & Carmeliet, J. (2005b). High-resolution wind-driven rain measurements on a low-rise building—experimental data for model development and model validation. *Journal of Wind Engineering and Industrial Aerodynamics*, 93(12), 905-928. <https://doi.org/10.1016/j.jweia.2005.09.004>
- Blocken, B., & Carmeliet, J. (2006a). The influence of the wind-blocking effect by a building on its wind-driven rain exposure. *Journal of Wind Engineering and Industrial Aerodynamics*, 94(2), 101-127. <https://doi.org/10.1016/j.jweia.2005.11.001>
- Blocken, B., & Carmeliet, J. (2006b). On the accuracy of wind-driven rain measurements on buildings. *Building and Environment*, 41(12), 1798-1810. <https://doi.org/10.1016/j.buildenv.2005.07.022>
- Blocken, B., & Carmeliet, J. (2006c). On the validity of the cosine projection in wind-driven rain calculations on buildings. *Building and Environment*, 41(9), 1182-1189. <https://doi.org/10.1016/j.buildenv.2005.05.002>
- Blocken, B., & Carmeliet, J. (2007a). On the errors associated with the use of hourly data in wind-driven rain calculations on building facades. *Atmospheric Environment*, 41(11), 2335-2343. <https://doi.org/10.1016/j.atmosenv.2006.11.014>
- Blocken, B., & Carmeliet, J. (2007b). *Wind-driven rain assessment on buildings using climatic databases: which time resolution is needed?* Paper presented at the Proceedings of the 10th Conference on the Thermal Performance of the Exterior Envelopes of Whole Buildings, 2-7 December 2007, Clearwater Beach, Florida. Retrieved from <https://tue.elsevierpure.com/nl/publications/wind-driven-rain-assessment-on-buildings-using-climatic-databases>
- Blocken, B., & Carmeliet, J. (2008). Guidelines for the required time resolution of meteorological input data for wind-driven rain calculations on buildings. *Journal of Wind Engineering and Industrial Aerodynamics*, 96(5), 621-639. <https://doi.org/10.1016/j.jweia.2008.02.008>
- Blocken, B., & Carmeliet, J. (2010). Overview of three state-of-the-art wind-driven rain assessment models and comparison based on model theory. *Building and Environment*, 45(3), 691-703. <https://doi.org/10.1016/j.buildenv.2009.08.007>
- Blocken, B., & Carmeliet, J. (2012). A simplified numerical model for rainwater runoff on building facades: Possibilities and limitations. *Building and Environment*, 53, 59-73. <https://doi.org/10.1016/j.buildenv.2012.01.010>
- Blocken, B., Carmeliet, J., Roels, S., & Abuku, M. (2009a). Wind-driven rain on building facades: some perspectives. *Wind-Driven Rain on Building Facades*, 1000-1004. Retrieved from <https://lirias.kuleuven.be/1565741?limo=0>

- Blocken, B., Derome, D., & Carmeliet, J. (2013). Rainwater runoff from building facades: a review. *Building and Environment*, 60, 339-361. <https://doi.org/10.1016/j.buildenv.2012.10.008>
- Blocken, B., Dezsö, G., van Beeck, J., & Carmeliet, J. (2009b). The mutual influence of two buildings on their wind-driven rain exposure and comments on the obstruction factor. *Journal of Wind Engineering and Industrial Aerodynamics*, 97(5-6), 180-196. <https://doi.org/10.1016/j.jweia.2009.06.003>
- Blocken, B., Dezsö, G., van Beeck, J., & Carmeliet, J. (2010). Comparison of calculation models for wind-driven rain deposition on building facades. *Atmospheric environment*, 44(14), 1714-1725. <https://doi.org/10.1016/j.atmosenv.2010.02.011>
- Blöschl, G., Hall, J., Parajka, J., Perdigão, R. A., Merz, B., Arheimer, B., . . . Borga, M. (2017). Changing climate shifts timing of European floods. *Science*, 357(6351), 588-590. <https://doi.org/10.1126/science.aan2506>
- Briggen, P., Blocken, B., & Schellen, H. (2009). Wind-driven rain on the facade of a monumental tower: numerical simulation, full-scale validation and sensitivity analysis. *Building and Environment*, 44(8), 1675-1690. <https://doi.org/10.1016/j.buildenv.2008.11.003>
- BS 8104. (1992). Code of Practice for Assessing Exposure of Walls to Wind-driven Rain. In: British Standards Institution.
- BSI, B. (1992). 8104 1992, British Standard Code of Practice for Assessing the Exposure of walls to Wind-driven Rain. In. British Standard Institution.
- Camerlengo, A., & Demmler, M. I. (1997). Wind-driven circulation of peninsular Malaysia's eastern continental shelf. *Scientia Marina*, 61, 203-211. Retrieved from <http://scimar.icm.csic.es/scimar/pdf/61/sm61n2203.pdf>
- Cauteruccio, A., & Lanza, L. G. (2023). *Competing roles of green roof in rain water harvesting systems: accounting for retention and detention in a behavioural model simulation*. EGU General Assembly, Vienna, Austria: Department of Civil, Chemical and Environmental Engineering, University of Genova, Genoa, Italy. https://ui.adsabs.harvard.edu/link_gateway/2023EGUGA..25.8630C/doi:10.5194/egusphere-egu23-8630
- CCC. (2021). *Cork City Development Plan 2022-2028*. Cork City Council, UK Retrieved from <https://tinyurl.com/3pjwtun5r>
- Cea, L., Garrido, M., & Puertas, J. (2010). Experimental validation of two-dimensional depth-averaged models for forecasting rainfall-runoff from precipitation data in urban areas. *Journal of Hydrology*, 382(1-4), 88-102. <https://doi.org/10.1016/j.jhydrol.2009.12.020>
- CEN. (2009). *Hygrothermal performance of buildings Climatic data Part 3: calculation of a driving rain index for vertical surfaces from hourly wind and rain data*. Retrieved from <https://www.sis.se/api/document/preview/910850/>
- Chacha, J. D. G. (2015). *Urban Water: Harvesting Rainwater at household level to improve the current water metabolism in Cuenca-Ecuador*. Universitat Politècnica De Catalunya, Barcelona Tech. Retrieved from <http://hdl.handle.net/2117/79256>
- Chan, Y. (2012). Rainfall-runoff processes in urban environments. *MEng thesis*. University of Cambridge, UK, 49.
- Che-Ani, A., Shaari, N., Sairi, A., Zain, M., & Tahir, M. (2009). Rainwater harvesting as an alternative water supply in the future. *European Journal of Scientific Research*, 34(1), 132-140. Retrieved from <http://www.eurojournals.com/ejsr.htm>
- Chen, C., Zhang, H., Feng, C., Xuan, Y., Qian, T., & Xie, J. (2022). Analysis of wind-driven rain characteristics acting on building surfaces in Shanghai based on

- long-term measurements. *Journal of Building Engineering*, 45, 103572. <https://doi.org/10.1016/j.jobbe.2021.103572>
- Chen, Y., Zhou, H., Zhang, H., Du, G., & Zhou, J. (2015). Urban flood risk warning under rapid urbanization. *Environmental research*, 139, 3-10. <https://doi.org/10.1016/j.envres.2015.02.028>
- Cho, E., Yoo, C., Kang, M., Song, S.-u., & Kim, S. (2020). Experiment of wind-driven-rain measurement on building walls and its in-situ validation. *Building and Environment*, 185, 107269. <https://doi.org/10.1016/j.buildenv.2020.107269>
- Choi, E. (1991). *Numerical simulation of wind-driven rain falling onto a 2-D building*. Paper presented at the The Asian Pacific Conference on Computational Mechanics, Hong Kong, Hong Kong, 12/11-13/91.
- Choi, E. (1994). Determination of wind-driven-rain intensity on building faces. *Journal of Wind Engineering and Industrial Aerodynamics*, 51(1), 55-69. [https://doi.org/10.1016/0167-6105\(94\)90077-9](https://doi.org/10.1016/0167-6105(94)90077-9)
- Choi, E. C. (1993). Simulation of wind-driven-rain around a building. *Journal of Wind Engineering and Industrial Aerodynamics*, 46, 721-729. [https://doi.org/10.1016/0167-6105\(93\)90342-L](https://doi.org/10.1016/0167-6105(93)90342-L)
- Coutu, S., Wyrsh, V., Rossi, L., Emery, P., Golay, F., & Carneiro, C. (2013). Modelling wind-driven rain on buildings in urbanized area using 3-D GIS and LiDAR datasets. *Building and environment*, 59, 528-535. <https://doi.org/10.1016/j.buildenv.2012.09.022>
- Critchley, W., Siegert, K., Chapman, C., & Finket, M. (1991). *Water harvesting: A manual for the design and construction of water harvesting schemes for plant production* (Reprint 2013 ed.): Scientific Publishers.
- CTBUH. (2018). The Global Tall Building Picture: Impact of 2017 - Council on Tall Buildings and Urban Habitat. *CTBUH Journal 2018(I)*. Retrieved from <https://global.ctbuh.org/resources/papers/download/3604-the-global-tall-building-picture-impact-of-2017.pdf>
- Daud, A., & Ishak, M. F. (2018). Defect on high rise government office buildings in Kelantan. Retrieved from <https://ir.uitm.edu.my/id/eprint/46115>
- de Campos, M. R., & Machado, R. E. (2018). Time distribution of intense rainfalls at Campinas, Brazil. *International Journal of Advanced Engineering Research and Science*, 5(12), 107-117. <https://dx.doi.org/10.22161/ijaers>
- Deb Nath, U. K. (2015). *Field Measurements of Wind-Driven Rain on Mid-and High-Rise Buildings in Two Canadian Regions*. Concordia University. Retrieved from <https://core.ac.uk/download/pdf/211518707.pdf>
- Defo, M., Lacasse, M. A., & Snell, N. (2019). *Assessing the climate resilience of buildings to the effects of hygrothermal loads: impacts of wind-driven rain calculation methods on the moisture performance of massive timber walls* (CRB-CPI-Y3-R06). 54. <https://doi.org/10.4224/40001821>
- Dobravalskis, M., Spūdys, P., Vaičiūnas, J., & Fokaides, P. (2018). Potential of harvesting rainwater from vertical surfaces. *Journal of Sustainable Architecture and Civil Engineering*, 23(2), 49-58. <https://doi.org/10.5755/j01.sace.23.2.21606>
- Donat, M. G., Angélil, O., & Ukkola, A. M. (2019). Intensification of precipitation extremes in the world's humid and water-limited regions. *Environmental Research Letters*, 14(6), 065003. <https://doi.org/10.1088/1748-9326/ab1c8e>
- Donat, M. G., Lowry, A. L., Alexander, L. V., O'Gorman, P. A., & Maher, N. (2016). More extreme precipitation in the world's dry and wet regions. *Nature Climate Change*, 6(5), 508-513. Retrieved from <https://www.nature.com/articles/nclimate2941>
- Dorsey, J., Pedersen, H. K., & Hanrahan, P. (1996). *Flow and changes in appearance*. Paper presented at the Proceedings of the 23rd annual conference on Computer

- graphics and interactive techniques. Retrieved from <https://dl.acm.org/doi/pdf/10.1145/237170.237280>
- Dottori, F., & Todini, E. (2013). Testing a simple 2D hydraulic model in an urban flood experiment. *Hydrological Processes, Special Issue: Flood Risk and Uncertainty*, 27(9), 1301-1320. <https://doi.org/10.1002/hyp.9370>
- Du, J., Qian, L., Rui, H., Zuo, T., Zheng, D., Xu, Y., & Xu, C.-Y. (2012). Assessing the effects of urbanization on annual runoff and flood events using an integrated hydrological modeling system for Qinhuai River basin, China. *Journal of Hydrology*, 464, 127-139. <https://doi.org/10.1016/j.jhydrol.2012.06.057>
- Dunbar, A. J. (2018). Study of the Evolution of Distortion During the Powder Bed Fusion Build Process Using a Combined Experimental and Modeling Approach. In *Thermo-Mechanical Modeling of Additive Manufacturing* (pp. 229-250): Elsevier. <https://doi.org/10.1016/B978-0-12-811820-7.00017-3>
- EcoWatch. (2023). Global freshwater demand will exceed supply 40% by 2030, experts warn. *NATURE AND BIODIVERSITY*. Retrieved from <https://www.weforum.org/agenda/2023/03/global-freshwater-demand-will-exceed-supply-40-by-2030-experts-warn/>
- El-Shimi, M., White, R., & Fazio, P. (1980). Influence of facade geometry on weathering. *Canadian journal of civil engineering*, 7(4), 597-613. <https://doi.org/10.1139/l80-073>
- Elsadek, M., Liu, B., & Lian, Z. (2019). Green façades: Their contribution to stress recovery and well-being in high-density cities. *Urban Forestry & Urban Greening*, 46, 126446. <https://doi.org/10.1016/j.ufug.2019.126446>
- EPA. (2023). Residential Toilets. Retrieved from <https://www.epa.gov/watersense/residential-toilets>
- Eslamian, S., & Eslamian, F. (2021). *Handbook of Water Harvesting and Conservation: Basic Concepts and Fundamentals*. doi:<https://doi.org/10.1002/9781119478911>.
- Fader, S. (2000). *Density by design: new directions in residential development*: Urban Land Inst.
- Fakhira, N., & Nazri, M. A. A. (2022). Implementation of Rainwater Harvesting System in Development Project Among Local Authorities in Malaysia. *Recent Trends in Civil Engineering and Built Environment*, 3(1), 1257-1267. <https://doi.org/10.30880/rctcebe.2022.03.01.143>
- Fang, A., Chen, Y., & Wu, L. (2021). Modeling and numerical investigation for hygrothermal behavior of porous building envelope subjected to the wind driven rain. *Energy and Buildings*, 231, 110572. <https://doi.org/10.1016/j.enbuild.2020.110572>
- FAO. (2020). MALAYSIA'S WATER VISION: THE WAY FORWARD - The Malaysian Water Partnership. Retrieved from <https://www.fao.org/3/AB776E/ab776e02.htm>. from Global Water Partnership - Malaysian Water Partnership <https://www.fao.org/3/AB776E/ab776e02.htm>
- Fath, B. D., & Jorgensen, S. E. (2020). *Managing Water Resources and Hydrological Systems*: CRC Press. doi:<https://doi.org/10.1201/9781003045045>.
- Fernando R, Waidyasekara K. G. A. S, & Mallawaarachchi H. (2014). *Driving Factors for Façade Rainwater Harvesting in High-rise Buildings*. Paper presented at the 5th International Conference on Sustainable Built Environment 2014, University of Peradeniya, Sri Lanka. <http://dl.lib.mrt.ac.lk/handle/123/14261>
- FJR van Mook. (2002). *Driving rain on building envelopes* (906814569X). Eindhoven University Press, Eindhoven, The Netherlands: Eindhoven University of Technology. Retrieved from <http://fabien.galerio.org/drivingrain/fjrvanmook2002/>

- Flori, J. (1992). *Influence des conditions climatiques sur le mouillage et le sechage d'une facade verticale*: CSTB.
- Foroushani, S. S. M. (2013). *A Numerical Study Of The Effects Of Overhangs On The Wind-Driven Rain Wetting Of Building Facades*. (Master). Ryerson University, Toronto, Ontario, Canada, <https://doi.org/10.1016/j.jweia.2013.10.007>
- Fowler, K. M., Demirkanli, D. I., Hostick, D. J., McMordie Stoughton, K. L., Solana, A. E., & Sullivan, R. S. (2017). *Federal Campuses Handbook for Net Zero Energy, Water, and Waste*. Pacific Northwest National Lab.(PNNL), Richland, WA (United States). Retrieved from https://www.pnnl.gov/main/publications/external/technical_reports/PNNL-26636.pdf
- Freitas, S., Barreira, E., & De Freitas, V. P. (2013). *Quantification of wind-driven rain and evaluation of façade humidification*. Paper presented at the Proceedings of the 2nd Central European Symposium on Building Physics (CESBP 2013). Retrieved from <https://repositorio-aberto.up.pt/handle/10216/93586>
- Freitas, S., & Brito, M. C. (2019). Solar façades for future cities. *Renewable energy focus*, 31, 73-79. <https://doi.org/10.1016/j.ref.2019.09.002>
- Fung, K. F., Huang, Y. F., & Koo, C. H. (2020). Seasonal hydrological drought indicator for tropical drought identification. *International Journal of Environmental Science*. <https://doi.org/10.18178/ijesd.2020.11.2.1233>
- Gabel, J., & Shehadi, A. (2017). CTBUH Year in Review: Tall Trends of 2016: 2016 Another Record-Breaker for Skyscraper Completions; 18" Tallest Titles" Bestowed. *CTBUH Journal*(1), 38-45.
- Gao, X., Yang, Z., Han, D., Gao, K., & Zhu, Q. (2021). The impact of wind on the rainfall-runoff relationship in urban high-rise building areas. *Hydrology and Earth System Sciences*, 25(11), 6023-6039. <https://doi.org/10.5194/hess-25-6023-2021>
- García-Ávila, F., Guanoquiza-Suárez, M., Guzmán-Galarza, J., Cabello-Torres, R., & Valdiviezo-Gonzales, L. (2023). Rainwater harvesting and storage systems for domestic supply: An overview of research for water scarcity management in rural areas. *Results in Engineering*, 18, 101153. <https://doi.org/10.1016/j.rineng.2023.101153>
- Gariano, S. L., & Guzzetti, F. (2016). Landslides in a changing climate. *Earth-Science Reviews*, 162, 227-252. <https://doi.org/10.1016/j.earscirev.2016.08.011>
- Ge, F., Zhu, S., Peng, T., Zhao, Y., Sielmann, F., Fraedrich, K., . . . Ji, L. (2019). Risks of precipitation extremes over Southeast Asia: does 1.5° C or 2° C global warming make a difference? *Environmental Research Letters*, 14(4), 044015. <https://doi.org/10.1088/1748-9326/aaff7e>
- Ge, H. (2015). Influence of time resolution and averaging techniques of meteorological data on the estimation of wind-driven rain load on building facades for Canadian climates. *Journal of Wind Engineering and Industrial Aerodynamics*, 143, 50-61. <https://doi.org/10.1016/j.jweia.2015.04.019>
- Ge, H., Chiu, V., Stathopoulos, T., & Souri, F. (2018). Improved assessment of wind-driven rain on building façade based on ISO standard with high-resolution on-site weather data. *Journal of Wind Engineering and Industrial Aerodynamics*, 176, 183-196. <https://doi.org/10.1016/j.jweia.2018.03.013>
- Ge, H., Nath, U. D., & Chiu, V. (2017). Field measurements of wind-driven rain on mid-and high-rise buildings in three Canadian regions. *Building and Environment*, 116, 228-245. <https://doi.org/10.1016/j.buildenv.2017.02.016>
- Ghisi, E., Bressan, D. L., & Martini, M. (2007). Rainwater tank capacity and potential for potable water savings by using rainwater in the residential sector of

- southeastern Brazil. *Building and Environment*, 42(4), 1654-1666. <https://doi.org/10.1016/j.buildenv.2006.02.007>
- Ghisi, E., & Ferreira, D. F. (2007). Potential for potable water savings by using rainwater and greywater in a multi-storey residential building in southern Brazil. *Building and Environment*, 42(7), 2512-2522. <https://doi.org/10.1016/j.buildenv.2006.07.019>
- Gholamalipour, P., Ge, H., & Stathopoulos, T. (2022). Wind-driven rain (WDR) loading on building facades: A state-of-the-art review. *Building and Environment*, 109314. <https://doi.org/10.1016/j.buildenv.2022.109314>
- Gomez Jr, J. E. A. (2017). The size of cities: A synthesis of multi-disciplinary perspectives on the global megalopolis. *Progress in Planning*, 116, 1-29. <https://doi.org/10.1016/j.progress.2016.03.001>
- Gould, J. (1999). *Contributions relating to rainwater harvesting*. Paper presented at the World Commission on Dams Secretariat (WCD) Thematic Review IV.3.
- Grimmond, C. S. B., & Oke, T. R. (1991). An evapotranspiration - interception model for urban areas. *Water resources research*, 27(7), 1739-1755. <https://doi.org/10.1029/91WR00557>
- Hall, C., & Kalimeris, A. (1982). Water movement in porous building materials—V. Absorption and shedding of rain by building surfaces. *Building and Environment*, 17(4), 257-262. [https://doi.org/10.1016/0360-1323\(82\)90018-X](https://doi.org/10.1016/0360-1323(82)90018-X)
- Hamdi, R., Termonia, P., & Baguis, P. (2011). Effects of urbanization and climate change on surface runoff of the Brussels Capital Region: a case study using an urban soil-vegetation-atmosphere - transfer model. *International Journal of Climatology*, 31(13), 1959-1974. <https://doi.org/10.1002/joc.2207>
- He, Y., Lin, H., Fu, J., Chan, P., Zheng, Q., & Deng, T. (2021). Dependence of wind load on air density for highrise buildings. *Journal of Wind Engineering and Industrial Aerodynamics*, 211, 104558. <https://doi.org/10.1016/j.jweia.2021.104558>
- Heidarinejad, G., & Esmaili, A. (2015). Numerical simulation of the dual effect of green roof thermal performance. *Energy Conversion and Management*, 106, 1418-1425. <https://doi.org/10.1016/j.enconman.2015.10.020>
- Hejazi, M. I., & Markus, M. (2009). Impacts of urbanization and climate variability on floods in Northeastern Illinois. *Journal of Hydrologic Engineering*, 14(6), 606-616. [https://doi.org/10.1061/\(ASCE\)HE.1943-5584.0000020](https://doi.org/10.1061/(ASCE)HE.1943-5584.0000020)
- Hens, H. (1996). *Applied Building Physics 1: boundary conditions and performances requirements* (In Dutch; Toegepaste Bouwphysica 1, Randvoorwaarden en prestatie-eisen), Third Edition. Acco, Leuven, Belgium.
- Hens, H. (2010). *Wind-driven rain: from theory to reality*. Paper presented at the Thermal Performance of the Exterior Envelopes of Whole Buildings-11th International Conference. Retrieved from <https://lirias.kuleuven.be/1569189?limo=0>
- Hens, H., & Ali Mohamed, F. (1994). *Preliminary results on driving rain estimation, Contribution to the IEA annex 24, Task 2 Environmental conditions T2-B-94/02*. Retrieved from <https://lib.ugent.be/en/catalog/rug01:000697882>
- Hogberg, A. (1998). *Microclimate description: to facilitate estimating durability and service life of building components exposed to natural outdoor climate*: Chalmers University of Technology.
- Hogberg, A. (1999a). *Measurement of microclimate near a building surface*. Paper presented at the Proceedings of the 10th International Symposium for Building Physics and Building Climatology, Dresden, Germany.

- Hogberg, A. (1999b). *Microclimate measurement focused on wind-driven rain striking building surfaces*. Paper presented at the Proc. of the 5th Symp. on building physics in the Nordic Countries, Gothenburg.
- Hogberg, A. (2002). *Microclimate Load: Transformed Weather Observations for Use in Durable Building Design*: Department of Building Physics, Chalmers University of Technology.
- Hogberg, A., Kragh, M., & van Mook, F. (1999). *A comparison of driving rain measurements with different gauges*. Paper presented at the Proceedings of the 5th Symposium of building physics in the Nordic Countries, Gothenburg. <http://citeseerx.ist.psu.edu/viewdoc/download?doi=10.1.1.606.3604&rep=rep1&type=pdf>
- Holmgren, O. (1972). Snow loads, driving rain and building design. Colloquium Teaching the Teachers on Building Climatology. Statens Institut for Byggnadsforskning, Stockholm. *Preprint*(35).
- Hoppestad, S. (1955). Slagregn i Norge (Driving rain in Norway, in Norwegian). *NBI Report*, 13.
- Huang, H.-H., & He, Q. (2024). Nonlinear regression analysis. *arXiv preprint arXiv:2402.05342*. <https://doi.org/10.1016/B978-0-12-818630-5.10068-5>
- Huang, M., & Jin, S. (2019). A methodology for simple 2-D inundation analysis in urban area using SWMM and GIS. *Natural Hazards*, 97(1), 15-43. <https://doi.org/10.1007/s11069-019-03623-2>
- Hughes, M., Hall, A., & Fovell, R. G. (2009). Blocking in areas of complex topography, and its influence on rainfall distribution. *Journal of the Atmospheric Sciences*, 66(2), 508-518. <https://doi.org/10.1175/2008JAS2689.1>
- Hugues, R. T. (2019). Rainwater harvesting as a solution in the past and present. *Ingeniería Hidráulica y Ambiental*, 40(2), 125-139. Retrieved from http://scielo.sld.cu/scielo.php?pid=S1680-0338201900020012&script=sci_arttext&tlng=en
- ICC. (2021). *International Green Construction Code: A Comprehensive Solution for High-performance Buildings (International Code Council)*. International Code Council publications, IL, USA: International Code Council (ICC) & ASHRAE.
- Iman, A. H. H. M. (2012). *Plenary Paper III: Financial Simulation of Rainwater Harvesting System for Sustainable Water Supply in Residential Area*. Paper presented at the International Real Estate Conference 2012 (INTEREC 2012), Grand Seasons Hotel, Kuala Lumpur, 9-11 June.
- Inyinbor Adejumo, A., Adebesein Babatunde, O., Oluyori Abimbola, P., Adelani Akande Tabitha, A., Dada Adewumi, O., & Oreofe Toyin, A. (2018). Water pollution: effects, prevention, and climatic impact. *Water Challenges of an Urbanizing World*, 33, 33-47. <http://dx.doi.org/10.5772/intechopen.72018>
- IPCC. (2014). *Climate change 2014: synthesis report. Contribution of Working Groups I, II and III to the fifth assessment report of the Intergovernmental Panel on Climate Change* (9291691437). 151 IPCC, Geneva, Switzerland. Retrieved from https://epic.awi.de/id/eprint/37530/1/IPCC_AR5_SYR_Final.pdf
- IPCC. (2018). *Global warming of 1.5° C: An IPCC special report on the impacts of global warming of 1.5° C above pre-industrial levels and related global greenhouse gas emission pathways, in the context of strengthening the global response to the threat of climate change, sustainable development, and efforts to eradicate poverty*: Intergovernmental Panel on Climate Change. Retrieved from <https://www.ipcc.ch/sr15/>.
- ISO 15927-3. (2009). Hygrothermal performance of buildings - calculation and presentation of climatic data-Part 3: Calculation of a driving rain index for

- vertical surfaces from hourly wind and rain data. In *BS EN ISO* (Vol. 2009, pp. 15927-15923). International Organization for Standardization; 2009.
- Istchuk, R. N., & Ghisi, E. (2023). Influence of Design Variables on the Financial Feasibility of Rainwater Harvesting Systems. *Water*, 15(6), 1112. <https://doi.org/10.3390/w15061112>
- Isyumov, N. (2012). Alan G. Davenport's mark on wind engineering. *Journal of Wind Engineering and Industrial Aerodynamics*, 104, 12-24. <https://doi.org/10.1016/j.jweia.2012.02.007>
- Iusupova, E., Aglyamova, Z., & Korotkova, S. (2019). Creating conceptual model of a multifunctional residential building based on sustainable design methods. *Izvestiya KGASU*, 2(48), 108-115.
- Jamaluddin, S., & Huang, Y. (2007). *NAHRIM's experince in rainwater utilisation system research*. Paper presented at the Rainwater Utilization Colloquium on 19 & 20 April 2007 at NAHRIM Mini Auditorium.
- Jedwab, R., Loungani, P., & Yezer, A. (2021). Comparing cities in developed and developing countries: Population, land area, building height and crowding. *Regional Science and Urban Economics*, 86, 103609. <https://doi.org/10.1016/j.regsciurbeco.2020.103609>
- Jiménez, A., Saikia, P., Giné, R., Avello, P., Leten, J., Liss Lymer, B., . . . Ward, R. (2020). Unpacking water governance: A framework for practitioners. *Water*, 12(3), 827. <https://doi.org/10.3390/w12030827>
- Johnson, M. S., Coon, W. F., Mehta, V. K., Steenhuis, T. S., Brooks, E. S., & Boll, J. (2003). Application of two hydrologic models with different runoff mechanisms to a hillslope dominated watershed in the northeastern US: a comparison of HSPF and SMR. *Journal of hydrology*, 284(1-4), 57-76. <https://doi.org/10.1016/j.jhydrol.2003.07.005>
- Jones, M. P., & Hunt, W. F. (2010). Performance of rainwater harvesting systems in the southeastern United States. *Resources, Conservation and Recycling*, 54(10), 623-629. <https://doi.org/10.1016/j.resconrec.2009.11.002>
- Juneng, L., Tangang, F., & Reason, C. (2007). Numerical case study of an extreme rainfall event during 9–11 December 2004 over the east coast of Peninsular Malaysia. *Meteorology and Atmospheric Physics*, 98(1-2), 81-98. <https://doi.org/10.1007/s00703-006-0236-1>
- Jung, C. G., & Kim, S. J. (2017). Evaluation of land use change and groundwater use impact on stream drying phenomena using a grid-based continuous hydrologic model. *Paddy and water environment*, 15, 111-122. <https://doi.org/10.1007/s10333-016-0533-3>
- Júnior, A. R. B. (2022). *Elementos de Hidrologia aplicada*: Editora Blucher.
- Juras, P., & Jakubcik, M. (2017). Comparison of driving rain index calculated according to EN 15927-3 to the CFD simulation and experimental measurement. *Applied Mechanics and Materials*, 861, 239-246. <https://doi.org/10.4028/www.scientific.net/AMM.861.239>
- Kahinda, J. M., Lillie, E., Taigbenu, A., Taute, M., & Boroto, R. (2008). Developing suitability maps for rainwater harvesting in South Africa. *Physics and Chemistry of the Earth, Parts A/B/C*, 33(8-13), 788-799. <https://doi.org/10.1016/j.pce.2008.06.047>
- Khoury-Nolde, N. (2010). Rainwater harvesting. *Zero-M organization, Germany*. Retrieved from https://jaaiwest.in/sites/default/files/idea_exchange_docs/Rainwater_Harvesting_-_an_overview_.pdf
- Kiernan, D. (2014). *Natural Resources Biometrics - Chapter 7*: Open SUNY. Retrieved from <https://milnepublishing.geneseo.edu/natural-resources-biometrics/>.

- Kim, E., Jung, J., Hapsari, G., Kang, S., Kim, K., Yoon, S., . . . Choe, J. K. (2018). Economic and environmental sustainability and public perceptions of rooftop farm versus extensive garden. *Building and Environment*, 146, 206-215. <https://doi.org/10.1016/j.buildenv.2018.09.046>
- Korsgaard, T. M. (1962). *Correlation between measured driving rain and computed driving rain*. Copenhagen: The Heat Insulation Laboratory. Technical University of Denmark.
- Kragh, M. K., & Svendsen, S. (1998). *Microclimatic conditions at the external surface of building envelopes*. (Ph. D). Technical University of Denmark. Retrieved from <https://core.ac.uk/download/pdf/13738237.pdf>
- Kristensen, L. (1992). *The cup anemometer and other exciting instruments*. 83 Risoe National Lab, Roskilde (Denmark), Meteorology and Wind Energy, Denmark: Risoe National Lab., Roskilde (Denmark). Meteorology and Wind Energy, Denmark. Retrieved from <https://www.osti.gov/etdeweb/biblio/7112367>
- Krpan, R. (2013). *Wind-driven Rain on Buildings in Metro Vancouver: Parameters for Rain Penetration Testing of Window Assemblies*. Concordia University. Retrieved from <https://spectrum.library.concordia.ca/id/eprint/975105/>
- Kubilay, A. (2014). *Numerical simulations and field experiments of wetting of building facades due to wind-driven rain in urban areas*. ETH Zurich, <https://doi.org/10.3929/ethz-a-010402114>
- Kubilay, A., Derome, D., Blocken, B., & Carmeliet, J. (2014a). High-resolution field measurements of wind-driven rain on an array of low-rise cubic buildings. *Building and Environment*, 78, 1-13. <https://doi.org/10.1016/j.buildenv.2014.04.004>
- Kubilay, A., Derome, D., Blocken, B., & Carmeliet, J. (2014b). Numerical simulations of wind-driven rain on an array of low-rise cubic buildings and validation by field measurements. *Building and environment*, 81, 283-295. <https://doi.org/10.1016/j.buildenv.2014.07.008>
- Lacy, R. (1965). *Driving-rain maps and the onslaught of rain on buildings*. Paper presented at the 2nd International CIB/RILEM Symposium on moisture problems in Buildings, August 16-19, 1965, Helsinki, Finland.
- Lacy, R. (1977). *Climate and building in Britain*. Her Majesty's Stationery Office, London.
- Lani, N. H. M., Syafiuddin, A., Yusop, Z., & Amin, M. Z. M. (2018a). Performance of small and large scales rainwater harvesting systems in commercial buildings under different reliability and future water tariff scenarios. *Science of the total environment*, 636, 1171-1179. <https://doi.org/10.1016/j.scitotenv.2018.04.418>
- Lani, N. H. M., Yusop, Z., & Syafiuddin, A. (2018b). A review of rainwater harvesting in Malaysia: Prospects and challenges. *Water*, 10(4), 506. <https://doi.org/10.3390/w10040506>
- LCC. (2007). *Tall Buildings - SPD & Final SA Environmental Report*. Leicester City Council (LCC), UK. Retrieved from <https://www.leicester.gov.uk/media/179117/tall-buildings-spd-april-2007.pdf>
- Leandro, J., & Martins, R. (2016). A methodology for linking 2D overland flow models with the sewer network model SWMM 5.1 based on dynamic link libraries. *Water Science and Technology*, 73(12), 3017-3026. <https://doi.org/10.2166/wst.2016.171>
- Lee, K. E., Mokhtar, M., Hanafiah, M. M., Halim, A. A., & Badusah, J. (2016). Rainwater harvesting as an alternative water resource in Malaysia: potential, policies and development. *Journal of Cleaner Production*, 126, 218-222. <https://doi.org/10.1016/j.jclepro.2016.03.060>

- Leggett, D., Brown, R., Stanfield, G., Brewer, D., & Holli, E. (2001). *Rainwater and Greywater Recycling in Buildings: Decision Making for Water Conservation*: Construction Industry Research and Information Association (CIRIA), London, UK.
- Lehmann, S. (2014). Low carbon districts: Mitigating the urban heat island with green roof infrastructure. *City, Culture and Society*, 5(1), 1-8. <https://doi.org/10.1016/j.ccs.2014.02.002>
- Lemonsu, A., Masson, V., & Berthier, E. (2007). Improvement of the hydrological component of an urban soil–vegetation–atmosphere–transfer model. *Hydrological Processes: An International Journal*, 21(16), 2100-2111. <https://doi.org/10.1002/hyp.6373>
- Li, G.-F., Xiang, X.-Y., Tong, Y.-Y., & Wang, H.-M. (2013). Impact assessment of urbanization on flood risk in the Yangtze River Delta. *Stochastic Environmental Research and Risk Assessment*, 27, 1683-1693. <https://doi.org/10.1007/s00477-013-0706-1>
- Li, Y., Huang, J. J., Hu, M., Yang, H., & Tanaka, K. (2020). Design of low impact development in the urban context considering hydrological performance and life - cycle cost. *Journal of Flood Risk Management*, 13(3), e12625. <https://doi.org/10.1111/jfr3.12625>
- Li, Z., Boyle, F., & Reynolds, A. (2010). Rainwater harvesting and greywater treatment systems for domestic application in Ireland. *Desalination*, 260(1-3), 1-8. <https://doi.org/10.1016/j.desal.2010.05.035>
- Lim, E., Das, U., Pan, C., Abdullah, K., & Wong, C. (2013). Investigating variability of outgoing longwave radiation over peninsular Malaysia using wavelet transform. *Journal of Climate*, 26(10), 3415-3428. <https://doi.org/10.1175/JCLI-D-12-00345.1>
- Liu, Z., Li, W., Chen, Y., Luo, Y., & Zhang, L. (2019). Review of energy conservation technologies for fresh air supply in zero energy buildings. *Applied Thermal Engineering*, 148, 544-556. <https://doi.org/10.1016/j.applthermaleng.2018.11.085>
- Lobelle, G. (2012). *Statistical analysis of field measured wind driven rain data in the coastal British Columbia* (Master). Universiteit Gent. Retrieved from https://libstore.ugent.be/fulltxt/RUG01/001/887/146/RUG01-001887146_2012_0001_AC.pdf
- Machado, R. E., Cardoso, T. O., & Mortene, M. H. (2022). Determination of runoff coefficient (C) in catchments based on analysis of precipitation and flow events. *International Soil and Water Conservation Research*, 10(2), 208-216. <https://doi.org/10.1016/j.iswcr.2021.09.001>
- Masters, F. J., Gurley, K. R., Prevatt, D. O., Rivers, B., & Kiesling, A. (2013). *Wind-Driven Rain Effects on Buildings, Task Committee on Wind-Driven Rain Effects, Environmental Wind Engineering Committee, Technical Council on Wind Engineering, ASCE* (12-00005-00). (E. W. E. C. Task Committee on Wind-Driven Rain Effects, Technical Council on Wind Engineering, ASCE., Trans. A. S. o. C. E. (ASCE) Ed.). 143: Engineering School for Sustainable Infrastructure & Environment, University of Florida. Retrieved from http://www.floridabuilding.org/fbc/commission/FBC_0613/HRAC/2012_2013_Task_3_Final_Report.pdf
- Mazzucato, M., Okonjo-Iweala, N., Rockström, J., & Shanmugaratnam, T. (2023). *Turning the Tide: A Call to Collective Action*. Global Commission on the Economics of Water. Retrieved from <https://turningthetide.watercommission.org/>

- Mbilinyi, B., Tumbo, S., Mahoo, H., Senkondo, E., & Hatibu, N. (2005). Indigenous knowledge as decision support tool in rainwater harvesting. *Physics and Chemistry of the Earth, Parts a/b/c*, 30(11-16), 792-798. <https://doi.org/10.1016/j.pce.2005.08.022>
- Mbua, R. L. (2013). *Water supply in Buea, Cameroon: analysis and the possibility of rainwater harvesting to stabilize the water demand*. BTU Cottbus-Senftenberg. Retrieved from <https://nbn-resolving.org/urn:nbn:de:kobv:co1-opus-29522>
- McManamay, R. A., DeRolph, C. R., Surendran-Nair, S., & Allen-Dumas, M. (2019). Spatially explicit land-energy-water future scenarios for cities: Guiding infrastructure transitions for urban sustainability. *Renewable and Sustainable Energy Reviews*, 112, 880-900. <https://doi.org/10.1016/j.rser.2019.06.011>
- Mekdaschi, R., & Liniger, H. (2013). *Water harvesting: guidelines to good practice*: Centre for Development and Environment. Retrieved from <https://boris.unibe.ch/id/eprint/46509>.
- MESTECC. (2018). *Malaysia's Third National Communication and Second Biennial Update Report submitted to the United Nations Framework Convention on Climate Change in September 2018*. Putrajaya, Malaysia: Ministry of Energy, Science, Technology, Environment and Climate Change Retrieved from https://unfccc.int/sites/default/files/resource/Malaysia%20NC3%20BUR2_final%20high%20res.pdf
- METMalaysia. (2017). *Annual Report 2017*. 90 Jabatan Meteorologi Malaysia. Retrieved from <https://www.met.gov.my/en/penerbitan/laporan-tahunan/>
- METMalaysia. (2018). *Annual Report 2018*. 92 Jabatan Meteorologi Malaysia. Retrieved from <https://www.met.gov.my/en/penerbitan/laporan-tahunan/>
- METMalaysia. (2019). *Annual Report 2019*. 94 Jabatan Meteorologi Malaysia. Retrieved from <https://www.met.gov.my/en/penerbitan/laporan-tahunan/>
- METMalaysia. (2020). *Annual Report 2020*. 73 Jabatan Meteorologi Malaysia. Retrieved from <https://www.met.gov.my/en/penerbitan/laporan-tahunan/>
- METMalaysia. (2021). *Annual Report 2021*. 121 Jabatan Meteorologi Malaysia. Retrieved from <https://www.met.gov.my/en/penerbitan/laporan-tahunan/>
- Mihaila, M. (2014). City architecture as cultural ingredient. *Procedia-Social and Behavioral Sciences*, 149, 565-569. <https://doi.org/10.1016/j.sbspro.2014.08.211>
- Mishra, A. (2014). Soil and Water Conservation Engineering - Module 9: Water Harvesting - Lesson 28 Water Harvesting. Retrieved from <http://ecoursesonline.iasri.res.in/course/view.php?id=54>. from Chhattisgarh Swami Vivekanand Technical University, India <http://ecoursesonline.iasri.res.in/course/view.php?id=54>
- MMD. (2024). Meteorological Instruments. Retrieved from <https://www.met.gov.my/en/pendidikan/peralatan-meteorologi/#Rain%20Gauge>. from Malaysian Meteorological Department (MMD), Ministry of Natural Resources and Environmental Sustainability <https://www.met.gov.my/en/pendidikan/peralatan-meteorologi/#Rain%20Gauge>
- Mohammed, T. A., Noor, M., & Ghazali, A. H. (2007). Study on potential uses of rainwater harvesting in urban areas. *Putrajaya Malaysia*. Retrieved from https://empslocal.ex.ac.uk/people/staff/fam203/developing%20countries%20database%20-%20Jacob%20Marsh/pdf_wat_tech_rain/University%20Putra%20-%20Rainwater%20in%20Urban%20Areas.pdf
- Mohd-Shawahid, H., Suhaimi, A., Rasyidah, M., Jamaluddin, S., Huang, Y., & Farah, M. (2007). *Policies and incentives for rainwater harvesting in Malaysia*. Paper presented at the Proceedings of the Colloquium on Rainwater Utilization, Putrajaya, Malaysia. Retrieved from

<http://www.thestar.com.my/news/story.asp?file=/2007/3/28/nation/17271769&sec=nation&=1>

- Monteiro, C. M., Calheiros, C. S., Pimentel-Rodrigues, C., Silva-Afonso, A., & Castro, P. M. (2016). Contributions to the design of rainwater harvesting systems in buildings with green roofs in a Mediterranean climate. *Water Science and Technology*, 73(8), 1842-1847. <https://doi.org/10.2166/wst.2016.034>
- Morakinyo, T. E., Lai, A., Lau, K. K.-L., & Ng, E. (2019). Thermal benefits of vertical greening in a high-density city: Case study of Hong Kong. *Urban Forestry & Urban Greening*, 37, 42-55. <https://doi.org/10.1016/j.ufug.2017.11.010>
- MSMA. (2012). *Urban Stormwater Management Manual for Malaysia* Department of Irrigation and Drainage (DID), Kuala Lumpur, Malaysia Retrieved from https://www.water.gov.my/jps/resources/PDF/MSMA2ndEdition_august_2012.pdf
- MWA. (2018). *Malaysia Water Industry Guide*. The Malaysian Water Association, Kuala Lumpur, Malaysia. Retrieved from <https://shorturl.at/MLKvd>
- Myers, L. E. (1975). Water harvesting--2000 BC to 1974 AD. *ARS W Agric Res Serv US Dep Agric*.
- Narula, P., & Sarkar, K. (2019). CHARACTERISATION OF DRIVING RAIN EXPOSURE IN INDIA USING DAILY GRIDDED DATA. Retrieved from <https://ukiericoncretecongress.com/1/files/Proceedings/pdf/UCC-2019-137.pdf>
- National Geographic. (2022). How Climate Change Impacts Water Access. Retrieved from <https://www.nationalgeographic.com/environment/article/freshwater-crisis>
- National Geographic. (2023). Freshwater Crisis - A Clean Water Crisis. Retrieved from <https://www.nationalgeographic.com/environment/article/freshwater-crisis>
- Nguyen, B. K. (2012). *Developing a Framework for Assessing Sustainability of Tall-building Projects*. (PhD). University of Sheffield. Retrieved from <https://theses.whiterose.ac.uk/2733/>
- Niemi, T. J., Kokkonen, T., Sillanpää, N., Setälä, H., & Koivusalo, H. (2019). Automated urban rainfall-runoff model generation with detailed land cover and flow routing. *Journal of Hydrologic Engineering*, 24(5), 04019011. [https://doi.org/10.1061/\(ASCE\)HE.1943-5584.0001784](https://doi.org/10.1061/(ASCE)HE.1943-5584.0001784)
- Nore, K., Blocken, B., Jelle, B. P., Thue, J. V., & Carmeliet, J. (2007). A dataset of wind-driven rain measurements on a low-rise test building in Norway. *Building and Environment*, 42(5), 2150-2165. <https://doi.org/10.1016/j.buildenv.2006.04.003>
- Novikov, S., & Gimazutdinova, E. (2021). *The vertical cities: reality or utopia of the future*. Paper presented at the E3S Web of Conferences. doi:<https://doi.org/10.1051/e3sconf/202127401014>
- O'Driscoll, M., Clinton, S., Jefferson, A., Manda, A., & McMillan, S. (2010). Urbanization effects on watershed hydrology and in-stream processes in the southern United States. *Water*, 2(3), 605-648. <https://doi.org/10.3390/w2030605>
- Oweis, T. Y. (2004). *Rainwater harvesting for alleviating water scarcity in the Drier environments of West Asia and North Africa*. Paper presented at the Proceedings of the International Workshop on Water Harvesting and Sustainable Agriculture, Moscow, Russia.
- Oweis, T. Y., Prinz, D., & Hachum, A. Y. (2012). *Rainwater harvesting for agriculture in the dry areas*: CRC press.
- Parés, M., Domene, E., & Pujol, D. S. (2004). Gestión del agua en la jardinería pública y privada de la Región Metropolitana de Barcelona. *Boletín de la Asociación de Geógrafos Españoles*.

- Patnaik, K., & Samantaray, B. (2010). *A Study of Wind Energy Potential in India*. Department of Electrical Engineering, National Institute of Technology, Rourkela. Retrieved from <http://ethesis.nitrkl.ac.in/1732/>
- Pérez-Bella, J., Domínguez-Hernández, J., Rodríguez-Soria, B., del Coz-Díaz, J., & Cano-Suñén, E. (2013a). A new method for determining the water tightness of building facades. *Building Research & Information*, 41(4), 401-414. <https://doi.org/10.1080/09613218.2013.774936>
- Pérez-Bella, J. M., Domínguez-Hernández, J., Cano-Suñén, E., Alonso-Martínez, M., & del Coz-Díaz, J. J. (2020a). Equivalence between the methods established by ISO 15927-3 to determine wind-driven rain exposure: Reanalysis and improvement proposal. *Building and Environment*, 174, 106777. <https://doi.org/10.1016/j.buildenv.2020.106777>
- Pérez-Bella, J. M., Domínguez-Hernández, J., Cano-Suñén, E., del Coz-Díaz, J. J., & Álvarez Rabanal, F. P. (2018). On the significance of the climate-dataset time resolution in characterising wind-driven rain and simultaneous wind pressure. Part II: directional analysis. *Stochastic environmental research and risk assessment*, 32, 1799-1815. <https://doi.org/10.1007/s00477-017-1480-2>
- Pérez-Bella, J. M., Domínguez-Hernández, J., Cano-Suñén, E., Martínez-Martínez, J. E., & del Coz-Díaz, J. J. (2020b). Avoiding the need to directionally determine the exposure to rainwater penetration for façade designs. *Building and Environment*, 176, 106850. <https://doi.org/10.1016/j.buildenv.2020.106850>
- Pérez-Bella, J. M., Domínguez-Hernández, J., Ibarz-Montaner, E., Orna-Carmona, M., Salesa-Bordanaba, Á., & Orr, S. A. (2024). Incorporating façade-specific climatic factors to improve the ISO 15927-3 characterisation of wind-driven rain spells: Dutch and Spanish case studies. *Developments in the Built Environment*, 17, 100326. <https://doi.org/10.1016/j.dibe.2024.100326>
- Pérez-Bella, J. M., Domínguez-Hernández, J., Rodríguez-Soria, B., del Coz-Díaz, J., Cano-Suñén, E., & Navarro-Manso, A. (2013b). An extended method for comparing watertightness tests for facades. *Building Research & Information*, 41(6), 706-721. <https://doi.org/10.1080/09613218.2013.823538>
- Pimentel-Rodrigues, C., & Silva-Afonso, A. (2017). Determination of runoff coefficients with a view to integration of green roofs with rainwater harvesting systems. *International Journal of Environmental Science*, 2. Retrieved from [https://iaras.org/iaras/filedownloads/ijes/2017/008-0052\(2017\).pdf](https://iaras.org/iaras/filedownloads/ijes/2017/008-0052(2017).pdf)
- Piñeiro, G., Perelman, S., Guerschman, J. P., & Paruelo, J. M. (2008). How to evaluate models: observed vs. predicted or predicted vs. observed? *Ecological modelling*, 216(3-4), 316-322. <https://doi.org/10.1016/j.ecolmodel.2008.05.006>
- Pinto, J., Maradni, A., Paul, J., & Azari, R. (2020). Development and Testing of a Tall Building Façade System to Collect Rainwater. *CTBUH Journal*, 2020(1), 20-25. Retrieved from <https://shorturl.at/xgMTd>
- Plescia, S., Lonescu, D., Simpson, B., Ge, H., & Krpan, R. (2008). *Wind-driven Rain Study in the Coastal Climate of British Columbia*. Sustainable Housing and Communities, Policy and Research Division, Canada Mortgage and Housing Corporation, Ottawa, Ontario, Canada Retrieved from <https://www.bchousing.org/sites/default/files/rcg-documents/2022-04/Wind-Driven-Rain-Study-BC.pdf>
- Prein, A. F., Rasmussen, R. M., Ikeda, K., Liu, C., Clark, M. P., & Holland, G. J. (2017). The future intensification of hourly precipitation extremes. *Nature climate change*, 7(1), 48-52. <https://doi.org/10.1038/nclimate3168>
- Prosdocimi, I., Kjeldsen, T., & Miller, J. (2015). Detection and attribution of urbanization effect on flood extremes using nonstationary flood - frequency

- models. *Water resources research*, 51(6), 4244-4262. <https://doi.org/10.1002/2015WR017065>
- Qin, X., Wu, X., Chiew, Y.-M., & Li, Y. (2013). A green roof test bed for stormwater management and reduction of urban heat island effect in Singapore. *British Journal of Environment and Climate Change*, 2(4), 410-420. <https://doi.org/10.9734/BJECC/2012/2704>
- Ragno, E., AghaKouchak, A., Love, C. A., Cheng, L., Vahedifard, F., & Lima, C. H. (2018). Quantifying changes in future intensity - duration - frequency curves using multimodel ensemble simulations. *Water Resources Research*, 54(3), 1751-1764. <https://doi.org/10.1002/2017WR021975>
- Rahman, A., Keane, J., & Imteaz, M. A. (2012). Rainwater harvesting in Greater Sydney: Water savings, reliability and economic benefits. *Resources, Conservation and Recycling*, 61, 16-21. <https://doi.org/10.1016/j.resconrec.2011.12.002>
- Rahman, H. A. (2021). Water Issues in Malaysia. *Int. J. Acad. Res. Bus. Soc. Sci*, 11, 860-875. <http://dx.doi.org/10.6007/IJARBSS/v11-i8/10783>
- Ratnayaka, D. D., Brandt, M. J., & Johnson, M. (2009). *Water supply* (6th Edition ed.): Butterworth-Heinemann.
- Roebuck, R., & Ashley, R. (2007). Predicting the hydraulic and life-cycle cost performance of rainwater harvesting systems using a computer based modelling tool. *Water Practice and Technology*, 2(2). <https://doi.org/10.2166/wpt.2007.046>
- Roebuck, R., Oltean - Dumbrava, C., & Tait, S. (2011). Whole life cost performance of domestic rainwater harvesting systems in the United Kingdom. *Water and Environment Journal*, 25(3), 355-365. <https://doi.org/10.1111/j.1747-6593.2010.00230.x>
- Ross, D. E. (2004). *HVAC design guide for tall commercial buildings*: American Society of Heating, Refrigerating and Air-Conditioning Engineers.
- Roy, A. H., Dybas, A. L., Fritz, K. M., & Lubbers, H. R. (2009). Urbanization affects the extent and hydrologic permanence of headwater streams in a midwestern US metropolitan area. *Journal of the North American Benthological Society*, 28(4), 911-928. <https://doi.org/10.1899/08-178.1>
- Saatcioglu, M. (2013). High-Rise buildings in natural disaster. *Encyclopedia of Natural Hazards, Encyclopedia of Earth Sciences Series; Bobrowsky, PT, Ed.* https://doi.org/10.1007/978-1-4020-4399-4_168
- Safarik, D., Wood, A., Carver, M., & Gerometta, M. (2015). A Year in Review: Tall Trends of 2014: An All-Time Record 97 Buildings of 200 Meters or Higher Completed in 2014. *CTBUH Journal*(1), 40-47.
- San, K. G. (2023). Rainwater harvesting the way to go. *The Star*. Retrieved from <https://www.thestar.com.my/news/nation/2023/05/27/rainwater-harvesting-the-way-to-go>
- Saraswat, C., Kumar, P., & Mishra, B. K. (2016). Assessment of stormwater runoff management practices and governance under climate change and urbanization: An analysis of Bangkok, Hanoi and Tokyo. *Environmental Science & Policy*, 64, 101-117. <https://doi.org/10.1016/j.envsci.2016.06.018>
- Scarano, A. (Producer). (2022). The Effects of Wind on Building Design. *Blog, education, News*. Retrieved from <https://scaranoarchitect.com/the-effects-of-wind-on-building-design/>
- Schubert, J. E., Sanders, B. F., Smith, M. J., & Wright, N. G. (2008). Unstructured mesh generation and landcover-based resistance for hydrodynamic modeling of urban flooding. *Advances in Water Resources*, 31(12), 1603-1621. <https://doi.org/10.1016/j.advwatres.2008.07.012>

- Sendanayake, S. (2016a). Life cycle analysis of ferro-cement rainwater tanks in Sri Lanka: A comparison with RRC and HDPE tanks. *International Journal of Applied Engineering Research*, 12(2), 1-8. Retrieved from https://ijaer.com/admin/upload/1501818511_S_Sendanayake_4.pdf
- Sendanayake, S. (2016b). Life cycle analysis of subsurface brick-dome rainwater tanks in Sri Lanka: a comparison with below ground RCC tanks. *International Journal of Scientific Research and Innovative Technology (IJSRIT)*, 3(8), 52-62.
- Sendanayake, S. (2016c). Optimum storage capacities for rooftop rainwater harvesting systems in Sri Lanka: development of a reference map. *Imp. J. Interdisc. Res.*, 2(10), 1722-1726.
- Sendanayake, S. (2016d). *Rainwater harvesting for urban living*: South Asian Institute of Technology and Medicine.
- Sendanayake, S., & Eslamian, S. (2021). Standards for Rainwater Catchment Design. In S. Eslamian & F. Eslamian (Eds.), *Handbook of Water Harvesting and Conservation: Basic Concepts and Fundamentals*. <https://doi.org/10.1002/9781119478911>
- Sendanayake, S., Miguntanna, N., & Jayasinghe, M. (2014). Validation of design methodology for rainwater harvesting for tropical climates. *Asian Journal of Water, Environment and Pollution*, 11(1), 87-93. <http://doi/full/10.5555/20143057076>
- Seyoum, S. D., Vojinovic, Z., Price, R. K., & Weesakul, S. (2012). Coupled 1D and noninertia 2D flood inundation model for simulation of urban flooding. *Journal of hydraulic engineering*, 138(1), 23-34. [https://doi.org/10.1061/\(ASCE\)HY.1943-7900.0000485](https://doi.org/10.1061/(ASCE)HY.1943-7900.0000485)
- Shaari, J. (2019). *Water Quantity Control For Urban Runoff*. Stormwater Management Division, Department of Irrigation and Drainage Malaysia. Retrieved from <https://tinyurl.com/5b4huv2u>
- Shaari, N., Che-Ani, A., Nasir, N., Tawil, N., & Jamil, M. (2009). *Implementation of rainwater harvesting in Sandakan: evolution of sustainable architecture in Malaysia*. Paper presented at the Proceedings of the Regional Engineering Postgraduate Conference, Kuantan, Malaysia.
- Shaari, S. M. (2020). An Overview of Rainwater Harvesting for Sustainable Future in Malaysia. *Environment-Behaviour Proceedings Journal*, 5(14), 255-261. <https://doi.org/10.21834/ebpj.v5i14.2232>
- Shafique, M., Kim, R., & Rafiq, M. (2018). Green roof benefits, opportunities and challenges—A review. *Renewable and Sustainable Energy Reviews*, 90, 757-773. <https://doi.org/10.1016/j.rser.2018.04.006>
- Shi, Y., Wang, J., Wang, J., & Qu, Y. (2016). A prior knowledge-based method to derivate high-resolution leaf area index maps with limited field measurements. *Remote Sensing*, 9(1), 13. <https://doi.org/10.3390/rs9010013>
- Silva, C. M., Sousa, V., & Carvalho, N. V. (2015). Evaluation of rainwater harvesting in Portugal: Application to single-family residences. *Resources, Conservation and Recycling*, 94, 21-34. <https://doi.org/10.1016/j.resconrec.2014.11.004>
- Simmonds, P. (2020). *ASHRAE design guide for tall, supertall, and megatall building systems* (Second ed.): ASHRAE.
- Sitterson, J., Knightes, C., Parmar, R., Wolfe, K., Avant, B., & Muche, M. (2018). *An overview of rainfall-runoff model types*. Office of Research and Development, National Exposure Research Laboratory, Athens, Georgia, 30605. Retrieved from https://cfpub.epa.gov/si/si_public_file_download.cfm?p_download_id=533906

- Skinn, H. (2020). *Bio-Chemical Analysis of the Sunk Island Drainage System, East Yorkshire*. Edge Hill University,
<http://dx.doi.org/10.13140/RG.2.2.10342.45124>
- Sonbol, M. A. (2006). *Sustainable systems of water harvesting in arid regions, a case study: Sinai Peninsula–Egypt*. Paper presented at the The 2nd International Conference on Water Resources & Arid Environment. Retrieved from
<https://icwrae-psipw.org/papers/2006/Water/12.pdf>
- Souri, F., Ge, H., & Stathopoulos, T. (2021). Wind-driven rain on buildings: Accuracy of the ISO semi-empirical model. *Journal of Wind Engineering and Industrial Aerodynamics*, 212, 104606.<https://doi.org/10.1016/j.jweia.2021.104606>
- SQL Associates. (2018). *Advancing The Foundational Capabilities in Governing Malaysia's Hydrological Resources to Achieve Water Security by leveraging EU sustainability leadership, in demand-driven innovation on collaborative solutions around allocation and water*. EU-Malaysia Chamber of Commerce and Industry (EUMCCI) Retrieved from
https://www.eurocham.my/data/ckfinder/files/Publications/Conservation_Sustainable_Mgmt_Msia_Water_Resources_20181204.pdf
- Straube, J. (2010). *Simplified prediction of driving rain on buildings: ASHRAE 160P and WUFI 4.0* Paper presented at the Proceedings of the international building physics conference. Retrieved from
https://buildingscience.com/sites/default/files/migrate/pdf/BSD-148_Simplified_Prediction_Driving_Rain.pdf
- Straube, J., & Burnett, E. (2000). *Simplified prediction of driving rain on buildings*. Paper presented at the Proceedings of the international building physics conference.
- Straube, J., & Schumacher, C. (2006). *Driving rain loads for Canadian building design*. Paper presented at the Proceedings of 10th Canadian Building Science and Technology Conference.
- Struk-Sokołowska, J., Gwoździej-Mazur, J., Jadwiszczak, P., Butarewicz, A., Ofman, P., Wdowikowski, M., & Kaźmierczak, B. (2020). The quality of stored rainwater for washing purposes. *Water*, 12(1), 252.<https://doi.org/10.3390/w12010252>
- Suhaila, J., & Jemain, A. A. (2009). Investigating the impacts of adjoining wet days on the distribution of daily rainfall amounts in Peninsular Malaysia. *Journal of Hydrology*, 368(1-4), 17-25.<https://doi.org/10.1016/j.jhydrol.2009.01.022>
- Sumner, G. (1981). The nature and development of rainstorms in Coastal East Africa. *Journal of Climatology*, 1(2), 131-152.<https://doi.org/10.1002/joc.3370010204>
- SWAMP. (2023). *Guidance Compendium for Watershed Monitoring and Assessment - Rainfall and Runoff - Section 5.1.3, Runoff Coefficient Fact Sheet*. The California Water Boards Retrieved from
https://www.waterboards.ca.gov/water_issues/programs/swamp/clean_water_team/guidance.html
- Tabari, H. (2020). Climate change impact on flood and extreme precipitation increases with water availability. *Scientific reports*, 10(1), 1-10.<https://doi.org/10.1038/s41598-020-70816-2>
- Tabari, H., Hosseinzadehtalaei, P., AghaKouchak, A., & Willems, P. (2019). Latitudinal heterogeneity and hotspots of uncertainty in projected extreme precipitation. *Environmental Research Letters*, 14(12), 124032.<https://doi.org/10.1088/1748-9326/ab55fd>
- Taib, N., Ali, Z., Abdullah, A., Yeok, F. S., & Prihatmanti, R. (2019). The performance of different ornamental plant species in transitional spaces in urban high-rise

- settings. *Urban Forestry & Urban Greening*, 43, 126393. <https://doi.org/10.1016/j.ufug.2019.126393>
- Tan, K. C. (2018). Trends of rainfall regime in Peninsular Malaysia during northeast and southwest monsoons. *Journal of Physics: Conference Series*, 995(1), 012122. <https://doi.org/10.1088/1742-6596/995/1/012122>
- Tangang, F. T. (2001). Low frequency and quasi - biennial oscillations in the Malaysian precipitation anomaly. *International Journal of Climatology: A Journal of the Royal Meteorological Society*, 21(10), 1199-1210. <https://doi.org/10.1002/joc.676>
- Toivonen, S., Rashidfarokhi, A., & Kyrö, R. (2021). Empowering upcoming city developers with futures literacy. *Futures*, 129, 102734. <https://doi.org/10.1016/j.futures.2021.102734>
- Toledo, S. A. (2015). *Environmental assessment of RWH strategies in urban areas from a life cycle perspective*. (PhD). Universitat Autònoma de Barcelona. Institut de Ciència i Tecnologia Ambientals. Retrieved from <http://hdl.handle.net/10803/311428>
- Trenberth, K. E., Jones, P. D., Ambenje, P., Bojariu, R., Easterling, D., Klein Tank, A., . . . Rusticucci, M. (2007). Observations. Surface and atmospheric climate change. Chapter 3. Retrieved from <http://www.ipcc.ch/pdf/assessment-report/ar4/wg1/ar4-wg1-chapter3.pdf>
- Tsoka, S., & Thiis, T. K. (2018). Calculation of the driving rain wall factor using ray tracing. *Journal of Wind Engineering and Industrial Aerodynamics*, 179, 190-199. <https://doi.org/10.1016/j.jweia.2018.06.008>
- Uhlenbrook, S., & Connor, R. (2019). The United Nations world water development report 2019: leaving no one behind. Retrieved from <http://hdl.handle.net/1834/42357>
- UNDESA. (2018). *68% of the world population projected to live in urban areas by 2050, says UN*. Department of Economic and Social Affairs, United Nations. Retrieved from <https://www.un.org/development/desa/en/news/population/2018-revision-of-world-urbanization-prospects.html>
- UNDESA. (2023). *International Decade for Action 'Water For Life'* Department of Economic and Social Affairs, United Nations Retrieved from https://www.un.org/waterforlifedecade/water_and_sustainable_development.shtml
- UNDP. (2006). *Coping With Water Scarcity - A strategic issue and priority for system-wide action*. (Vol. 18). Retrieved from https://www.un.org/waterforlifedecade/pdf/2006_unwater_coping_with_water_scarcity_eng.pdf
- UNFCCC. (2017). *Rainwater Harvesting as an Alternative Sources of Clean Water in Semarang City – Indonesia*. United Nations - Climate Change. Retrieved from <https://unfccc.int/climate-action/momentum-for-change/activity-database/momentum-for-change-rain-water-harvesting-as-an-alternative-sources-of-clean-water-in-semarang-city>
- Van den Brande, T., Blocken, B., & Roels, S. (2014). *Wind-driven rain and runoff on a medium-rise building: Experimental and numerical analysis*. Paper presented at the Proceedings of the Nordic Symposium on Building Physics. Retrieved from <https://lirias.kuleuven.be/1729299?limo=0>
- Van der Hoven, I. (1957). Power spectrum of horizontal wind speed in the frequency range from 0.0007 to 900 cycles per hour. *Journal of Meteorology*, 14(2), 160-164. [https://doi.org/10.1175/1520-0469\(1957\)014%3C0160:PSOHS%3E2.0.CO;2](https://doi.org/10.1175/1520-0469(1957)014%3C0160:PSOHS%3E2.0.CO;2)

- Van Gerrewey, T., Boon, N., & Geelen, D. (2022). Vertical farming: The only way is up? *Agronomy*, 12(1), 2. <https://doi.org/10.3390/agronomy12010002>
- Van Goethem, S. (2014). Rainwater runoff on building facades: numerical simulations and analysis of wetting patterns. *Universiteit Gent, Gent*.
- Van Mook, F. (1998). Description of the measurement set-up for wind and driving rain at the TUE. *Report FAGO*, 98, 44. Retrieved from <https://www.persistent-identifier.nl/urn:nbn:nl:ui:25-f00fc883-07f8-4d9d-873e-e898d80750f1>
- Vargas, D. (2009). *Rainwater harvesting: a sustainable solution to stormwater management*. The Pennsylvania State University. Retrieved from <https://etda.libraries.psu.edu/catalog/9171>
- Vázquez-Barquero, A., & Rodríguez-Cohard, J. C. (2016). Endogenous development and institutions: Challenges for local development initiatives. *Environment and Planning C: Government and Policy*, 34(6), 1135-1153. <https://doi.org/10.1177/0263774X15624924>
- Vilane, B., & Mwendera, E. (2011). An inventory of rainwater harvesting technologies in Swaziland. *African Journal of Agricultural Research*, 6(6), 1313-1321. Retrieved from <https://fr.ircwash.org/sites/default/files/Vilane-2011-inventory.pdf>
- Viljoen, N. S. (2014). *The feasibility of rainwater and stormwater harvesting within a winter rainfall climate context: A Commercial Building Focus*. University of South Africa, Pretoria. Retrieved from <http://hdl.handle.net/10500/14391>
- Wang, X., Li, Q., & Li, J. (2020). Field measurements and numerical simulations of wind-driven rain on a low-rise building during typhoons. *Journal of Wind Engineering and Industrial Aerodynamics*, 204, 104274. <https://doi.org/10.1016/j.jweia.2020.104274>
- WASH. (2018). Distribution of water resources. In *OpenWASH*: The Open University, UK. Retrieved from <https://www.open.edu/openlearncreate/mod/oucontent/view.php?id=79936§ion=4>
- White, M. (2018). *Watering the Paris Agreement at COP24*. Stockholm International Water Institute (SIWI). <https://siwi.org/latest/watering-the-paris-agreement-at-cop24/>
- WHO. (2019). *Drinking-water Factsheet*. (W. H. O. (WHO) Ed.). Retrieved from <https://www.who.int/en/news-room/fact-sheets/detail/drinking-water>
- WHO. (2020). *Rainwater collection and storage*. Water, Sanitation, Hygiene and Health Unit, Avenue Appia 20, 1211 Geneva 27, Switzerland. Retrieved from https://www.who.int/docs/default-source/wash-documents/sanitary-inspection-packages/2-tfs-rainwater-collection-storage-d.pdf?sfvrsn=8dfb1bf8_6
- WMO. (2018). *World Meteorological Organization, Guide to meteorological instruments and methods of observation* (Vol. WMO-No. 8). Retrieved from <https://library.wmo.int/idurl/4/41650>.
- WMO. (2022). *State of the Global Climate 2021*. (W. M. Organization Ed.). 57 World Meteorological Association. Retrieved from <https://shorturl.at/Cy5XP>
- Wong, C., Liew, J., Yusop, Z., Ismail, T., Venneker, R., & Uhlenbrook, S. (2016). Rainfall characteristics and regionalization in Peninsular Malaysia based on a high resolution gridded data set. *Water*, 8(11), 500. <https://doi.org/10.3390/w8110500>
- Worm, J., & Hattum, T. v. (2006). *AD43E Rainwater harvesting for domestic use*: Agromisa Foundation.
- WOW. (2018). How we measure wind. Retrieved from <https://www.metoffice.gov.uk/weather/guides/observations/how-we-measure-wind>. from Met Office, Met Office College National Meteorological Library &

- Archive, Weather Observations Website (WOW)
<https://www.metoffice.gov.uk/weather/guides/observations/how-we-measure-wind>
- Wu, W., Dandy, G. C., Maier, H. R., Maheepala, S., Marchi, A., & Mirza, F. (2017). Identification of optimal water supply portfolios for a major city. *Journal of water resources planning and management*, 143(9), 05017007.[https://doi.org/10.1061/\(ASCE\)WR.1943-5452.0000811](https://doi.org/10.1061/(ASCE)WR.1943-5452.0000811)
- WWAP. (2019). *The United Nations World Water Development Report 2019: Leaving No One Behind*. (S. a. C. O. United Nations Educational Ed.). 202: UNESCO Paris. Retrieved from <https://shorturl.at/xUB5M>
- WWDR. (2020). *Water and climate change - The United Nations World Water Development Report 2020*. UNESCO: Paris, France. Retrieved from <https://unesdoc.unesco.org/ark:/48223/pf0000373060>.
- WWF. (2014). Freshwater. Retrieved from https://www.wwf.org.my/our_work/freshwater/
- Yang, W.-Y., Li, D., Sun, T., & Ni, G.-H. (2015). Saturation-excess and infiltration-excess runoff on green roofs. *Ecological Engineering*, 74, 327-336.<https://doi.org/10.1016/j.ecoleng.2014.10.023>
- Yao, L., Wei, W., & Chen, L. (2016). How does imperviousness impact the urban rainfall-runoff process under various storm cases? *Ecological indicators*, 60, 893-905.<https://doi.org/10.1016/j.ecolind.2015.08.041>
- Yatim, Y. M. (2009). *Fire Safety Models for High-Rise Residential Building in Malaysia*. Heriot-Watt University Edinburgh. Retrieved from <http://hdl.handle.net/10399/2281>
- Yoo, C., Cho, E., Lee, M., & Kim, S. (2022). Observation Experiment of Wind-Driven Rain Harvesting from a Building Wall. *Water*, 14(4), 603.<https://doi.org/10.3390/w14040603>
- Yoo, C., Cho, E., Na, W., Kang, M., & Lee, M. (2021). Change of rainfall-runoff processes in urban areas due to high-rise buildings. *Journal of Hydrology*, 597, 126155.<https://doi.org/10.1016/j.jhydrol.2021.126155>
- Yuvaraj, D., Babu, V. M., Sunil, P., Rafi, S., Ashok, S., & Arshiya, S. (2022). Study of Wind Loads on Steel Building with and Without Different Braced System Using Tekla Structures. *International Research Journal of Engineering and Technology (IRJET)* 09(04), 8. Retrieved from <https://www.irjet.net/archives/V9/i4/IRJET-V9I429.pdf>
- Zambon, I., Colantoni, A., & Salvati, L. (2019). Horizontal vs vertical growth: Understanding latent patterns of urban expansion in large metropolitan regions. *Science of the Total Environment*, 654, 778-785.<https://doi.org/10.1016/j.scitotenv.2018.11.182>
- Zhang, G., He, B.-J., & Dewancker, B. J. (2020). The maintenance of prefabricated green roofs for preserving cooling performance: A field measurement in the subtropical city of Hangzhou, China. *Sustainable Cities and Society*, 61, 102314.<https://doi.org/10.1016/j.scs.2020.102314>
- Zhong, Q., Tong, D., Crosson, C., & Zhang, Y. (2022). A GIS-based approach to assessing the capacity of rainwater harvesting for addressing outdoor irrigation. *Landscape and Urban Planning*, 223, 104416.<https://doi.org/10.1016/j.landurbplan.2022.104416>
- Zhou, J., Liu, J., Wang, H., Wang, Z., & Mei, C. (2018). Water dissipation mechanism of residential and office buildings in urban areas. *Science China Technological Sciences*, 61, 1072-1080.<https://doi.org/10.1007/s11431-017-9193-8>
- Zhou, J., Liu, J., Yan, D., Wang, H., Wang, Z., Shao, W., & Luan, Y. (2019). Dissipation of water in urban area, mechanism and modelling with the

- consideration of anthropogenic impacts: A case study in Xiamen. *Journal of Hydrology*, 570, 356-365.<https://doi.org/10.1016/j.jhydrol.2018.12.054>
- Zhou, X., Kubilay, A., Derome, D., & Carmeliet, J. (2023). Comparison of wind-driven rain load on building facades in the urban environment and open field: A case study on two buildings in Zurich, Switzerland. *Building and Environment*, 233, 110038.<https://doi.org/10.1016/j.buildenv.2023.110038>
- Zhu, K., Zhang, L., Hart, W., Liu, M., & Chen, H. (2004). Quality issues in harvested rainwater in arid and semi-arid Loess Plateau of northern China. *Journal of arid environments*, 57(4), 487-505.[https://doi.org/10.1016/S0140-1963\(03\)00118-6](https://doi.org/10.1016/S0140-1963(03)00118-6)

Universiti Malaysia